

1993

# Investigation of the phase equilibria and phase transformations associated with the $\text{Bi}_2\text{Sr}_2\text{CaCu}_2\text{O}_y$ superconductor

Terry George Holesinger  
*Iowa State University*

Follow this and additional works at: <https://lib.dr.iastate.edu/rtd>

 Part of the [Condensed Matter Physics Commons](#), and the [Materials Science and Engineering Commons](#)

---

## Recommended Citation

Holesinger, Terry George, "Investigation of the phase equilibria and phase transformations associated with the  $\text{Bi}_2\text{Sr}_2\text{CaCu}_2\text{O}_y$  superconductor" (1993). *Retrospective Theses and Dissertations*. 10449.  
<https://lib.dr.iastate.edu/rtd/10449>

This Dissertation is brought to you for free and open access by the Iowa State University Capstones, Theses and Dissertations at Iowa State University Digital Repository. It has been accepted for inclusion in Retrospective Theses and Dissertations by an authorized administrator of Iowa State University Digital Repository. For more information, please contact [digirep@iastate.edu](mailto:digirep@iastate.edu).

## **INFORMATION TO USERS**

This manuscript has been reproduced from the microfilm master. UMI films the text directly from the original or copy submitted. Thus, some thesis and dissertation copies are in typewriter face, while others may be from any type of computer printer.

**The quality of this reproduction is dependent upon the quality of the copy submitted.** Broken or indistinct print, colored or poor quality illustrations and photographs, print bleedthrough, substandard margins, and improper alignment can adversely affect reproduction.

In the unlikely event that the author did not send UMI a complete manuscript and there are missing pages, these will be noted. Also, if unauthorized copyright material had to be removed, a note will indicate the deletion.

Oversize materials (e.g., maps, drawings, charts) are reproduced by sectioning the original, beginning at the upper left-hand corner and continuing from left to right in equal sections with small overlaps. Each original is also photographed in one exposure and is included in reduced form at the back of the book.

Photographs included in the original manuscript have been reproduced xerographically in this copy. Higher quality 6" x 9" black and white photographic prints are available for any photographs or illustrations appearing in this copy for an additional charge. Contact UMI directly to order.

# **U·M·I**

University Microfilms International  
A Bell & Howell Information Company  
300 North Zeeb Road, Ann Arbor, MI 48106-1346 USA  
313/761-4700 800/521-0600



**Order Number 9321166**

**Investigation of the phase equilibria and phase transformations  
associated with the  $\text{Bi}_2\text{Sr}_2\text{CaCu}_2\text{O}_y$  superconductor**

**Holesinger, Terry George, Ph.D.**

**Iowa State University, 1993**

**U·M·I**  
300 N. Zeeb Rd.  
Ann Arbor, MI 48106



**Investigation of the phase equilibria and phase transformations  
associated with the  $\text{Bi}_2\text{Sr}_2\text{CaCu}_2\text{O}_y$  superconductor**

**by**

**Terry George Holesinger**

**A Dissertation Submitted to the  
Graduate Faculty in Partial Fulfillment of the  
Requirements for the Degree of  
DOCTOR OF PHILOSOPHY**

**Department: Physics and Astronomy  
Major: Condensed Matter Physics**

**Approved:**

Signature was redacted for privacy.

**In Charge of Major Work**

Signature was redacted for privacy.

**For the Major Department**

Signature was redacted for privacy.

**For the Graduate College**

**Iowa State University  
Ames, Iowa**

**1993**

## TABLE OF CONTENTS

ACKNOWLEDGMENTS .....	iv
ABSTRACT .....	v
1. INTRODUCTION .....	1
2. BACKGROUND .....	3
2.1. Structure of $\text{Bi}_2\text{Sr}_2\text{CaCu}_2\text{O}_y$ .....	3
2.2. Phase Equilibria .....	8
2.2.1 The phase rule .....	8
2.2.2 Previous work on $\text{Bi}_2\text{Sr}_2\text{CaCu}_2\text{O}_y$ .....	9
2.3. Formation Process of $\text{Bi}_2\text{Sr}_2\text{CaCu}_2\text{O}_y$ .....	11
2.3.1 Processing in the partially molten state .....	12
2.3.2 Crystallization from the melt .....	13
2.3.3 Crystallization from the glassy state .....	14
3. EXPERIMENTAL .....	16
3.1. Material Preparation .....	16
3.1.1 Starting materials .....	16
3.1.2 Solid state processing .....	16
3.1.3 Glass processing .....	17
3.1.4 Melt processing .....	17
3.1.5 Furnace setup .....	18
3.2. Material Analysis .....	19
3.2.1 X-ray diffraction (XRD) .....	19
3.2.2 Thermal analysis .....	19
3.2.3 Analytical electron microscopy .....	20
3.2.4 Superconducting properties .....	22
4. INTRODUCTION TO THE RESULTS .....	23
4.1. Phase Relations .....	23
4.2. Phase Transformations .....	23
5. SOLID SOLUTION REGION OF THE 2212 SUPERCONDUCTOR .....	25
5.1. Secondary Phases found with 2212 .....	26
5.1.1 Secondary phases .....	26
5.1.2 Liquid phases during sintering .....	40
5.2.1 Apparent and actual compositions .....	44
5.2.2 Solid solution regions .....	45
5.2.3 Lattice parameters .....	57
5.2.4 Transition temperatures .....	59
5.3. Discussion .....	61
5.4. Summary .....	66

6. CRYSTALLIZATION FROM THE GLASSY STATE.....	68
6.1. Characterization of the Glassy State.....	68
6.1.1 Microstructural analysis.....	68
6.1.2 Thermal analysis of the glassy material.....	69
6.1.3 Crucible reactions .....	76
6.2. Crystallization .....	85
6.2.1 Isochronal anneals.....	85
6.3. Isothermal Anneals .....	96
6.3.1 Kinetically limited phase formation.....	96
6.3.2 Equilibrium phase assemblage.....	100
6.4. Discussion .....	103
6.5. Summary .....	108
7. SOLIDIFICATION FROM THE MELT.....	110
7.1. Starting Materials.....	110
7.2. Melting and Solidification of 2201 and 2212 .....	114
7.2.1 $\text{Bi}_2\text{Sr}_{1.75}\text{Ca}_{0.25}\text{CuO}_y$ .....	114
7.2.2 $\text{Bi}_2\text{Sr}_2\text{CaCu}_2\text{O}_y$ .....	118
7.3. Formation Process of 2212 .....	129
7.4. Reversibility of Phase Formation in Ar and $\text{O}_2$ .....	131
7.5. Recovery of the Superconducting Properties.....	133
7.6. Discussion .....	134
7.7. Summary .....	142
8. DIRECTIONAL ISOTHERMAL GROWTH .....	143
8.1. Oxygen Deficient Melt-Processing.....	143
8.1.1 The oxygen deficient melt .....	144
8.1.2 Solidification in an oxygen gradient .....	145
8.1.3 Composition of the superconducting phase .....	154
8.2. Superconducting Properties .....	157
8.3. Discussion .....	159
8.4. Summary .....	161
9. CONCLUSIONS.....	162
REFERENCES .....	167



## ACKNOWLEDGMENTS

The author would like to express his gratitude to the many friends and colleagues who have helped and supported his studies for the past seven years. The author is especially thankful for the support, encouragement, and understanding of his parents, Carol and Allen Holesinger. The patience and hard work required to complete this work were learned at an early age from them.

The author would also like to extend a special thanks Dean Miller who supervised the author's work while at Argonne National Laboratories. His friendship and support are very much appreciated. The author would also like to thank his advisors, Scott Chumbley and Douglas Finnemore, for providing guidance and encouragement during the course of this research. The author would also like to thank the many members of the research groups at Argonne and Ames who assisted him in this studies and whose input has certainly influenced this work . Specifically, the author would like to thank Kevin Dennis and Matt Kramer for their help in the x-ray and magnetization measurements and Art Youngdahl for the critical current measurements. The author is also indebted to Bill McCallum, Alan Goldman, and Fran Laabs at Ames Laboratory and Iowa State University for their interesting and intriguing discussions. He is also very thankful for the expertise of and discussions with Ken Gray, Jeff Hettinger, Jay Hu, Mike Lanagan, Ken Goretti, Wai Kwok, Ulrich Welp, John Zasadzinski, Bob Kampwirth, Russ Cook, and Nestor Zaluzec.

There are also many people not directly associated with the group whom the author is deeply thankful for their help and support. He is very thankful for the expert skills of Janice Coble and Patti Boone. He is also very thankful for the friendship and understanding of his fellow graduate students Steve Fleshler, Steve Sanders, Tim Roberts, Ian Bearden, and Kelly Kirkpatrick.

Finally, the author would like to extend his gratitude to the National Science Foundation and the Department of Educational Physics at Argonne for their support.

## ABSTRACT

The solid solution region and reaction kinetics of the  $\text{Bi}_2\text{Sr}_2\text{CaCu}_2\text{O}_y$  (2212) superconductor were examined as a function of temperature and oxygen partial pressure. Compositional measurements of the 2212 solid solution region in the TEM were necessary to separate intergrowth and solid solubility effects. Based on these measurements, most of the solid solubility was determined to exist between Sr and Ca with a smaller amount between Bi and (Sr+Ca). The Bi content of the superconducting phase was never observed to drop below the stoichiometric 28.5 molar percent. In addition, the Cu concentration within the 2212 superconducting phase was found to be nearly constant and was always measured to be close to the stoichiometric 28.5 molar percent. Two substitution schemes were suggested by these results. The first is just the interchange between Sr and Ca. The second is slightly more involved. It appears that Bi can substitute for Sr and/or Ca. However, it appears to be unfavorable for the reverse substitution to occur. Only small changes in the extent of the solid solution were noticed with increasing temperatures in pure oxygen. On the other hand, a significant portion of the Ca-rich end of the solid solution was found to be unstable at low oxygen partial pressures at 800°C. The 2212 phase was found with 12 other phases in this work, most of which were also solid solutions. Hence variations in the overall cation stoichiometry and oxygen partial pressure were accommodated by changes in (1) the amount, types, and composition of the secondary phases, (2) the number of intergrowths within the 2212 phase (apparent composition), and/or (3) the solid solution composition of the 2212 phase (actual composition).

Crystallization studies from the glassy and molten states were undertaken to determine the phase transformation and kinetics associated with the formation of 2212 and other competing phases. Crystallization of nominal 2212 glasses was found to proceed in two steps with the formation of  $\text{Bi}_2\text{Sr}_{2-x}\text{Ca}_x\text{CuO}_y$  (2201) and  $\text{Cu}_2\text{O}$  followed by  $\text{Bi}_2\text{Sr}_{3-x}\text{Ca}_x\text{O}_y$ ,  $\text{CaO}$ , and  $\text{SrO}$ . The 2212 phase converts from the 2201 phase with increasing temperatures. However, its formation below 800°C was kinetically limited. At 800°C and above, a nearly full conversion to the 2212 phase was achieved after only one minute although considerably longer anneal times were necessary for the system to reach equilibrium. In low oxygen partial pressures, the solidus is reduced to approximately 750°C. Solidification studies revealed an eutectic structure separating the incongruently melting 2212 / 2201 phases at high oxygen partial pressures from the congruently melting  $\text{Bi}_2\text{Sr}_{3-x}\text{Ca}_x\text{O}_y$  (23x) and

$\text{Bi}_2\text{Sr}_{2-x}\text{Ca}_x\text{O}_y$  (22x) phases present at low oxygen partial pressures. During solidification in various oxygen partial pressures, the separation of CaO in the melt and the initial crystallization of alkaline-earth cuprates leaves behind a Bi-rich liquid from which it is impossible to form single-phase 2212. Hence, significant amounts of 2201 were also present in these samples. These problems could be reduced by melt processing in inert atmospheres. The significant reduction in the liquidus in low oxygen partial pressures was used to directionally solidify a pure melt at a constant temperature using an oxygen gradient. Bulk 2212 material produced in this manner was found to possess high transition temperatures, high intergranular critical current densities below 20K, and modest critical current densities at 77K.

## 1. INTRODUCTION

A great deal of excitement was generated with the discovery of a new class of high-temperature superconductors (HTS) having transition temperatures ( $T_c$ ) in the range of 100K[1]. Several examples of these new superconductors are  $\text{Bi}_2\text{Sr}_2\text{CaCu}_2\text{O}_y$  ( $T_c \approx 90\text{K}$ ),  $\text{YBa}_2\text{Cu}_3\text{O}_7$  ( $T_c \approx 92\text{K}$ ), and  $\text{Tl}_2\text{Ba}_2\text{Ca}_2\text{Cu}_3\text{O}_y$  ( $T_c \approx 125\text{K}$ ). One general application area for these new materials that has received a large amount of attention is the development of practical conductors for use as transmission lines or current leads. Commercial conductor applications have been limited, however, due to difficulties in fabricating these materials into practical conductor form. Two significant problems that have been encountered during processing are the presence of "weak-link" high-angle grain boundaries (HAGB) [2] and impurity phases, both of which limit intergranular critical current densities. These problems are dependent on both the techniques or processes used to texture the material to eliminate HAGB and the materials properties which determine the stable or metastable phases. The purpose of this work was to investigate the materials properties of the  $\text{Bi}_2\text{Sr}_2\text{CaCu}_2\text{O}_y$  superconductor in order to gain a deeper understanding of the phase equilibria, reaction kinetics, and high-temperature phase transformations associated with this material.

The detrimental effect of HAGB has been demonstrated in several of the high-temperature superconductors[2,3,4]. For example, HAGB were shown to reduce critical current densities in the  $\text{YBa}_2\text{Cu}_3\text{O}_{7-y}$  superconductor[5,6,7]. However, various attempts to fabricate textured  $\text{YBa}_2\text{Cu}_3\text{O}_{7-y}$  into practical lengths for conductor applications have been only partially successful. Presently, the Bi-Sr-Ca-Cu-O (BSCCO) superconductors,  $\text{Bi}_2\text{Sr}_2\text{CaCu}_2\text{O}_y$  (2212)  $T_c=90\text{K}$  and  $\text{Bi}_2\text{Sr}_2\text{Ca}_2\text{Cu}_3\text{O}_y$  (2223)  $T_c=110\text{K}$ , have been the only HTS fabricated into wires and tapes in which the weak-link problems have been successfully

suppressed[8,9]. The use of Ag substrates and/or melt-processing in the partially molten state for producing highly-textured BSCCO conductors have been well documented[8,9].

Further development of the BSCCO superconductors has been limited due to difficulties in obtaining textured material that is single-phase. Secondary phases are often found within the material after the processing. These secondary phases create barriers to the supercurrents flowing in conductors made from the BSCCO superconductors. In the case of long, thin wires, the presence of one single secondary phase anywhere along the length of the wire may be enough to completely block the current flow rendering the conductor useless. The reasons why these secondary phases are sometimes found after processing are not fully understood. Obviously, it would be beneficial to have an understanding of the materials properties of the BSCCO superconductor in order to help determine the causes for secondary phase formation during processing. However, the complexity of the five-component system has made progress in these areas slow and tedious. It was within this framework that the present studies were undertaken. This work was limited to the  $\text{Bi}_2\text{Sr}_2\text{CaCu}_2\text{O}_y$  superconductor in order to succeed at gaining a good, in-depth understanding of the phase relations, solid solution region, and phase transformations associated with this material. While the results presented here are by no means comprehensive, they do represent a significant contribution on the materials properties of the  $\text{Bi}_2\text{Sr}_2\text{CaCu}_2\text{O}_y$  superconductor.

## 2. BACKGROUND

### 2.1. Structure of $\text{Bi}_2\text{Sr}_2\text{CaCu}_2\text{O}_y$

Superconductivity in the Bi-Sr-Cu-O system was discovered by Michel *et al* in 1987[10]. The low temperature superconductor,  $\text{Bi}_2\text{Sr}_2\text{CuO}_y$ , has a transition temperature ( $T_c$ ) between 7K and 22K. Two additional high-temperature superconductors (HTS),  $\text{Bi}_2\text{Sr}_2\text{CaCu}_2\text{O}_y$  and  $\text{Bi}_2\text{Sr}_2\text{Ca}_2\text{Cu}_3\text{O}_y$ , with  $T_c$ 's of approximately 85K and 110K respectively were found by Maeda *et al* with the addition of Ca to the system[11]. The series of superconducting phases in the Bi-Sr-Ca-Cu-O system are generally described by the general formula  $\text{Bi}_2\text{Sr}_2\text{Ca}_{1-n}\text{Cu}_n\text{O}_{4+2n\pm\delta}$  where  $n = 1, 2$ , or  $3$ . These phases are often referred to by their cation stoichiometries as 2201, 2212, and 2223. Single and multiple intergrowths of phases with stacking sequences of  $n = 4, 5, 6$ , or even  $7$  can sometimes be observed in these materials[12]. However, they have not been successfully produced as single-phase material.

The 2212 superconductor can be described in terms of a cell containing perovskite-like blocks in the cell center bounded on each end by rock-salt type structures[13,14,15]. The perovskite nature of the crystal structure is a common feature of the HTS. Figure 2.1 shows the ideal  $\text{ABO}_3$  perovskite unit cell in which cation A occupies the corners of the cubic cell and is coordinated with twelve oxygen atoms while the B cation occupies the center position and is coordinated with 6 oxygen atoms[16]. In order to understand the full structure of the 2212 phase, it is instructive to consider the perovskite-like middle blocks and the rock-salt end blocks separately. Shown in Figure 2.2 is the middle portion of the cell consisting of two layers of perovskite-like blocks. The Ca and Sr atoms occupy the A sites in the ideal perovskite structure while the Cu atoms occupy the B sites. One significant deviation from the perovskite structure is a missing oxygen atom in the Ca plane. This places the Cu atoms

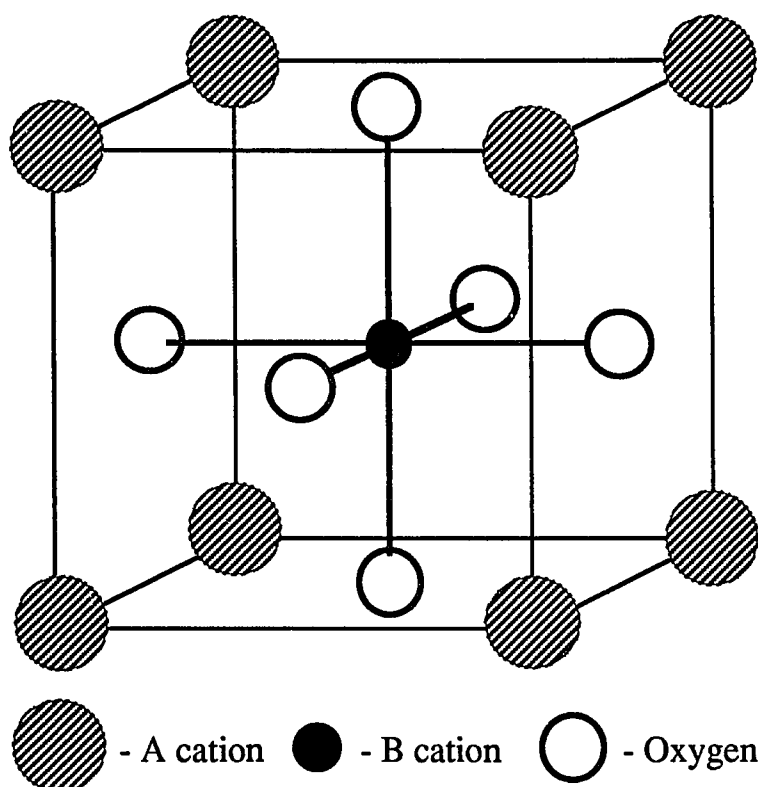


Figure 2.1 Ideal perovskite structure showing the relationship between the oxygen atoms and the cations.

in a square pyramidal coordination with the oxygen atoms. Figure 2.3 shows an idealized formulation of the rock-salt end sections. The Bi atoms occupy half of the "Na" sites and are octahedrally coordinated with six oxygen atoms. However, deviations from the ideal structure were found by several groups which give rise to the incommensurate modulation structure found in this material[17,18]. The Bi octahedra are distorted and the Bi-O distances vary substantially.

The unit cell was determined to be orthorhombic (space group Fmmm) with lattice parameters of  $5.414\text{\AA} \times 5.418\text{\AA} \times 30.89\text{\AA}$ [17,19]. Half of the unit cell of the  $\text{Bi}_2\text{Sr}_2\text{CaCu}_2\text{O}_y$  superconductor is shown in Figure 2.4. The Bi double layers are displaced from one another by one-half of the Bi-Bi spacing in the [010] direction leading to a doubling of the unit cell

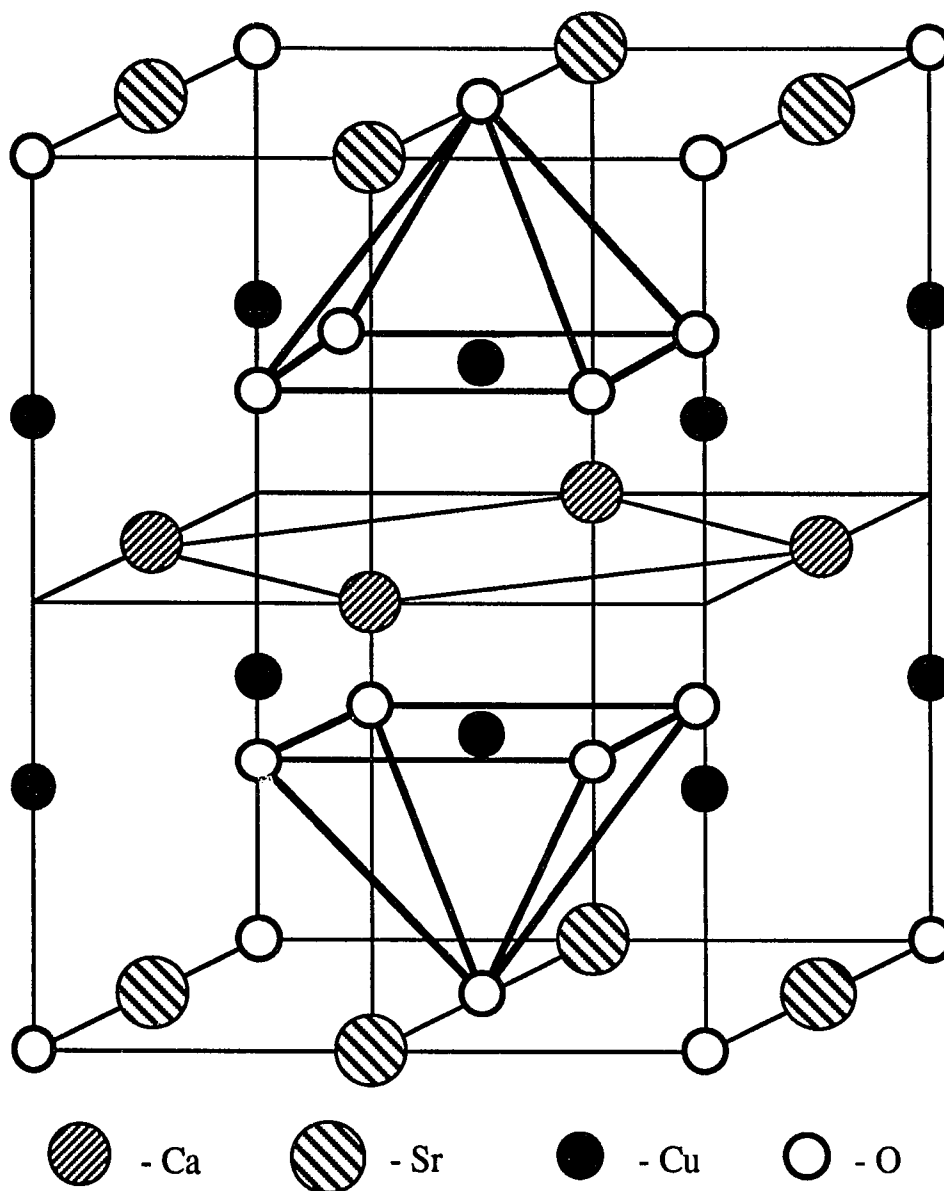


Figure 2.2 Middle section of the 2212 unit cell showing the insertion into the perovskite structure of a Ca metal layer which does not incorporate oxygen. Hence, the Cu atoms are coordinated to the oxygen atoms in square pyramidal sites.



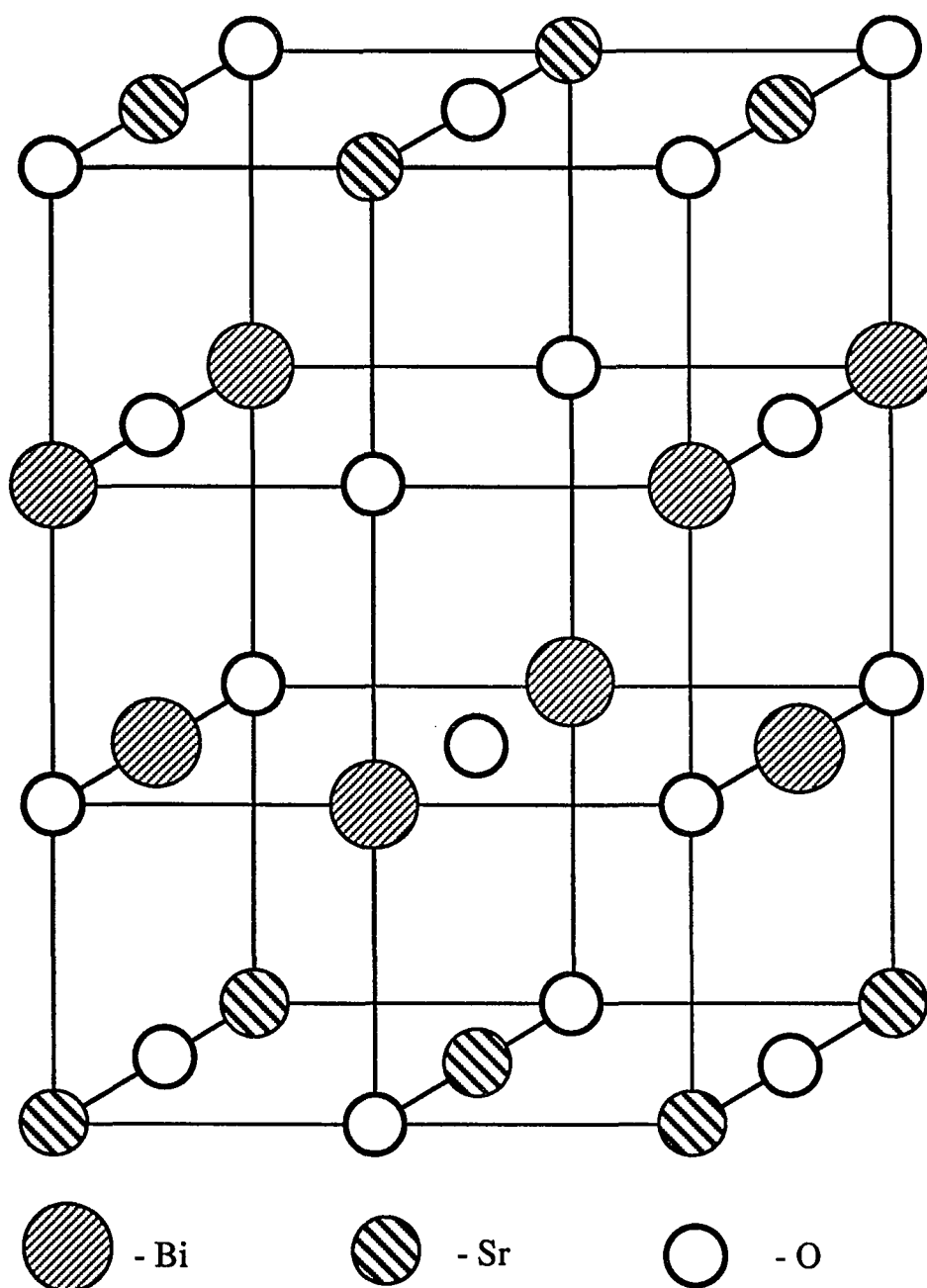


Figure 2.3 Idealized top or bottom section of the 2212 unit cell based on the NaCl structure. The Bi atoms occupy half of the "Na" sites while Sr occupies the other half. Since this unit is linked with the other unit below and above the Sr-O layers, the Sr atoms are coordinated with only five oxygen instead of six.

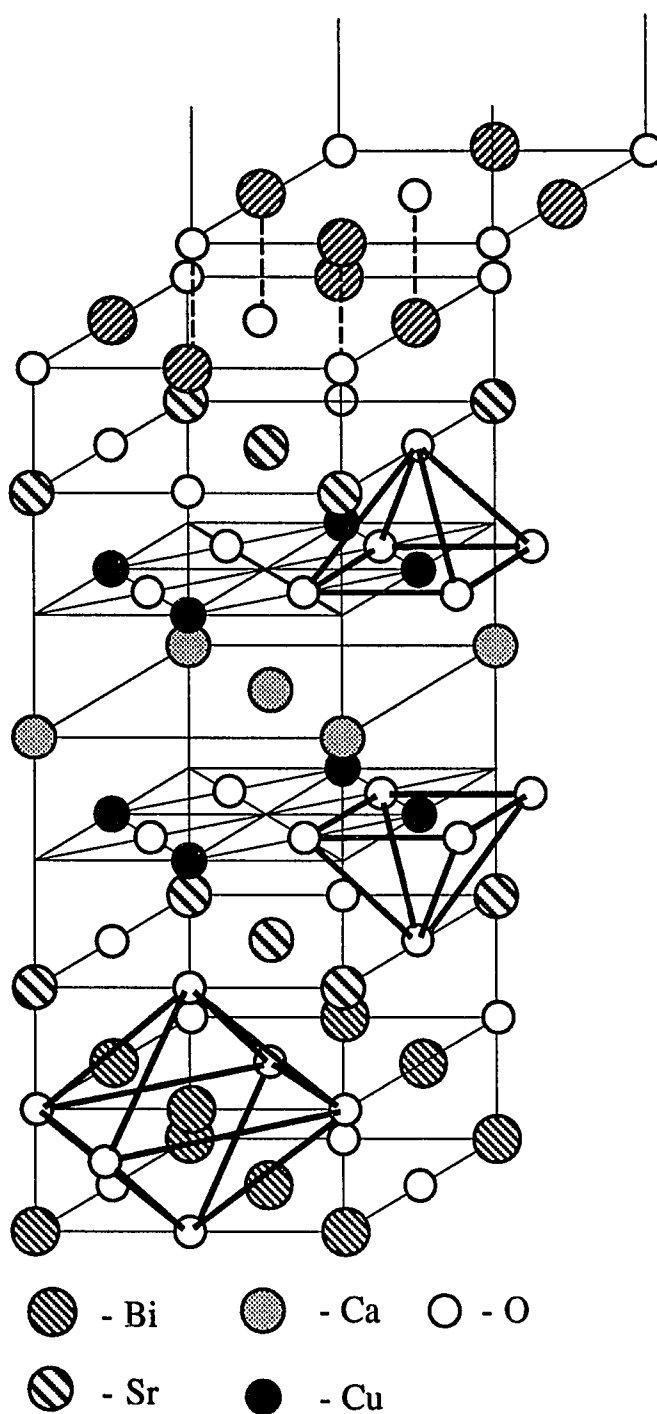


Figure 2.4 Half-unit cell of  $\text{Bi}_2\text{Sr}_2\text{CaCu}_2\text{O}_y$ . The crystallographic shear in the Bi-O layers causes a doubling of the unit cell along the c-axis from  $15.45\text{\AA}$  to  $30.9\text{\AA}$ .

along the c-axis from 15.45Å to 30.9Å. The incommensurate modulation structure that exists along the [010]. direction increases the unit cell by  $4.76 \times 5.418\text{\AA}$ [17]. The morphology of the 2212 phase is very similar to that of mica due to the Bi-O double layers. This material cleaves very easily along the basal plane.

## 2.2. Phase Equilibria

### 2.2.1 The phase rule

The basis for studies of phase equilibria lies in the Phase Rule as proposed by Willard Gibbs[20,21]. This rule may be expressed as follows:

$$F = C - P + 2 \quad (2.1)$$

where P is the number of phases present, C is the number of components of the system, and F is the number of degrees of freedom. Phases are considered as distinct, homogenous parts of the system that in principle can be mechanically separated from one another. The components of a system are usually considered as the smallest set of independent constituents that can adequately account for all phases present. Finally, the number of degrees of freedom is the number of conditions, i.e. temperature, pressure, etc., that can be varied without changing the state of the system. Since the pressure is commonly fixed during phase diagram studies, one less degree of freedom is present and the Phase Rule reduces to:

$$F = C - P + 1 \quad (2.2)$$

Applied to the present system under study, a suitable choice of components would be  $1/2\text{Bi}_2\text{O}_3$ , SrO, CaO, and CuO. If only one phase were present, the system would have four degrees of freedom and four variables could be changed, i.e. temperature and the amounts of three of the components present, without changing the state of the system. Note that fixing

the composition of three of the components is sufficient to define the alloy composition of a four component system. If three phases were present, two degrees of freedom would be present. Hence two of the five variables, temperature and the four components, could be changed without changing the state of the system. If five phases are present, there are no degrees of freedom present for the system and any change in the components or temperature would change the state of the system.

### 2.2.2 Previous work on $\text{Bi}_2\text{Sr}_2\text{CaCu}_2\text{O}_y$

It is important to understand the phase relationships between the 2212 phase and secondary phases that form equilibria with it. Likewise, a complete determination the solid-solution region for the 2212 phase is important. This information is needed for advancements in the development of these materials into practical conductors and devices. A complete understanding of the phase diagram for the Bi-Sr-Ca-Cu-O system is not yet available due to the large number of compositional and processing variables. Therefore, studies of the Bi-Sr-Ca-Cu-O system are generally simplified by fixing the partial pressure of oxygen (typically air or pure oxygen), choosing one or more temperatures that are of immediate interest, and limiting the study to specific compositional ranges or cross-sections. The system is generally represented at one temperature and oxygen partial pressure as a tetrahedron with  $\text{Bi}_2\text{O}_3$ , SrO, CaO, and CuO marking the four corners. The 2212 phase is commonly found as part of the equilibrium phase assemblage for a large volume of starting compositions within this tetrahedron. Binary and ternary systems of these oxides make up the edges and faces respectively of this tetrahedron. Most of the binaries and ternaries have been investigated and summarized in several recent works[22,23,24,25,26,27].

The 2212 and 2223 phases are the only compounds found so far that exist only as quaternary phases in this system[25,28,29]. The 2223 compound is difficult to produce as single-phase material without anneals close to the melting point, additions of Pb, and/or heat

treatments under reduced oxygen partial pressures[30,31]. This problem is illustrated by the absence of 2223 in studies carried out at temperatures below 850°C[29]. At 850°C, 2223 was observed in only one cross section through the tetrahedron with a fixed Sr:Ca ratio of 1:1[32]. In contrast, 2212 forms easily above 800°C for a large number of compositions. The 2201 phase has been reported to extend into the tetrahedron from the  $1/2\text{Bi}_2\text{O}_3\text{-SrO-CuO}$  ternary with the addition of Ca[32,33]. The 2201 phase has an orthorhombic structure and is generally reported to have an excess in Bi and deficiency in Sr[18]. This phase should be differentiated from a non-superconducting, monoclinic phase that actually has the ideal 2201 stoichiometry[34].

$\text{Bi}_2\text{Sr}_2\text{CaCu}_2\text{O}_y$  can be found in the phase assemblages for a large volume of starting compositions within the tetrahedron[27,28,29,32]. Hence, it is important to determine the exact solid solution region. A substantial amount of solid solubility is present in all three superconducting phases[27,33,35,36,37,38]. Therefore, reference to these phases as 2201, 2212, or 2223 is for identification only and does not imply specific compositions. In the case of the 2212 phase, it is generally agreed upon that the interchange between Sr and Ca accounts for most of the solid solubility exhibited by this phase. In addition, Bi concentrations in excess of the ideal stoichiometric ratio are generally found in 2212. However, there is no consensus on the exact ranges and amount of participation of each cation in the solid solution.

Pinpointing the solid solution range is difficult for several reasons. Small amounts of secondary phases are easily masked in powder x-ray scans hampering determination of phase-pure material by x-ray diffraction. As starting compositions are varied, changes occur in both the composition of 2212 and several of the secondary phases which are also solid solutions. Direct measurement of the composition of the 2212 phase by energy dispersive spectroscopy (EDS) can be affected by the presence of grain boundary phases. This problem can be particularly troublesome due to the micaous nature of the 2212 phase. Finally, each of

the superconducting phases in this system is commonly found with single or multiple intergrowths of the other superconducting phases. A compositional analysis of a 2212 grain containing significant numbers of intergrowths of 2223 and/or 2201 will represent an average of two or three phases rather than a measure of a single phase. Only when these factors are considered in any compositional analysis of the 2212 phase will an exact determination of the solid solution region be possible.

### 2.3. Formation Process of $\text{Bi}_2\text{Sr}_2\text{CaCu}_2\text{O}_y$

Knowledge of the phase equilibria and solid solution region of the 2212 superconductor is important for producing single phase material. This information in and of itself, however, is insufficient for the development of the 2212 superconductor into practical conductors and thin film devices. An understanding of the formation route, kinetics, and competing phase formation is also a necessity. Ideally, one wants to fabricate single-phase material having good superconducting properties. In reality, the enhancement of one of these properties generally occurs at the expense of the other.

Heat treatments in the partially-molten state are commonly employed during processing of the  $\text{Bi}_2\text{Sr}_2\text{CaCu}_2\text{O}_y$  (2212) superconductor in order to fabricate highly textured wires, tapes, and thick films capable of handling high critical current densities ( $J_c$ )[39,40]. In this manner, the problems associated with HAGB appear to have been reduced. Short lengths of wires or tapes processed in the partially-molten state have been reported to have  $J_c$ 's in excess of  $1 \times 10^4 \text{ A/cm}^2$  at 4.2 K in magnetic fields greater than 20 T[41,42,43]. However, it has been difficult to scale up a process to produce long length wires or tapes having comparable properties. The reason for this can be traced directly to the fact that the  $\text{Bi}_2\text{Sr}_2\text{CaCu}_2\text{O}_y$  superconductor, like so many of the HTS, melts incongruently.

### 2.3.1 Processing in the partially molten state

Due to the peritectic nature of the melting process of 2212, it is difficult to control the microstructure and phase assemblage after heat treating samples in the partially-molten state[44,45,46]. Some of the alkaline-earth cuprates that form during melt-processing of nominal 2212 samples do not disappear upon annealing below the peritectic even though they are not part of the reported equilibrium phase assemblage for the 2212 composition[46]. However, it may be possible to circumvent some of the reported problems with a suitable choice for the oxygen partial pressure during melt processing. For example, it was reported that essentially single-phase 2212 material could be produced from oxygen-deficient melt-cast samples provided the sample is not oxidized too quickly during the subsequent anneal[47].

Very little information is available in the literature on the effects of oxygen partial pressure on crystallization or solidification processes although such information is clearly needed. Oxygen deficiencies which exist in the melt can be retained in melt-cast or glassy material[47,48]. Differential thermal analysis (DTA) has shown a significant lowering of the solidus as a function of oxygen partial pressure from roughly 850°C in O<sub>2</sub> to 750°C in nitrogen[31]. Anneals in N<sub>2</sub> result in a eutectic structure consisting of Bi<sub>2</sub>Sr<sub>3-x</sub>Ca<sub>x</sub>O<sub>6</sub> and Cu<sub>2</sub>O[49]. These phases were found to be unstable when annealed in air, and, when present in melt-cast samples, helped promote the recovery of single-phase material during post-annealing. These studies all suggest that oxygen plays a key role in determining phase formation during solidification from the molten state. An understanding of how it affects phase formation is crucial for developing methods for controlling phase formation during melt-processing.

### 2.3.2 Crystallization from the melt

Previous studies have shown that  $\text{Sr}_{1-x}\text{Ca}_x\text{CuO}_2$  and a Bi-rich liquid result from the incongruent melting of 2212 around 870°C in air[50,51,52,53]. With further heating,  $\text{Sr}_{1-x}\text{Ca}_x\text{Cu}_1\text{O}_2$  transforms into  $\text{Sr}_{2-x}\text{Ca}_x\text{Cu}_1\text{O}_3$  and finally  $(\text{Sr,Ca})\text{O}$ [53]. Excesses of Bi or the presence of Ag were also found to lower the melting point by as much as 30°C. In contrast, less is understood about the sequence of crystallization events that occurs during solidification from the molten state. One study reported that the 2212 phase crystallizes from the melt around 850°C and coexists with a liquid phase[51]. With further cooling, the liquid phase crystallizes at 730°C as the low-temperature superconductor  $\text{Bi}_2\text{Sr}_{2-x}\text{Ca}_x\text{CuO}_y$  (2201). Another study reported that the 2212 phase that forms upon cooling around 870°C is unstable below 800°C and transforms into 2201[52]. There is also considerable debate as to whether the 2212 phase crystallizes directly from the melt[44,50,51,52]. or via an intermediate state involving the 2201 phase[39,40,45].

Difficulties in determining the sequence of crystallization events that occurs on cooling from the melt could stem, in part, from the experimental techniques used to examine these processes. While each of the methods may have specific advantages, they also have limitations on what can be learned from them. For example, high-temperature x-ray or neutron diffraction are appealing techniques to use in that they provide a direct look at the high-temperature phases. However, data acquisition times can be long and any transient phases that may have been present before the formation of the 2212 phase may be missed. The presence of the liquid phases at these high temperatures greatly accelerates the kinetics of phase formation. Other types of studies must rely on an interpretation of the microstructure that results from either quenching or solidification. Quenching studies must be done very carefully as different quenching techniques applied to the same material can lead to quite different results[50]. Determining the formation process from solidification studies has its drawbacks because of the many variables that can be changed during



solidification which will affect the resulting microstructures. Hence, a number of samples need to be examined in order to get a full picture of the process under investigation. Only when these limitations are addressed in a consistent manner will an accurate determination be made of the phase transformations that occur during crystallization from the melt.

### 2.3.3 Crystallization from the glassy state

It was found early on that a significant volume of compositions in the Bi-Sr-Ca-Cu-O system could be produced as glassy material by rapid solidification[54]. This processing route attracted a great deal of attention because it offered the possibility of producing extremely dense superconducting shapes using conventional glass forming and shaping techniques. From a scientific point of view, investigations of the crystallization process offered an alternative route, compared to the high-temperature studies discussed above, for examining the formation of the 2212 phase from a completely homogenous amorphous precursor.

In principle, a fully dense sample that is homogeneous on the atomic level can be obtained by glass formation. Various methods for producing the glassy state in the Bi-Sr-Ca-Cu-O system have been employed. Methods with high quench rates ( $10^5$ - $10^7$ K/s) have included splat-quenching[54], and twin-roller quenching[55]. These and other comparable methods generally produce completely or nearly amorphous material with thicknesses ranging from several hundred to a few tens of microns. Methods with slower quench rates ( $\leq 10^3$ K/s) such as pressing between metal plates can be used to produce glassy material, but often with significant amounts of one or more crystalline phases[56]. Conversion of these materials to a superconducting phase requires an understanding of the crystallization process in order to maximize the superconducting properties while controlling the microstructure and phase assemblage.

Several groups have investigated various aspects of crystallization of the 2212 phase from the amorphous state[54,55,57,58,59,60,61]. Typically, the glassy state was identified by a diffuse halo in x-ray diffraction. Differential thermal analysis (DTA) was used to identify a glass transition and one or more crystallization exotherms. Although the properties of the glass are dependent upon the quenching rate, several general characteristics of the crystallization process from DTA are evident; 1) a glass transition is generally noted around 400°C, 2) one or more crystallization exotherms have been observed starting around 450°C, 3) a small endotherm is sometimes observed around 700°C while the main melting events occur between 850°C and 900°C. Most of these studies found the low  $T_c$  phase  $\text{Bi}_2(\text{SrCa})_2\text{Cu}_1\text{O}_y$  to crystallize first. One work suggested the first crystallization product to be  $(\text{Sr,Ca})_3\text{Cu}_5\text{O}_y$ [61]. The 2212 phase was then reported to form at some point from the initial crystallization products with continued heating to higher temperatures. However, differences exist between these studies as to when the 2212 phase actually starts to form.

It is perplexing that differing interpretations of the crystallization process are found in the above studies given the fact that similarities in the DTA data suggests one general crystallization process. These discrepancies may be due to the fact that short anneals of 10 minutes or less in which oxygen uptake is limited were not used to investigate the crystallization process. As a consequence, information regarding intermediate phase formation may have been missed. Oxygen deficiencies in these quenched glasses [55]. can be expected to affect phase formation from the glassy state much in the same way as it affects the crystallization process from the melt. From this perspective, it is clear that a determination of the crystallization sequence from the glassy state would serve as an aid in determining the crystallization events that occur during solidification from the melt.

### 3. EXPERIMENTAL

#### 3.1. Material Preparation

The choice of a processing route for material preparation was dependent upon the type of sample needed in a particular study and the complex phase equilibria both above and below the peritectic involving 2212. The effects of phase equilibria on processing will be discussed in later chapters. The basic methods used in this work for the preparation of samples are presented here.

##### 3.1.1 Starting materials

The starting powders used in all experiments were  $\text{Bi}_2\text{O}_3$ ,  $\text{SrCO}_3$ ,  $\text{CaCO}_3$ , and  $\text{CuO}$ . These were obtained commercially and were of a specified purity of 99.99% or better. Powders were mixed in the appropriate molar ratios and ground in an alumina mortar and pestle until the resulting mixture was visually homogenous. The loose powders were placed in a metallurgical grade alumina crucible and calcined in a box furnace in two steps at  $780^\circ\text{C}$  and  $800^\circ\text{C}$  for at least 12 hours with thorough grindings after each step. This powder was then used as the starting material in each of the processing routes described below.

##### 3.1.2 Solid state processing

Samples initially processed by solid state reactions were never taken above  $820^\circ\text{C}$  in order to avoid the formation of  $\text{CaO}$  or alkaline-earth cuprates that occurs above the melting point of 2212[53]. Calcined powders were pressed in a 13mm diameter steel die under a force of 22,000 Newtons. The pressed pellets were then annealed for a period of 25 to 100 hours; longer anneal times were employed for lower anneal temperatures. Samples were removed from the furnace, reground, and repressed in the 13mm die under 44,500 Newtons

of force. Pellets were then annealed between 25 and 100 hours with two additional repetitions of this step. Solid state processing was generally limited to samples with high Ca contents ( $x > 1.2 \text{ Bi}_2\text{Sr}_{3-x}\text{Ca}_x\text{Cu}_2\text{O}_y$ ) for which it was difficult to splat-quench completely amorphous material.

### 3.1.3 Glass processing

Amorphous samples were prepared by a splat-quench technique[54]. Calcined powders were placed in metallurgical grade alumina or platinum crucibles and held for 45 minutes at temperatures between 1050°C and 1100°C. The molten oxide was then poured onto a stainless steel plate heated to 200°C and immediately quenched from above with a large Cu anvil. A heated plate was used in this process since it improved the integrity of the glassy material. The thickness of the glass pieces averaged 350µm with lateral dimensions extending up to a few centimeters. Processing with a cold plate resulted in shards with lateral dimensions generally less than one cm. The splat-quench method was a useful process for producing highly calcined, homogeneous material for compositions near the ideal 2212 stoichiometry. Additional information about this process can be found in Chapter 6.

### 3.1.4 Melt processing

The melt-processing steps used in the solidification study discussed in Chapter 7 generally followed the same heating and cooling rates used in differential thermal analysis (DTA) experiments. The goal of this particular study was to determine the sequence of phase transformations and reaction kinetics as a function of temperature, composition, and oxygen partial pressure. Single-crystal MgO substrates were used in these experiments since very little reaction with the molten BSCCO material was ever found and the MgO could withstand the processing temperatures of up to 1000°C used in these experiments. Melt-processing of large 2212 superconducting bars was performed as a test of the information gained in the

basic studies of crystallization and solidification. In this case, Ag or alumina boats were used to hold the molten oxide. Initial powders to be used during melt-processing were prepared as glassy material using the splat-quench technique described above. These powders were then placed in the Ag or  $\text{Al}_2\text{O}_3$  boats and melted in Ar at  $900^\circ\text{C}$ . The temperature was then lowered to  $850^\circ\text{C}$  and allowed to stabilize. At this point, the gas flow in the furnace was switched to oxygen resulting in the directional solidification of the 2212 phase from the oxygen-deficient melt. Specific details of this process can be found in Chapter 8.

### 3.1.5 Furnace setup

The bulk of the processing work was carried out in a sealed quartz-tube furnace connected to a set of mass flow controllers and a small mechanical roughing pump. The pump was used for evacuating the furnace chamber and backfilling with Ar. One end of the quartz tube was sealed while the other contained the sample holder / flange assembly which was attached to the quartz tube with epoxy. The sample holder was fashioned from Inconel 600 tube and flat stock. The gas flow within the tube originated at the sample with the outlet located on the flange. The gas flow consisted of oxygen, argon, or a mixture of the two. For the mixtures, the  $\text{O}_2$  content was set between 0.1% and 100% by volume using mass flow controllers. The balance of the gas flow was Ar and total pressure was always kept at one atmosphere. Temperatures within the furnace were monitored with type K thermocouples encased. Thermocouples used within the quartz tube were sealed in inconel sheaths for protection from the oxidizing atmospheres used during heat treatments. The furnace had a four inch hot zone in which the temperature was measured to be within  $\pm 2^\circ\text{C}$  of the setpoint.

### 3.2. Material Analysis

#### 3.2.1 X-ray diffraction (XRD)

Major phases were identified by x-ray diffraction using Philips or Rigaku powder diffractometers, both equipped with a Cu target and operated at 40 kV. Samples were prepared as fine powders that were either placed in a hollowed-out quartz glass slide (Philips) or sprinkled on silicone vacuum grease spread in a thin film on a quartz glass slide (Rigaku or Philips). Scans were typically performed using a step size of  $0.05^\circ 2\theta$  with a counting time of 3 seconds. In the case of lattice parameter measurements, step sizes of  $0.02^\circ 2\theta$  and counting times of 10 seconds were used. The lattice parameters of the 2212 phase were refined by a least squares method from powder scans using Si as an internal standard. Peak positions were identified by fitting five to seven data points around each peak to a parabola[62]. Indexing of the 2212 phase followed an orthorhombic structure (space group Fmmm)[17]. Reflections used in the calculations were (008), (113), (115), (0010), (117), (020), (200)/(202), (2010), (1115), (135), (137), (139), and (400)/(040).

#### 3.2.2 Thermal analysis

Differential thermal analysis (DTA) Temperatures of thermal events for amorphous or annealed samples were determined by DTA using a Perkin Elmer 1700 system. Samples used in the DTA consisted of approximately 40 mg of freshly ground powder. Heating rates were set at either  $2^\circ\text{C}/\text{min}$  or  $10^\circ\text{C}/\text{min}$ . All cooling rates were set at  $10^\circ\text{C}/\text{min}$ . The slower heating rate was used for an accurate determination of the melting events of the 2212 phase as a function of oxygen partial pressure. All experiments were performed under a gas flow of  $50\text{ cm}^3/\text{min}$ . Gas flows consisted of  $\text{O}_2$ , Ar, or a mixture of the two with the volume ratios set with mass flow controllers. DTA temperatures were checked against reference materials  $\text{SrCO}_3$  and  $\text{SiO}_2$  and found to be within  $\pm 3^\circ\text{C}$  of accepted values. Both the extrapolated

onset and peak temperatures are reported. Baseline changes are given in terms of onset and midpoint values.

Thermogravimetric analysis (TGA) Oxygen uptake of the glassy material was measured by a Perkin-Elmer TGA 7 system. Glass pieces of a nominal  $\text{Bi}_2\text{Sr}_2\text{Ca}_{1.2}\text{Cu}_2\text{O}_y$  stoichiometry were used. The total mass of these pieces was approximately 80mg. The heating rate was  $2^\circ\text{C}/\text{min}$  in  $\text{O}_2$  and the final temperature was  $850^\circ\text{C}$ .

### 3.2.3 Analytical electron microscopy

Scanning electron microscopy (SEM) Microstructural and compositional analysis were performed using a JEOL JXA-840A SEM equipped with an energy dispersive x-ray spectrometer (EDS) for chemical analysis. The microscope was operated at 15kV in order to minimize the excitation volume, yet provide enough over voltage in order to excite the  $\text{Cu } \alpha$  x-ray line for chemical analysis. Microstructures were examined in both the secondary and backscattered electron imaging modes. Samples were prepared for SEM analysis using standard metallographic techniques. Samples were mounted for polishing via thermo-setting plastic resins or cold-mount epoxies that cure at room temperature. Rough polishing of the samples was performed with SiC paper starting with 120 grit paper and ending with 600 grit paper. Fine polishing was performed with  $9\mu\text{m}$  and  $3\mu\text{m}$  diamond pastes and slurries. No water was used during polishing as several of the secondary phases found with 2212 react with  $\text{H}_2\text{O}$ . Final polishing was done with  $1\mu\text{m}$  and  $0.1\mu\text{m}$  diamond pastes and oil-based slurries.

Transmission electron microscopy (TEM) Transmission electron microscopy was employed to obtain additional microstructural information, determine individual grain compositions, and identify phases by electron diffraction and chemical analysis. This work was performed using a Philips CM-30 TEM equipped with an energy dispersive x-ray spectrometer (EDS). During analytical work, the microscope was operated at 100kV in order

to minimize beam damage to the thin foils. Diffraction data was obtained by selected area diffraction (SAD) and convergent beam electron diffraction (CBED). Sample preparation consisted of standard dimpling and ion-milling techniques. During ion-milling, the voltage was limited to 4kV to minimize ion damage to the samples.

Quantitative analysis with standards Quantitative chemical analysis of the superconducting and secondary phases was performed by EDS analysis using both the SEM and TEM. The standard consisted of a splat-quenched glass whose composition was determined to be  $\text{Bi}_{2.24}\text{Sr}_{1.89}\text{Ca}_{1.04}\text{Cu}_{2.02}\text{O}_y$  by an inductively coupled plasma technique (ICP). The accuracy of the ICP measurement is reported to be within  $\pm 3\%$  of the amount of each cation present. This error was found to be the principal factor which limits the accuracy of the analysis[63]. Quantitative corrections were made in the SEM and TEM by the ZAF and elemental ratio methods, respectively[64,65]. In either case, quantitative analysis was used to determine only the cation content of each phase. The measurement of the oxygen content could not, unfortunately, be easily measured by these techniques. This is an important point to consider since this work will show that changing the oxygen partial pressure during heat treatments does affect phase formation. In this work, changes that occurred in the samples as a function of oxygen partial pressure were documented by identifying changes in the phase assemblage, cation compositions, and microstructure.

Comparison of XRD, SEM, and TEM The use of each of these techniques in this work depended greatly upon the needs of the particular study. X-ray diffraction was used for the identification of primary phases and lattice parameter measurements. It was found to be inadequate in some cases for the detection of phases present in small amounts. Diffraction peaks from the primary phase(s) often overlapped the expected positions of the strongest lines for the minor phases. SEM analysis was found to be particularly important for checking on sample homogeneity and determining the composition of any minor phases that may be present in addition to the primary phases. Positive identification of the secondary phases was



obtained in the TEM by diffraction and chemical analysis. Compositional analysis of the 2212 superconducting phase was typically performed in the TEM where the effects of intergrowths and grain boundary phases on the measured composition could be accurately determined and eliminated. Obviously, the intergrowths within the superconducting phases cannot be seen in the SEM. In addition, the plate-like morphology of the 2212 superconducting phase made it difficult to exclude grain boundary phases from influencing the compositional measurements. Hence, most of the studies in this work consisted of a complimentary examination by XRD, SEM and TEM in which XRD was used to identify the primary phases, SEM was used to ascertain sample homogeneity, examine overall microstructures, and analyze compositions of secondary phases, and TEM was used for accurate compositional measurements of the superconducting phases, structural identification of the secondary phases, and examination of the fine microstructures.

#### 3.2.4 Superconducting properties

Superconducting properties were monitored by standard four-probe resistivity and magnetization measurements. Resistivity measurements were performed in a closed-cycle refrigerator with contacts made to the samples with silver paint. Additional measurements of the transition temperature were performed in a non-commercial rf-SQUID magnetometer[66]. Samples were zero-field cooled to either 40K or 4.2K at which point a 0.5 or 1.0 Oe field was applied and flux-exclusion measured on warming. Critical current densities were calculated from hysteresis loops via Bean's critical state model[67]:

$$J_c = (3/2 * (10^3/4\pi) * \Delta M) / R_0 \quad (3.1)$$

where  $\Delta M$  is in gauss,  $R_0$  is in meters, and  $J_c$  is in A/cm<sup>2</sup>. Hysteresis measurements were performed in a Quantum Design Magnetometer containing a 5T superconducting magnet. Samples for these measurement consisted of 3mm discs cut from bulk samples.

## 4. INTRODUCTION TO THE RESULTS

### 4.1. Phase Relations

Attempts to form single phase material from the multi-component Bi-Sr-Ca-Cu-O system would be greatly facilitated with information dealing with the phase equilibria and solid solution region of the primary phase of interest. In Chapter 5, a detailed study of the solid solution region of the 2212 superconductor is presented. The problems associated with intergrowths and grain boundary phases during compositional measurements have been eliminated by performing the chemical analysis in the TEM. Hence, the sum of these compositional measurements represents the most precise and accurate determination of the solid solution region of the 2212 superconductor to date. In addition, results are presented on the types of secondary phases that can be found with 2212 as a function of composition, temperature, and oxygen partial pressure. Liquid phases that are present during sintering were also identified as a function of composition and temperature. Results show that it is possible to produce single-phase material from compositions lying within the solid solution region.

### 4.2. Phase Transformations

Determination of phase formation and transformations is an important part of ultimately understanding the kinetics associated with, and the stability of, the primary phase under study. Any process by which the material of interest is produced is best served by a thorough understanding of the formation path from starting material to final product. Whether the material to be produced is for commercial purposes or for scientific study, the resulting properties should be intrinsic to the material itself and not artifacts of the process by which it was produced. This is especially true of the  $\text{Bi}_2\text{Sr}_2\text{CaCu}_2\text{O}_y$  superconductor. The wide

range of melting points of each of the simple oxides in themselves ( $\text{Bi}_2\text{O}_3$ -825°C,  $\text{SrO}$ -2430°C,  $\text{CaO}$ -2614°C, and  $\text{CuO}$ -1326°C)[68]. provide insight into the complexity of forming one single phase from four different materials with vastly different physical properties. In Chapter 6, the crystallization sequence of the 2212 phase from an amorphous precursor is determined. In this case, the material from which the superconducting phase will be formed consists of all four elements thoroughly mixed on the atomic scale in the form of a glass. In Chapter 7, the formation of the 2212 phase is examined during controlled solidification of the oxide melts. This information is of considerable use in the processing of the 2212 phase and other similar oxide phases. Chapter 8 is one such application of the these studies in which large 2212 superconducting bars are melt-processed in such a way as to minimize secondary phase formation and enhance the superconducting properties. By controlling the addition of oxygen to the sample, 2212 can be directionally solidified from the melt without the use of a temperature gradient that is normally associated with directional growth from a pure melt.

The basic studies presented in Chapters 5-7 are by no means comprehensive. However, they do provide good insight into the formation mechanism and phase stability of the 2212 superconductor and highlight competing phase developments. The results of Chapter 8 demonstrate the usefulness of the information gained in the basic studies in developing the 2212 superconductor for practical conductor applications.

## 5. SOLID SOLUTION REGION OF THE 2212 SUPERCONDUCTOR

The complexity of a four component system precludes a complete determination of the phase diagram in the foreseeable future. However, the need for equilibria data on the 2212 phase has been a driving force for at least a partial determination of the phase equilibria and solid solution region of the 2212 superconductor. In this chapter, the phases that form equilibria with 2212 were identified and the actual solid solution region of the 2212 phase was determined. The results presented here are the summation of two separate studies. The initial study covered most of the 2212 solid solution and shed some light on the causes for the discrepancies in the literature regarding the solid solution region. However, it was determined that additional work was needed to further define the Ca-rich end of the 2212 solid solution region. Hence, a second complimentary study was undertaken to address this deficiency and further extend this work to other temperatures and oxygen partial pressures.

The solid solution region of 2212 and the secondary phases that form equilibria with it were determined at temperatures of 800°C, 865°C, and 885°C in 100% O<sub>2</sub> and in oxygen partial pressures of 1.0% and 0.1% O<sub>2</sub> (balance Ar) at 800°C. Several series of samples around the ideal 2212 stoichiometry were prepared for these two studies. In the initial study, four series of samples were made in which the molar ratio of one element was varied from the "ideal" Bi<sub>2</sub>Sr<sub>2</sub>Ca<sub>1</sub>Cu<sub>2</sub>O<sub>y</sub> composition by ±0.2 and ±0.5. For example, the Bi-series consisted of samples mixed with the molar ratios of Bi<sub>x</sub>Sr<sub>2</sub>Ca<sub>1</sub>Cu<sub>2</sub>O<sub>y</sub> with x = 2.5, 2.2, 2, 1.8, and 1.5. Based on the results of the first study, a second series of samples was constructed in which the overall Cu content, relative to the other cations, of the samples was held at 28.5%. This set of compositions completely encircled the solid solution region as shown in Figure 5.1. Sample #64 was added later in the study in order to verify Bi<sub>4</sub>Sr<sub>8-x</sub>Ca<sub>x</sub>Cu<sub>5</sub>O<sub>y</sub> as an equilibrium phase with 2212. Most of the samples were initially

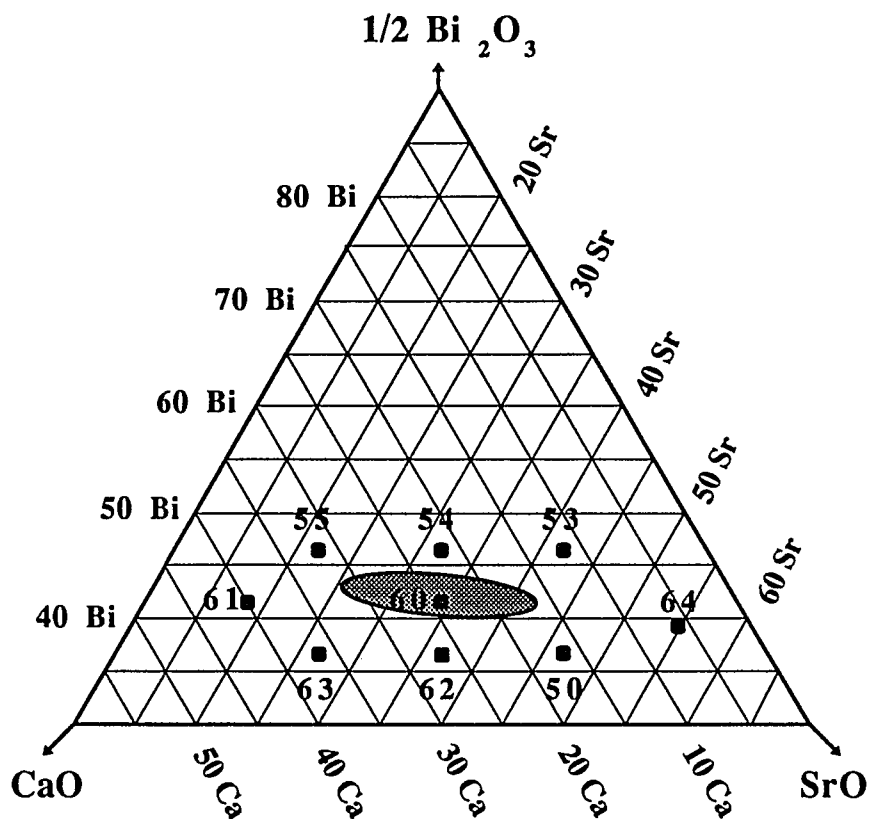


Figure 5.1 Plot of the starting compositions used in the second study. For reference, the 2212 solid solution at 865°C is also shown.

processed as a splat-quenched glasses in order to start with material that was homogeneously mixed on the atomic level. For several of the Ca-rich compounds however, significant amounts of large ( $>10\mu\text{m}$  in diameter) CaO particles were found in the glassy material. Therefore, these samples were prepared again by solid state techniques.

## 5.1. Secondary Phases found with 2212

### 5.1.1 Secondary phases

The secondary phases found with 2212 and their measured compositional ranges are listed in Table 5.1 and are in agreement with previously published works except for SrO (Ca

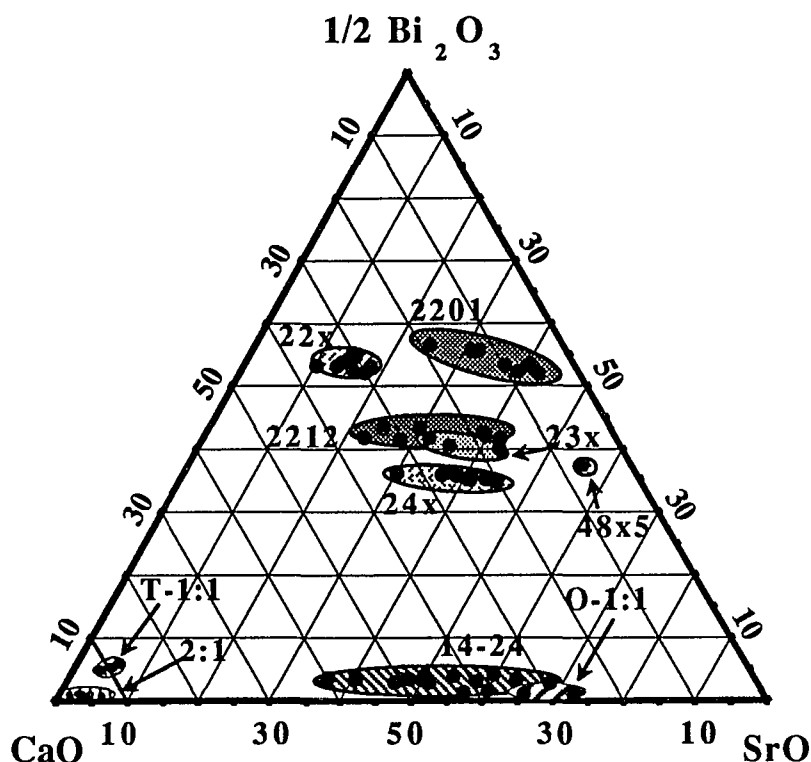


Figure 5.2 Plot of all measured secondary phase compositions along with the 2212 solid solution region on the 28.5% constant Cu-plane.

< 5 at. %)[25,27,28,29]. It should be noted that the measured compositional ranges of the secondary phases found with 2212 only partially define the solid solution region for each of these phases[22]. All of the secondary phases listed in Table 5.1, except for CuO, are solid solutions. Most of the solid solubility exists between Sr and Ca. This is clearly illustrated in Figure 5.2 where all measured compositions of the secondary phases are projected onto the 28.5% constant Cu-plane with the 2212 solid solution region.

Considerably more samples would have been needed in these studies to accurately determine phase boundaries. For illustrative purposes, the general regions around the 2212

Table 5.1 List of secondary phases found with 2212. The endpoints of the measured compositional ranges for each of the phases are also listed.

Secondary Phases	Reference Code	Max Sr	Min Sr	
$\text{Bi}_2\text{Sr}_{2-x}\text{Ca}_x\text{CuO}_y$	2201	$\text{Bi}_{2.10}\text{Sr}_{1.73}\text{Ca}_{0.13}\text{Cu}_{1.04}\text{O}_y$	$\text{Bi}_{2.25}\text{Sr}_{0.99}\text{Ca}_{0.75}\text{Cu}_{1.00}\text{O}_y$	
$\text{Bi}_2\text{Sr}_{2-x}\text{Ca}_x\text{O}_5$	22x	$\text{Bi}_{2.11}\text{Sr}_{0.80}\text{Ca}_{1.00}\text{Cu}_{0.09}\text{O}_y$	$\text{Bi}_{2.09}\text{Sr}_{0.40}\text{Ca}_{1.38}\text{Cu}_{0.14}\text{O}_y$	
$\text{Bi}_2\text{Sr}_{3-x}\text{Ca}_x\text{O}_6$	23x	$\text{Bi}_{1.96}\text{Sr}_{2.01}\text{Ca}_{0.92}\text{Cu}_{0.10}\text{O}_y$	$\text{Bi}_{2.01}\text{Sr}_{1.54}\text{Ca}_{1.30}\text{Cu}_{0.16}\text{O}_y$	
$\text{Bi}_2\text{Sr}_{4-x}\text{Ca}_x\text{O}_7$	24x	$\text{Bi}_{2.12}\text{Sr}_{2.71}\text{Ca}_{0.95}\text{Cu}_{0.22}\text{O}_y$	$\text{Bi}_{2.13}\text{Sr}_{2.18}\text{Ca}_{1.46}\text{Cu}_{0.23}\text{O}_y$	
$\text{Bi}_4\text{Sr}_{8-x}\text{Ca}_x\text{Cu}_5\text{O}_{19}$	4805	$\text{Bi}_{4.56}\text{Sr}_{6.76}\text{Ca}_{0.96}\text{Cu}_{4.71}\text{O}_y$	$\text{Bi}_{4.42}\text{Sr}_{6.71}\text{Ca}_{1.13}\text{Cu}_{4.74}\text{O}_y$	
$\text{Sr}_{14-x}\text{Ca}_x\text{Cu}_{24}\text{O}_{41}$	14-24	$\text{Bi}_{0.46}\text{Sr}_{10.66}\text{Ca}_{4.31}\text{Cu}_{22.57}\text{O}_y$	$\text{Bi}_{0.60}\text{Sr}_{5.13}\text{Ca}_{8.51}\text{Cu}_{23.75}\text{O}_y$	$\infty$
$(\text{Sr}_x\text{Ca}_{1-x})\text{CuO}_2$ $x \approx 0.15^a$	T-1:1	$\text{Bi}_{0.04}\text{Sr}_{0.05}\text{Ca}_{0.90}\text{Cu}_{1.09}\text{O}_y$	$\text{Bi}_{0.03}\text{Sr}_{0.03}\text{Ca}_{0.83}\text{Cu}_{1.03}\text{O}_y$	
$(\text{Sr,Ca})\text{CuO}_2^b$	O-1:1	$\text{Bi}_{0.01}\text{Sr}_{0.62}\text{Ca}_{0.40}\text{Cu}_{0.96}\text{O}_y$	$\text{Bi}_{0.01}\text{Sr}_{0.70}\text{Ca}_{0.34}\text{Cu}_{0.95}\text{O}_y$	
$(\text{Sr,Ca})_2\text{CuO}_3$	2:1	$\text{Sr}_{0.29}\text{Ca}_{1.75}\text{Cu}_{0.95}\text{O}_y$	$\text{Sr}_{0.04}\text{Ca}_{2.01}\text{Cu}_{0.94}\text{O}_y$	
SrO	SrO	Ca < 0.05		
CaO	CaO	Sr < 0.05		
CuO	CuO			

<sup>a</sup>This phase has a primitive tetragonal structure.

<sup>b</sup>This phase is orthorhombic.

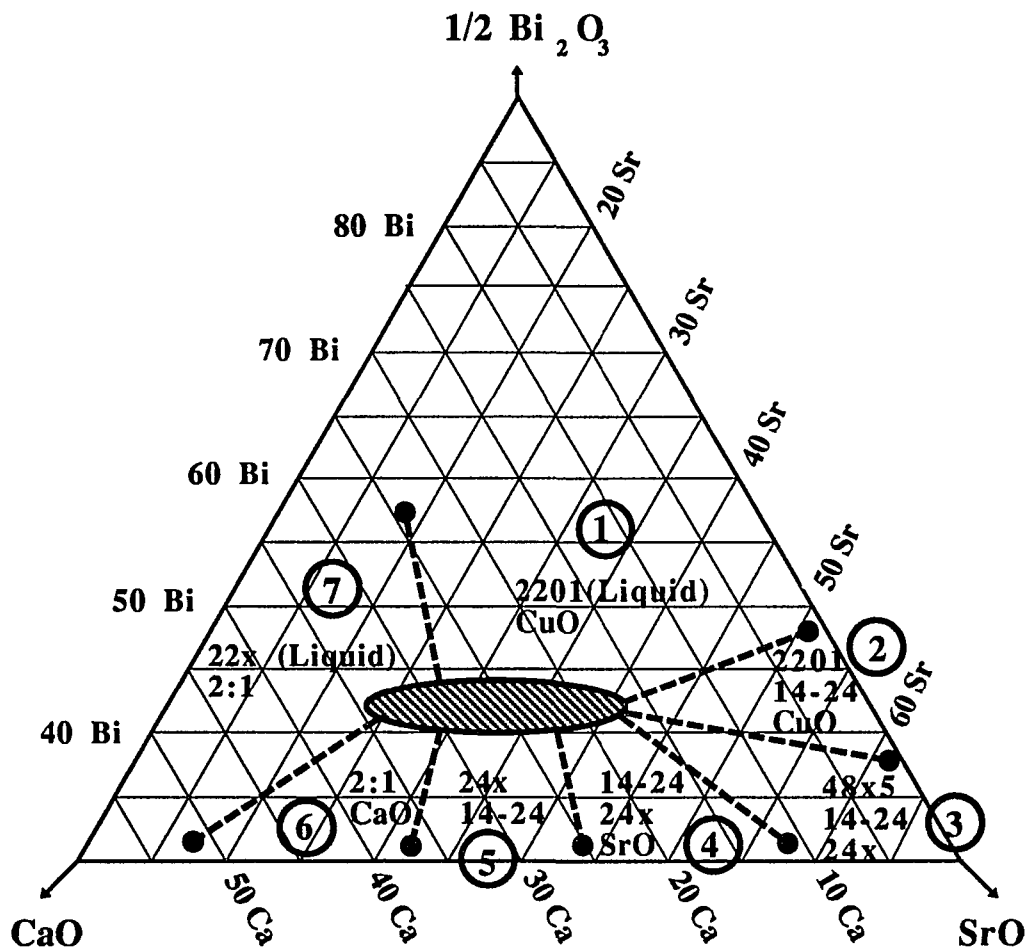


Figure 5.3 Approximate regions showing where each of the secondary phases make contact with the 2212 solid solution region at  $865^\circ\text{C}$  in  $\text{O}_2$ . At this temperature, several of the secondary phases exist as liquids as indicated above.



solid solution where the secondary phases were found are qualitatively drawn on the 28.5% Cu plane in Figure 5.3 at 865°C in oxygen. The secondary phases present in each of samples annealed at the temperatures and oxygen partial pressures used in these two studies are tabulated in Tables 5.2 - 5.7. Most annealed samples contained low volume-fractions of secondary phases making a true determination of the equilibrium phases difficult. The presence of some secondary phases was probably due to the preparation techniques. Certainly, the number of phases present cannot violate the phase rule. Such a violation would occur if all of the phases found in some samples were considered as equilibrium phases.

Simple oxides Three of the four constituent oxides, CaO, CuO, and SrO, were found in combination with the 2212 phase in annealed samples. In some cases, their presence is probably related to the preparation techniques. For example, the presence of SrO may be an artifact of the crystallization process of the glass precursors. SrO is one of the initial phases that forms during crystallization of these glasses in oxygen as will be shown in Chapter 6. It may be present simply because equilibrium has not quite been reached. For samples enriched in the alkaline earths and containing relatively more SrO after the crystallization process, 100 hours may not have been enough time for all the SrO to react and be incorporated into the other phases. This would not be surprising given the refractory nature of SrO (melting point 2430°C). The presence of CuO and CaO as equilibrium phases in some of the samples is also questionable. Shown in Figure 5.4 is a micrograph of a CuO particle embedded in sample #62 (region 5 of Figure 5.3) that was annealed in 0.1% O<sub>2</sub> at 800°C for 250 hours. The relatively large size of the particle and the lack of any homogenous distribution of CuO particles within the sample suggests that this particle is a result of insufficient grindings during the solid state preparation process. Hence, CuO is not listed in regions 5 or 6 of Figure 5.3. On the other hand, CuO is definitely one of the equilibrium phases for the Bi-rich compositions in regions 1 and 2. The same reasoning could also be applied to CaO although

Table 5.2      Phases found in equilibrium with 2212 for each of the four series of samples from study #1. (L) signifies that the phase was present as a liquid during heat treatment and solidifies when the sample is quenched in air. These samples were annealed at 865°C for 100 hours in 100% oxygen and quenched in air.

	Sample #	Process History	2201	24x	23x	22x	4 8 x 5	14-24	2:1	1:1	CuO	CaO	SrO
$\text{Bi}_2\text{Sr}_2\text{CaCu}_2\text{O}_y$	10	glass											
$\text{Bi}_{2+x}\text{Sr}_2\text{CaCu}_2\text{O}_y$													
$x = 0.5$	16	glass	L								X		
$x = 0.2$	15	glass									X		
$x = -0.2$	17	glass						X					X
$x = -0.5$	18	glass						X					X
$\text{Bi}_2\text{Sr}_{2+x}\text{CaCu}_2\text{O}_y$													
$x = 0.5$	24	glass		X				X					X
$x = 0.2$	21	glass		X				X					X
$x = -0.2$	22	glass									X		
$x = -0.5$	23	glass	L								X		
$\text{Bi}_2\text{Sr}_2\text{Ca}_{1+x}\text{Cu}_2\text{O}_y$													
$x = 0.75$	32	glass							X				X
$x = 0.5$	14	glass						X					X
$x = 0.2$	12	glass						X					
$x = -0.2$	11	glass	X					X					
$x = -0.5$	13	glass	X					X					
$\text{Bi}_2\text{Sr}_2\text{CaCu}_{2+x}\text{O}_y$													
$x = 0.5$	25	glass						X					
$x = 0.2$	26	glass						X					
$x = -0.2$	27	glass						X					
$x = -0.5$	28	glass		X									X

Table 5.3      Phases found in equilibrium with 2212 for the samples from the second study to compliment the earlier study performed at 865°C in O<sub>2</sub>. (L) signifies that the phase was present as a liquid during heat treatment and solidifies when the sample is quenched in air. These samples were annealed at 865°C for 150 hours in 100% oxygen and quenched in air.

	Sample #	Process History	2201	24x	23x	22x	4 8 x 5	14-24	2:1	1:1	CuO	CaO	SrO
Bi <sub>2.35</sub> Sr <sub>2.05</sub> Ca <sub>0.6</sub> Cu <sub>2</sub> O <sub>y</sub>	53	glass	X								X		
Bi <sub>2.35</sub> Sr <sub>1.55</sub> Ca <sub>1.1</sub> Cu <sub>2</sub> O <sub>y</sub>	54	glass	Melted										
Bi <sub>2.35</sub> Sr <sub>1.05</sub> Ca <sub>1.6</sub> Cu <sub>2</sub> O <sub>y</sub>	55	glass	Melted										
Bi <sub>2.1</sub> Sr <sub>1.7</sub> Ca <sub>1.2</sub> Cu <sub>2</sub> O <sub>y</sub>	60	solid st.				X							
Bi <sub>2.1</sub> Sr <sub>0.9</sub> Ca <sub>2.0</sub> Cu <sub>2</sub> O <sub>y</sub>	61	solid st.				L			X	X <sup>a</sup>	X	X	
Bi <sub>1.85</sub> Sr <sub>2.3</sub> Ca <sub>0.85</sub> Cu <sub>2</sub> O <sub>y</sub>	50	glass											
Bi <sub>1.85</sub> Sr <sub>1.8</sub> Ca <sub>1.35</sub> Cu <sub>2</sub> O <sub>y</sub>	62	solid st.		X				X			X		
Bi <sub>1.85</sub> Sr <sub>1.3</sub> Ca <sub>1.85</sub> Cu <sub>2</sub> O <sub>y</sub>	63	solid st.							X		X	X	

<sup>a</sup>Tetragonal 1:1 phase.

Table 5.4      Phases found in equilibrium with 2212 for the samples from the second study. (L) signifies that the phase was present as a liquid during heat treatment and solidifies when the sample is quenched in air. These samples were annealed at 885°C for 50 hours in 100% oxygen and quenched in air.

	Sample #	Process History	2201	24x	23x	22x	4 8 x 5	14-24	2:1	1:1	CuO	CaO	SrO
Bi <sub>2.35</sub> Sr <sub>2.05</sub> Ca <sub>0.6</sub> Cu <sub>2</sub> O <sub>y</sub>	53	glass	L	X							X		
Bi <sub>2.35</sub> Sr <sub>1.55</sub> Ca <sub>1.1</sub> Cu <sub>2</sub> O <sub>y</sub>	54	glass	Melted										
Bi <sub>2.35</sub> Sr <sub>1.05</sub> Ca <sub>1.6</sub> Cu <sub>2</sub> O <sub>y</sub>	55	glass	Melted										
Bi <sub>2.1</sub> Sr <sub>1.7</sub> Ca <sub>1.2</sub> Cu <sub>2</sub> O <sub>y</sub>	60	solid st.						X					
Bi <sub>2.1</sub> Sr <sub>0.9</sub> Ca <sub>2.0</sub> Cu <sub>2</sub> O <sub>y</sub>	61	solid st.	Melted										
Bi <sub>1.85</sub> Sr <sub>2.3</sub> Ca <sub>0.85</sub> Cu <sub>2</sub> O <sub>y</sub>	50	glass		X				X					X
Bi <sub>1.85</sub> Sr <sub>1.8</sub> Ca <sub>1.35</sub> Cu <sub>2</sub> O <sub>y</sub>	62	solid st.		X				X	X				
Bi <sub>1.85</sub> Sr <sub>1.3</sub> Ca <sub>1.85</sub> Cu <sub>2</sub> O <sub>y</sub>	63	solid st.				X			X				
Bi <sub>1.95</sub> Sr <sub>2.7</sub> Ca <sub>0.5</sub> Cu <sub>2</sub> O <sub>y</sub>	64	glass		X			X	X					X

Table 5.5      Phases found in equilibrium with 2212 for the samples from the second study. These samples were annealed at 800°C for 250 hours in 100% oxygen and quenched in air.

	Sample #	Process History	2201	24x	23x	22x	4 8 x 5	14-24	2:1	1:1	CuO	CaO	SrO
Bi <sub>2.35</sub> Sr <sub>2.05</sub> Ca <sub>0.6</sub> Cu <sub>2</sub> O <sub>y</sub>	53	glass	X					X			X		
Bi <sub>2.35</sub> Sr <sub>1.55</sub> Ca <sub>1.1</sub> Cu <sub>2</sub> O <sub>y</sub>	54	glass	X								X		
Bi <sub>2.35</sub> Sr <sub>1.05</sub> Ca <sub>1.6</sub> Cu <sub>2</sub> O <sub>y</sub>	55	glass	X			X					X		
Bi <sub>2.1</sub> Sr <sub>1.7</sub> Ca <sub>1.2</sub> Cu <sub>2</sub> O <sub>y</sub>	60	solid st.				X					X	X	
Bi <sub>2.1</sub> Sr <sub>0.9</sub> Ca <sub>2.0</sub> Cu <sub>2</sub> O <sub>y</sub>	61	solid st.				X					X	X	
Bi <sub>1.85</sub> Sr <sub>2.3</sub> Ca <sub>0.85</sub> Cu <sub>2</sub> O <sub>y</sub>	50	glass		X				X					X
Bi <sub>1.85</sub> Sr <sub>1.8</sub> Ca <sub>1.35</sub> Cu <sub>2</sub> O <sub>y</sub>	62	solid st.		X				X					
Bi <sub>1.85</sub> Sr <sub>1.3</sub> Ca <sub>1.85</sub> Cu <sub>2</sub> O <sub>y</sub>	63	solid st.		X		X				X <sup>a</sup>		X	
Bi <sub>1.95</sub> Sr <sub>2.7</sub> Ca <sub>0.5</sub> Cu <sub>2</sub> O <sub>y</sub>	64	glass		X			X	X					X

<sup>a</sup>Tetragonal 1:1 phase.

Table 5.6      Phases found in equilibrium with 2212 for samples from the second study. These samples were annealed at 800°C for 250 hours in 1% oxygen (balance Ar) and quenched in air.

	Sample #	Process History	2201	24x	23x	22x	4 8 x 5	14-24	2:1	1:1	CuO	CaO	SrO
Bi <sub>2.35</sub> Sr <sub>2.05</sub> Ca <sub>0.6</sub> Cu <sub>2</sub> O <sub>y</sub>	53	glass	X								X		
Bi <sub>2.35</sub> Sr <sub>1.55</sub> Ca <sub>1.1</sub> Cu <sub>2</sub> O <sub>y</sub>	54	glass	X								X		
Bi <sub>2.35</sub> Sr <sub>1.05</sub> Ca <sub>1.6</sub> Cu <sub>2</sub> O <sub>y</sub>	55	glass	X			X			X		X		
Bi <sub>2.1</sub> Sr <sub>1.7</sub> Ca <sub>1.2</sub> Cu <sub>2</sub> O <sub>y</sub>	60	solid st.			X								
Bi <sub>2.1</sub> Sr <sub>0.9</sub> Ca <sub>2.0</sub> Cu <sub>2</sub> O <sub>y</sub>	61	solid st.				X			X		X		
Bi <sub>1.85</sub> Sr <sub>2.3</sub> Ca <sub>0.85</sub> Cu <sub>2</sub> O <sub>y</sub>	50	glass								X <sup>a</sup>	X		X
Bi <sub>1.85</sub> Sr <sub>1.8</sub> Ca <sub>1.35</sub> Cu <sub>2</sub> O <sub>y</sub>	62	solid st.			X					X <sup>a</sup>		X	
Bi <sub>1.85</sub> Sr <sub>1.3</sub> Ca <sub>1.85</sub> Cu <sub>2</sub> O <sub>y</sub>	63	solid st.							X			X	
Bi <sub>1.95</sub> Sr <sub>2.7</sub> Ca <sub>0.5</sub> Cu <sub>2</sub> O <sub>y</sub>	64	glass			X		X			X <sup>a</sup>			X

<sup>a</sup>Orthorhombic 1:1 phase.

Table 5.7 Phases found in equilibrium with 2212 for samples from the second study. (L) signifies that the phase was present as a liquid during heat treatment and solidifies when the sample is quenched in air. These samples were annealed at 800°C for 250 hours in 0.1% oxygen (balance Ar) and quenched in air. Several of these samples melted completely as indicated below.

	Sample #	Process History	2201	24x	23x	22x	4 8 x 5	14-24	2:1	1:1	CuO	CaO	SrO
Bi <sub>2.35</sub> Sr <sub>2.05</sub> Ca <sub>0.6</sub> Cu <sub>2</sub> O <sub>y</sub>	53	glass	L								X		
Bi <sub>2.35</sub> Sr <sub>1.55</sub> Ca <sub>1.1</sub> Cu <sub>2</sub> O <sub>y</sub>	54	glass	Melted										
Bi <sub>2.35</sub> Sr <sub>1.05</sub> Ca <sub>1.6</sub> Cu <sub>2</sub> O <sub>y</sub>	55	glass	Melted										
Bi <sub>2.1</sub> Sr <sub>1.7</sub> Ca <sub>1.2</sub> Cu <sub>2</sub> O <sub>y</sub>	60	solid st.							X				
Bi <sub>2.1</sub> Sr <sub>0.9</sub> Ca <sub>2.0</sub> Cu <sub>2</sub> O <sub>y</sub>	61	solid st.	Melted										
Bi <sub>1.85</sub> Sr <sub>2.3</sub> Ca <sub>0.85</sub> Cu <sub>2</sub> O <sub>y</sub>	50	glass											
Bi <sub>1.85</sub> Sr <sub>1.8</sub> Ca <sub>1.35</sub> Cu <sub>2</sub> O <sub>y</sub>	62	solid st.			X				X		X		
Bi <sub>1.85</sub> Sr <sub>1.3</sub> Ca <sub>1.85</sub> Cu <sub>2</sub> O <sub>y</sub>	63	solid st.				X			X			X	
Bi <sub>1.95</sub> Sr <sub>2.7</sub> Ca <sub>0.5</sub> Cu <sub>2</sub> O <sub>y</sub>	64	glass					X			X <sup>a</sup>			

<sup>a</sup>Orthorhombic 1:1 phase.

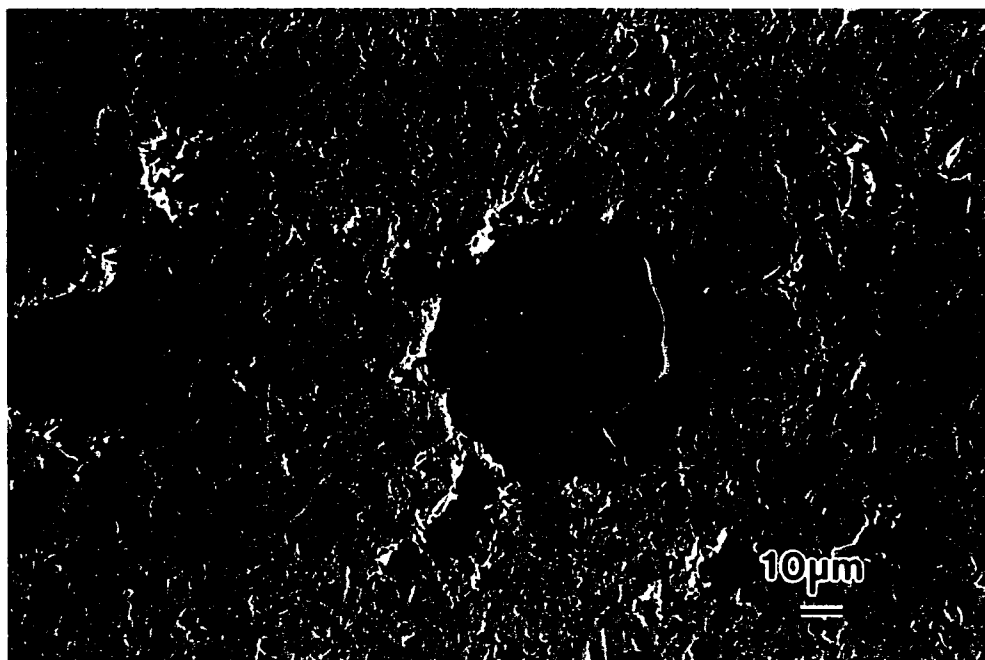


Figure 5.4 SEM secondary electron micrograph showing a large CuO particle in a sample prepared by solid state techniques. The large size of the particle and lack of any homogeneous distribution of CuO particles within the sample suggests that the particle shown above is an artifact of the preparation process.



it is less clear in this case. There did seem to be some sort of distribution of CaO particles within the samples. CaO is listed as a phase that forms equilibria with 2212 in region 6 of Figure 5.3 although its presence can still be considered as questionable.

Alkaline-earth bismuthates Three alkaline-earth bismuthates [22].,  $\text{Bi}_2\text{Sr}_{2-x}\text{Ca}_x\text{O}_y$  (22x),  $\text{Bi}_2\text{Sr}_{3-x}\text{Ca}_x\text{O}_y$  (23x), and  $\text{Bi}_2\text{Sr}_{4-x}\text{Ca}_x\text{O}_y$  (24x), were found in these studies. The 22x phase was found to form equilibria with 2212 in the Ca-rich samples of region 7 in Figure 5.3. DTA results suggested that 22x melts around 820°C in samples in which it is present. Hence, the 22x phase was present as a liquid during some of the anneals as noted in Tables 5.3-5.7. The 24x phase was found in compositions from regions 3, 4, and 5 of Figure 5.3. It was stable at all of the temperatures examined in 100%  $\text{O}_2$ . Measured compositions of the 22x and 24x phases were found to be Bi-rich and alkaline-earth deficient compared to their ideal stoichiometries. The 23x was found to replace the 24x phase in the samples annealed at 800°C in 1% and 0.1%  $\text{O}_2$ . Apparently, 24x is stable only at high oxygen partial pressures. In contrast to 22x and 24x, measured compositions of the 23x phase were nearly stoichiometric.

Alkaline-earth cuprates Four alkaline-earth cuprates, tetragonal  $\text{Sr}_1\text{Ca}_{1-x}\text{CuO}_2$  (T-1:1), orthorhombic  $\text{Sr}_{1-x}\text{Ca}_1\text{CuO}_2$  (O-1:1),  $\text{Sr}_{2-x}\text{Ca}_x\text{CuO}_3$  (2:1), and  $\text{Sr}_{14-x}\text{Ca}_x\text{Cu}_{24}\text{O}_{38}$  (14-24), were identified in annealed samples[23,69]. The tetragonal T-1:1 phase was found only in samples from region 6 of Figure 5.3 annealed at 800°C in 100%  $\text{O}_2$ . The 14-24 phase was found in regions 2-5 in Figure 5.3 at all temperatures in pure oxygen. It was replaced in samples annealed in 1%  $\text{O}_2$  by the O-1:1 phase. The 2:1 phase was found in samples from regions 6 and 7 of Figure 5.3 that were processed at 865° in 100% oxygen. In 0.1%  $\text{O}_2$ , the 2:1 phase was found to replace the O-1:1 phase and occupy regions 4-6 of Figure 5.3.

Quaternary phases Two phases,  $\text{Bi}_2\text{Sr}_2\text{CuO}_y$  (2201) [18]. and  $\text{Bi}_4\text{Sr}_8\text{Cu}_5\text{O}_y$  (4805) [70]. were found to have significant extensions of their solid solution regions into the tetrahedron with the addition of Ca to the system. The 2201 phase was found to form

equilibria with 2212 in compositions enriched in Bi. Significant amounts of Ca substitution into the 2201 phase was found to lower its melting point. Hence this phase was present as a liquid phase for some of the temperatures and oxygen partial pressures used in these studies. The 4805 phase was found in combination with Sr-rich compositions of the 2212 solid solution as shown in Figure 5.3 at all temperatures and oxygen partial pressures used in these studies.

Decomposition products As will be shown in Chapters 6 and 7, the solidus is lowered to approximately 750°C in inert atmospheres for compositions around the 2212 stoichiometry. Hence, it is of interest to determine what phases are stable or metastable below the solidus in inert atmospheres such as Ar. For this experiment, a separate series of samples was constructed of the form  $\text{Bi}_2\text{Sr}_{2-x}\text{Ca}_{1+x}\text{Cu}_2\text{O}_y$  where  $x = 0, 0.2, 0.5, 0.8, \text{ and } 1$ . These samples were first prepared by solid state processing in oxygen with the final heat treatment at 865°C for 100 hours. Analysis showed these samples to consist primarily of 2212 with small amounts of 22x present for the Ca-rich samples and 14-24 for the Sr-rich samples. The middle sample,  $\text{Bi}_2\text{Sr}_{1.5}\text{Ca}_{1.5}\text{Cu}_2\text{O}_y$  was essentially single-phase 2212. This series of samples was then annealed in flowing Ar at 750°C for 100 hours. The phases found in these samples were 23x, 22x,  $\text{Cu}_2\text{O}$ , and  $\text{CaO}$ . Measured compositions are listed in Table 5.8. These phases should be considered as the stable intermediate phases since, in principle, these samples should be reducible to their metallic states. None of the superconducting phases were found in these samples after the anneal in Ar. In addition, Cu was not found in any compounds with the other cations. The decomposition of the superconducting phases in Ar for samples close to the ideal 2212 stoichiometry proceeded according to the reaction:

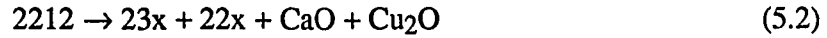


However, it is clear from Table 5.8 that additional phases result from the decomposition of the Ca-rich superconducting compositions. For the Ca-rich samples, Equation 5.1 becomes:

Table 5.8 List of the phases found in the series of samples,  $\text{Bi}_2\text{Sr}_{2-x}\text{Ca}_{1+x}\text{Cu}_2\text{O}_y$  ( $x = 0, 0.2, 0.5, 0.8, \text{ and } 1$ ), which were decomposed in Ar at  $750^\circ\text{C}$

Sample	Sample #	Phases	Measured Compositions
$\text{Bi}_2\text{Sr}_2\text{CaCu}_2\text{O}_y$	40	23x, $\text{Cu}_2\text{O}$	$\text{Bi}_{1.98}\text{Sr}_{1.82}\text{Ca}_{1.04}\text{Cu}_{0.15}\text{O}_y$
		22x <sup>a</sup>	$\text{Bi}_{2.07}\text{Sr}_{1.14}\text{Ca}_{0.66}\text{Cu}_{0.13}\text{O}_y$
$\text{Bi}_2\text{Sr}_{1.8}\text{Ca}_{1.2}\text{Cu}_2\text{O}_y$	37	23x, $\text{Cu}_2\text{O}$	$\text{Bi}_{2.01}\text{Sr}_{1.77}\text{Ca}_{1.08}\text{Cu}_{0.14}\text{O}_y$
$\text{Bi}_2\text{Sr}_{1.5}\text{Ca}_{1.5}\text{Cu}_2\text{O}_y$	41	23x, 22x,	$\text{Bi}_{1.97}\text{Sr}_{1.60}\text{Ca}_{1.26}\text{Cu}_{0.17}\text{O}_y$
		$\text{CaO}$ , $\text{Cu}_2\text{O}$	$\text{Bi}_{2.07}\text{Sr}_{1.04}\text{Ca}_{0.76}\text{Cu}_{0.13}\text{O}_y$
$\text{Bi}_2\text{Sr}_{1.2}\text{Ca}_{1.8}\text{Cu}_2\text{O}_y$	39	23x, 22x,	$\text{Bi}_{2.00}\text{Sr}_{1.49}\text{Ca}_{1.37}\text{Cu}_{0.14}\text{O}_y$
		$\text{CaO}$ , $\text{Cu}_2\text{O}$	$\text{Bi}_{2.09}\text{Sr}_{0.98}\text{Ca}_{0.84}\text{Cu}_{0.10}\text{O}_y$
$\text{Bi}_2\text{Sr}_1\text{Ca}_2\text{Cu}_2\text{O}_y$	38	23x, 22x,	$\text{Bi}_{1.98}\text{Sr}_{1.51}\text{Ca}_{1.38}\text{Cu}_{0.13}\text{O}_y$
		$\text{CaO}$ , $\text{Cu}_2\text{O}$	$\text{Bi}_{2.11}\text{Sr}_{1.01}\text{Ca}_{0.81}\text{Cu}_{0.07}\text{O}_y$

<sup>a</sup>Phase was present in very small amounts.



Apparently, the upper solubility limit of Ca in the 23x phase is  $x \approx 1.4$ . The differences in the decomposition reactions 5.1 and 5.2 may explain the changes in the 2212 solid solution region that occur at low oxygen partial pressures as discussed below.

### 5.1.2 Liquid phases during sintering

The presence of liquid phases during the annealing process for some of the samples was inferred from DTA data and the observation of shape distortions of the sample after annealing. Partial melting generally could be associated with compositions that were Bi and/or Ca rich and contained the Bi-rich secondary phases 2201 and 22x. DTA scans of several samples from the second study are shown in Figure 5.5. Temperatures of thermal events are listed in Table 5.9. The large endotherms around  $885^\circ\text{C}$  correspond to the melting point of 2212. The smaller endotherms are associated with melting of the 2201 and 22x phases in samples #54 and #61 respectively. Samples in regions 1 and 7 of Figure 5.3

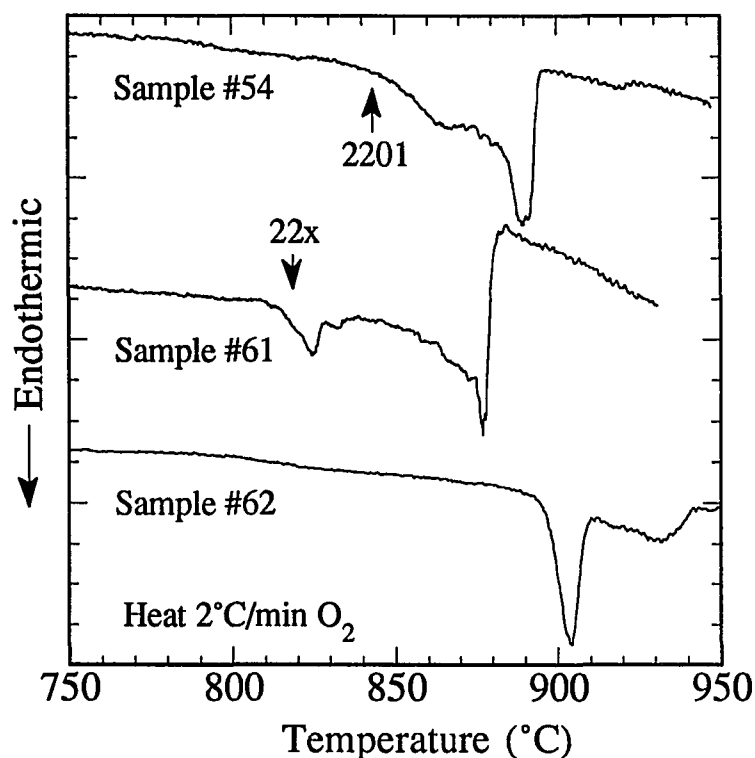


Figure 5.5 DTA heating scans of several samples from the second study. These particular samples were annealed in O<sub>2</sub> at 800°C for a total of 250 hours prior to their use in the DTA.

generally exhibited various degrees of partial melting below the melting point of 2212. For comparison, the DTA heating curve for sample #62 (region 5 of Figure 5.3) is also shown in Figure 5.5. This scan is typical of sample compositions lying in the 2212 solid solution region or in regions 3 - 6 of Figure 5.3. No other melting events are seen below the melting point of 2212.

The presence of liquid phases was found to have a significant effect on the microstructure of the samples. Severe shape distortions of the samples were generally found to accompany partial melting. In some cases, the samples became fluid enough to flow and appeared to completely melt as noted in Tables 5.2-5.7. The presence of liquid phases substantially reduced the amount of porosity in samples processed by solid state techniques.

Table 5.9 Temperature of thermal events taken from DTA heating curves in O<sub>2</sub> for the series of samples used in the second study. Material used in the DTA experiments was initially annealed in oxygen at 800°C for 250 hours

Composition	#	2212 Melting Point		Partial Melting Events			
		Onset	Peak	Onset	Peak	Onset	Peak
Bi <sub>1.85</sub> Sr <sub>2.3</sub> Ca <sub>0.85</sub> Cu <sub>2</sub> O <sub>y</sub> <sup>a</sup>	50	885°C	892°C	868°C	874°C		
Bi <sub>2.35</sub> Sr <sub>2.05</sub> Ca <sub>0.6</sub> Cu <sub>2</sub> O <sub>y</sub>	53	885°C	889°C	874°C	881°C		
Bi <sub>2.35</sub> Sr <sub>1.55</sub> Ca <sub>1.1</sub> Cu <sub>2</sub> O <sub>y</sub>	54	883°C	889°C	844°C	867°C		
Bi <sub>2.35</sub> Sr <sub>1.05</sub> Ca <sub>1.6</sub> Cu <sub>2</sub> O <sub>y</sub>	55	870°C	873°C	856°C	867°C	818°C	822°C
Bi <sub>2.1</sub> Sr <sub>0.9</sub> Ca <sub>2.0</sub> Cu <sub>2</sub> O <sub>y</sub>	61	875°C	877°C	813°C	825°C		
Bi <sub>1.85</sub> Sr <sub>1.3</sub> Ca <sub>1.85</sub> Cu <sub>2</sub> O <sub>y</sub>	63	888°C	902°C				
Bi <sub>1.85</sub> Sr <sub>1.8</sub> Ca <sub>1.35</sub> Cu <sub>2</sub> O <sub>y</sub>	62	895°C	904°C				
Bi <sub>2.1</sub> Sr <sub>1.7</sub> Ca <sub>1.2</sub> Cu <sub>2</sub> O <sub>y</sub> <sup>a</sup>	60	900°C	906°C	886°C	892°C		

<sup>a</sup> Event corresponding to partial melting is small.

Shown in Figure 5.6 are SEM micrographs of two samples, one of which underwent partial melting during sintering. Sample #60 was annealed in O<sub>2</sub> at 885°C. This sample composition lies in the solid solution region and was shown by SEM analysis to be essentially single-phase 2212. This sample contains a considerable amount of porosity which is typical of 2212 samples processed by solid-state techniques in which no partial melting occurs. On the other hand, sample #61, shown in Figure 5.6b, was annealed in O<sub>2</sub> at 865°C where a liquid phase is present due to the melting of the 22x phase around 810°C. The porosity so clearly evident in Figure 5.6a is absent in this sample. However, it appears from the microstructure that the 22x phase completely coats the 2212 grains. Such a two-phase microstructure of superconducting (2212) and non-superconducting (22x) phases is clearly detrimental to efforts aimed at maximizing critical current densities.

(a)



(b)



Figure 5.6 Backscattered electron micrographs of (a) sample # 60,  $\text{Bi}_{2.1}\text{Sr}_{1.7}\text{Ca}_{1.2}\text{Cu}_2\text{O}_y$ , annealed in  $\text{O}_2$  at  $885^\circ\text{C}$  and (b) sample #61,  $\text{Bi}_{2.1}\text{Sr}_{0.9}\text{Ca}_2\text{Cu}_2\text{O}_y$ , annealed in  $\text{O}_2$  at  $865^\circ\text{C}$ . The white phase in (b) is 22x.

## 5.2. Solid Solution Region

### 5.2.1 Apparent and actual compositions

Three types of compositional measurements on the 2212 phase were performed in these studies in order to correctly outline the solid solution region and address various discrepancies that exist in the literature regarding the solid solution region. The first measurements of the apparent 2212 composition were performed by EDS analysis in the SEM. Measurement of the apparent and actual composition were also performed in the TEM. In measuring the apparent composition in the TEM or SEM, the number of intergrowths contained within the 2212 phase was not taken into account. Hence, EDS measurements of the apparent composition are a measure of both the solid-solution composition and any intergrowths which may be present. Actual compositions were determined by sampling grains or parts of grains that were identified by lattice imaging as having no intergrowths. Examples of both types of measurements in the TEM are shown in Figure 5.7. An overall measurement of the grain in Figure 5.7 revealed an apparent composition of  $\text{Bi}_{2.30}\text{Sr}_{2.07}\text{Ca}_{0.77}\text{Cu}_{1.85}\text{O}_y$  while measurement of the intergrowth free region revealed an actual composition of  $\text{Bi}_{2.09}\text{Sr}_{1.99}\text{Ca}_{0.91}\text{Cu}_{2.02}\text{O}_y$ . The high Bi and low Cu contents of the apparent composition, relative to the ideal 2212 stoichiometry, result from the inclusion of the 2201 intergrowths in the compositional measurements. Apparent and actual compositions were nearly the same when the number of intergrowths within the 2212 grains was low.

The differences between the actual and apparent compositions are further illustrated in Figure 5.8 which shows the 2212 solid solution regions at 800°C in 1%O<sub>2</sub> as determined by SEM and TEM compositional measurements. The apparent compositions measured by SEM and TEM were very similar. Note that the Bi-rich side of the solid solution is not contained within the boundaries set by the starting compositions shown in Figure 5.1. In general, the number of 2201 intergrowths within the 2212 phase was found to increase as the starting

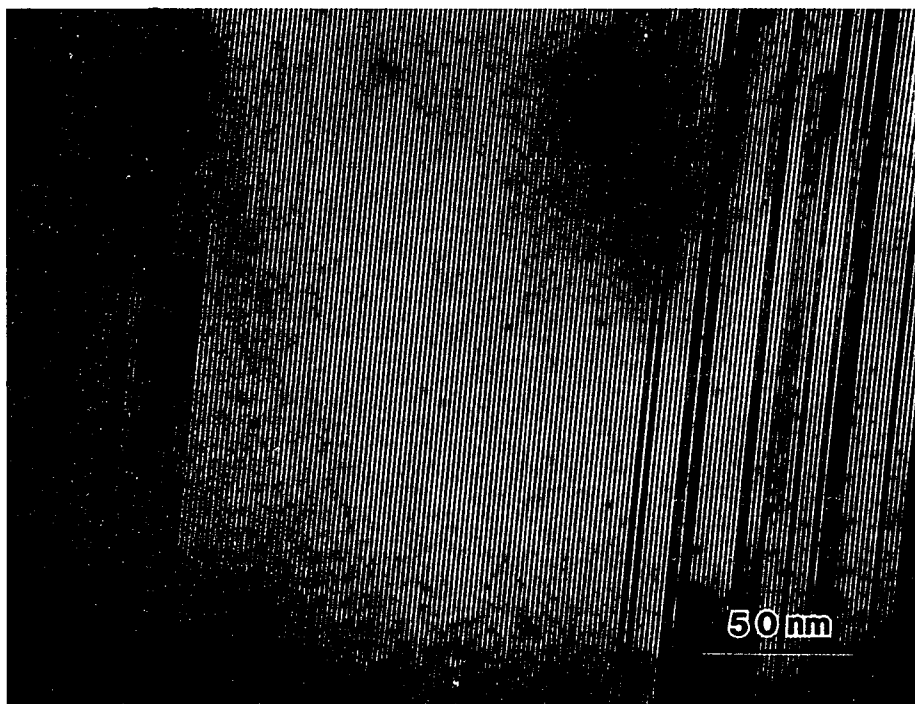


Figure 5.7 TEM micrograph of a 2212 grain from a sample with an overall composition of  $\text{Bi}_2\text{Sr}_2\text{Ca}_{0.5}\text{Cu}_2\text{O}_y$ .

samples were enriched in Bi or depleted of Sr, Ca, or Cu compared to the ideal 2212 stoichiometry. Bi-poor samples typically contained very few 2201 intergrowths. In the latter case, the apparent and actual compositional measurements were nearly the same resulting in better agreement among the three types of measurements regarding the lower boundary of the 2212 solid solution regions.

### 5.2.2 Solid solution regions

Table 5.10 summarizes the results of the compositional measurements made in the SEM and TEM. Intergrowths within grains of the 2212 phase account for most of the differences between the actual and apparent compositional measurements. Both types of measurements show most of the solid solubility exhibited by the 2212 phase to exist between Sr and Ca. A



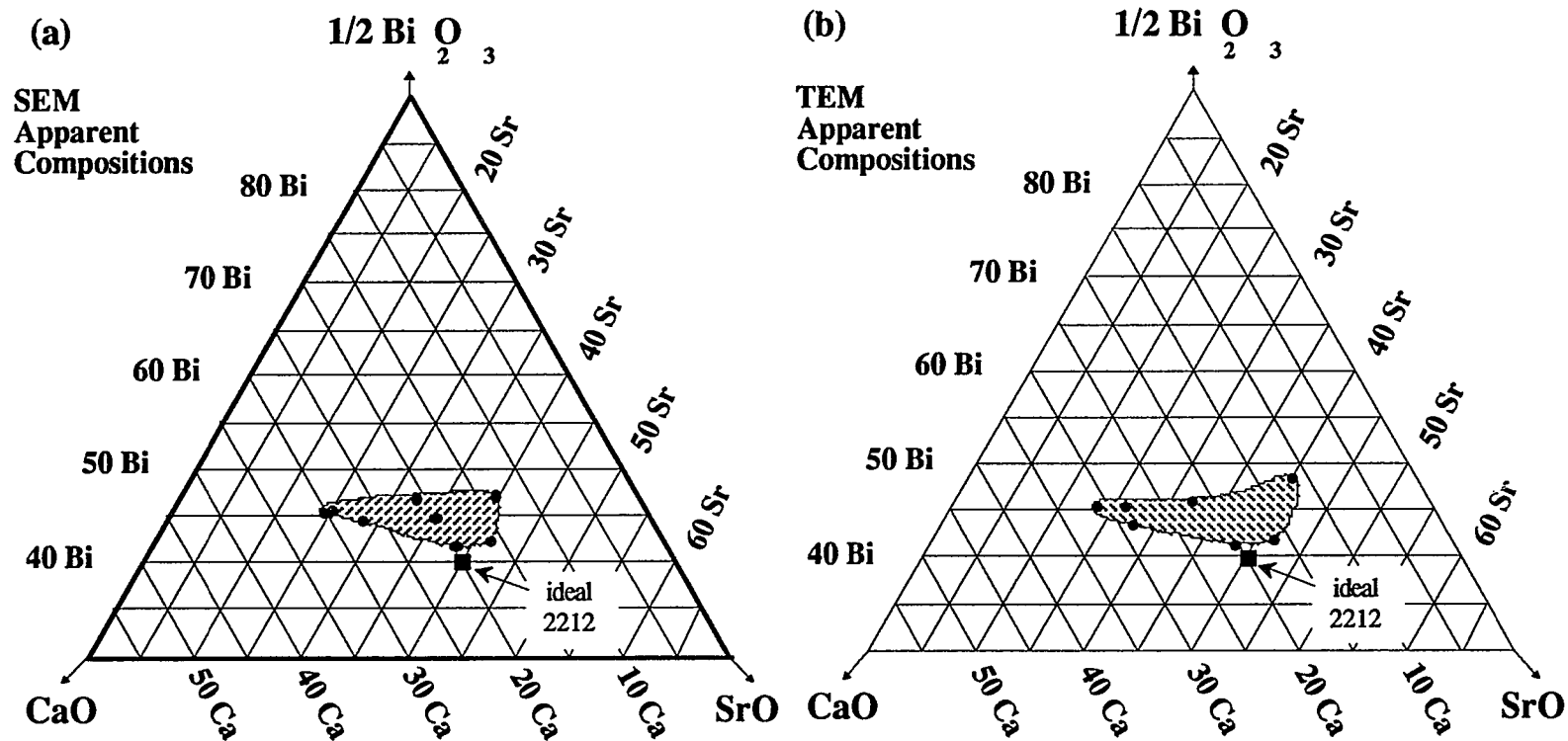


Figure 5.8 Solid solution regions determined at 800°C and 1.0% O<sub>2</sub> by measurements of the apparent composition in (a) the SEM and (b) the TEM. The solid solution region determined by measurements of the actual compositions in the TEM is shown in (c).

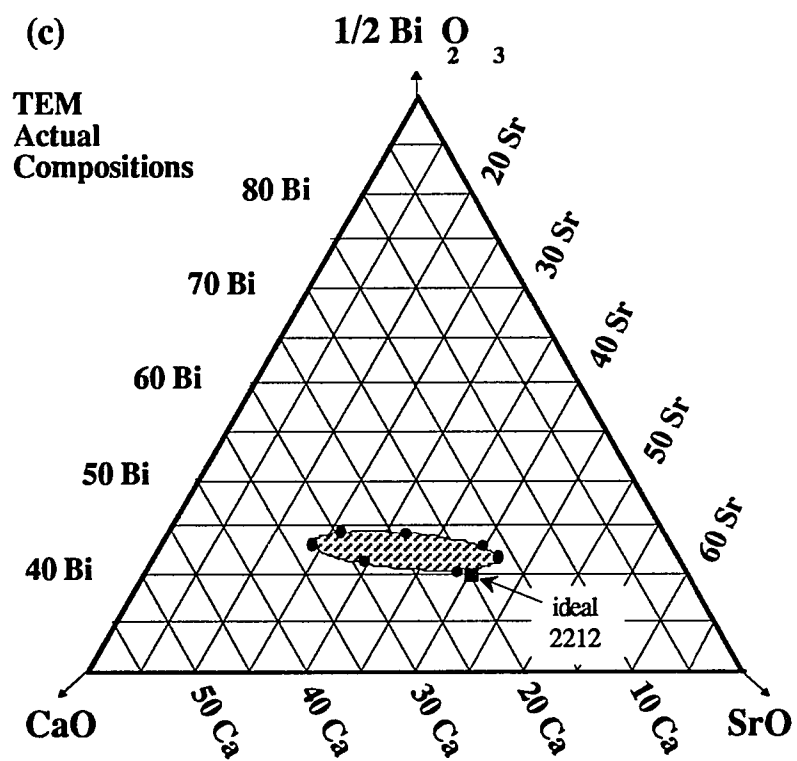


Figure 5.8 (continued)

Table 5.10 Summary of the compositional measurements made in the SEM and TEM. The last column represents the difference between the maximum and minimum measured Cu concentrations.

	Max and Min Sr Compositions		Max and Min Bi Compositions		Sr:Ca		Bi:(Sr+Ca)		Cu
	Max Sr	Min Sr	Max Bi	Min Bi	Max	Min	Max	Min	$\Delta$
865°C 100% O <sub>2</sub> <sup>a</sup>									
TEM actual	2.09/2.04/0.90/1.96	2.12/1.17/1.71/2.01	2.18/1.70/1.17/1.95	2.02/1.98/1.02/1.98	2.27	0.68	0.76	0.67	0.07
TEM apparent	2.13/2.04/0.89/1.94	2.17/1.13/1.67/2.03	2.36/1.99/0.73/1.91	2.04/1.99/1.03/1.94	2.29	0.68	0.87	0.67	0.17
SEM apparent	2.11/2.18/0.87/1.84	2.15/1.21/1.62/2.02	2.41/1.85/1.02/1.72	2.06/1.87/1.18/1.89	2.49	0.75	0.84	0.67	0.31
800°C 100% O <sub>2</sub>									
TEM actual	2.06/2.09/0.83/2.01	2.09/1.13/1.79/1.99	2.18/1.96/0.92/1.95	2.01/1.76/1.23/2.00	2.52	0.63	0.76	0.67	0.06
TEM apparent	2.12/2.10/0.82/1.96	2.15/1.17/1.69/1.99	2.40/2.08/0.74/1.78	2.11/1.79/1.11/1.99	2.56	0.69	0.85	0.73	0.21
SEM apparent	2.51/2.12/0.66/1.71	2.20/1.27/1.62/1.91	2.51/2.12/0.66/1.71	2.16/1.29/1.56/1.99	3.24	0.78	0.90	0.76	0.29
885°C 100% O <sub>2</sub> <sup>b</sup>									
TEM actual	2.11/2.02/0.86/2.01	2.06/1.48/1.45/2.01	2.11/2.02/0.86/2.01	2.03/1.78/1.17/2.02	2.34	1.02	0.73	0.70	0.02
TEM apparent	2.20/2.08/0.79/1.93	2.05/1.46/1.46/2.02	2.20/2.08/0.79/1.93	2.05/1.46/1.46/2.02	2.63	1.00	0.77	0.70	0.09
SEM apparent	2.22/2.10/0.77/1.91	2.15/1.51/1.35/1.99	2.22/2.08/0.80/1.91	2.09/1.76/1.13/2.02	2.74	1.12	0.77	0.72	0.11
800°C 1% O <sub>2</sub>									
TEM actual	2.13/2.07/0.83/1.97	2.16/1.19/1.64/2.01	2.25/1.58/1.19/1.99	2.05/1.93/1.03/1.99	2.50	0.73	0.81	0.69	0.07
TEM apparent	2.52/2.11/0.63/1.74	2.26/2.11/0.63/1.74	2.52/2.11/0.63/1.74	2.09/1.91/1.02/1.97	3.37	0.75	0.92	0.71	0.26
SEM apparent	2.11/2.06/0.81/2.02	2.30/1.23/1.56/1.91	2.39/2.05/0.70/1.86	2.11/2.06/0.81/2.02	2.55	0.79	0.87	0.74	0.19
800°C 0.1% O <sub>2</sub> <sup>b</sup>									
TEM actual	2.11/1.94/0.97/1.98	2.16/1.66/1.17/2.01	2.17/1.84/1.10/1.95	2.11/1.94/0.97/1.98	2.00	1.42	0.74	0.73	0.06
TEM apparent	2.13/1.94/0.93/1.99	2.20/1.64/1.16/2.00	2.28/1.74/1.02/1.96	2.13/1.94/0.93/1.99	2.07	1.41	0.83	0.74	0.06
SEM apparent	2.62/2.14/0.56/1.68	2.21/1.71/1.11/1.97	2.62/2.14/0.56/1.68	2.14/1.86/1.00/2.00	3.82	1.54	0.97	0.75	0.32

<sup>a</sup> Represents the collection of data from both studies.

<sup>b</sup> Several of the samples subjected to these conditions were destroyed due to the partial melting of one of the secondary phases present. In this case, the maximum and minimum values listed are derived from only the samples that did survive the anneal.

for the second study were used to map out the solid solution region at the other temperatures and oxygen partial pressures examined in these studies. For this particular part of the study, samples were heat treated at 800°C for a total of 250 hours in flowing O<sub>2</sub>. A plot of the actual compositions of the 2212 phase as determined by TEM is shown in Figure 5.10a. This plot is very similar to that shown in Figure 5.9. No difference is found in the Bi:(Sr+Ca) ratios for the actual compositions in Table 5.10 indicating that very little change occurs in the limits of Bi substitution for Sr or Ca between 800°C and 865°C. The data does suggest that limits of Sr and Ca solubility in the 2212 phase are slightly larger than at 865°C.

800°C in 1.0% O<sub>2</sub> Samples were prepared for this part of the study with an anneal in 1.0% O<sub>2</sub> (Ar balance) at 800°C for a total of 250 hours. The actual compositions of the 2212 phase as determined in the TEM are plotted in Figure 10b. The extent of the solid solution region is nearly identical to the solid solution at 800°C in 100% O<sub>2</sub> except for a slight decrease in the amount of Ca solubility in the 2212 phase.

885°C in 100% O<sub>2</sub> Several of the Bi and Ca-rich samples, #61, #55, and #54, were found to melt during the heat treatment at 885°C for 50 hours due to the presence of 22x and a lower melting point for Ca-rich 2212 compositions. Hence, the determination of the solid solution region at 885°C around these samples is incomplete. However, it appears that the Ca-solubility in the solid solution region shrinks slightly as the temperature is raised to 885°C based on measurements of the 2212 composition in samples that survived the anneal at 885°C. For example, the actual composition of the 2212 phase in sample #63, Bi<sub>1.85</sub>Sr<sub>1.3</sub>Ca<sub>1.85</sub>Cu<sub>2</sub>O<sub>y</sub> after the anneal at 865°C was Bi<sub>2.08</sub>Sr<sub>1.42</sub>Ca<sub>1.52</sub>Cu<sub>1.98</sub>O<sub>y</sub>. After the anneal at 885°C, the actual composition of the 2212 phase in sample #63 was Bi<sub>2.06</sub>Sr<sub>1.48</sub>Ca<sub>1.45</sub>Cu<sub>2.01</sub>O<sub>y</sub>. It appears that the solid solution region of the 2212 phase is relatively stable up to the melting point of each particular 2212 composition. The solid solution region is sketched in Figure 11a. Table 5.9 shows the melting point of the 2212 phase for the Bi and/or Ca rich compositions to be around 870°C-875°C. Hence,

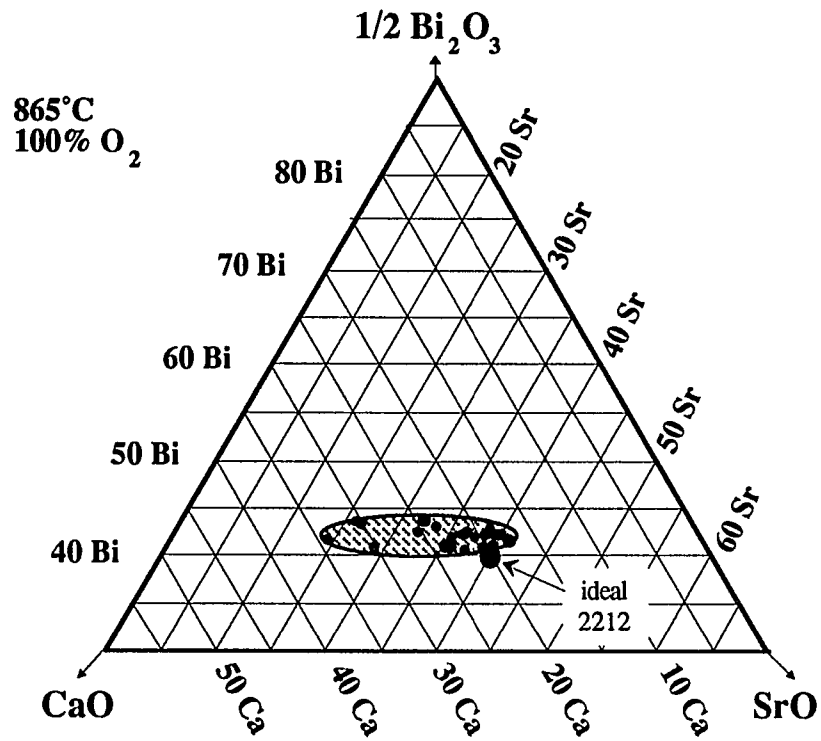


Figure 5.9 Solid solution region at 865°C in O<sub>2</sub> as determined by measurements of the actual compositions in the TEM. The data shown above is taken from samples used in both studies.

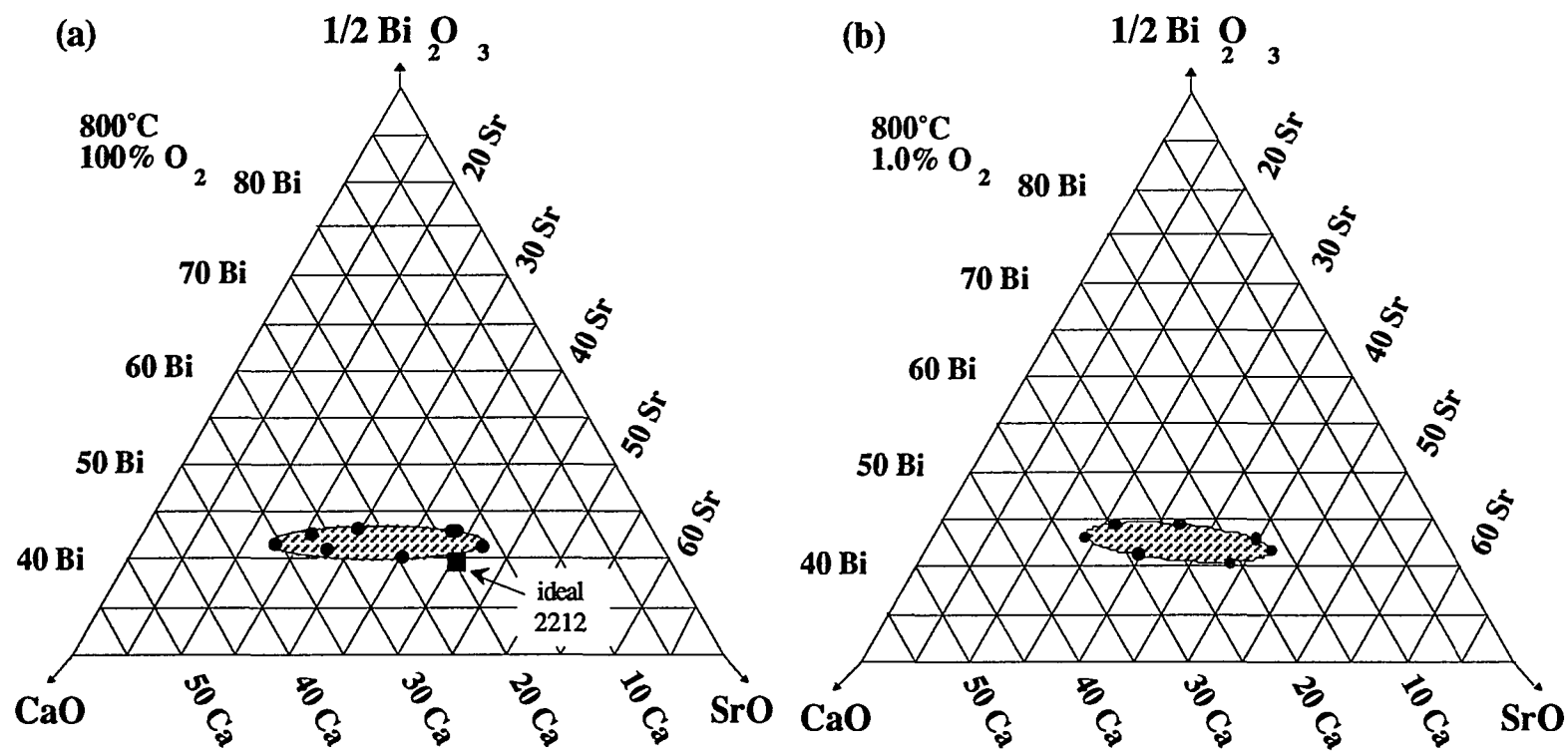


Figure 5.10 Solid solution region as determined by the actual compositional measurements at (a) 800°C and 100%  $\text{O}_2$  and (b) 800°C and 1.0%  $\text{O}_2$ . Data was taken from only samples in the second study.

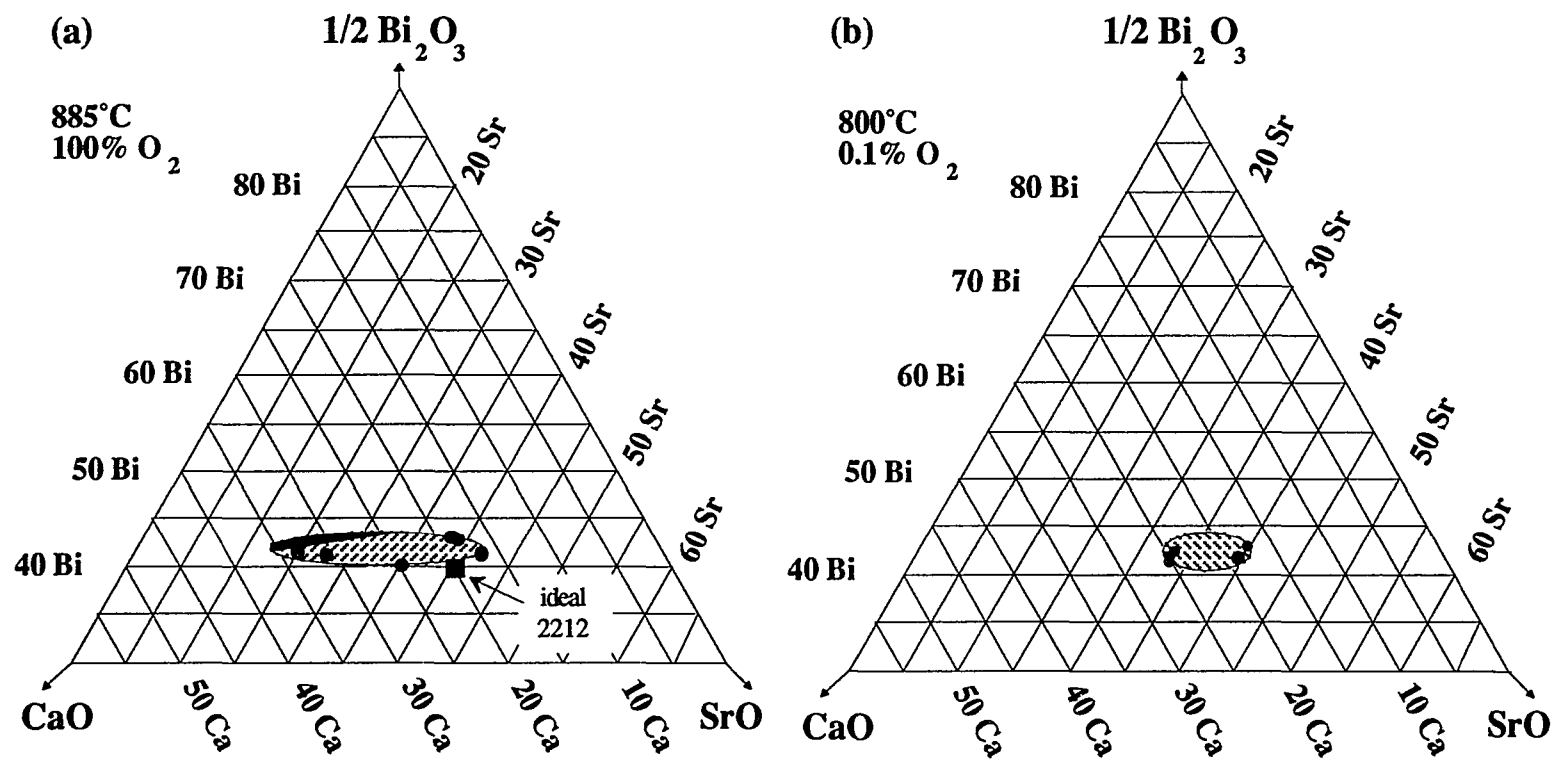


Figure 5.11 Solid solution region as determined by the actual compositional measurements at (a) 885°C and 100%  $\text{O}_2$  and (b) 800°C and 0.1%  $\text{O}_2$ . The darkened area of (a) represents the part of the solid solution region that has already melted at 885°C in  $\text{O}_2$ .

Table 5.11 List of the apparent and actual compositions determined from TEM/EDS measurements for the samples equilibrated in oxygen at 865°C.

Starting Composition	Process	Sample Number	Apparent "2212" Composition	Actual "2212" Composition	Actual Sr+Ca	T <sub>C</sub> (K)
2/2/1/2 Bi-Series	glass	10	2.15 / 1.86 / 1.04 / 1.95	2.14 / 1.92 / 0.98 / 1.97	2.90	86
2.5/2/1/2	glass	16	2.29 / 1.77 / 1.08 / 1.87	2.18 / 1.70 / 1.17 / 1.95	2.88	85
2.2/2/1/2	glass	15	2.18 / 1.87 / 1.04 / 1.91	2.13 / 1.83 / 1.09 / 1.95	2.92	85
1.8/2/1/2	glass	17	2.06 / 2.01 / 0.96 / 1.97	2.05 / 1.98 / 0.97 / 2.00	2.95	93
1.5/2/1/2	glass	18	2.06 / 1.88 / 1.07 / 1.99	2.02 / 1.93 / 1.06 / 1.98	2.99	93
Sr-Series						
2/2.5/1/2	glass	24	2.13 / 2.04 / 0.89 / 1.94	2.09 / 2.04 / 0.90 / 1.96	2.94	93
2/2.2/1/2	glass	21	2.04 / 1.99 / 1.03 / 1.94	2.02 / 1.98 / 1.02 / 1.98	3.00	93
2/1.8/1/2	glass	22	2.15 / 1.80 / 1.11 / 1.94	2.12 / 1.76 / 1.14 / 1.97	2.90	85
2/1.5/1/2	glass	23	2.23 / 1.59 / 1.24 / 1.94	2.16 / 1.56 / 1.29 / 1.99	2.85	80
Ca-Series						
2/2/1.75/2	glass	32	2.07 / 1.79 / 1.17 / 1.96	2.07 / 1.79 / 1.17 / 1.96	2.96	92
2/2/1.5/2	glass	14	2.09 / 1.76 / 1.19 / 1.96	2.07 / 1.79 / 1.16 / 1.97	2.96	93
2/2/1.2/2	glass	12	2.11 / 1.73 / 1.20 / 1.96	2.09 / 1.75 / 1.19 / 1.97	2.94	90
2/2/0.8/2	glass	11	2.18 / 1.97 / 0.89 / 1.95	2.13 / 1.97 / 0.91 / 1.99	2.88	84
2/2/0.5/2	glass	13	2.36 / 1.99 / 0.73 / 1.91	2.12 / 1.99 / 0.92 / 1.97	2.91	83
Cu-Series						
2/2/1/2.5	glass	25	2.14 / 1.84 / 1.03 / 2.00	2.10 / 1.87 / 1.04 / 1.99	2.91	87
2/2/1/2.2 <sup>a</sup>	glass	26	2.16 / 1.89 / 1.00 / 1.95			88
2/2/1/1.8 <sup>a</sup>	glass	27	2.13 / 1.87 / 1.06 / 1.94			91
2/2/1/1.5	glass	28	2.19 / 1.87 / 1.05 / 1.89	2.06 / 1.88 / 1.12 / 1.94	3.00	90
1.85/2.3/0.85/2 <sup>b</sup>	glass	50	2.14 / 2.04 / 0.87 / 1.95	2.14 / 2.00 / 0.86 / 2.00	2.86	
2.1/0.9/2/2 <sup>b</sup>	solid st.	61	2.17 / 1.13 / 1.67 / 2.03	2.12 / 1.17 / 1.71 / 2.01	2.88	
1.85/1.3/1.85/2 <sup>b</sup>	solid st.	63	2.10 / 1.42 / 1.49 / 1.99	2.08 / 1.42 / 1.52 / 1.98	2.94	

<sup>a</sup>Actual composition was not measured.

<sup>b</sup>T<sub>C</sub> was not measured.



Table 5.12 List of the apparent and actual compositions determined from TEM/EDS measurements for samples that were equilibrated at 800°C in 100% O<sub>2</sub> or 1.0% O<sub>2</sub> for a total of 250 hours.

Starting Composition	Process	Sample Number	Apparent "2212" Composition	Actual "2212" Composition	Actual Sr+Ca
800°C 100% O <sub>2</sub>					
1.85 / 2.3 / 0.85 / 2	glass	50	2.12 / 2.10 / 0.82 / 1.96	2.06 / 2.09 / 0.83 / 2.01	2.92
2.35 / 2.05 / 0.6 / 2	glass	53	2.40 / 2.08 / 0.74 / 1.78	2.18 / 1.96 / 0.92 / 1.95	2.88
2.35 / 1.55 / 1.1 / 2	glass	54	2.39 / 1.57 / 1.21 / 1.83	2.17 / 1.47 / 1.35 / 2.01	2.82
2.35 / 1.05 / 1.6 / 2	glass	55	2.29 / 1.21 / 1.60 / 1.89	2.17 / 1.23 / 1.60 / 2.00	2.83
2.1 / 0.9 / 2 / 2	solid st.	61	2.15 / 1.17 / 1.69 / 1.99	2.09 / 1.13 / 1.79 / 1.99	2.92
1.85 / 1.8 / 1.35 / 2	solid st.	62	2.11 / 1.79 / 1.11 / 1.99	2.01 / 1.76 / 1.23 / 2.00	2.99
1.85 / 1.3 / 1.85 / 2	solid st.	63	2.18 / 1.48 / 1.40 / 1.94	2.12 / 1.98 / 0.90 / 2.00	2.88
800°C 1.0% O <sub>2</sub>					
1.85 / 2.3 / 0.85 / 2	glass	50	2.13 / 2.09 / 0.81 / 1.96	2.13 / 2.07 / 0.83 / 1.97	2.90
2.35 / 2.05 / 0.6 / 2	glass	53	2.52 / 2.11 / 0.63 / 1.74	2.20 / 1.98 / 0.86 / 1.95	2.84
2.35 / 1.55 / 1.1 / 2	glass	54	2.33 / 1.63 / 1.13 / 1.91	2.25 / 1.58 / 1.19 / 1.99	2.77
2.35 / 1.05 / 1.6 / 2	glass	55	2.27 / 1.30 / 1.46 / 1.97	2.23 / 1.28 / 1.47 / 2.03	2.75
2.1 / 0.9 / 2 / 2	solid st.	61	2.26 / 1.17 / 1.56 / 2.01	2.16 / 1.19 / 1.64 / 2.01	2.83
1.85 / 1.8 / 1.35 / 2	solid st.	62	2.09 / 1.91 / 1.02 / 1.97	2.05 / 1.93 / 1.03 / 1.99	2.96
1.85 / 1.3 / 1.85 / 2	solid st.	63	2.18 / 1.47 / 1.36 / 1.98	2.09 / 1.46 / 1.42 / 2.02	2.88

Table 5.13 List of the apparent and actual compositions determined from TEM/EDS measurements for samples in the second study. Samples were equilibrated in oxygen at 885°C or at 800°C in 0.1% O<sub>2</sub>.

Starting Composition	Process	Sample Number	Apparent "2212" Composition	Actual "2212" Composition	Actual Sr+Ca
885°C 100% O <sub>2</sub>					
1.85 / 2.3 / 0.85 / 2	glass	50	2.20 / 2.08 / 0.79 / 1.93	2.11 / 2.02 / 0.86 / 2.01	2.88
2.35 / 2.05 / 0.6 / 2 <sup>a</sup>	glass	53			
2.35 / 1.55 / 1.1 / 2	glass	54		melted	
2.35 / 1.05 / 1.6 / 2	glass	55		melted	
2.1 / 1.7 / 1.2 / 2	solid st.	60	2.13 / 1.69 / 1.20 / 1.97	2.03 / 1.72 / 1.25 / 2.00	2.97
2.1 / 0.9 / 2 / 2	solid st.	61		melted	
1.85 / 1.8 / 1.35 / 2	solid st.	62	2.10 / 1.77 / 1.15 / 1.99	2.03 / 1.78 / 1.17 / 2.02	2.95
1.85 / 1.3 / 1.85 / 2	solid st.	63	2.05 / 1.46 / 1.46 / 2.02	2.06 / 1.48 / 1.45 / 2.01	2.93
800°C 0.1% O <sub>2</sub>					
1.85 / 2.3 / 0.85 / 2	glass	50	2.22 / 1.78 / 1.03 / 1.96	2.17 / 1.84 / 0.98 / 2.00	2.82
2.35 / 2.05 / 0.6 / 2 <sup>a</sup>	glass	53			
2.35 / 1.55 / 1.1 / 2	glass	54		melted	
2.35 / 1.05 / 1.6 / 2	glass	55		melted	
2.1 / 1.7 / 1.2 / 2	solid st.	60	2.28 / 1.74 / 1.02 / 1.96	2.17 / 1.78 / 1.10 / 1.95	2.88
2.1 / 0.9 / 2 / 2	solid st.	61		melted	
1.85 / 1.8 / 1.35 / 2	solid st.	62	2.13 / 1.94 / 0.93 / 1.99	2.11 / 1.94 / 0.97 / 1.98	2.91
1.85 / 1.3 / 1.85 / 2	solid st.	63	2.20 / 1.64 / 1.16 / 2.00	2.16 / 1.66 / 1.17 / 2.01	2.83

<sup>a</sup>Sample was not measured.

compositions in Bi and Ca regions of the solid solution region have already melted at 885°C as indicated in Figure 5.11a. Elsewhere around the edge of the solid solution region, the melting point of the 2212 phase varies from 885°C to 895°C. The one sample whose composition lies within the solid solution region, sample #60, was found to have the highest melting temperature of 900°C for the 2212 phase. The small endotherm around 885°C listed for this particular composition may be related to the slightly lower melting point of 2212 found at the edges of the solid solution region.

800°C in 0.1% O<sub>2</sub> Samples for this part of the study were annealed at 800°C in a gas flow of 0.1% O<sub>2</sub> (Ar balance) for a total of 250 hours. A complete determination of the solid solution region from this series of samples was not quite possible due to the fact that several of the samples decomposed and melted in the furnace. However, based on the samples that survived the heat treatment, it can be concluded that the Ca solubility in the 2212 phase at 800°C and 0.1%O<sub>2</sub> has been substantially reduced. A plot of the actual compositions can be found in Figure 5.11b. The reduction in the solid solution region appears to be related to the decomposition products in Ar discussed earlier in this chapter. The Ca-rich compositions were found to decompose in Ar into 23x, 22x, CaO, and Cu<sub>2</sub>O instead of just 23x and Cu<sub>2</sub>O. The upper limit for Ca substitution in the 23x phase appears to be around Bi<sub>1.98</sub>Sr<sub>1.51</sub>Ca<sub>1.38</sub>Cu<sub>0.13</sub>O<sub>y</sub>. The composition of the 2212 phase in sample #63 is Bi<sub>2.16</sub>Sr<sub>1.66</sub>Ca<sub>1.17</sub>Cu<sub>2.01</sub>O<sub>y</sub>. The ratios of Bi, Sr, and Ca places this latter composition just to the Sr-rich side of the 23x composition when both are projected onto the 1/2Bi<sub>2</sub>O<sub>3</sub>-SrO-CaO ternary phase diagram. For comparison, the composition of the 2212 phase in sample #63 annealed at 800°C and 1.0% O<sub>2</sub> was Bi<sub>2.09</sub>Sr<sub>1.46</sub>Ca<sub>1.42</sub>Cu<sub>2.02</sub>O<sub>y</sub>.

### 5.2.3 Lattice parameters

Measured values of the c-axis lattice parameter are plotted in Figures 5.12a and b for the Bi, Sr, Ca, and Cu series used in the first study. One sample from the Ca series, sample #13

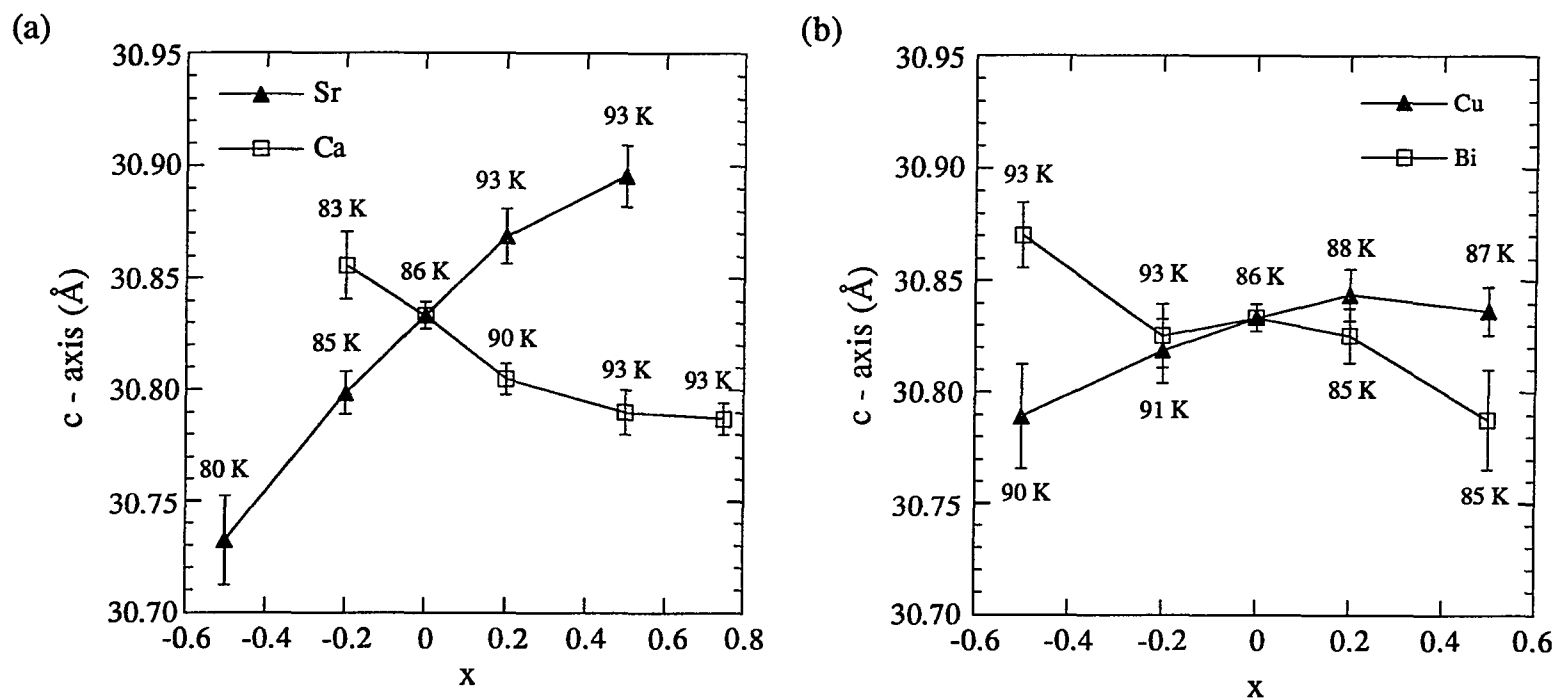


Figure 5.12 Plots of the c-axis lattice parameter vs. nominal composition for (a) the Sr and Ca series and (b) the Bi and Cu series. X represents the molar deviation from the ideal 2212 composition for each of the cations. Also plotted next to each data point is the corresponding transition temperature. These samples were all annealed at 865°C for 100 hours followed by an air quench.

$\text{Bi}_2\text{Sr}_2\text{Ca}_{0.5}\text{Cu}_2\text{O}_y$ , could not be accurately measured because it contained a significant amount of 2201 as a secondary phase which obscured many of the 2212 peaks used in the determination of lattice parameters. Continuous changes in the length of the lattice parameter were found for all series. Comparison with the actual compositions listed earlier in Tables 5.10-13, however, reveals that the solid substitution occurs mainly between Sr and Ca. As illustrated in Figure 5.13, the expansion of the lattice occurs with an increased Sr content in the 2212 phase, presumably due to the larger ionic radius of the  $\text{Sr}^{2+}$  ion compared to the other cations. This general trend is in agreement with the works of several other groups[33,35,38,71]. No substitution between Cu and the other cations seems to occur since the measured Cu content in all of the actual compositions was always close to the ideal stoichiometric molar value of 2. The apparent change in the c-axis length in Figure 5.12b for the Cu-series reflects the changes that occur in the Bi, Sr, and Ca concentrations in the 2212 phase as it adjusts to variations in the overall sample stoichiometry and the surrounding secondary phases.

#### 5.2.4 Transition temperatures

Transition temperatures for all the samples from the initial study, which were annealed at  $865^\circ\text{C}$  in oxygen, are listed in Table 5.11. Transition temperatures were not measured for the samples from the second series of samples.  $T_c$  was found to depend upon the total Sr+Ca content in the superconducting phase. The highest transition temperatures occurred in actual compositions of the 2212 phase for which the sum of Sr+Ca is near the ideal stoichiometric value of 3 (42.86 at.%). No correlation between lattice constants and  $T_c$  was found as illustrated in Figures 5.12a and b. These results are in contrast to other works which reported  $T_c$  to increase in direct proportion to the Sr content and the c-axis length of the 2212 phase[33,37,71]. The effect of composition on the transition temperature seems to be real and separate from previous reports for the need of an oxygen deficiency to maximize

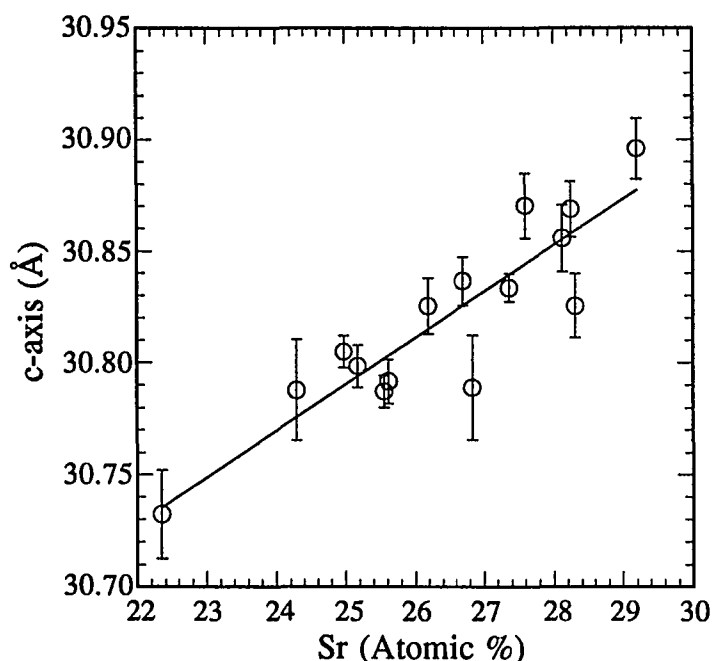


Figure 5.13 Plot of the c-axis vs. Sr content of the actual compositional measurements of the samples in the first study.

$T_c$ [72,73]. For example, composition #23,  $\text{Bi}_2\text{Sr}_{1.5}\text{Ca}_1\text{Cu}_2\text{O}_y$ , had a  $T_c$  of 80K after the 100 hour anneal at 865°C. Annealing other samples of this composition for 100 hours at various temperatures between 800°C and 865°C did not raise the transition temperature higher than 84K whereas a transition temperature of 93K was readily achieved for  $\text{Bi}_2\text{Sr}_{2.2}\text{Ca}_1\text{Cu}_2\text{O}_y$  (#21) and  $\text{Bi}_2\text{Sr}_{2.5}\text{Ca}_1\text{Cu}_2\text{O}_y$  (#24) without special regard for heat treatment. Although oxygen deficiencies may lead to increases in  $T_c$ , the transition temperatures of those samples with depressed  $T_c$ 's could not be increased regardless of thermal treatment in oxygen. Hence it appears that the transition temperature is dependent upon the composition, although more work will be needed to completely determined the relationships among transition temperature, cation composition, and oxygen stoichiometry.

### 5.3. Discussion

It is not possible to accurately construct the phase boundaries around the 2212 solid solution region from these two sets of experiments. The compositions used in these two studies were purposely chosen to be close to the 2212 solid solution region in order to maximize the amount of the 2212 phase in the samples and reduce the number of TEM thin specimens needed for EDS analysis. Conventional dimpling and ion-milling techniques were used to prepare TEM thin specimens because of the need to tilt to the [100] or [010] axes and image the lattice planes in order to identify the locations of intergrowths within the 2212 grains. If the samples had contained appreciable amounts of secondary phases, several samples of each composition from each of the anneals would have had to be made in order to sample enough grains for a complete EDS analysis.

Because there were so few secondary phases in these annealed samples, it was difficult to verify if some of the phases listed in Tables 5.2-5.7 are actually equilibrium phases or artifacts of the sample preparation processes. It is obvious that the phase rule is violated for some of the samples in these tables. For example, sample #61 in Table 5.3 has 5 secondary phases listed as being in equilibrium with 2212. For a four component system at a fixed pressure, the phase rule specifies a maximum of five phases total for an invariant region. Hence, at least one or two of the phases present are artifacts of the preparation processes. In order to ascertain the phase boundaries around the 2212 solid solution region, significantly more samples of compositions further removed from the 2212 solid solution would have to be made. Several studies dealing with the equilibrium phases found with 2212 in air have recently been reported in the literature[25,27,28,29].

In spite of the problem in identifying the correct equilibrium phases, a few useful points can be made about the secondary phases present and their relationships to the 2212 solid solution region. Almost all of the secondary phases found with 2212, with the exception of

CuO, are solid solutions. This fact, taken together with the solid solution nature of the 2212 phase and the propensity of the latter phase to accommodate intergrowths of the other superconducting phases, implies that systematic variations in starting compositions can be accommodated by changes in (1) the amounts, types, and composition of any secondary phases which may be present, (2) the number of intergrowths within grains of 2212 (apparent composition), and (3) the solid solution composition of the 2212 phase (actual composition).

The types of secondary phases found with 2212 were found to change as a function of temperature and oxygen partial pressure. The 23x phase was found to replace the 24x phase at low oxygen partial pressures. The 14-24 phase was found to be replaced at 1.0% O<sub>2</sub> by the O-1:1 which is replaced at 0.1% O<sub>2</sub> by the 2:1 phase. Hence, the Cu content of the secondary phases decreases with the lower oxygen partial pressures. In inert atmospheres, the only phase found to contain Cu was Cu<sub>2</sub>O. The 2212 phase is no longer stable and decomposes into 23x and Cu<sub>2</sub>O for Sr-rich compositions. For Ca-rich compositions, a slightly different decomposition process was found that results in 23x, 22x, CaO, and Cu<sub>2</sub>O.

Finally, several of the secondary phases, 22x and 2201 specifically, have melting points lower than that of the 2212 phase. Samples containing these phases undergo partial melting around 820°C to 840°C in oxygen. The use of liquid phases would seem to be an attractive approach to densifying these Bi-based ceramics. Indeed, a significant difference is seen in terms of porosity between the two samples shown in Figure 5.6. However, this liquid phase was observed to coat and solidify around the 2212 grains on cooling. Given the need for clean grain boundaries due to the short coherence length of the high-temperature superconductors, a process that uses a low-melting secondary phase for densification would appear to be very difficult to control in terms of maximizing the superconducting properties.

The use of TEM to distinguish between solid solution and intergrowth effects during compositional measurements showed the extent of Bi substitution for Sr and/or Ca to be smaller than previously reported[27,32,33,37,38,74]. The present study is the only one to



date that has taken into account the effects of intergrowths in measurements of the 2212 solid solution. Figure 5.8 clearly shows the solid solution regions determined by apparent compositions measured in either the SEM or TEM to be ill-defined and skewed in the direction of the 2201 solid solution region shown in Figure 5.2. The solid solution region determined by measuring the actual compositions was much more symmetric and can be approximated by an ellipse. Sr and Ca account for most of the observed solid solubility in the 2212 phase as indicated in Figures 5.9-5.11 and Tables 5.10-5.13. A smaller amount of Bi substitution for Sr or Ca accounts for the rest. The measured Bi content in any one sample was never observed to fall below the ideal stoichiometric molar ratio of 2. The Cu concentration, as determined by measurements of the actual composition, was nearly stoichiometric and varied very little over the entire compositional range. Based on these results, two substitution schemes can be explicitly stated. The first is simply the interchange between Sr and Ca. The second is slightly more involved. It appears that Bi can substitute for Sr and/or Ca. However, it appears that the reverse substitution of Sr or Ca for Bi does not occur since the measured Bi content of the superconducting phase was never found to dip below the ideal stoichiometric molar ratio of 2.

The solid solution region was found to be quite stable with temperature in 100% oxygen. The extent of the Sr-Ca interchange was found to slightly decrease with increasing temperatures. Likewise, very little change was observed when the oxygen partial pressure was dropped to 1.0% oxygen at 800°C. However, a further decrease to 0.1% O<sub>2</sub> at 800°C significantly decreased the Ca-solubility in the 2212 phase. The Sr-rich end of the 2212 solid solution region remained essentially unchanged. The large decrease seems to be related to the decomposition reactions 5.1 and 5.2. Apparently, compositions of the 2212 phase that decompose in Ar via reaction 5.1 are stable in an oxygen partial pressure of 0.1% O<sub>2</sub> at 800°C while those that decompose by reaction 5.2 are not.

The ideal 2212 composition appears to lie on or just outside the edge of the solid solution region based on measurements of the actual composition. This observation is in general agreement with two previous works by Hong *et al* and Sinclair *et al*[33,74]. The proximity to the edge of the solid solution region may explain why it is difficult to produce single-phase material starting with the ideal 2212 stoichiometry. Other studies in which x-ray microanalysis in the SEM was used for compositional analysis have shown the ideal compositions of the superconducting phases to clearly lie outside of the measured solid solution regions[32,37,38]. The solid solution region determined by Golden *et al* [38] appears to be similar in shape to the one determined by the SEM and TEM apparent measurements shown in Figure 5.7. However, their region was shifted to higher Bi contents and did not contain the ideal 2212 composition. The authors reported a significant heterogeneity in compositional measurements of the 2212 phase for any given film and the presence of a liquid phase during sintering of their thin films. Hence, the compositional measurements reported by Golden *et al* could have been influenced by significant numbers of 2201 intergrowths within the 2212 phase and/or the presence of solidified liquid phases that are known to be Bi-rich. In a recent work, Majewski *et al* determined a single phase region for the 2212 superconductor that showed an increase in the Sr solubility of the 2212 phase with increasing temperatures. They also showed compositions of the 2212 phase that were Ca-rich and stable at 820°C to decompose upon heating to higher temperatures[37]. The ranges found in the present work for Sr and Ca at 800°C are in good agreement with the latter study. However, only a small amount of change was observed in the Ca-rich end while essentially no change in the Sr-rich end of the solid solution region occurred with increasing temperatures in the present studies. Various compositions of the 2212 phase were determined to be stable up to their respective melting points. It was found that Ca and Bi-rich 2212 compositions melted approximately 20°C lower than other compositions in the solid solution region. Some of the differences between the present work and that of

Majewski *et al* may arise from the fact that the former work was carried out in 100% O<sub>2</sub> while the latter work was performed in air. Note that in the present study, a significant portion of the Ca-rich end of the solid solution region was found to be unstable in low oxygen partial pressures. Finally, Majewski *et al* suggested that the Cu layers are not completely occupied in order to account for the Bi in excess of the ideal stoichiometric amount of 2. Clearly, such a statement cannot be made in light of the present work showing the influence of intergrowths on the compositional measurements.

It is logical to assume that compositions near the middle of the solid solution region will be the easiest to process into single-phase material. Based on these results, this would be a composition such as Bi<sub>2.1</sub>Sr<sub>1.7</sub>Ca<sub>1.2</sub>Cu<sub>2</sub>O<sub>y</sub>, which is slightly enriched in Bi and deficient in Sr+Ca with some extra Ca substituted for Sr. This particular composition was made in the second study and was found to be essentially single phase as shown in Figure 5.6a. This particular composition was also found to have the highest melting point of all 2212 compositions examined by DTA. One further consideration in choosing a composition for a particular application is the compositional effect on the superconducting transition temperature. As noted earlier, T<sub>c</sub> was found to be highest for compositions of the 2212 phase that were near the bottom edge of the solid solution region where the sum of Sr+Ca was closest to the ideal stoichiometric ratio of 3. However, compositions closest to the lower boundary may not be as easy to process into single-phase material due to the small solubility limits of Cu in the 2212 phase. Fluctuations in the local stoichiometry in any part of the sample will be more likely to lead to the formation of secondary phases for compositions near the boundaries of the solid solution region as opposed to compositions directly in the middle. Hence, compromises may have to be made in order to prepare single-phase material with the highest possible T<sub>c</sub>.

#### 5.4. Summary

Several series of samples from two separate studies were used to characterize the phase relationships and solid solution region of the  $\text{Bi}_2\text{Sr}_2\text{CaCu}_2\text{O}_y$  superconductor. TEM analysis of the 2212 superconducting phase was necessary in order to separate solid solution and intergrowth effects in the compositional measurements. Based on the compositional measurements of the 2212 and secondary phases, variations in the overall stoichiometry can be accommodated by changes in (1) the amounts, types, and compositions of any secondary phases which may be present, (2) the number of intergrowths within the 2212 phase (apparent composition), and/or (3) the solid solution composition of the superconducting phase (actual composition). Most of the solid solubility exhibited by the 2212 phase exist between Sr and Ca. A smaller amount exist between Bi and (Sr+Ca). Based on the compositional measurements, two substitution schemes are presented. This first is just the interchange between Sr and Ca. The second involves the substitution of Bi for Sr or Ca. The reverse substitution of Sr or Ca for Bi appears to be unfavorable. The length (c-axis) of the unit cell was found by lattice parameter measurements to increase in direct proportion to the amount of Sr substituted for Ca in the 2212 phase. No correlation was found between lattice constants and transition temperatures. Rather, the highest  $T_c$ 's were found in annealed samples for which the Sr+Ca content of the superconducting phase was closest to the ideal stoichiometric ratio of 3 (42.86 at.%) although much more work will be needed to completely determine the relationships between the cation compositions, oxygen partial pressure, and  $T_c$ .

The whole solid solution region appears to be quite stable and shrinks only slightly with increasing temperatures in oxygen. It was found that several of the Bi and Ca-rich 2212 compositions have substantially lower melting points compared to the rest of the solid solution region. At the reduced oxygen partial pressure of 0.1%, a substantial part of the Ca-rich solid solution region is unstable. This appears to be related to the decomposition products of the 2212 phase in inert atmospheres. The ideal 2212 composition appears to lie

on or just outside the edge of the solid solution region. This may explain why nominal 2212 samples are difficult to produce in single phase form. The small solubility limit of Cu in the 2212 phase makes local compositional fluctuations within the samples more likely to form secondary phases for overall compositions near the boundaries of the solid solution region rather than for compositions in the middle. Hence, one may have to compromise on the choice of an overall composition to use in order to prepare single-phase material with the highest possible  $T_c$ .

## 6. CRYSTALLIZATION FROM THE GLASSY STATE

The crystallization of  $\text{Bi}_2\text{Sr}_2\text{CaCu}_2\text{O}_y$  glasses provides a convenient format for examining the formation process of the 2212 phase and other competing phase developments. In this chapter, a detailed look at the phase transformations and reactions kinetics of the crystallization process is presented. The results of this chapter compliment the solidification studies presented in Chapter 7.

### 6.1. Characterization of the Glassy State

#### 6.1.1 Microstructural analysis

Glassy material produced by splat-quenching typically had smooth surfaces, a glossy-black appearance, and an average thickness of  $300\mu\text{m}$  with lateral dimensions extending up to several centimeters. Figure 6.1 contains a powder diffraction scan of amorphous material with a nominal composition of 2212 and is typical of material processed with alumina crucibles in this work. The amorphous state can be inferred from XRD by the presence of two broad peaks. X-ray diffraction sometimes detected a small peak at  $33.1^\circ$  (2201), as indicated in Figure 6.1, although this phase was never observed by TEM or SEM. The presence of the 2201 may result from a small amount of surface crystallization during the quench[57]. On a microscopic scale, most of the glasses were found to be uniform in composition as determined by SEM and TEM. Only samples with high Ca contents ( $\text{Bi}_2\text{Sr}_2\text{Ca}_x\text{Cu}_2\text{O}_y$   $x \geq 1.5$ ) were found to have CaO as a significant secondary phase. Occasionally, several submicron SrO particles could be observed in glassy material examined in the TEM. Shown in Figure 6.2 is a TEM micrograph of glassy material with a nominal composition of  $\text{Bi}_2\text{Sr}_2\text{Ca}_{1.2}\text{Cu}_2\text{O}_y$ . In this particular sample, no crystalline phases are

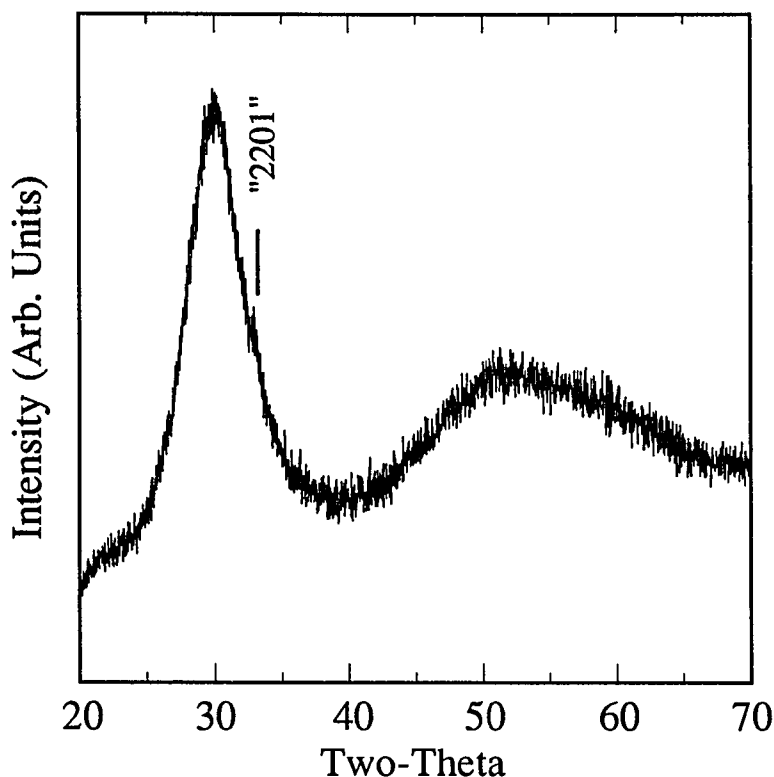


Figure 6.1 A typical XRD scan of the glassy material used in this work.

present nor are any indicated in the selected area diffraction (SAD) pattern. In general, the glasses used in the study were considered to be free of crystalline phases.

#### 6.1.2 Thermal analysis of the glassy material

DTA and TGA heating curves are shown in Figure 6.3 for a glass sample with a nominal  $\text{Bi}_2\text{Sr}_2\text{Ca}_{1.2}\text{Cu}_2\text{O}_y$  stoichiometry. A complete list of thermal events can be found in Table 6.1 SEM/EDS measurements of the glass matrix from this sample revealed an overall composition of  $\text{Bi}_{2.08}\text{Sr}_{1.90}\text{Ca}_{1.21}\text{Cu}_{2.02}\text{O}_y$ . The glass transition was observed at  $398^\circ\text{C}$  in Ar and  $415^\circ\text{C}$  in  $\text{O}_2$ . The two crystallization exotherms at  $488^\circ\text{C}$  and  $519^\circ\text{C}$  in  $\text{O}_2$  are replaced by one at  $467^\circ\text{C}$  plus two smaller exotherms at higher temperatures in Ar. In this work, the second exotherm observed by DTA in oxygen was always the strongest in contrast

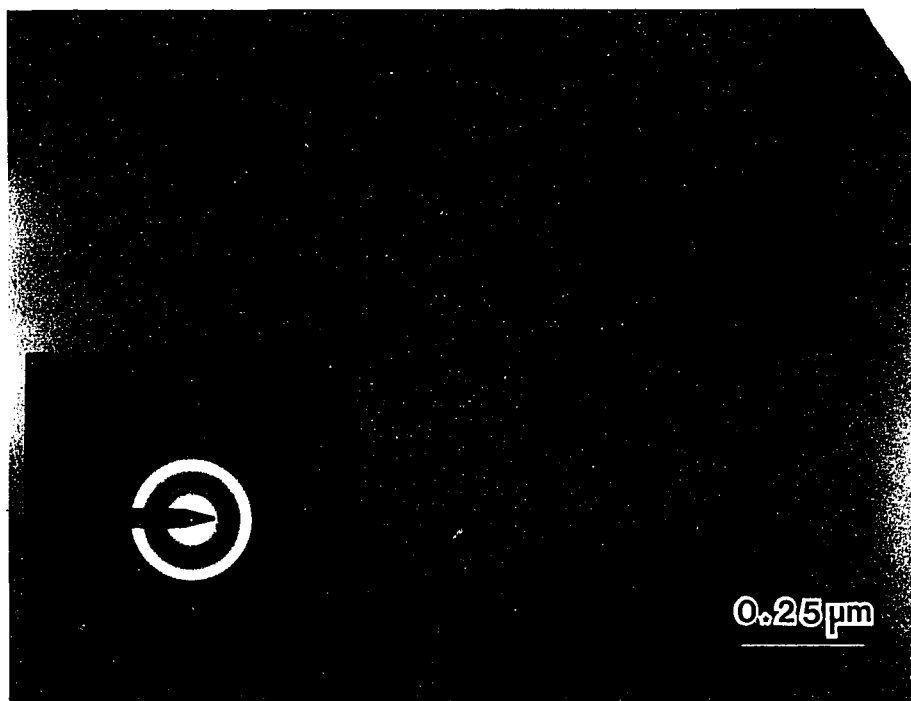


Figure 6.2 TEM micrograph of a nominal  $\text{Bi}_2\text{Sr}_2\text{Ca}_{1.2}\text{Cu}_2\text{O}_y$  glass.

to other studies[54,55,56,61]. It is difficult to ascribe a particular reason for this. Several factors such as starting compositions, quenching techniques, sample preparation, or conditions for DTA experiments can account for differences between these works. For example, it was found that grinding powders just prior to the DTA experiments was essential for reproducibility.

Two smaller endotherms at  $691^\circ\text{C}$  and  $852^\circ\text{C}$  precede the main melting event at  $886^\circ\text{C}$  in oxygen. Melting in argon is seen to occur at a much lower temperature with an onset of  $748^\circ\text{C}$ . The presence of the second endotherm in Ar is questionable since no comparable thermal event is seen in the cooling curve, nor is it reproduced upon sequential DTA scans in Ar. Most likely, it corresponds to a phase that is stable in  $\text{O}_2$  and, in this case, forms during initial crystallization in Ar with whatever oxygen is available in the glass. Upon melting, the oxygen is lost and the phase does not form on cooling.



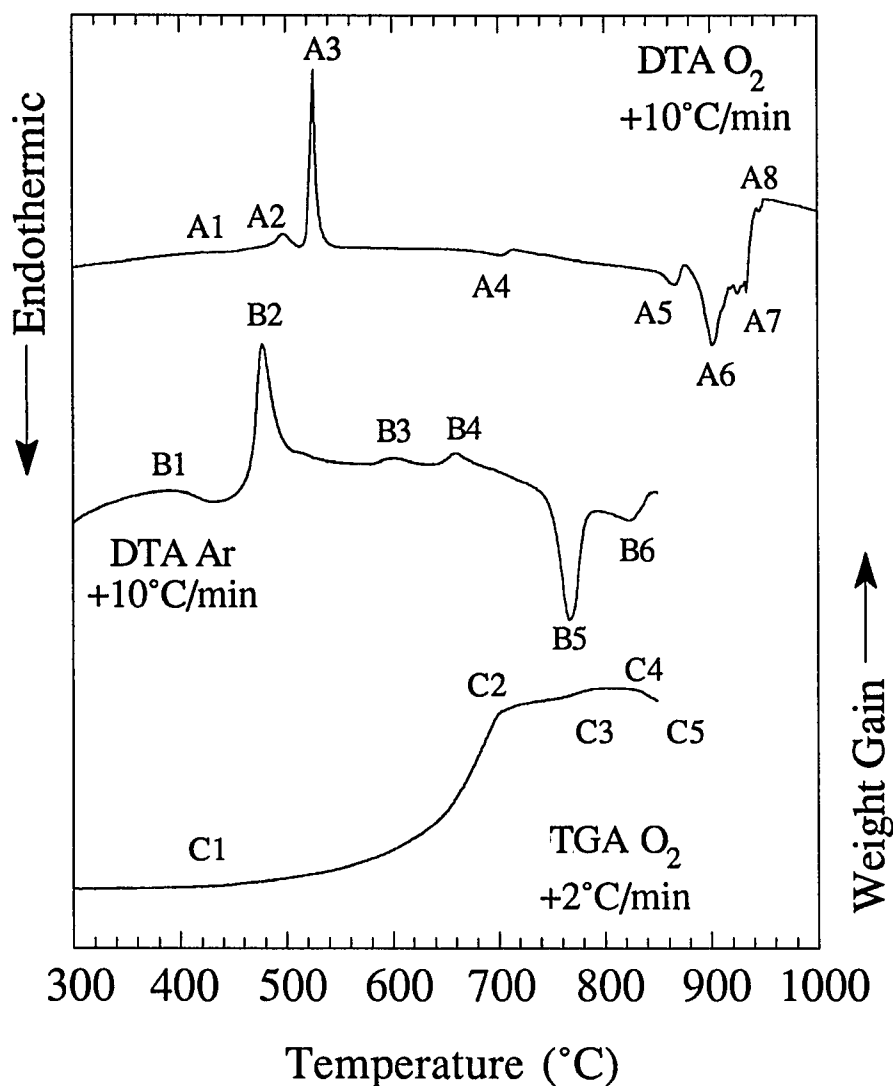


Figure 6.3 DTA and TGA heating scans in oxygen and DTA heating scan in Ar of a glass sample with a nominal starting composition of  $\text{Bi}_2\text{Sr}_2\text{Ca}_{1.2}\text{Cu}_2\text{O}_y$ . Onset and peak values for the indicated thermal events are listed in Table 6.1.

TGA results indicate a substantial amount of oxygen absorption takes place upon heating the glass in oxygen. Although oxygen absorption starts near the glass transition temperature, most occurs between 600 $^{\circ}\text{C}$  and 700 $^{\circ}\text{C}$ . The amount of oxygen picked up by the sample amounted to the equivalent of 0.41 oxygen atoms per copper atom in the sample assuming  $y$

Table 6.1 List of thermal events from the DTA and TGA experiments on the glass sample with a nominal composition of  $\text{Bi}_2\text{Sr}_2\text{Ca}_{1.2}\text{Cu}_2\text{O}_y$ .

Differential Thermal Analysis					
Heating Curve in $\text{O}_2$			Heating Curve in Ar		
Thermal Event	Onset Temperature	Peak Temperature	Thermal Event	Onset Temperature	Peak Temperature
A1. Glass Transition	415°C		B1. Glass Transition	398°C	
A2. Exotherm	488°C	498°C	B2. Exotherm	467°C	478°C
A3. Exotherm	519°C	526°C	B3. Exotherm	582°C	600°C
A4. Endotherm	691°C	701°C	B4. Exotherm	645°C	660°C
A5. Endotherm	852°C	866°C	B5. Endotherm	748°C	768°C
A6. Endotherm	886°C	901°C	B6. Endotherm	815°C	826°C
A7. Endotherm	922°C	925°C			
A8. Baseline Shift	934°C	937°C			

Thermogravimetric Analysis		
Event	Temperature	Weight Percent
C1. Start $\text{O}_2$ absorbtion	420°C	100.00%
C2. Change $\text{O}_2$ absorbion rate	700°C	101.30%
C3. Stop $\text{O}_2$ absorbtion	790°C	101.47%
C4. Start $\text{O}_2$ loss	830°C	101.47%
C5. End Experiment	850°C	101.39%

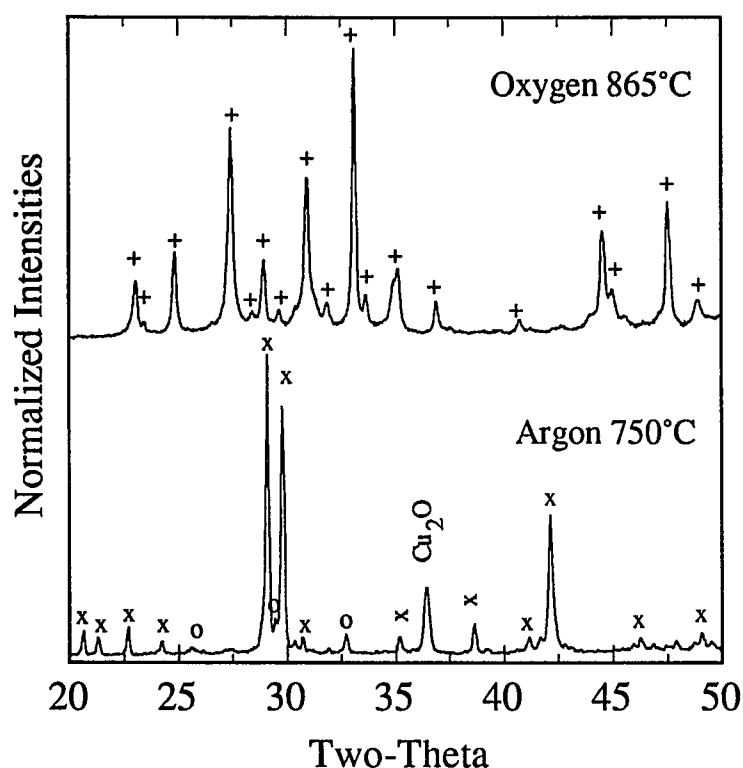


Figure 6.4 XRD scans of a nominal  $\text{Bi}_2\text{Sr}_2\text{Ca}_{1.2}\text{Cu}_2\text{O}_y$  glass heat treated in oxygen at  $865^\circ\text{C}$  for 100 hours and Ar at  $750^\circ\text{C}$  for 25 hours. The symbols associated with each of the phases are as follows: (+) - 2212, (o) - 2201, and (x) -  $\text{Bi}_2\text{Sr}_{3-x}\text{Ca}_x\text{O}_y$ .

= 8.2 for the composition  $\text{Bi}_2\text{Sr}_2\text{Ca}_{1.2}\text{Cu}_2\text{O}_y$  and full oxidation at the peak in the TGA curve. An abrupt change in the oxygen uptake was noted around  $700^\circ\text{C}$  which is in the temperature range of the first endotherm observed by DTA. At  $830^\circ\text{C}$ , the sample started to undergo a weight loss which was continuous to  $850^\circ\text{C}$  where the experiment was stopped.

As a reference point for the crystallization study, powder diffraction scans of  $\text{Bi}_2\text{Sr}_2\text{Ca}_{1.2}\text{Cu}_2\text{O}_y$  samples annealed at  $750^\circ\text{C}$  in argon and  $865^\circ\text{C}$  in oxygen for 25 and 100 hours respectively are presented in Figure 6.4. A list of phases and compositions as determined by XRD, SEM, and TEM for this particular sample can be found in Table 6.2. The Ar anneal was limited to 25 hours as the furnace tube was observed to darken. Upon

Table 6.2 List of average compositions for phases found in the  $\text{Bi}_2\text{Sr}_2\text{Ca}_{1.2}\text{Cu}_2\text{O}_y$  sample after various anneals as discussed in the text. The measured compositions for all elements are listed. The compositions listed in bold are for the 2212 phase and are an average of at least ten separate grain measurements. All other phases are an average of at least five separate grains. Compositions were determined by SEM and TEM analysis as indicated.

Sample History	Phases and Composition
As-Quenched	(glass) $\text{Bi}_{2.08}\text{Sr}_{1.90}\text{Ca}_{1.21}\text{Cu}_{2.02}\text{O}_y$ (SEM) (glass) $\text{Bi}_{2.05}\text{Sr}_{1.86}\text{Ca}_{1.26}\text{Cu}_{2.03}\text{O}_y$ (TEM)
650°C in $\text{O}_2$ for 1 min	<b><math>\text{Bi}_{2.24}\text{Sr}_{1.97}\text{Ca}_{1.02}\text{Cu}_{1.77}\text{O}_y</math></b> , $\text{Bi}_{1.87}\text{Sr}_{1.38}\text{Ca}_{1.41}\text{Cu}_{0.34}\text{O}_y$ , CuO/Cu <sub>2</sub> O, SrO (TEM)
650°C in $\text{O}_2$ for 100 hours	<b><math>\text{Bi}_{2.39}\text{Sr}_{1.88}\text{Ca}_{0.94}\text{Cu}_{1.79}\text{O}_y</math></b> , $\text{Bi}_{0.90}\text{Sr}_{0.92}\text{Ca}_{2.01}\text{Cu}_{0.17}\text{O}_y$ , $\text{Bi}_{1.67}\text{Sr}_{1.51}\text{Ca}_{1.56}\text{Cu}_{0.27}\text{O}_y$ , $\text{Bi}_{0.04}\text{Sr}_{0.08}\text{Ca}_{0.89}\text{Cu}_{0.97}\text{O}_y$ , CuO, SrO (TEM)
750°C in $\text{O}_2$ for 1 min	<b><math>\text{Bi}_{2.18}\text{Sr}_{1.77}\text{Ca}_{1.12}\text{Cu}_{1.93}\text{O}_y</math></b> , CuO, SrO (TEM)
750°C in $\text{O}_2$ for 100 hours	<b><math>\text{Bi}_{2.17}\text{Sr}_{1.72}\text{Ca}_{1.19}\text{Cu}_{1.93}\text{O}_y</math></b> , $\text{Bi}_{0.05}\text{Sr}_{0.10}\text{Ca}_{0.82}\text{Cu}_{1.03}\text{O}_y$ , CuO, SrO (TEM)
750°C in Ar for 25 hours	$\text{Bi}_{2.00}\text{Sr}_{1.64}\text{Ca}_{1.19}\text{Cu}_{0.17}\text{O}_y$ , Cu <sub>2</sub> O, $\text{Bi}_{2.13}\text{Sr}_{1.10}\text{Ca}_{0.73}\text{Cu}_{0.04}\text{O}_y$ (SEM)
800°C in $\text{O}_2$ for 1 min	<b><math>\text{Bi}_{2.19}\text{Sr}_{1.75}\text{Ca}_{1.17}\text{Cu}_{1.88}\text{O}_y</math></b> , CuO, SrO, $\text{Bi}_{0.04}\text{Sr}_{0.10}\text{Ca}_{0.82}\text{Cu}_{1.03}\text{O}_y$ (TEM)
865°C in $\text{O}_2$ for 1 min	<b><math>\text{Bi}_{2.13}\text{Sr}_{1.64}\text{Ca}_{1.27}\text{Cu}_{1.96}\text{O}_y</math></b> , CuO, SrO (TEM)
865°C in $\text{O}_2$ for 25 hours	<b><math>\text{Bi}_{2.12}\text{Sr}_{1.69}\text{Ca}_{1.21}\text{Cu}_{1.98}\text{O}_y</math></b> , CuO, SrO (TEM) $\text{Bi}_{0.37}\text{Sr}_{5.62}\text{Ca}_{8.28}\text{Cu}_{23.74}\text{O}_y$ (SEM)
865°C in $\text{O}_2$ for 100 hours	<b><math>\text{Bi}_{2.10}\text{Sr}_{1.72}\text{Ca}_{1.20}\text{Cu}_{1.99}\text{O}_y</math></b> , SrO (TEM) $\text{Bi}_{0.44}\text{Sr}_{6.06}\text{Ca}_{8.24}\text{Cu}_{23.25}\text{O}_y$ (SEM)

exposure to oxygen, the film on the tube wall turned yellow, the color of  $\text{Bi}_2\text{O}_3$ . However, Bi loss was not detected by either SEM/EDS or ICP analysis and was assumed to be negligible. Phases found in the sample annealed at  $750^\circ\text{C}$  in Ar were identified by XRD as  $\text{Cu}_2\text{O}$  and  $\text{Bi}_2\text{Sr}_{3-x}\text{Ca}_x\text{O}_y$ [22]. A small amount of another Bi-Sr-Ca-O phase was detected in the SEM and compositional measurements suggested it to be similar to  $\text{Bi}_2\text{Sr}_{2-x}\text{Ca}_x\text{O}_y$ [22]. Resistivity measurements showed the argon-annealed sample to be semiconducting. No differences between this sample and the glass were observed by DTA in Ar and the endotherm marked B5 in Figure 6.3 is assigned to the melting of  $\text{Bi}_2\text{Sr}_{3-x}\text{Ca}_x\text{O}_y$ . Melting of  $\text{Bi}_2\text{Sr}_{3-x}\text{Ca}_x\text{O}_y$  around  $750^\circ\text{C}$  in Ar seems to be related to an oxygen deficiency as Roth *et al* reported a similar rhombohedral  $\text{Bi}_2\text{Sr}_3\text{O}_y$  phase to melt incongruently in air between  $1200^\circ\text{C}$  and  $1220^\circ\text{C}$ [22].

Almost all peaks in the x-ray scan in Figure 6.4 of the oxygen-annealed sample could be indexed to the 2212 phase[17]. Small amounts of  $\text{Sr}_{14-x}\text{Ca}_x\text{Cu}_{24}\text{O}$  and  $\text{SrO}$  were found by SEM and TEM analysis[69]. Zero-resistance ( $T_{R=0}$ ) for this sample was measured at 72K. DTA in  $\text{O}_2$  of this sample did not detect the lower two endotherms around  $700^\circ\text{C}$  and  $860^\circ\text{C}$  noted earlier for the amorphous sample. Therefore, melting of the 2212 phase is associated with the endotherm marked A6 in Figure 6.3 with an extrapolated onset temperature of  $886^\circ\text{C}$ .

Finally, the results of the crystallization process discussed in sections 6.2 and 6.3 for  $\text{Bi}_2\text{Sr}_2\text{Ca}_{1.2}\text{Cu}_2\text{O}_y$  are not restricted to this particular composition. DTA scans shown in Figure 6.5 for the series  $\text{Bi}_2\text{Sr}_2\text{Ca}_{1+x}\text{Cu}_2\text{O}_y$  ( $x = 0.5, 0.2, 0, -0.2, -0.5$ ) indicate that the crystallization process in  $\text{O}_2$  is the same for all compositions around the 2212 stoichiometry. Variations in peak intensities and onset temperatures can be attributed to changes in the starting composition. With increasing Ca, the two crystallization exotherms labeled 1 and 2 move closer together and slightly upwards in temperature with a shift in intensity to peak 2. Differences in onset temperatures and intensities can be seen for the endotherms labeled 3, 4,

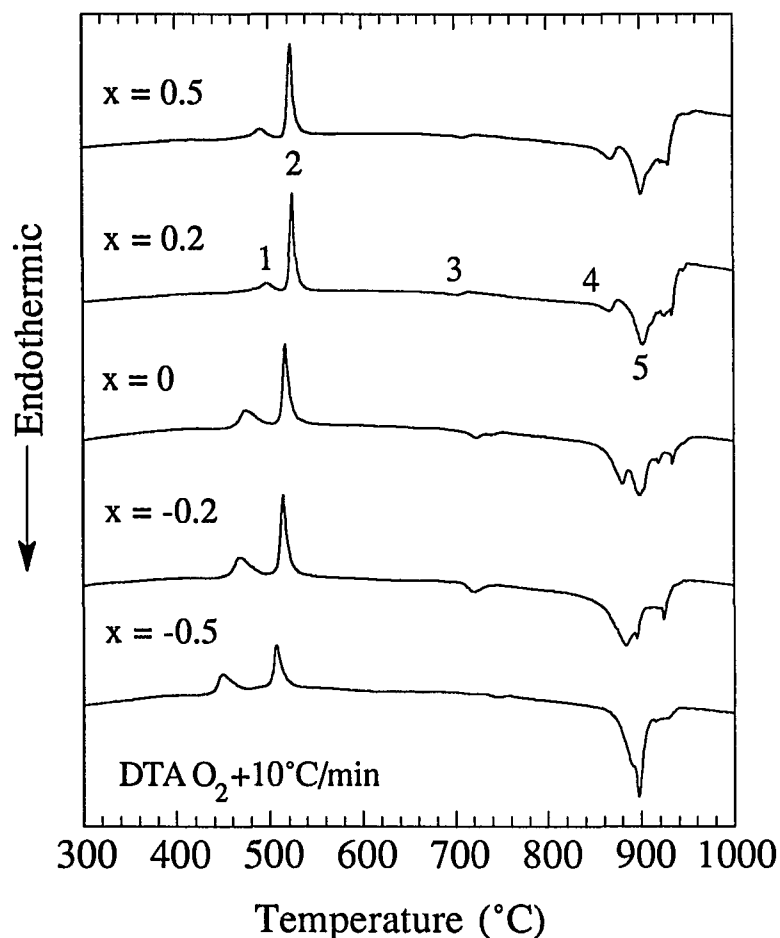


Figure 6.5 DTA heating curves in oxygen for the series of samples  $\text{Bi}_2\text{Sr}_2\text{Ca}_{1+x}\text{Cu}_2\text{O}_y$  ( $x = 0.5, 0.2, 0, -0.2, -0.5$ ).

and 5 in Figure 6.5. As will be shown in Section 6.2, these endotherms are associated with the melting of  $\text{Bi}_2\text{Sr}_{3-x}\text{Ca}_x\text{O}_y$ , 2201 and 2212 respectively. The shift in intensity from endotherm 5 to 4 can be correlated with previous work discussed in Chapter 5 on this series of compositions in which greater amounts of 2201 were found in the final equilibrium phase assemblage as the starting Ca content was decreased.

### 6.1.3 Crucible reactions

Glassy material processed with alumina crucibles was found by ICP analysis to contain approximately 2.25 at.% Al. In order to determine the effects of the Al contamination, two samples with nominal compositions of 2212 were processed as glassy material using alumina and platinum crucibles respectively. These samples were then examined and compared in the as-quenched and crystallized states for any significant differences.

XRD scans of samples processed with  $\text{Al}_2\text{O}_3$  (sample A) or Pt (sample B) crucibles in

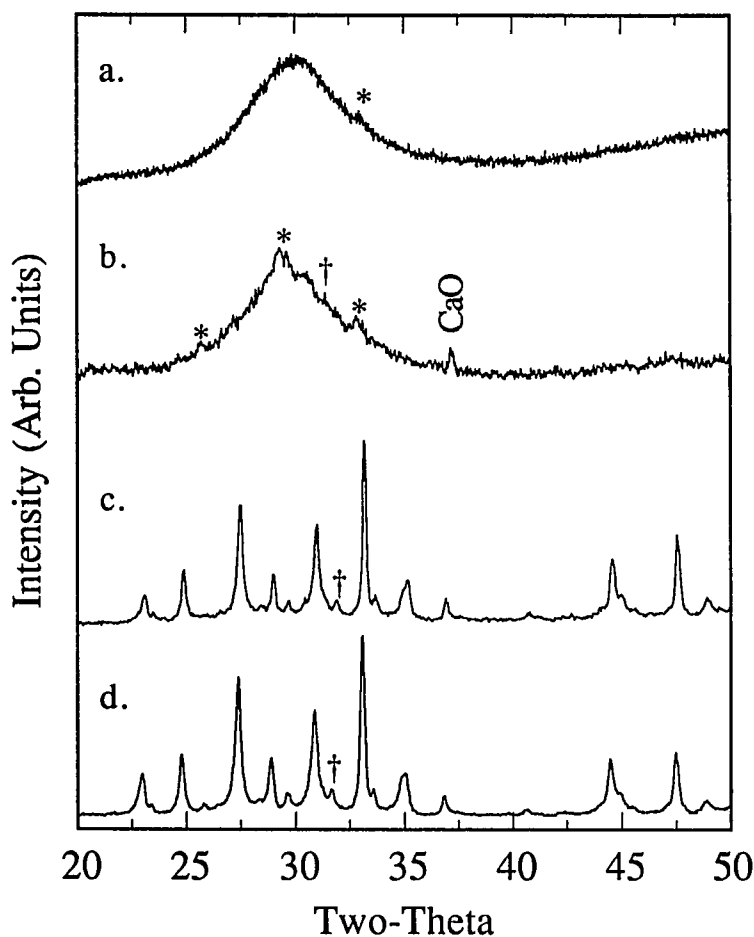


Figure 6.6 XRD scans of (a) sample A and (b) sample B in the as quenched state and (c) sample A and (d) sample B after annealing at 865°C in oxygen for 25 hours. Secondary phases 2201 and  $\text{Sr}_{14-x}\text{Ca}_x\text{Cu}_{24}\text{O}_y$  are denoted as \* and † respectively. All other peaks in annealed samples could be indexed to 2212.

the as-quenched and fully crystallized states are shown in Figure 6.6. Sample A was found to contain a trace of a secondary phase that may be 2201 although investigations by SEM and TEM revealed a completely homogeneous material with no crystalline phases. This may be the result of a small amount of surface crystallization as discussed earlier. ICP analysis results in Table 6.3 showed sample A to contain approximately 2.25 atomic percent Al. This contamination was detected in the TEM only, presumably due to the better peak-to-background ratio. SEM/EDS analysis of the glass matrix was in agreement with ICP results for the Bi, Sr, Ca, and Cu when the Al content determined by ICP was taken into account.

Sample B was found to contain several secondary phases in the as-quenched state. Using a processing temperature of 1075°C, CaO was always found in samples splat-quenched with platinum crucibles regardless of the starting composition while only samples with high Ca contents ( $\text{Bi}_2\text{Sr}_2\text{Ca}_x\text{Cu}_2\text{O}_y$   $x \geq 1.5$ ) were found to have CaO as a second phase when alumina crucibles were used. The other peaks detected by XRD in sample B correspond to 2201 and  $\text{Sr}_{14-x}\text{Ca}_x\text{Cu}_{24}\text{O}_{41}$  (14-24 phase)[69]. Of these two phases, only a few widely scattered grains of the 14-24 phase were ever observed by TEM within the glass sample while SEM revealed only the glass matrix and CaO. ICP results in Table 6.3 showed that Pt contamination accounted for approximately 0.02 atomic percent of the sample and was not detected by EDS analysis in either the SEM or TEM. The presence of secondary phases, particularly CaO, did not affect the composition of the glass matrix to any appreciable extent. SEM/EDS measurements listed in Table 6.3 show only a slight deficiency in the Ca content compared to the ICP results.

DTA scans of samples A and B in the as-quenched state are shown in Figure 6.7. Most thermal events in the two scans can be matched suggesting that the crystallization processes for both samples are essentially the same. Onset and peak temperatures listed in Table 6.4 for the melting of the 2212 phase (endotherms A6 and B8) were nearly identical. However, some minor differences in these scans suggest that the small amount of aluminum in sample



Table 6.3 Summary of results from ICP and EDS compositional measurements. Unless otherwise noted, EDS measurements were performed in the SEM.

	Bi	Sr	Ca	Cu	Al	Pt
As-Quenched						
Sample A - ICP analysis	28.64	26.56	13.91	28.63	2.26	
Sample B - ICP analysis	30.19	27.85	12.62	29.30		0.02
Sample A - glass matrix <sup>a</sup>	28.88	26.20	13.64	29.03		
Sample B - glass matrix	30.59	27.74	11.75	29.93		
Sample A Annealed <sup>b</sup>						
2212 <sup>c</sup>	31.59	27.16	13.06	28.19		
14-24 phase	1.04	18.45	18.61	61.90		
Sr-Ca-Al-O <sup>c</sup>		≈33.3	≈33.3		≈33.3	
CuO				100		
Sample B Annealed <sup>b</sup>						
2212 <sup>c</sup>	30.52	27.78	13.30	28.40		
14-24 phase	0.83	22.66	13.91	62.60		
CaO	0.26	2.15	97.59			

<sup>a</sup>Sample composition was normalized to 97.75% to account for the Al contamination determined by ICP analysis. All other compositions were normalized to 100%.

<sup>b</sup>Sample was annealed for 25 hours at 865°C in O<sub>2</sub> followed by an air quench to room temperature.

<sup>c</sup>Average composition determined from measurements in the TEM.

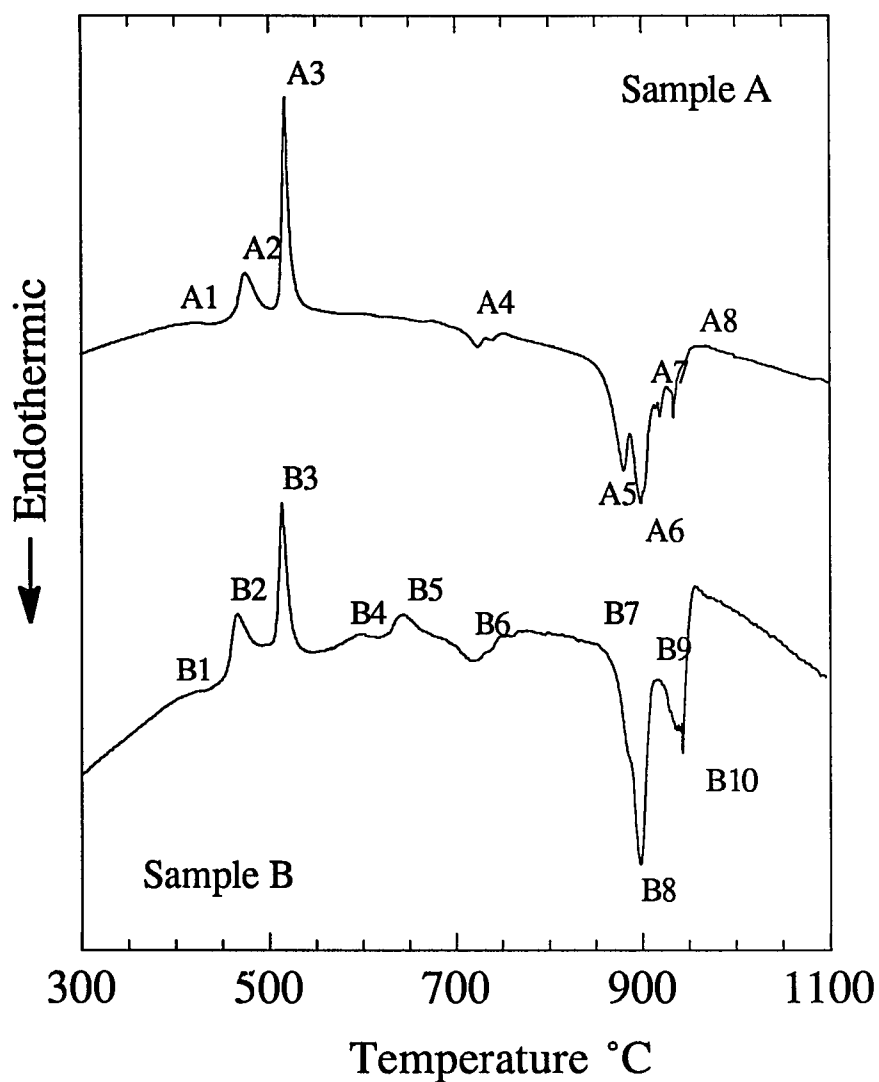


Figure 6.7 DTA scans of as-quenched material from samples A and B. Both scans were performed in flowing oxygen with a heating rate of 10°C/min.

**Table 6.4** List of thermal events from DTA for Sample A and Sample B

Thermal Event	Onset Temperature	Peak Temperature
<b>Sample A<sup>a</sup></b>		
A1. Glass Transition	409°C	
A2. Exotherm	462°C	475°C
A3. Exotherm	512°C	517°C
A4. Endotherm	710°C	724°C
A5. Endotherm	859°C	880°C
A6. Endotherm	887°C	899°C
A7. Endotherm	922°C	925°C
A8. Baseline Shift	934°C	937°C
<b>Sample B<sup>b</sup></b>		
B1. Glass Transition	405°C	
B2. Exotherm	454°C	466°C
B3. Exotherm	507°C	514°C
B4. Exotherm	569°C	596°C
B5. Exotherm	628°C	643°C
B6. Endotherm	697°C	717°C
B7. Endothermic Onset	869°C	
B8. Endotherm	889°C	898°C
B9. Endotherm	920°C	935°C
B10. Baseline Shift	942°C	947°C

<sup>a</sup>Sample A was processed as a glass using an alumina crucible.

<sup>b</sup>Sample B was processed as a glass using a platinum crucible.

A inhibits the formation process of 2212 and affects phase formation in the partially molten state. Differences were found in endotherms A5 and B7 which correspond to the melting of 2201 which is an intermediate phase in the formation of 2212 for these compositions. This formation process will be discussed in greater detail later in this chapter. Two exotherms between 600°C and 700°C were found by DTA for sample B while only a little unevenness in the baseline is seen in this temperature range during DTA of sample A. One or both of these additional exotherms may correspond to the transformation of 2212 from 2201 since this process begins between 550°C and 650°C. Although no 2201 was detected in either sample after anneals at 865°C, as will be discussed below, the substantially larger intensity for thermal event A5 and the lack of any exotherms around 650°C in the DTA scan of sample A is consistent with a reduced formation rate for 2212. Finally, comparison of thermal events above the peritectic involving 2212 suggest substantial differences in the partially melted state. Since no CaO was found in the glassy material processed with the alumina crucible, it appears that a small amount of Al introduced into the Bi-Sr-Ca-Cu-O system lowers the liquidus and/or inhibits the separation of CaO in the partially molten state. It is interesting to note that  $\text{Al}_2\text{O}_3$  as well as  $\text{Bi}_2\text{O}_3$  are conditional glass formers[75]. The relative ease of producing glass free of secondary phases with alumina crucibles under the conditions used in this study and the reduced formation rate of 2212 upon crystallization may be attributed to the small contamination of Al resulting in a slightly more stable glass. Alternatively, the lack of heterogeneous nucleation sites in sample A could also account for the slower kinetics, although this seems less likely since the secondary phases found in sample B in the glassy state were rather large and unevenly distributed. In any case, the actual sequence of phase transformations associated with the crystallization process do not appear to change with the small addition of Al.

XRD scans of samples A and B annealed for 25 hours at 865°C and quenched in air are also shown in Figure 6.6. All major peaks could be indexed to 2212 and secondary phases

were estimated to comprise less than 5% of either sample. No CaO peaks were observed by XRD in sample B indicating that most of it had reacted during heat treatment. Bright field TEM micrographs in Figure 6.8 show a random grain orientation for both samples. Grain sizes on the average were slightly larger in sample B and no secondary phases containing Pt were ever found by either SEM or TEM analysis. On the other hand, sample A contained small Al-rich crystals at some of the grain boundaries as shown in Figure 6.8. These particles were only observable by TEM. Semiquantitative analysis in the TEM gave an approximate composition of  $\text{SrCaAlO}_y$ . Aside from any weak-link problems that may be present, these particles may adversely effect transport properties by disrupting contact between superconducting grains. This could especially be a problem in thin films where the size of these particles becomes comparable to the film thickness or the width of any device features. On the other hand, the small size of these particles suggests a possible use as a flux pinning center provided they could be produced as very small ( $< 5\text{nm}$ ) inclusions within the grains rather than as a grain-boundary phase. In any case, Al contamination should be considered a possibility during bulk or thin film processing using alumina crucibles or substrates.

Compositional measurements of the superconducting and secondary phases are listed in Table 6.3. TEM/EDS was used for analysis of the superconducting phase due to the small grain sizes as shown in Figure 6.8. Compositions of the 2212 phase in both samples were found to be similar with identical transition temperatures of 88K determined from the onset of the diamagnetic signal in the low-field SQUID. Within the limits of the EDS technique, neither Pt nor Al were detected in the superconducting phase. While the small amounts of Al did not affect the superconducting phase, the effects of Pt on the superconducting properties of the 2212 phase cannot be determined from this work because so little contamination from the crucible was encountered. Intentional additions of Pt to the Bi-Sr-Ca-Cu-O system are needed to investigate possible Pt substitution into the superconducting phase and any resulting effects on  $T_c$ .

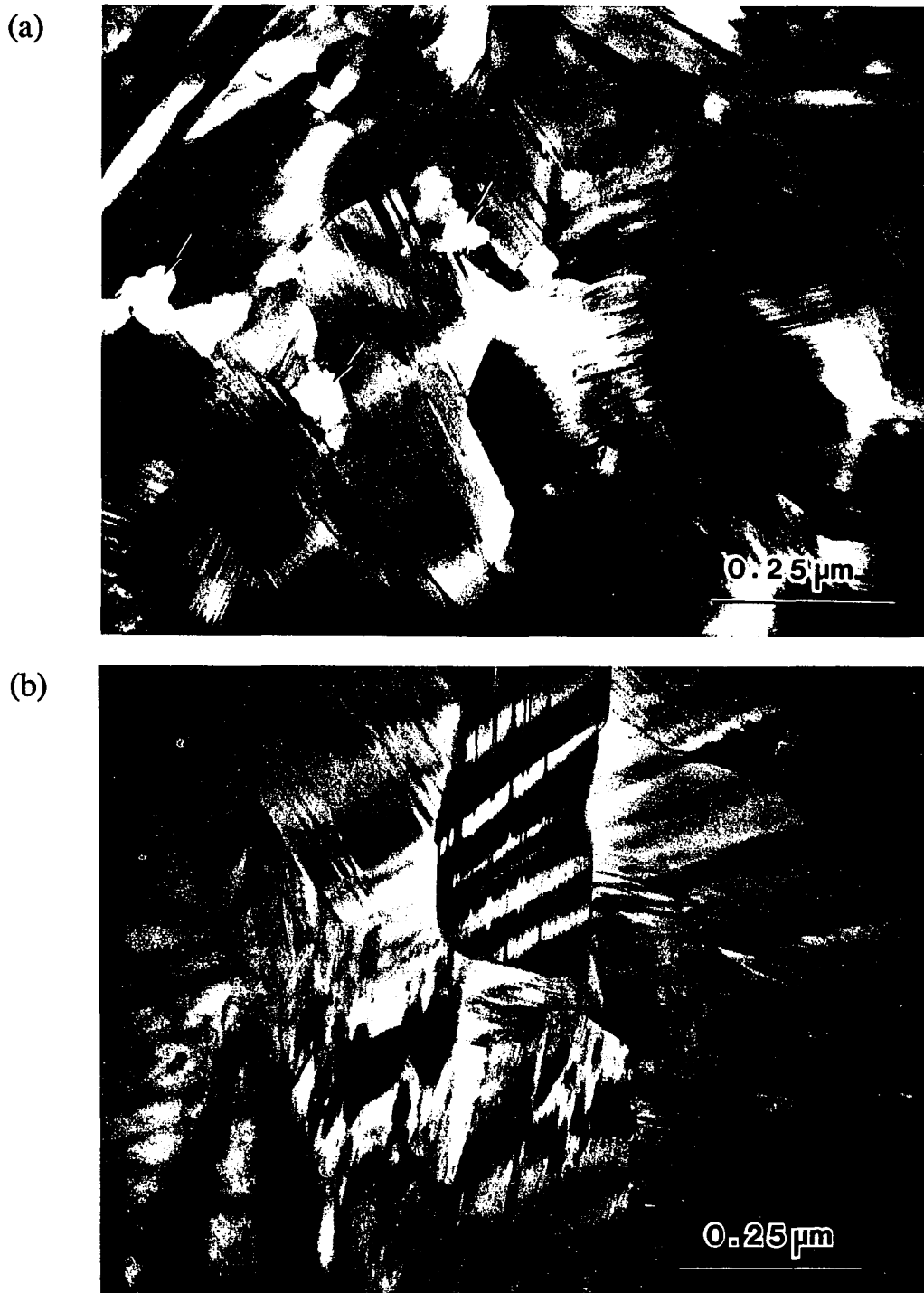


Figure 6.8 TEM bright field micrographs of (a) sample A and (b) sample B annealed at 865°C for 25 hours. Some of the  $\text{SrCaAlO}_y$  particles in (a) are marked with arrows.

Identification of secondary phases such as  $\text{Sr}_{14-x}\text{Ca}_x\text{Cu}_{24}\text{O}_{41}$  in annealed samples was performed in the TEM. For statistical purposes, however, SEM analysis was used for compositional analysis of the secondary phases because of their low volume fraction and the ability in the SEM to examine a larger amount of material compared to TEM. As shown in Table 6.3, sample B contained the 14-24 phase and a few unreacted CaO particles. Sample A contained the 14-24 phase, CuO, and the  $\text{SrCaAlO}_y$  particles observed in the TEM. CuO probably forms in order to balance the amount of Sr and Ca that preferentially combine with Al. Hence, small differences in overall compositions of the samples and changes in effective stoichiometry introduced by the small amount of Al contamination were accommodated largely by changes in the number, composition, and possibly the volume fraction of secondary phases present.

## 6.2. Crystallization

### 6.2.1 Isochronal anneals

Phase formation associated with the crystallization process as recorded by DTA was investigated using a series of one minute anneals at temperatures from 475°C to 865°C. Pieces of the glassy material were heated at a rate of 10°C per minute, held for one minute, and then quenched in air. The results presented here are for the  $\text{Bi}_2\text{Sr}_2\text{Ca}_{1.2}\text{Cu}_2\text{O}_y$  composition. Powder diffraction scans of the one-minute anneals can be found in Figure 6.9. Various phases have been marked to note their presence as a function of temperature. Figure 6.10 contains TEM micrographs and selected area diffraction patterns (SAD) for the anneals at 475°C, 500°C, and 550°C.

One minute at 475°C and 500°C For the sample annealed at 475°C, XRD and SAD revealed only broad, diffuse rings as seen in Figure 6.9 and 6.10a. However, small crystallites with a lattice spacing of 12Å were observed in the bright-field (BF) TEM image,

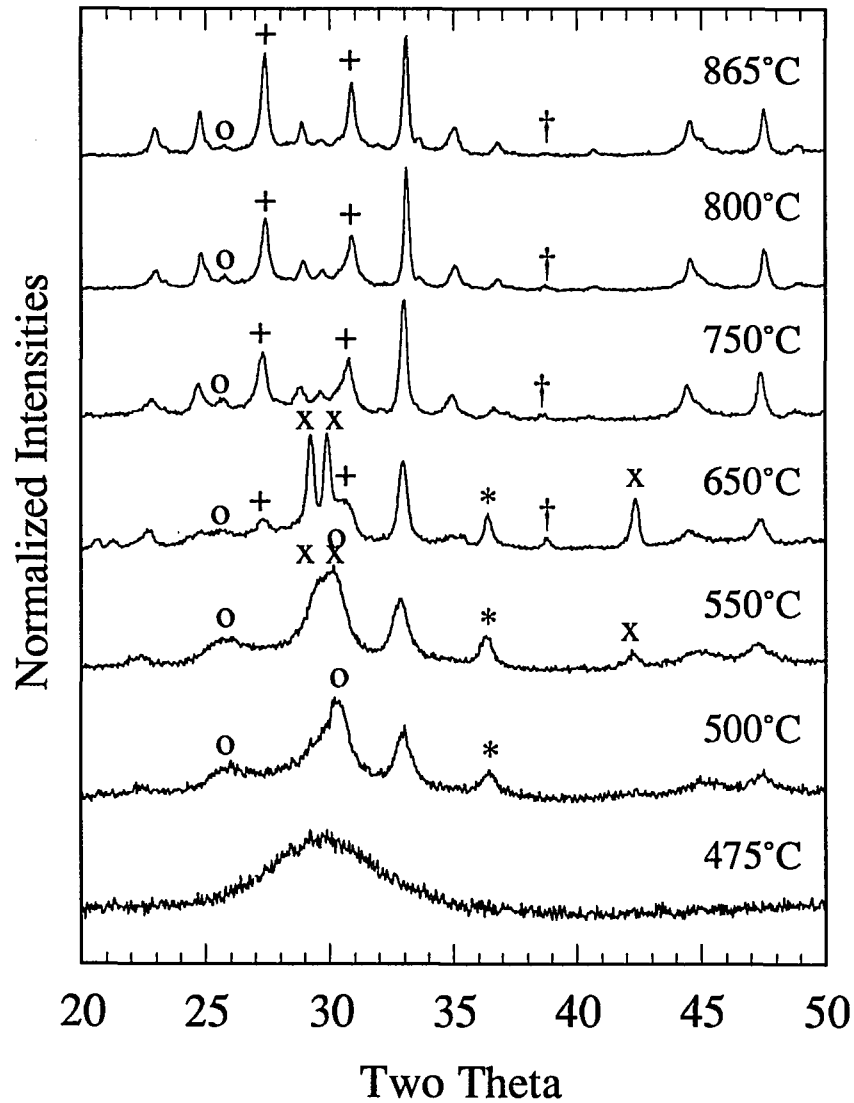


Figure 6.9 XRD scans of the one-minute anneals in the temperature range of 475°C to 865°C. The symbols associated with each phase are as follows: (+) "2212", (o) "2201", (x)  $\text{Bi}_2\text{Sr}_{3-x}\text{Ca}_x\text{O}_y$ , (†) CuO, and (\*)  $\text{Cu}_2\text{O}$ .



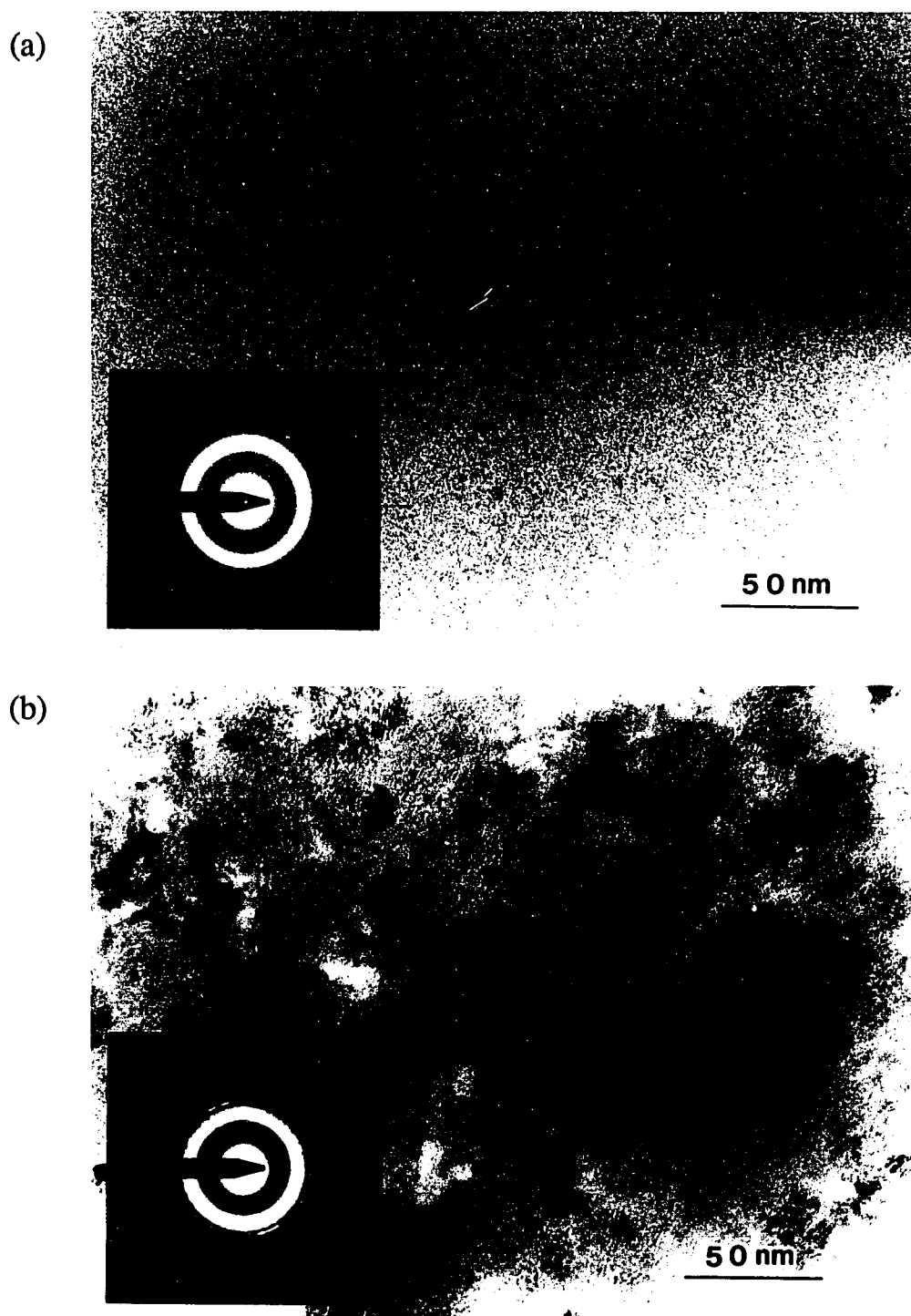


Figure 6.10 TEM bright field micrographs and SAD patterns from the samples annealed for one minute at (a) 475°C, (b) 500°C, and (c) 550°C.

(c)

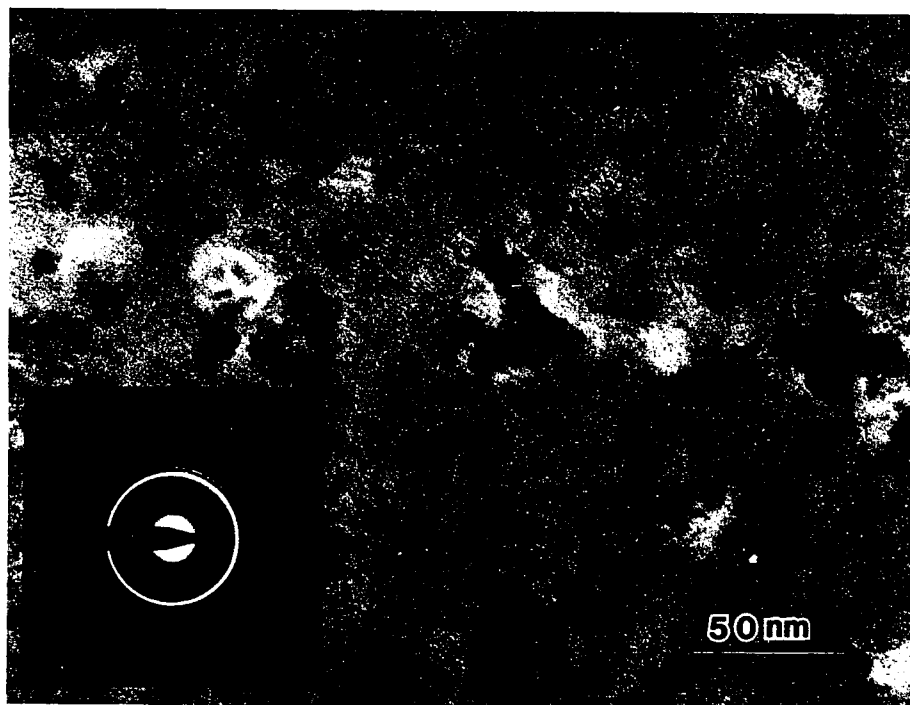


Figure 6.10 (continued)

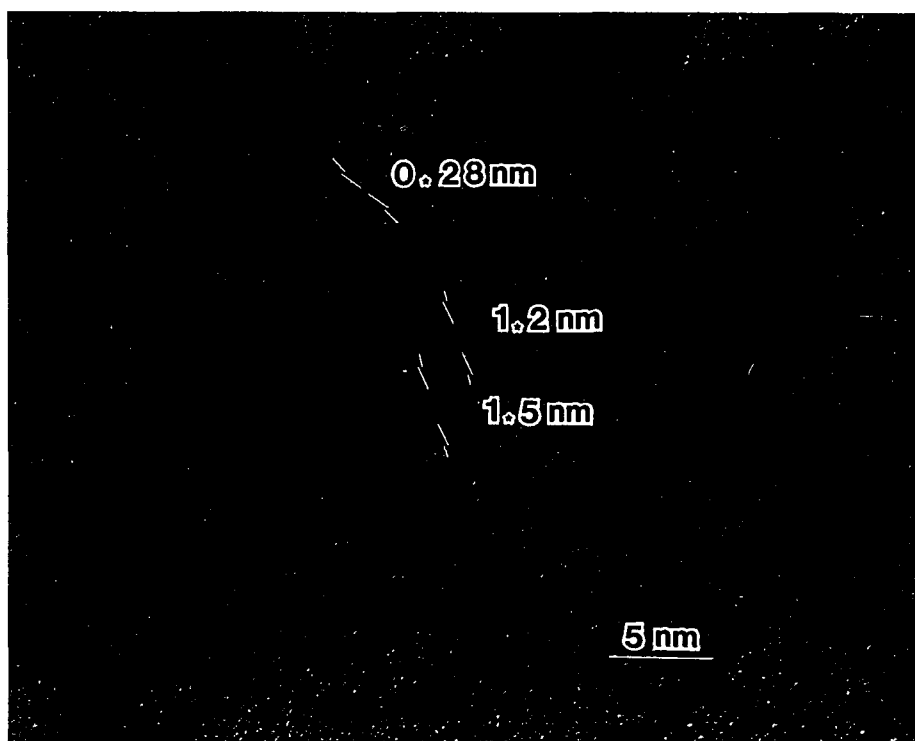


Figure 6.11 Lattice image of a 2201 crystallite from the one-minute anneal at 500°C. Intergrowths of a 15Å phase are marked. The lattice fringes marked as 2.8Å correspond to [200], or [020], planes of these phases.

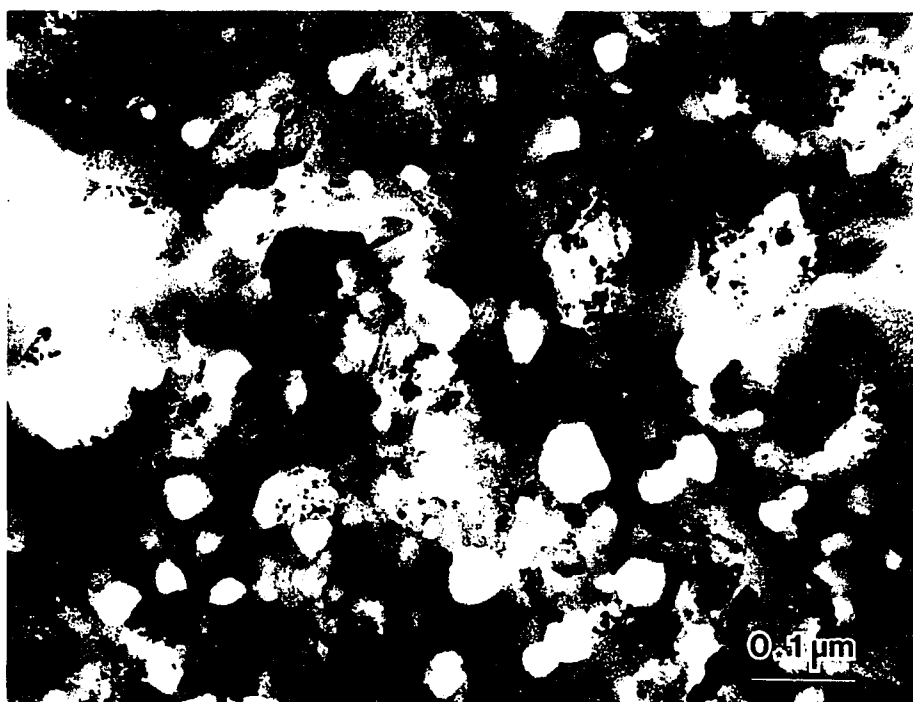
many of which contained intergrowths of a 15Å phase. Several broad peaks are evident in XRD from the sample annealed at 500°C and can be indexed to 2201 and Cu<sub>2</sub>O. TEM analysis revealed only the crystallites and Cu<sub>2</sub>O as shown in Figure 6.10b. These crystallites and intergrowths probably correspond to the 2201 and 2212 phases respectively since 12Å and 15Å are approximately one-half of the c-axis repeat distance for each phase. Figure 6.11 shows a typical 2201 crystallite with several 2212 intergrowths from the sample annealed at 500°C. Not all of the material had crystallized at this point as convergent beam electron diffraction (CBED) revealed a significant amount of amorphous material surrounding the Cu<sub>2</sub>O and 2201 crystallites. This was also confirmed by selected area diffraction (SAD) which showed ring patterns from the 2201 and Cu<sub>2</sub>O phases superimposed upon a broad diffuse halo.

One minute at 550°C The addition of  $\text{Bi}_2\text{Sr}_{3-x}\text{Ca}_x\text{O}_y$  to those phases already present was noted by x-ray diffraction. The  $\text{Bi}_2\text{Sr}_{3-x}\text{Ca}_x\text{O}_y$  phase can be distinguished from 2201 and 2212 by a peak at  $42.4^\circ$  as shown in Figure 6.4. In addition, some CaO and a significant amount of SrO were also observed by TEM. Both BF and SAD micrographs shown in Figure 6.10c indicate that very little amorphous material is left at this point. The SAD pattern does not show the broad halos present in SAD patterns from the samples annealed at  $475^\circ\text{C}$  and  $500^\circ\text{C}$ . None of these phases were large enough to be readily detected by SEM as no differences were found in backscattered electron micrographs of polished cross sections of this sample, the lower temperature anneals, and the as-quenched material.

One minute at 650°C At this point, XRD detected the presence of 2212 which was confirmed by TEM analysis. However, most of the grains had multiple intergrowths of the 2201 phase. TEM/EDS measurements listed in Table 6.2 show the average composition of the 2212 phases to be Bi-rich and Cu-deficient, consistent with the observed number of intergrowths. No grains measured by compositional analysis in the TEM could be considered purely 2201 or 2212. Further examination of the XRD scan in Figure 6.9 reveals that the x-ray diffraction peaks corresponding to  $\text{Bi}_2\text{Sr}_{3-x}\text{Ca}_x\text{O}_y$ ,  $\text{Cu}_2\text{O}$ , and CuO have sharpened considerably. Grain sizes were approximately  $0.5\text{ }\mu\text{m}$ . However, these phases could not be distinguished from each other in the SEM as shown in Figure 6.13a.

One minute at 750°C Considerably more of the 2212 phase was found by XRD in this sample along with small amounts of 2201 and CuO. Grains of the 2212 phase were much larger and clearly defined compared to the sample annealed at  $650^\circ\text{C}$ . A few regions of 2201 could be still be found within these 2212 grains as marked in Figure 6.12b. Small grains of the  $\text{Al}(\text{Sr,Ca})_2\text{O}_y$  phase that results from  $\text{Al}_2\text{O}_3$  crucible contamination were observable along some of the grain boundaries. The  $\text{Bi}_2\text{Sr}_{3-x}\text{Ca}_x\text{O}_y$  phase was not detected in this sample by either XRD or TEM analysis. Partial melting in the interior of the sample seems to have occurred as suggested by the layered microstructure of SrO particles observed in the

(a)



(b)



Figure 6.12 TEM bright field micrographs from samples annealed at (a) 650°C for one minute, (b) 750°C for one minute, (c) 865°C for one minute, and (d) 865°C for 100 hours.

(c)



(d)



Figure 6.12 (continued)

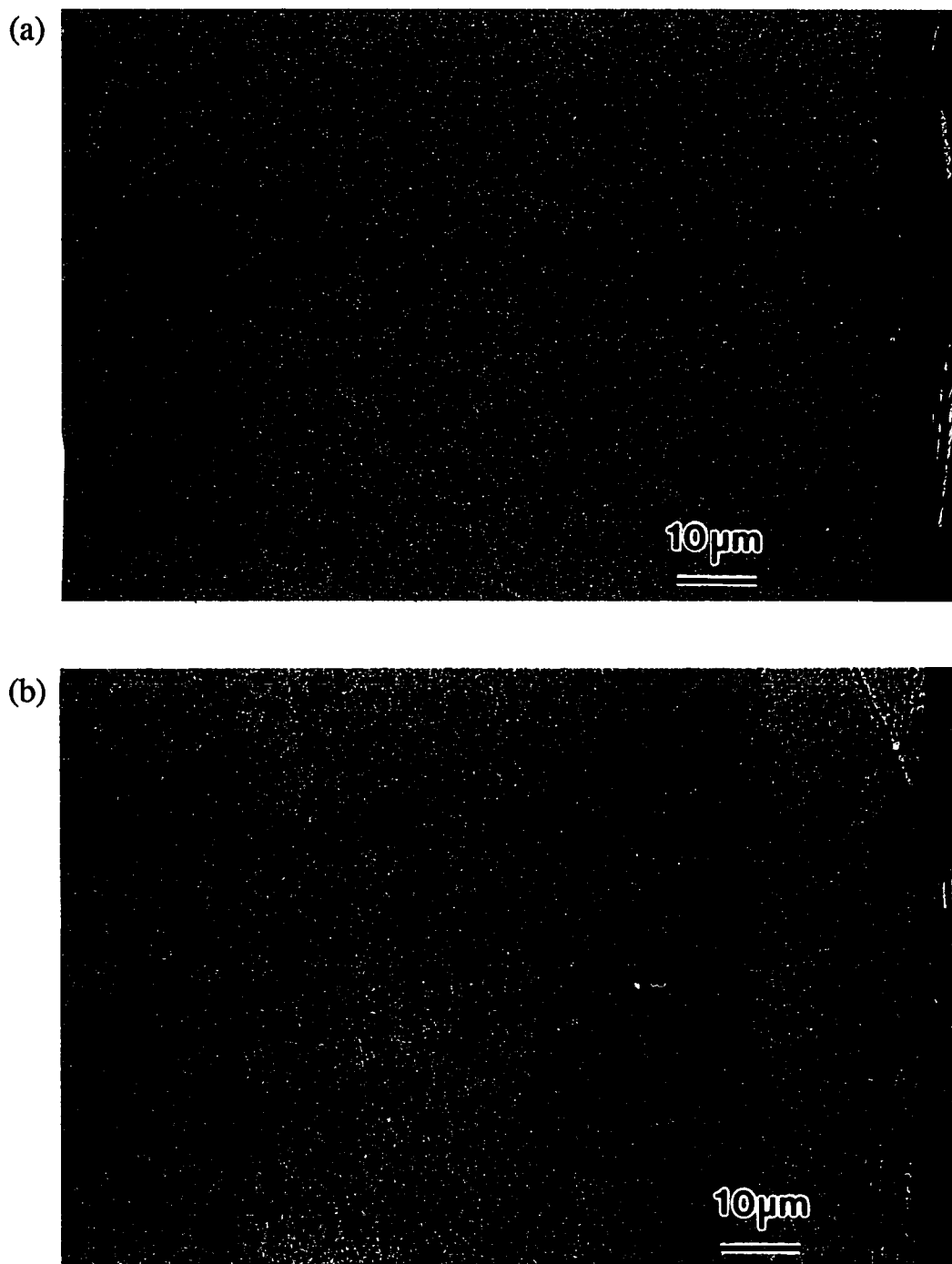
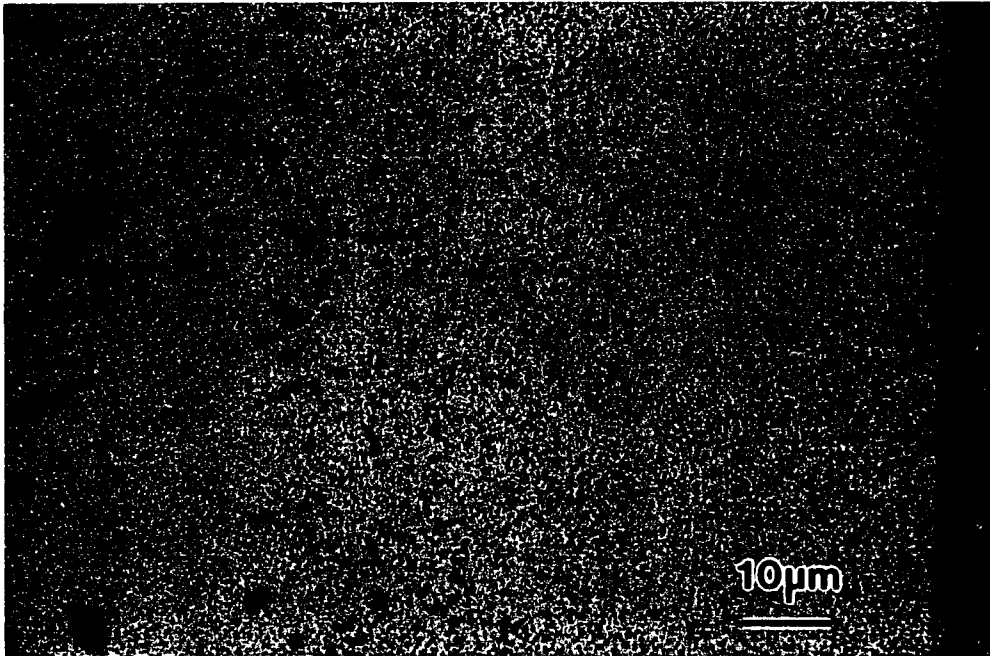


Figure 6.13 Backscattered electron micrographs from polished cross sections of samples annealed for one minute in oxygen at (a) 650°C, (b) 750°C, (c) 800°C, and (d) 865°C.

(c)



(d)

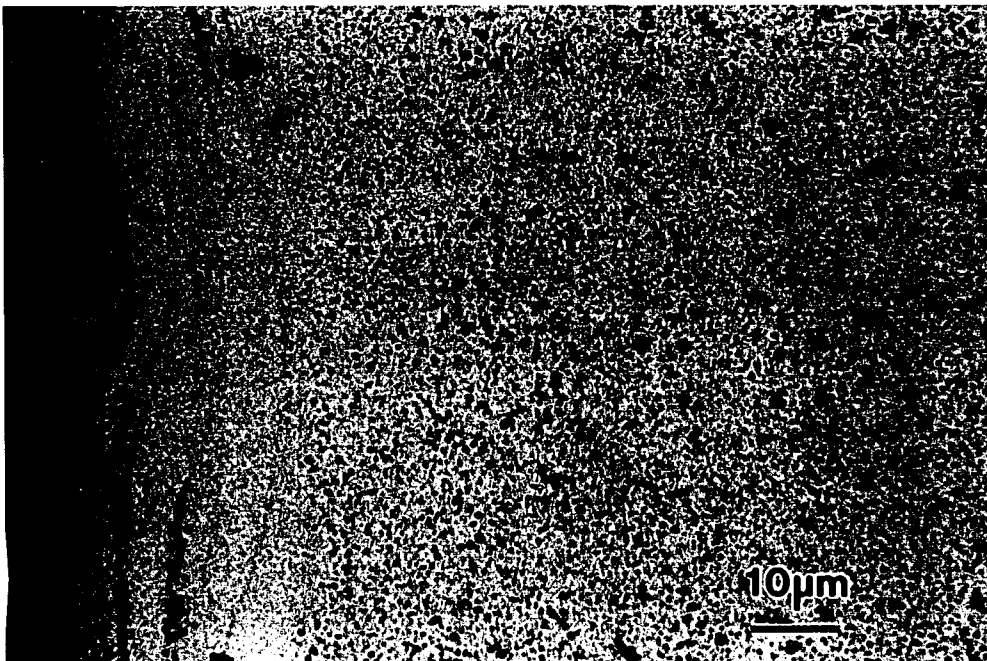


Figure 6.13 (continued)



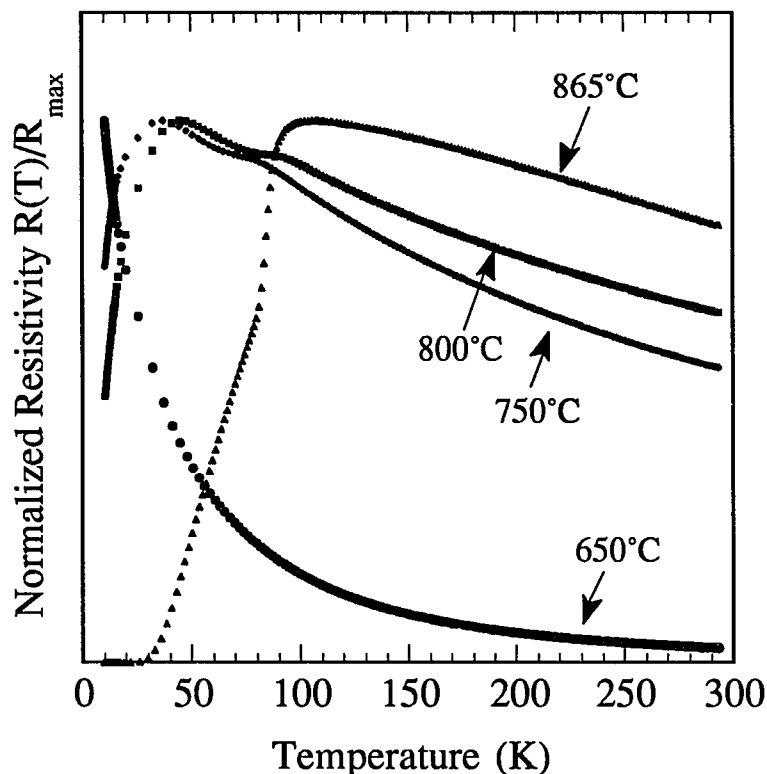


Figure 6.14 Resistivity curves for samples annealed for one minute at 650°C, 750°C, 800°C, and 865°C.

SEM. This layered structure is present for all of the one-minute anneals above 750°C as shown in Figure 6.13. The presence of a liquid would explain the large difference in microstructure observed in the TEM and SEM between the samples annealed for one minute at 650°C and 750°C. Partial melting is consistent with DTA results which show the oxygen-deficient  $\text{Bi}_2\text{Sr}_{3-x}\text{Ca}_x\text{O}_y$  phase to melt in Ar at 750°C. Since  $\text{Cu}_2\text{O}$  was still present at 650°C after one minute in oxygen, it is reasonable to assume that at least part of the sample is still oxygen deficient. Hence, endotherm A4 in Figure 6.3 corresponds to melting of the  $\text{Bi}_2\text{Sr}_{3-x}\text{Ca}_x\text{O}_y$  phase. The lower onset temperature of approximately 690°C is most likely a compositional effect.

One minute at 800°C and 865°C The 2212 phase was the major phase identified in samples annealed at 800°C and 865°C. Relative peak intensities for the sample annealed at 865°C are similar to those shown in Figure 6.4 for the sample annealed for 100 hours. The relative amounts of 2201 and CuO diminished as indicated by XRD. Since 2201 was the only other phase found above 800°C, besides SrO and CuO, the endotherm labeled A5 in Figure 6.3 is associated with the melting of the 2201 phase. TEM micrographs in Figure 6.12 show very little change in grain size between the samples annealed for one-minute at 750°C and 865°C. However, compositional analysis revealed the average compositions of the 2212 phase to approach the ideal ratios for Bi, Sr+Ca, and Cu with increasing anneal temperatures as shown in Table 6.2. The results of these compositional changes are also apparent in the SEM micrographs of Figure 6.13. Fewer large CuO grains and SrO particles were found in the samples annealed at 800°C and 865°C.

Resistivity measurements on the three samples annealed at 475°C, 500°C, and 550°C found them to be semiconducting with no signs of a superconducting transition. Resistivity curves for the samples annealed for one minute at 650°C and above are shown in Figure 6.14. All of these samples showed a semiconducting behavior in the normal state. Samples annealed at 750°C and 800°C showed a small transition around 90K and a larger downward trend starting around 40K. Zero resistance ( $T_{R=0}$ ) values could not be measured below the 10K limit of the closed-cycle cooling system of the resistivity setup. The sample annealed at 865°C for one minute had a broad, single transition starting around 90K with  $T_{R=0}$  at 26K.

### 6.3. Isothermal Anneals

#### 6.3.1 Kinetically limited phase formation

By simply heating the glassy material used in this study to a temperature of 800°C or greater for only one minute, it was found that a majority of the amorphous starting sample

could be converted to the 2212 phase. This was not true for temperatures below 800°C. Therefore, phase formation of the 2212 phase was also studied as a function of time by several isothermal anneals at 550°C, 650°C, 750°C in O<sub>2</sub>.

550°C As shown in Figure 6.15, XRD did not detect the presence of 2212 even after 1000 hours of annealing time. The major phase present was 2201. Peak widths from x-ray diffraction and grain sizes observed in the TEM were similar for both of the samples annealed for one minute and 1000 hours respectively. It was found that with the extended anneals, Cu<sub>2</sub>O converts to CuO and the Bi<sub>2</sub>Sr<sub>3-x</sub>Ca<sub>x</sub>O<sub>y</sub> phase disappears. The phases to which Bi<sub>2</sub>Sr<sub>3-x</sub>Ca<sub>x</sub>O<sub>y</sub> converted could not be accurately determined from either XRD or TEM due to the very small grain sizes. Resistivity measurements for all anneals at 550°C showed a semiconducting behavior with no indication of a superconducting transition down to 10K.

650°C Shown in Figure 6.16 are x-ray diffraction scans from three samples annealed for one minute, 10, and 100 hours. XRD peaks belonging to both 2201 and 2212 were observed to increase with extended anneals. As shown in Figure 6.17, both of these phases were often contained within the same grain. The average composition of these grains from the sample annealed for 100 hours reflected the presence of these two phases. No single measured grain composition was found to be purely 2201 or 2212. Cu<sub>2</sub>O and Bi<sub>2</sub>Sr<sub>3-x</sub>Ca<sub>x</sub>O<sub>y</sub> were again found to disappear with extended annealing times. TEM analysis was needed to completely determine all phases present since an unambiguous identification of all XRD peaks was not possible. Counting 2201 and 2212 separately, eight phases were observed by TEM in the sample annealed for 100 hours. Measured compositions of these phases can be found in Table II. CuO and SrO were present in various amounts after the 100 hour anneal along with a CaCuO phase that was indexed according to an orthorhombic subcell

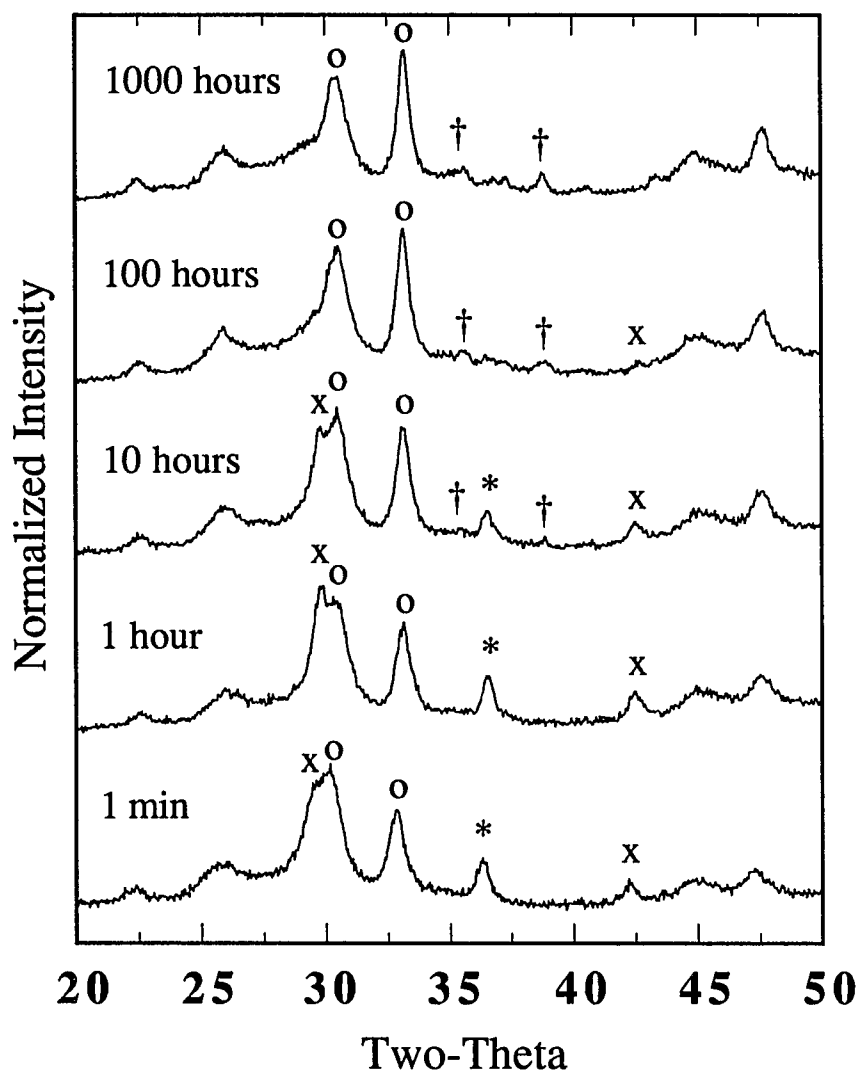


Figure 6.15 XRD scans of several samples following extended anneals at 550°C. Symbols associated with the various phases are as follows: (o) "2201", (x)  $\text{Bi}_2\text{Sr}_{3-x}\text{Ca}_x\text{O}_y$ , (†) CuO, and (\*)  $\text{Cu}_2\text{O}$ .

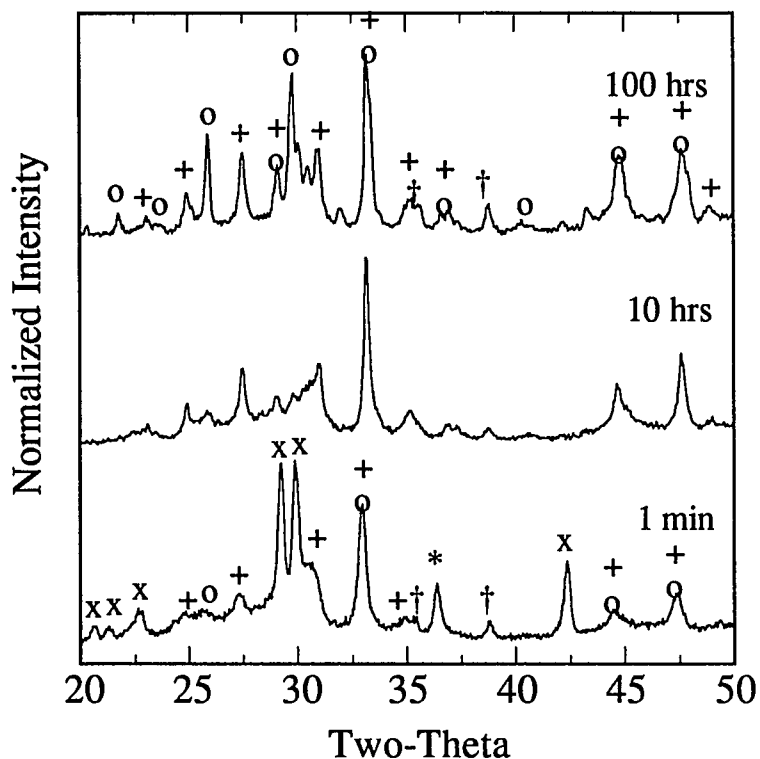


Figure 6.16 XRD scans of samples annealed at 650°C for one minute, 10, and 100 hours respectively. Several peaks in the 100 hour anneal could not be clearly indexed. The phases are designated as follows: (+) 2212, (o) 2201, (x)  $\text{Bi}_2\text{Sr}_{3-x}\text{Ca}_x\text{O}_y$ , (†) CuO, and (\*)  $\text{Cu}_2\text{O}$ .

structure[23]..  $\text{Bi}_2\text{Sr}_{3-x}\text{Ca}_x\text{O}_y$  was also found by TEM analysis, but in much smaller amounts compared to the one minute anneal. Another phase with an approximate composition of  $\text{Bi}_2(\text{SrCa}_2)_2\text{O}_y$  seems to have formed at the expense of  $\text{Bi}_2\text{Sr}_{3-x}\text{Ca}_x\text{O}_y$  and appears to be related to a  $\text{Sr}_6\text{Bi}_2\text{O}_y$  phase reported by Roth *et al*[22]. It is probable that this same phase evolution is also occurring at 550°C, but at a much slower rate.

**750°C** Significant amounts of 2201 developed as a function of time although not to the extent found during anneals at 650°C. XRD and TEM revealed the 2212 phase to be the major phase although many of these grains contained intergrowths and distinct regions of the

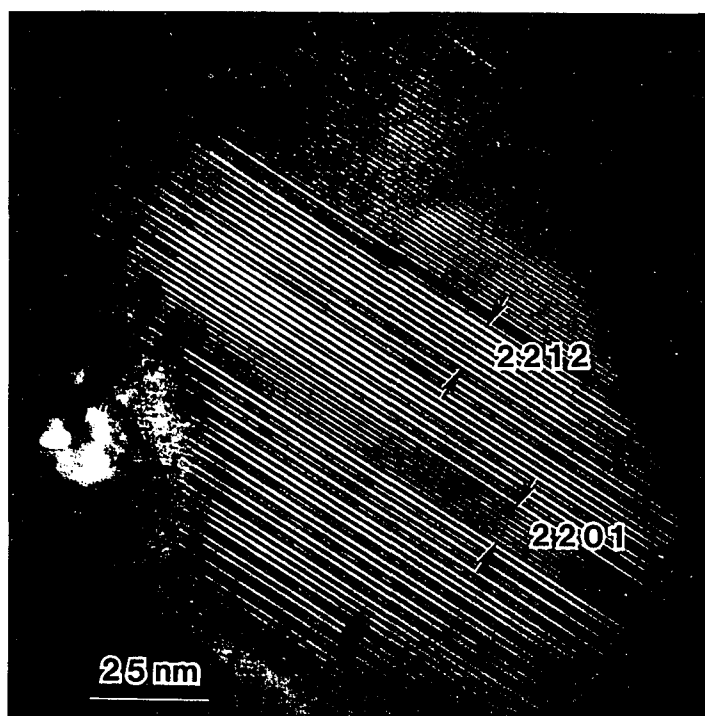


Figure 6.17 Lattice image of a 2212 grain from the sample annealed at 650°C for 100 hours that actually is composed of regions of 2212 and 2201 as indicated. Also visible below the marked 2201 phase is a region of alternating layers of 2212 and 2201 of various thicknesses.

2201 phase. Small amounts of  $\text{CaCuO}$ ,  $\text{CuO}$ , and  $\text{SrO}$  were also identified by TEM. Hence, the formation of 2212 at 750°C is still kinetically limited.

### 6.3.2 Equilibrium phase assemblage

800°C and 865°C The dominant phase in all anneals was 2212 as determined by XRD, SEM, and TEM. The small amount of 2201 observed by XRD after the one minute anneals at these temperatures quickly disappeared with extended annealing times. Resistivity data shown in Figure 6.18 for the samples annealed at 865°C show a change from a semiconducting to metallic behavior in the normal state and a sharpening of the superconducting transition as the annealing time increased. However, resistivity results for

the sample annealed for 100 hours still show a rather broad transition with an onset around 90K and zero-resistance at 72K. Overall, SEM analysis on samples heat treated at 865°C showed a gradual disappearance of CuO needles and the appearance of a  $\text{Sr}_{14-x}\text{Ca}_x\text{Cu}_{24}\text{O}_y$  phase as the anneals were extended to 100 hours. A backscattered electron micrograph of a polished-cross section from the sample annealed for 25 hours at 865°C is shown in Figure 6.19. The larger, dark needles are  $\text{Sr}_{14-x}\text{Ca}_x\text{Cu}_{24}\text{O}_y$  while the very fine black particles are SrO. On either surface of the sample, a region of grain growth of the 2212 phase perpendicular to the surface was observed. Grain sizes in this region were much larger than in the middle sections of the sample, and it is separated from the bulk of the sample by a layer consisting of small grains of  $\text{Sr}_{14-x}\text{Ca}_x\text{Cu}_{24}\text{O}_y$  and voids. Within the bulk of the

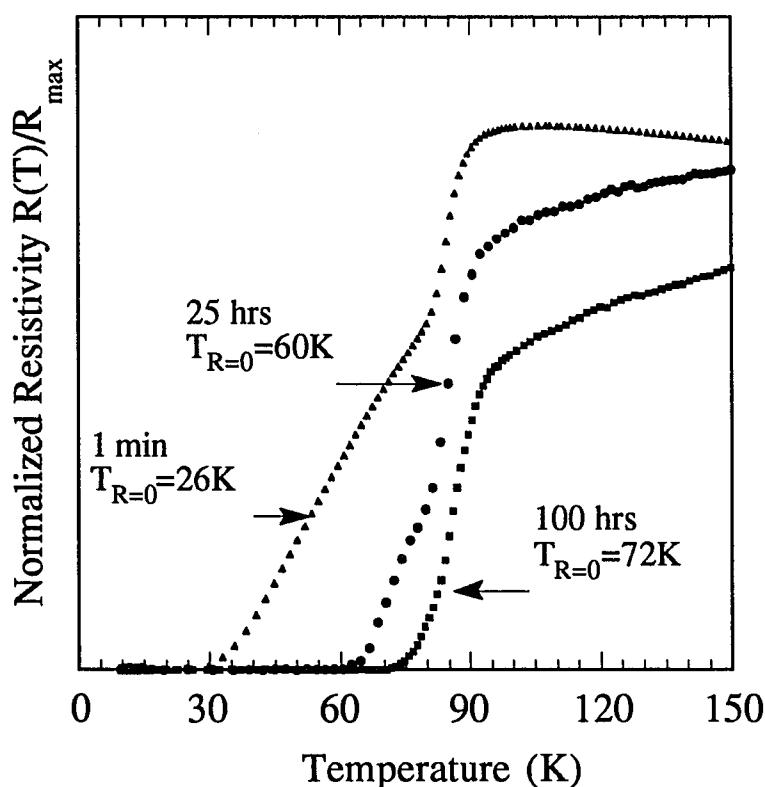


Figure 6.18 Resistivity curves from the  $\text{Bi}_2\text{Sr}_2\text{Ca}_{1.2}\text{Cu}_2\text{O}_y$  glass samples annealed at 865°C for 1 minute, 25, and 100 hours showing an improvement in the superconducting transition with annealing time.

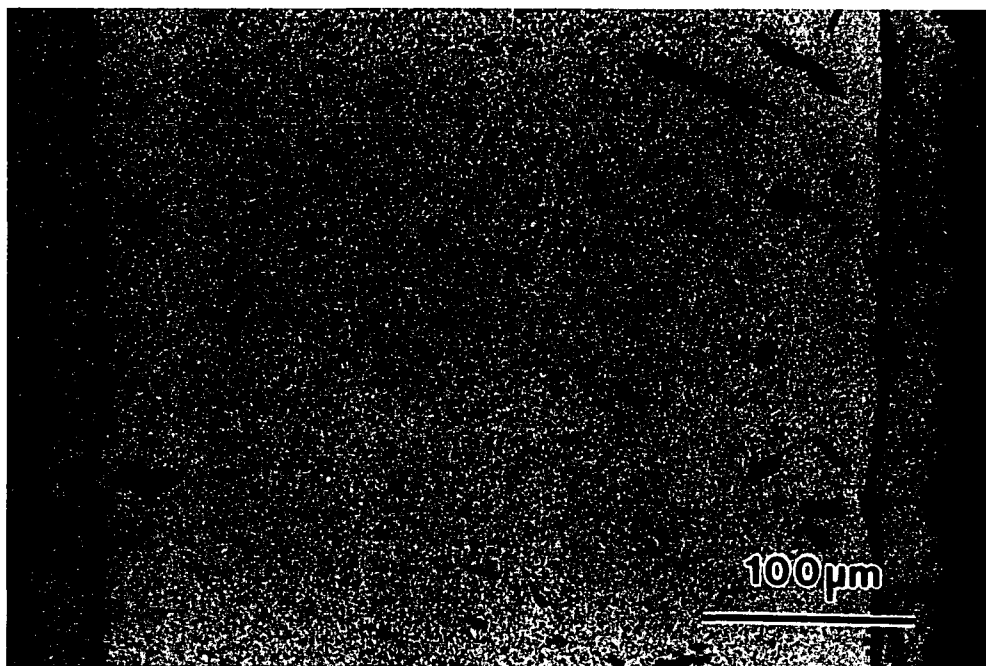


Figure 6.19 Backscattered electron micrograph of a cross section of the  $\text{Bi}_2\text{Sr}_2\text{Ca}_{1.2}\text{Cu}_2\text{O}_y$  sample annealed for 25 hours at  $865^\circ\text{C}$ . The layer of grain growth perpendicular to the surface is typical of these glasses when heat treated at  $800^\circ\text{C}$  and above.

sample, no noticeable change in grain size of 2212 was observed by TEM with the extended annealing times at  $865^\circ\text{C}$ . However, EDS analysis detected small changes in the average composition of the 2212 phase for all the samples annealed at  $865^\circ\text{C}$ . A gradual trend towards the ideal  $\text{Bi}_2(\text{Sr,Ca})_3\text{Cu}_2\text{O}_y$  was observed with extended anneals although the measured composition of the 2212 phase from the 100 hour anneal at  $865^\circ\text{C}$  was still slightly Bi rich as shown in Table 6.2.

2212 Stability Due to the number of phases present at  $650^\circ\text{C}$  after 100 hours of annealing time, a simple test was undertaken to determine the stability of the 2212 phase at



650°C for 100 hours. The initial sample, as shown in Figure 6.4, was almost completely single-phase 2212. After the anneal at 650°C, no changes could be detected by XRD indicating that 2212, once formed, is quite stable and does not decompose at lower temperatures into any of the phases observed during the crystallization process.

#### 6.4. Discussion

The aim of the present study was to investigate the crystallization and low-temperature phase formation of compositions in the Bi-Sr-Ca-Cu-O system close to the nominal 2212 stoichiometry. No systematic study was undertaken to determine an optimal heat treatment schedule to maximize the superconducting properties. It was observed, however, that a majority of the material could be converted to the 2212 phase at 800°C and above after one minute of annealing in oxygen.

One important note to make before discussing the results of this study is that the initial state of the glassy material and the heating rate used during crystallization will affect phase formation from the glassy state. These considerations should be taken into consideration when comparing results between the various crystallization studies found in the literature. In this work, characterization of the glassy state revealed a significant oxygen deficiency. Furthermore, glass pieces were crystallized as pieces rather than powders which limits the uptake of oxygen. The phases that form during crystallization of the glass pieces in this study reflect this oxygen deficiency. Different results may be obtained, for example, if the glassy material is crystallized as a powder in which the higher surface to volume ratio of the powder allows for a faster equilibration with the surrounding atmosphere. Since crystallization from the glassy state is a non-equilibrium process, it is not surprising that there may be several different crystallization routes. In the end, however, these various crystallization paths must arrive at the same equilibrium phase(s).

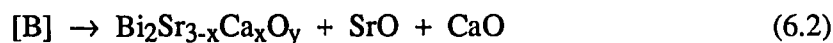
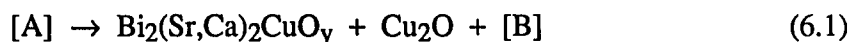
It is not surprising that glasses can be obtained in this system given that  $\text{Bi}_2\text{O}_3$  is a conditional glass former[75]. However, a better understanding of the glass formation process in the Bi-Sr-Ca-Cu-O system can be obtained from the standpoint of kinetics. On cooling through the liquidus, there must be kinetic factors that limit the crystallization process. For example, direct crystallization of complex crystal structures is more difficult compared to simple, open structures. Another consideration is the effect of the liquidus temperature. A lowering of the liquidus corresponds to a decrease in the amount of energy available for breaking bonds in the liquid necessary for crystallization to proceed[75]. Compositions near a eutectic, for example, are easier to form as a glass by a suitable quenching technique since the liquid phase can exist at a lower temperature compared to other compositions further away from the eutectic. For the case at hand, similar effects occur due to oxygen deficiencies since this results in a lowering of the solidus temperature.

From the results of the TGA experiment on the as-quenched material, the amount of oxygen absorbed on heating was calculated to be the equivalent of 0.41 oxygen per copper atoms in the material. This is close to the value of 0.44 found by Nassau *et al*[55]. Based on this result, it can be assumed that at the processing temperature of 1075°C used in this study, the melt is oxygen deficient. It is generally known that the high- $T_c$  phases do not form in deficiencies of oxygen. None of the superconducting phases were present, for example, in the sample annealed in Ar at 750°C. For comparison, a large amount of 2212 was found in the sample annealed for only one minute in  $\text{O}_2$  at 750°C. In a related study, the perovskite structure was found to be dependent upon the stability of the  $\text{Cu}^{+2}$  state in the Cu-O planes[76]. In this crystallization study, one of the first phases to appear upon crystallization of the oxygen-deficient glasses is  $\text{Cu}_2\text{O}$  indicating that the oxidation state for a large amount of the Cu is in the +1 state. In addition, DTA has shown that the absence of  $\text{O}_2$  lowers the solidus temperature. Given the oxygen deficiency in the melt, some undercooling of the 2212 phase can be expected during solidification. Polanka *et al* have observed such an

undercooling of 2212 by high-temperature x-ray studies of the melting and solidification processes[53]. Therefore, an oxygen deficiency in the melt inhibits formation of the superconducting phases and lowers the liquidus, both of which create favorable conditions for quenching to the amorphous state.

Almost all compositions around the 2212 stoichiometry could be produced in glass form without significant amounts of secondary phases using alumina crucibles, although some Al contamination was found by ICP. No Al was observed to substitute into the superconducting phases by TEM/EDS analysis. Impurity phases that contained Al were found along some of the grain boundaries as shown in Figures 6.8 and 6.12. The presence of Al within the sample, however, does not appear to have altered the crystallization sequence. The SrCaAlO<sub>y</sub> particles may have restricted grain growth since no difference in grain sizes can be seen between the one minute and 100 hour anneal at 865°C. It is uncertain if the broad transitions and tails seen in the resistivity measurements of Figure 15 are the result of these particles at the grain boundaries. The same general distribution of Sr-Ca-Al-O particles was found by TEM for both of the samples annealed for one minute and 100 hours at 865°C. The main differences between these anneals were in the types of impurity phases present and the final composition of the superconducting phase, suggesting that compositional changes were, to a large extent, responsible for the improvement in resistivity results.

The two exotherms that occur in the temperature ranges of approximately 440°C to 490°C and 500°C to 520°C were found to correspond to specific crystallization events in pure O<sub>2</sub> based on the XRD, SEM, and TEM results from the one-minute anneals. These can be written in their order of occurrence as:



where [A]. is the original glass composition and [B]. is the resulting glass composition after the first crystallization event. The composition of [B]. could not be accurately determined by TEM/EDS analysis due to the small size of the residual amorphous regions. It might differ from [A]. in cation content, oxygen content, or, more likely, a combination of the two. The amounts and actual composition of each phase will be, in general, dependent upon the starting composition. However, the same general crystallization events were found to occur for all compositions around the 2212 stoichiometry as illustrated in Figure 6.5 by DTA. This was confirmed by x-ray analysis of one-minute anneals of another sample with composition  $\text{Bi}_2\text{Sr}_2\text{Ca}_{0.8}\text{Cu}_2\text{O}_y$ .

The initial crystallization of 2201 is clearly illustrated in the TEM micrograph of Figure 6.10a and is in agreement with most works by other groups on these glasses. The phase that has not been reported to occur during initial crystallization is the oxygen-deficient  $\text{Bi}_2\text{Sr}_{3-x}\text{Ca}_x\text{O}_y$ . This phase was found to convert to other phases upon extended anneals at 550°C and 650°C in oxygen. Hence, this intermediate phase was probably missed in other studies simply for a lack of short anneals. No 2212 was ever found at 550°C except as intergrowths within the 2201 crystallites even after 1000 hours of annealing. Apparently no grain growth occurred during the 1000 hour anneal since broad peaks were still present in XRD scans of Figure 6.15, an observation also noted by Nassau *et al*[55]. The lack of grain growth result is probably related to the oxygen deficiency within the glass. 2201 nuclei form with whatever oxygen can be taken from the surrounding material. Further grain growth or conversion to the 2212 phase is limited by an oxygen deficiency surrounding the nuclei as indicated by the simultaneous formation of  $\text{Cu}_2\text{O}$  instead of  $\text{CuO}$ . Upon further heating, the second crystallization of the residual glass between 500°C and 550°C results in the oxygen-deficient  $\text{Bi}_2\text{Sr}_{3-x}\text{Ca}_x\text{O}_y$  phase plus various amounts of  $\text{SrO}$  and  $\text{CaO}$ . Hence, five separate phases are present and continued formation of the 2201 and possibly 2212 phases during

extended anneals at 550°C is kinetically limited due to the low temperature and the phase separation that occurred on crystallization.

At 650°C, XRD and TEM revealed the presence of the 2212 phase in the sample annealed for one minute although no specific thermal event between 550°C and 650°C from DTA scans can be matched to this observation. Based on the results from the short and extended anneals, the formation of the 2212 phase appears to be a kinetically limited process involving the conversion of the 2201 nuclei formed during the first stage of the crystallization process. As shown in Figure 6.17, grains of the 2212 phase from the sample annealed for 100 hours at 650°C are actually a combination of both the 2212 and 2201 phases. This mixed structure results due to a combination of limited diffusion and the phase separation that occurred during the earlier crystallization events. Eight separate phases were found in the sample annealed for 100 hours at 650°C. It is evident that the system has not reached equilibrium after 100 hours at 865°C since the presence of eight phases is a clear violation of the phase rule. As growth of the 2212 and 2201 phases proceeds at 650°C, changes in the composition of the surrounding material is accommodated by the formation of other phases. In this study, for example, CaCuO and  $\text{Bi}_2(\text{SrCa}_2)_2\text{O}_y$  were observed to form upon extended anneals at 650°C even though they were not initial crystallization products. 2212 is the stable phase at this temperature as noted above.

Some authors have ascribed the small endotherm that occurs between 700°C and 750°C as the thermal event(s) connected with the formation of the 2212 phase[57,58]. Based on results from this study, the endotherm labeled A4 in Figure 6.3 was found to be associated with the melting of the oxygen-deficient  $\text{Bi}_2\text{Sr}_{3-x}\text{Ca}_x\text{O}_y$  phase that formed during the second crystallization event. Sample melting was also encountered around 700°C by Kramer *et al* during crystallization under pressure in oxygen of similar glass samples[77]. The large increase in the amount of 2212 between the samples annealed at 750°C and 650°C for one minute is probably a result of liquid-aided diffusion. However, the formation of the 2212

phase is still kinetically limited at 750°C since 2201 and CaCuO were still present after 100 hours of annealing. Only at 800°C and above was the small amount of 2201 present after the one-minute anneals found to disappear with extended anneals. As shown in Figure 6.12, there is no apparent difference in grain sizes between the samples annealed for one minute at 750°C and 100 hours at 865°C. The main differences are in the types of secondary phases present and the average composition of the 2212 phase. As the temperature of the anneal increased, the measured composition of the 2212 phase tended towards the ideal  $\text{Bi}_2(\text{Sr,Ca})_3\text{Cu}_2\text{O}_y$  composition. Based on the results of Chapter 5, this trend is probably associated with a reduction in the number of intergrowths within the 2212 phase. The measured composition of the 2212 phase was also observed to approach the ideal composition for extended anneals at 865°C as depicted in Table 6.2. Given the x-ray data, it is clear that a majority of the sample had been converted to the 2212 phase after only one minute of annealing at 800°C and above. However, longer anneals were needed for the sample to reach an equilibrium state and improve the superconducting properties as indicated by compositional measurements of the 2212 grains and resistivity results.

## 6.5. Summary

A detailed crystallization study of compositions near the 2212 stoichiometry was undertaken to determine the sequence of events leading to the formation of the 2212 phase as a function of annealing temperature and time in an oxygen environment. Glasses were prepared with both Pt and  $\text{Al}_2\text{O}_3$  crucibles. Although the melt wets both crucible materials, very little reaction with the Pt crucible was observed. The glasses processed with Pt crucibles typically contained some CaO,  $\text{Sr}_{14-x}\text{Ca}_x\text{Cu}_{24}\text{O}_y$ , and 2201 as secondary phases. Glasses processed with alumina crucibles were nearly free of secondary phases, but contained approximately 2.5 atomic percent Al in solution. The crystallization process for

both samples was determined to be essentially the same although the small addition of Al seemed to inhibit the formation rate of the "2212" phase during crystallization. For comparable samples processed with alumina and platinum crucibles, no differences in the transition temperatures of the superconducting phase were found.

Crystallization of the glassy material was found to be influenced by an oxygen deficiency present in the as-quenched glass. The crystallization process was found to occur in two steps with the formation of 2201,  $\text{Bi}_2\text{Sr}_{3-x}\text{Ca}_x\text{O}_y$ , and some simple oxides. The  $\text{Bi}_2\text{Sr}_{3-x}\text{Ca}_x\text{O}_y$  phase resulting from the crystallization process converts to other phases upon annealing in oxygen below  $700^\circ\text{C}$ , and it melts during heating of the glass around  $700^\circ\text{C}$ . The 2212 phase evolves from 2201 nuclei that form during initial crystallization. Its formation from 2201 below  $800^\circ\text{C}$  was found to be kinetically limited, presumably by diffusion. In contrast, a majority of the sample could be converted to the 2212 phase after only one minute of annealing in  $\text{O}_2$  at  $800^\circ\text{C}$  and above. However, extended anneals at these higher temperatures were needed for the system to reach its equilibrium state as shown by compositional measurements on individual grains and changes in the secondary phases present.

## 7. SOLIDIFICATION FROM THE MELT

In order to develop a reliable and efficient process for melt-processing of wires, tapes, or bulk forms, the melting and solidification of both the 2201 and 2212 phases must be clearly understood. In this chapter, the phases and microstructures that result during solidification from the melt as a function of the oxygen partial pressure were identified in order to understand and control the formation of the 2212 and other competing phases. A representative 2201 sample was included in this investigation for comparison purposes since the 2201 phase is commonly found in solidified samples with a nominal 2212 stoichiometry.

### 7.1. Starting Materials

Two compositions,  $\text{Bi}_2\text{Sr}_2\text{Ca}_1\text{Cu}_2\text{O}_y$  and  $\text{Bi}_2\text{Sr}_{1.75}\text{Ca}_{0.25}\text{Cu}_1\text{O}_y$ , were used in this study.  $\text{Bi}_2\text{Sr}_{1.75}\text{Ca}_{0.25}\text{Cu}_1\text{O}_y$  was chosen as a representative composition for 2201 since it usually contains around 5 at.% Ca when found in combination with 2212. Samples of  $\text{Bi}_2\text{Sr}_{1.75}\text{Ca}_{0.25}\text{Cu}_1\text{O}_y$  and  $\text{Bi}_2\text{Sr}_2\text{Ca}_1\text{Cu}_2\text{O}_y$  were annealed in Ar or  $\text{O}_2$  and characterized prior to their use in DTA and solidification experiments. X-ray scans and compositional measurements of the phases present in these samples can be found in Figure 7.1 and Tables 7.1 and 7.2 respectively. The 2201 sample,  $\text{Bi}_2\text{Sr}_{1.75}\text{Ca}_{0.25}\text{Cu}_1\text{O}_y$ , was initially processed as a glass with an alumina crucible and, hence, contains a small amount of Al contamination as described in Chapter 6. Heat treatment of this sample in  $\text{O}_2$  resulted in 2201 as the major phase with minor amounts of 2212 and  $\text{Sr}_{14-x}\text{Ca}_x\text{Cu}_{24}\text{O}_y$ . After the argon anneal, the phases identified were  $\text{Bi}_2\text{Sr}_{2-x}\text{Ca}_x\text{O}_y$  and  $\text{Cu}_2\text{O}/\text{CuO}$  plus a small amount of 2201. A complete decomposition of this sample in argon was not quite achieved as indicated by the small amount of 2201 still present.



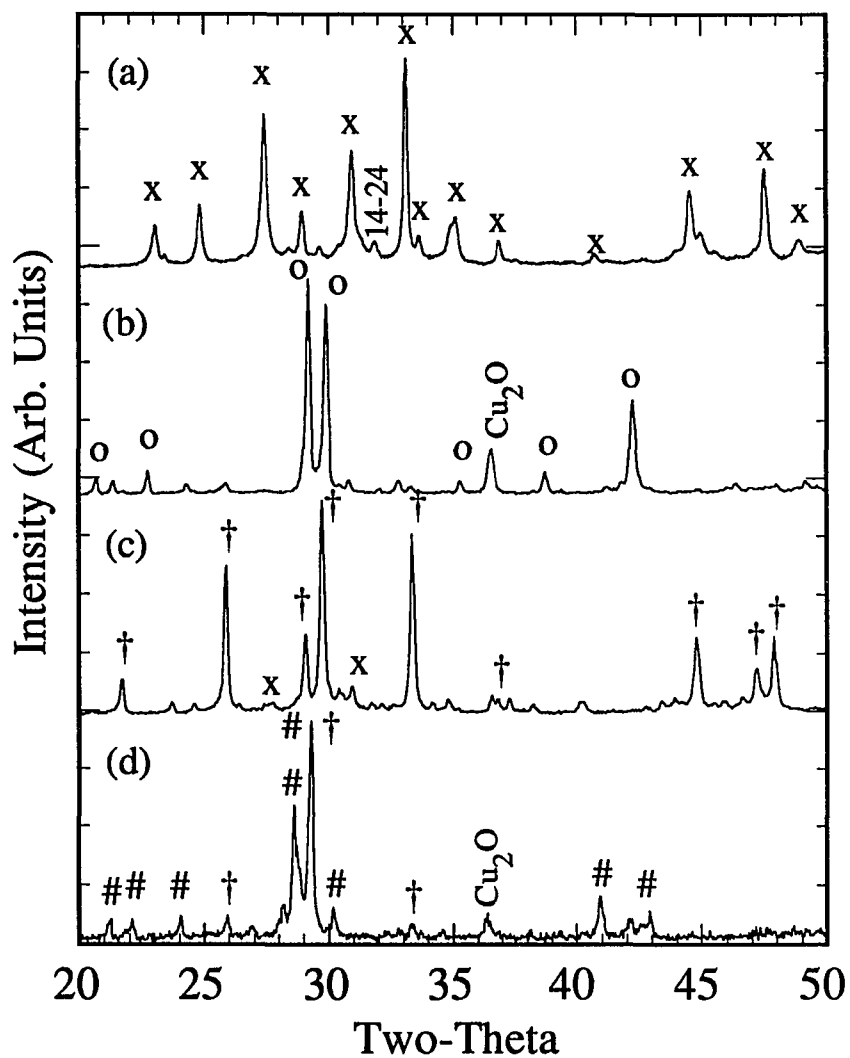


Figure 7.1 X-ray diffraction scans of the  $\text{Bi}_2\text{Sr}_2\text{CaCu}_2\text{O}_y$  sample annealed in a)  $\text{O}_2$  and b) Ar. Also shown are the x-ray scans of the  $\text{Bi}_2\text{Sr}_{1.75}\text{Ca}_{0.25}\text{CuO}_y$  sample annealed in c)  $\text{O}_2$  and d) Ar. The major phases are marked as: (x) - 2212, (o) -  $\text{Bi}_2\text{Sr}_{3-x}\text{Ca}_x\text{O}_y$ , (†) - 2201, and (#) -  $\text{Bi}_2\text{Sr}_{2-x}\text{Ca}_x\text{O}_y$ .

Table 7.1 Phases and compositions found during SEM compositional analysis of melt-processed and annealed samples for  $\text{Bi}_2\text{Sr}_{1.75}\text{Ca}_{0.25}\text{Cu}_1\text{O}_y$ . Compositions of the 2201 phase are listed in bold type.

Melt / Anneal	Phases
Anneal in $\text{O}_2$ at $865^\circ\text{C}$ for 100 hours	<b><math>\text{Bi}_{2.09}\text{Sr}_{1.60}\text{Ca}_{0.27}\text{Cu}_{1.04}\text{O}_y</math></b> $\text{Bi}_{0.56}\text{Sr}_{8.55}\text{Ca}_{5.65}\text{Cu}_{23.24}\text{O}_y$
Anneal in Ar $750^\circ\text{C}$ for 100 hours	$\text{Bi}_{2.09}\text{Sr}_{1.53}\text{Ca}_{0.29}\text{Cu}_{0.09}\text{O}_y$ $\text{Cu}_2\text{O} / \text{CuO}$ <b><math>\text{Bi}_{2.18}\text{Sr}_{1.84}\text{Ca}_{0.11}\text{Cu}_{0.87}\text{O}_y</math></b> <sup>c</sup>
Melt in $\text{O}_2$ at $1000^\circ\text{C}$ <sup>a</sup> heat / cool $\pm 10^\circ\text{C}/\text{min}$	<b><math>\text{Bi}_{2.20}\text{Sr}_{1.71}\text{Ca}_{0.12}\text{Cu}_{0.97}\text{O}_y</math></b> $\text{Bi}_{2.12}\text{Sr}_{1.22}\text{Ca}_{0.64}\text{Cu}_{0.04}\text{O}_y$ $\text{CuO} / \text{Cu}_2\text{O}$ $\text{Bi}_{2.00}\text{Sr}_{1.92}\text{Ca}_{1.09}\text{O}_y$ <sup>c</sup> $\text{CaO}^c$
Melt in Ar at $900^\circ\text{C}$ <sup>b</sup> heat / cool $\pm 10^\circ\text{C}/\text{min}$	$\text{Bi}_{2.14}\text{Sr}_{1.60}\text{Ca}_{0.24}\text{O}_y$ $\text{Cu}_2\text{O} / \text{Cu}_2\text{O}$ <b><math>\text{Bi}_{2.23}\text{Sr}_{1.63}\text{Ca}_{0.17}\text{Cu}_{0.97}\text{O}_y</math></b> <sup>c</sup>

<sup>a</sup>Material used was initially annealed in  $\text{O}_2$  at  $865^\circ\text{C}$  for 100 hours.

<sup>b</sup>Material used was initially annealed in Ar at  $750^\circ\text{C}$  for 100 hours

<sup>c</sup>Present in minor amounts

Table 7.2 Phases and compositions found during SEM compositional analysis of melt-processed and annealed samples for the nominal 2212 sample. Compositions of the 2212 phase are listed in bold print. During melting and solidification, all heating and cooling rates were maintained at 10°C/min

Melt / Anneal	Phases
Anneal in O <sub>2</sub> at 865°C for 100 hours	<b>Bi<sub>2.15</sub>Sr<sub>1.95</sub>Ca<sub>0.91</sub>Cu<sub>1.99</sub>O<sub>y</sub></b> Bi <sub>0.25</sub> Sr <sub>8.46</sub> Ca <sub>5.94</sub> Cu <sub>23.35</sub> O <sub>y</sub> <sup>a</sup>
Anneal in Ar 750°C for 100 hours	Bi <sub>1.98</sub> Sr <sub>1.82</sub> Ca <sub>0.66</sub> Cu <sub>0.15</sub> O <sub>y</sub> CuO/Cu <sub>2</sub> O Bi <sub>2.07</sub> Sr <sub>1.14</sub> Ca <sub>0.66</sub> Cu <sub>0.13</sub> O <sub>y</sub> <sup>a</sup>
Anneal in O <sub>2</sub> at 865°C for 100 hours Melt in O <sub>2</sub> at 1000°C	<b>Bi<sub>2.35</sub>Sr<sub>2.15</sub>Ca<sub>0.66</sub>Cu<sub>1.84</sub>O<sub>y</sub></b> Bi <sub>2.17</sub> Sr <sub>2.15</sub> Ca <sub>0.66</sub> Cu <sub>0.97</sub> O <sub>y</sub> Bi <sub>0.01</sub> Sr <sub>0.60</sub> Ca <sub>1.43</sub> Cu <sub>0.97</sub> O <sub>y</sub> Bi <sub>0.16</sub> Sr <sub>9.10</sub> Ca <sub>5.41</sub> Cu <sub>23.33</sub> O <sub>y</sub> Sr <sub>0.68</sub> Ca <sub>0.34</sub> Cu <sub>0.98</sub> O <sub>y</sub> Bi <sub>2.16</sub> Sr <sub>2.60</sub> Ca <sub>1.21</sub> Cu <sub>0.04</sub> O <sub>y</sub> CaO Bi <sub>2.08</sub> Sr <sub>0.79</sub> Ca <sub>1.00</sub> Cu <sub>0.12</sub> O <sub>y</sub> <sup>a</sup> + Cu <sub>2</sub> O
Anneal in O <sub>2</sub> at 865°C for 100 hours Melt in 20% O <sub>2</sub> at 1000°C	<b>Bi<sub>2.38</sub>Sr<sub>2.12</sub>Ca<sub>0.58</sub>Cu<sub>1.91</sub>O<sub>y</sub></b> Bi <sub>2.17</sub> Sr <sub>1.62</sub> Ca <sub>0.21</sub> Cu <sub>1.00</sub> O <sub>y</sub> Sr <sub>0.68</sub> Ca <sub>0.32</sub> Cu <sub>1.00</sub> O <sub>y</sub> CaO Bi <sub>1.99</sub> Sr <sub>2.04</sub> Ca <sub>0.94</sub> Cu <sub>0.03</sub> O <sub>y</sub> + Cu <sub>2</sub> O/CuO Bi <sub>2.10</sub> Sr <sub>1.06</sub> Ca <sub>0.69</sub> Cu <sub>0.15</sub> O <sub>y</sub> <sup>a</sup>
Anneal in O <sub>2</sub> at 865°C for 100 hours Melt in 1% O <sub>2</sub> at 1000°C	<b>Bi<sub>2.31</sub>Sr<sub>1.96</sub>Ca<sub>0.72</sub>Cu<sub>2.00</sub>O<sub>y</sub></b> Bi <sub>2.19</sub> Sr <sub>1.58</sub> Ca <sub>0.20</sub> Cu <sub>1.03</sub> O <sub>y</sub> Sr <sub>0.70</sub> Ca <sub>0.29</sub> Cu <sub>1.01</sub> O <sub>y</sub> CaO Bi <sub>2.07</sub> Sr <sub>2.03</sub> Ca <sub>0.87</sub> Cu <sub>0.03</sub> O <sub>y</sub> + Cu <sub>2</sub> O/CuO Bi <sub>2.10</sub> Sr <sub>0.87</sub> Ca <sub>0.93</sub> Cu <sub>0.11</sub> O <sub>y</sub> <sup>a</sup>
Anneal in Ar 750°C for 100 hours Melt in Ar at 900°C	Bi <sub>2.00</sub> Sr <sub>2.25</sub> Ca <sub>0.69</sub> Cu <sub>0.06</sub> O <sub>y</sub> + Cu <sub>2</sub> O/CuO CaO Bi <sub>2.20</sub> Sr <sub>1.46</sub> Ca <sub>0.34</sub> Cu <sub>1.01</sub> O <sub>y</sub> <sup>a</sup> Bi <sub>2.09</sub> Sr <sub>1.47</sub> Ca <sub>0.35</sub> Cu <sub>0.09</sub> O <sub>y</sub> <sup>a</sup>
Anneal in O <sub>2</sub> at 865°C for 100 hours Melt in O <sub>2</sub> at 1000°C Anneal O <sub>2</sub> at 850°C for 100 hours	<b>Bi<sub>2.22</sub>Sr<sub>1.88</sub>Ca<sub>0.89</sub>Cu<sub>2.01</sub>O<sub>y</sub></b> Bi <sub>2.17</sub> Sr <sub>1.62</sub> Ca <sub>0.21</sub> Cu <sub>1.00</sub> O <sub>y</sub> CaO Sr <sub>0.66</sub> Ca <sub>1.33</sub> Cu <sub>1.00</sub> O <sub>y</sub> Bi <sub>0.18</sub> Sr <sub>8.30</sub> Ca <sub>5.54</sub> Cu <sub>23.98</sub> O <sub>y</sub> Bi <sub>2.20</sub> Sr <sub>2.49</sub> Ca <sub>1.28</sub> Cu <sub>0.03</sub> O <sub>y</sub>
Anneal in Ar 750°C for 100 hours Melt in Ar at 900°C Anneal O <sub>2</sub> at 850°C for 100 hours	<b>Bi<sub>2.18</sub>Sr<sub>1.96</sub>Ca<sub>0.85</sub>Cu<sub>2.02</sub>O<sub>y</sub></b> Bi <sub>2.20</sub> Sr <sub>1.56</sub> Ca <sub>0.20</sub> Cu <sub>1.03</sub> O <sub>y</sub> CaO Bi <sub>0.25</sub> Sr <sub>7.79</sub> Ca <sub>6.24</sub> Cu <sub>23.73</sub> O <sub>y</sub> Bi <sub>2.17</sub> Sr <sub>2.41</sub> Ca <sub>1.34</sub> Cu <sub>0.08</sub> O <sub>y</sub> CuO

<sup>a</sup>Present in minor amounts

To avoid the Al contamination, the composition  $\text{Bi}_2\text{Sr}_2\text{Ca}_1\text{Cu}_2\text{O}_y$  was initially processed as a glass using a platinum crucible. The glass was then ground, pressed into pellets, and annealed at  $865^\circ\text{C}$  in oxygen for 100 hours with one intermediate grinding. This resulted in a sample comprised mainly of the 2212 phase with only a minor amount of  $\text{Sr}_{14-x}\text{Ca}_x\text{Cu}_{24}\text{O}_{41}$ . Annealing this sample in argon produced  $\text{Bi}_2\text{Sr}_{3-x}\text{Ca}_x\text{O}_y$  and  $\text{Cu}_2\text{O}/\text{CuO}$  as the major phases plus a small amount of  $\text{Bi}_2\text{Sr}_{2-x}\text{Ca}_x\text{O}_y$ . The phases that form in Ar for both of these compositions can be considered as the stable intermediate oxide phases since, in principle, these compositions should be reducible to the metallic state.

## 7.2. Melting and Solidification of 2201 and 2212

### 7.2.1 $\text{Bi}_2\text{Sr}_{1.75}\text{Ca}_{0.25}\text{CuO}_y$

DTA scans in  $\text{O}_2$  and Ar of annealed  $\text{Bi}_2\text{Sr}_{1.75}\text{Ca}_{0.25}\text{CuO}_y$  samples are shown in Figure 7.2. Onset and peak temperatures are listed in Table 7.3. In order to identify the thermal events, samples were melted and solidified in Ar or  $\text{O}_2$  on MgO single-crystal wafers using the same conditions as in DTA. Backscattered electron micrographs of these solidified samples are shown in Figure 7.3. A complete list of the phases present can be found in Table 7.1. Since this composition was processed using an alumina crucible, a small amount of aluminum contamination ( $< 2$  at.%) occurs resulting in the formation of an Al-Sr-Ca-O phase as discussed in Chapter 6. From the DTA scans, it is readily apparent that the solidus is substantially reduced from  $875^\circ\text{C}$  in  $\text{O}_2$  to  $745^\circ\text{C}$  in Ar. The small endotherm around  $800^\circ\text{C}$  in the DTA scan in Ar most likely results from some residual 2201 phase left in the Ar annealed sample. No corresponding event is seen on cooling. As shown in Figure 7.3a, the phases that formed during solidification in Ar were large grains of  $\text{Bi}_2\text{Sr}_{2-x}\text{Ca}_x\text{O}_y$  (22x) plus a divorced eutectic structure consisting of  $\text{Cu}_2\text{O}$  and  $\text{Bi}_2\text{Sr}_{2-x}\text{Ca}_x\text{O}_y$  with small amounts of 2201 and 23x. Based on the microstructure, the first exotherm seen on cooling in

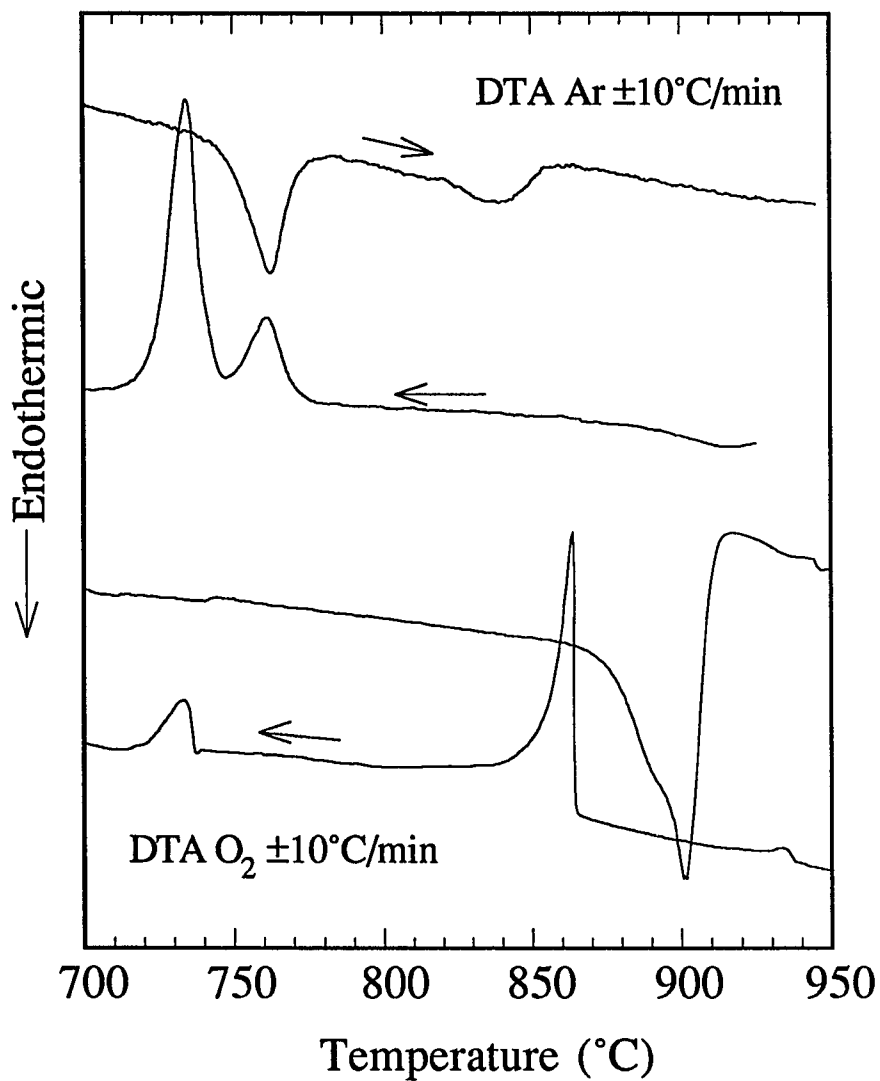


Figure 7.2 DTA heating and cooling scans in Ar and O<sub>2</sub> of Bi<sub>2</sub>Sr<sub>1.75</sub>Ca<sub>0.25</sub>CuO<sub>y</sub> samples annealed in Ar and O<sub>2</sub> respectively. Temperatures of the thermal events can be found in Table 7.3.

Table 7.3 Onset and peak temperatures of thermal events taken from DTA heating and cooling curves.

$\text{Bi}_2\text{Sr}_{1.75}\text{Ca}_{0.25}\text{CuO}_y$										
	Heating Endotherm		Heating Endotherm		Cooling Exotherm		Cooling Exotherm		Cooling Exotherm	
	Onset	Peak	Onset	Peak	Onset	Peak	Onset	Peak	Onset	Peak
Ar <sup>a</sup>	747°C	763°C	819°C	839°C	770°C	761°C	742°C	735°C		
O <sub>2</sub>	875°C	901°C	944°C	946°C	939°C	934°C	865°C	863°C	736°C	733°C

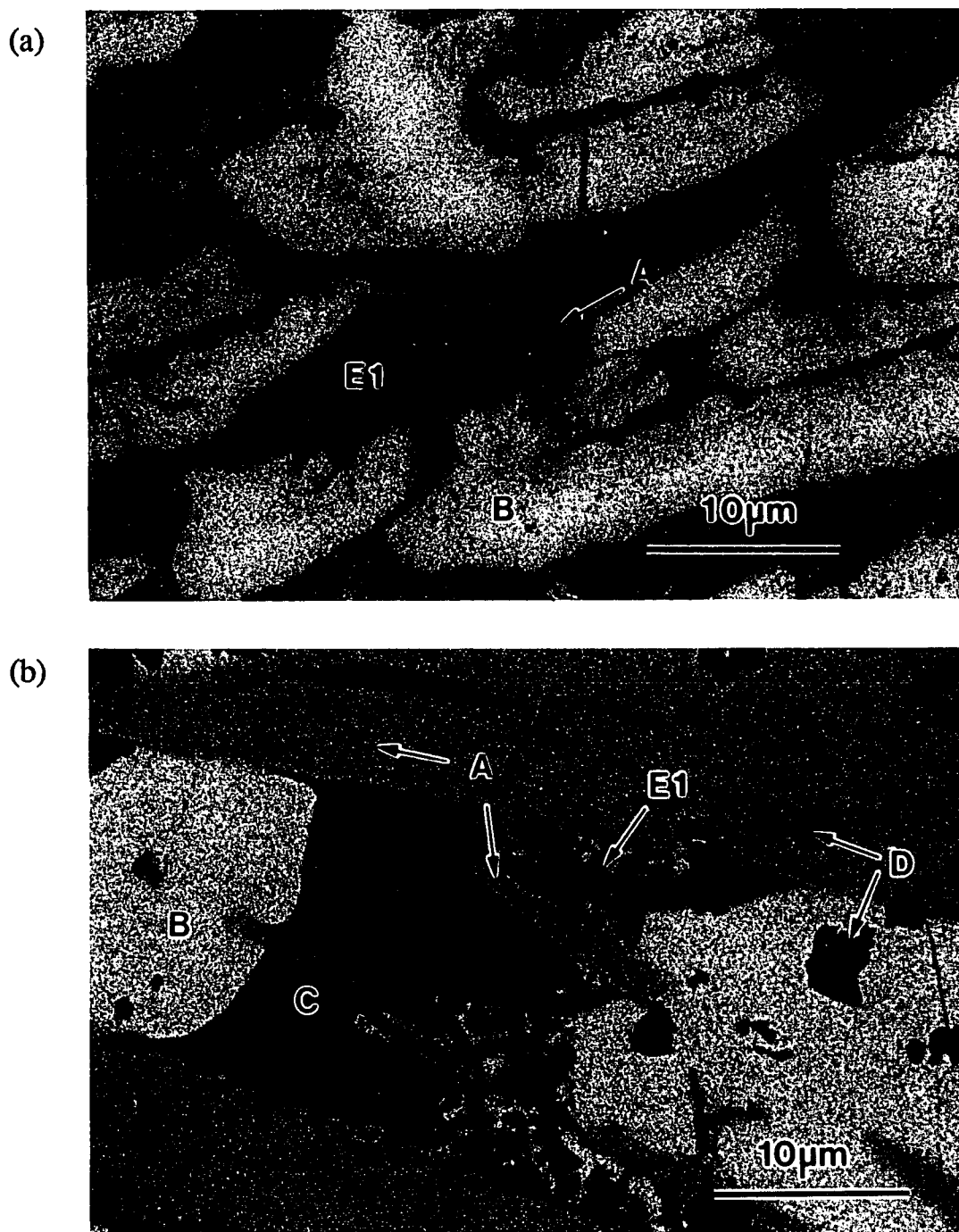
  

$\text{Bi}_2\text{Sr}_2\text{CaCu}_2\text{O}_y$										
	Heating Endotherm		Heating Endotherm		Cooling Exotherm		Cooling Exotherm		Cooling Exotherm	
	Onset	Peak	Onset	Peak	Onset	Peak	Onset	Peak	Onset	Peak
Ar <sup>a</sup>	777°C	795°C	820°C	833°C	815°C	802°C	757°C	749°C		
Ar	801°C	834°C			785°C	776°C	754°C	739°C		

	Heating Endotherm		Cooling Exotherm		Cooling Exotherm		Cooling Exotherm	
	Onset	Peak	Onset	Peak	Onset	Peak	Onset	Peak
1% O <sub>2</sub>	840°C	855°C	842°C	826°C	804°C	777°C	760°C	742°C
8% O <sub>2</sub>	869°C	878°C	881°C	872°C	839°C	823°C	750°C	732°C
20% O <sub>2</sub>	884°C	890°C	902°C	893°C	851°C	839°C	751°C	721°C
100% O <sub>2</sub>	895°C	903°C	921°C	902°C	866°C	833°C	743°C	738°C

<sup>a</sup>Samples were annealed in Ar at 750°C prior to use in the DTA. All other DTA experiments used material initially annealed in O<sub>2</sub> at 865°C.



**Figure 7.3** Backscattered electron micrographs of  $\text{Bi}_2\text{Sr}_{1.75}\text{Ca}_{0.25}\text{CuO}_y$  samples solidified in (a) Ar from 900°C at 10°C/min and (b) O<sub>2</sub> from 1000°C at 10°C/min. The phases and structures present are: A - 2201, B - 22x, C - 23x, D -  $\text{SrCaAlO}_y$ , and E1 - divorced eutectic structure of 22x and  $\text{Cu}_2\text{O}/\text{CuO}$ .

Ar can be assigned to the primary crystallization of 22x. The second exotherm represents the eutectic solidification of the remaining liquid resulting primarily as Cu<sub>2</sub>O and 22x. The small amount of 2201 also found in this eutectic structure probably results from the partition of remaining oxygen during solidification of the final phases. Any excess oxygen is available is used to form 2201 while the remainder of the liquid solidifies as Cu<sub>2</sub>O and 22x.

Solidification of Bi<sub>2</sub>Sr<sub>1.75</sub>Ca<sub>0.25</sub>Cu<sub>1</sub>O<sub>y</sub> in oxygen resulted in large, well formed grains of the 2201 phase with small regions of a divorced eutectic structure interspersed between them. This microstructure is shown in Figure 7.3b. The divorced eutectic structure consists of 22x and CuO/Cu<sub>2</sub>O with small amounts of 2201 and Bi<sub>2</sub>Sr<sub>3-x</sub>Ca<sub>x</sub>O<sub>y</sub> (23x) also present. Cooling at a rate of 10°C/min did not allow the sample to regain all the oxygen lost during melting resulting in the presence of the eutectic structure. This non-equilibrium process may result in the presence of both Cu<sub>2</sub>O and CuO as indicated above. The small amount of 23x found in the eutectic structure can be accounted for by small variations between the nominal stoichiometry of the sample and the actual compositions of the primary phases. Based on this microstructure, the two exotherms seen in DTA can be assigned to the solidification of 2201 around 865°C followed by eutectic solidification of the remaining liquid around 750°C as 22x, 23x, 2201, and CuO/Cu<sub>2</sub>O. The small exotherm found around 940°C is probably associated with the formation of the Al-Sr-Ca-O phase as this phase was found to be evenly distributed throughout the sample.

### 7.2.2 Bi<sub>2</sub>Sr<sub>2</sub>CaCu<sub>2</sub>O<sub>y</sub>

Considerably more effort was devoted to the 2212 composition due to the complexity of the melting and crystallization processes. Shown in Figures 7.4 and 7.5 are DTA scans run with several partial pressures of oxygen using heating and cooling rates of 2°C/min and 10°C/min respectively. Temperatures of thermal events can be found in Table 7.3. The starting material in all but one scan was initially annealed in oxygen. The melting point of



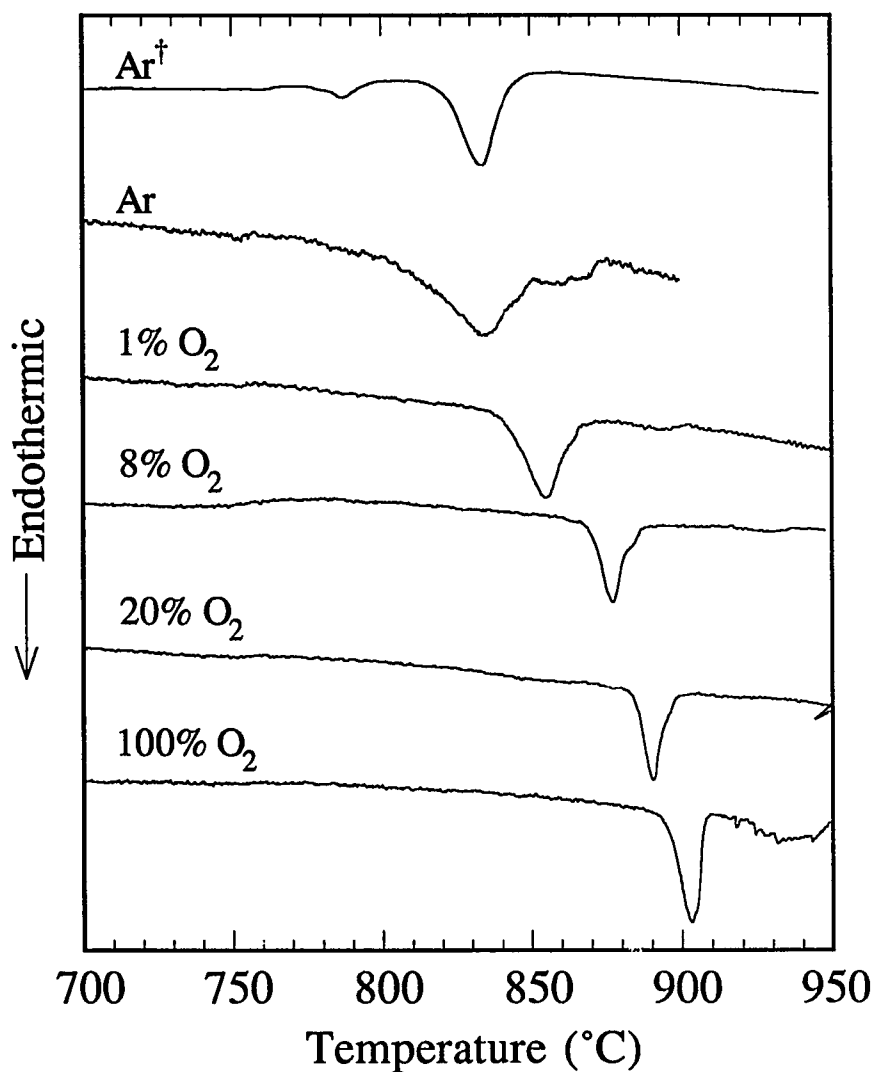


Figure 7.4 Melting events determined by DTA as a function of oxygen partial pressure for the 2212 composition that was initially annealed in  $\text{O}_2$ . In one case, ( $\dagger$ ), the initial material was annealed in Ar. Temperatures of thermal events can be found in Table 7.3.

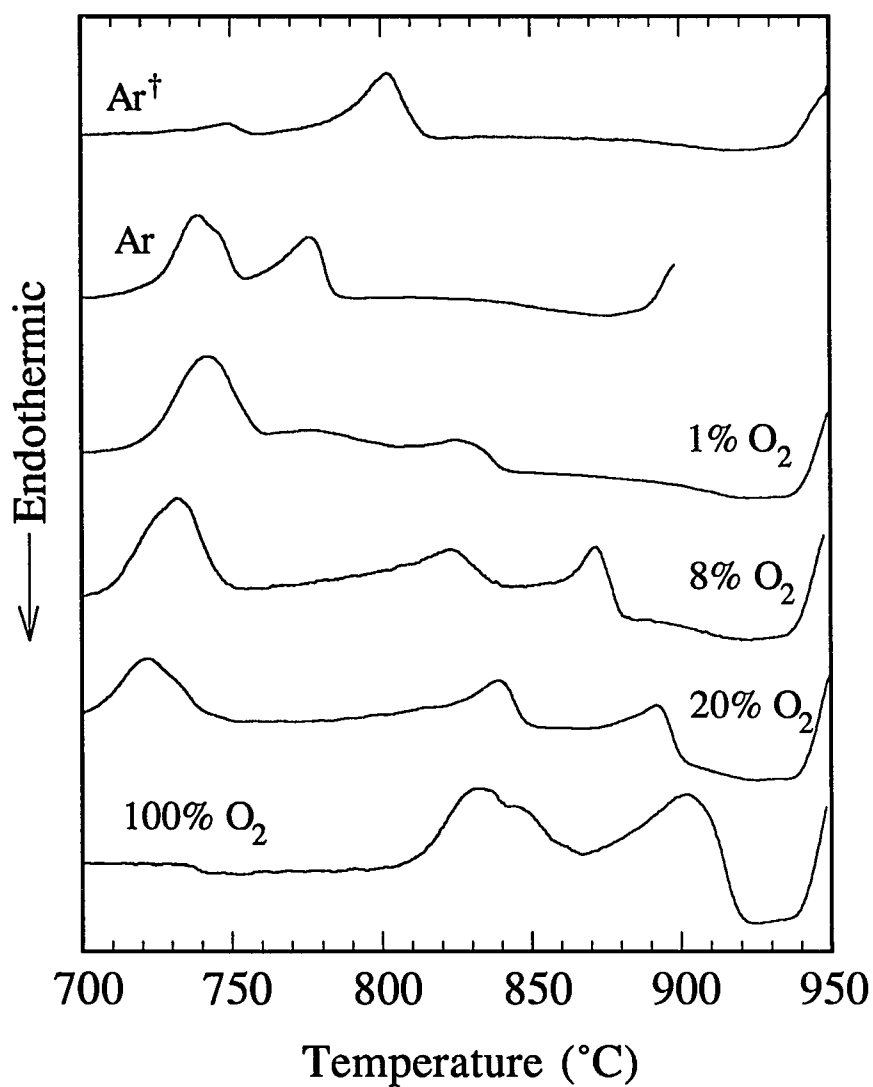


Figure 7.5 Cooling curves from DTA for 2212 samples initially annealed in  $O_2$ . In one case, ( $\dagger$ ), the starting material was initially annealed in Ar. Temperatures of thermal events can be found in Table 7.3.

2212 was found to be 895°C in 100% O<sub>2</sub>, 884°C in 20% O<sub>2</sub>, 869°C in 8% O<sub>2</sub>, and 840°C in 1% O<sub>2</sub>. All anneals were carried out at atmospheric conditions with Ar comprising the balance of the gas flow. An additional scan was performed in Ar on material initially annealed in Ar in order to resolve the melting events in Ar. In the latter case, the main melting event occurs around 800°C with only a small endotherm present at 750°C. The broad endotherm seen in the DTA scan in Ar of the O<sub>2</sub>-annealed sample is believed to result from an undetermined oxygen partial pressure due to the evolution of oxygen from the sample during heating.

In order to identify each event seen in the cooling curves of Figure 7.5, samples were melted and solidified on MgO wafers in Ar and 1%, 20%, and 100% O<sub>2</sub> using the same conditions as in the DTA experiments. The segregation of large CaO particles in the melt was common among all the samples melted on MgO. These particles were found to accumulate towards the top of the melts. As illustrated in Figure 7.6, many of the alkaline-earth cuprate needles found in samples solidified in an oxygen partial pressure contained embedded CaO particles suggesting that CaO acts as a nucleation site for the formation of these phases during both solidification and subsequent anneals.

Figures 7.7a and b show the resulting microstructure of the Ar-annealed sample after melting on MgO at 900°C and cooling at 10°C/min. This sample consisted of large grains of Bi<sub>2</sub>Sr<sub>3-x</sub>Ca<sub>x</sub>O<sub>y</sub> (23x) surrounded by a divorced eutectic structure of 23x and Cu<sub>2</sub>O. Small amounts of 2201 and Bi<sub>2</sub>Sr<sub>2-x</sub>Ca<sub>x</sub>O<sub>y</sub> (22x) were also found in this latter structure and are present to account for compositional variations. In addition, CaO particles could be found throughout the sample and a few longer needles of the 2201 phase could be found near the bottom as shown in Figure 7.7a. The small amount of 2201 that forms instead of 22x and Cu<sub>2</sub>O is probably due to some residual oxygen present in the sample as discussed previously. Based on this microstructure, the solidification events seen in the DTA cooling scan in Ar of the Ar-annealed sample can be identified as the crystallization of 23x around 800°C followed

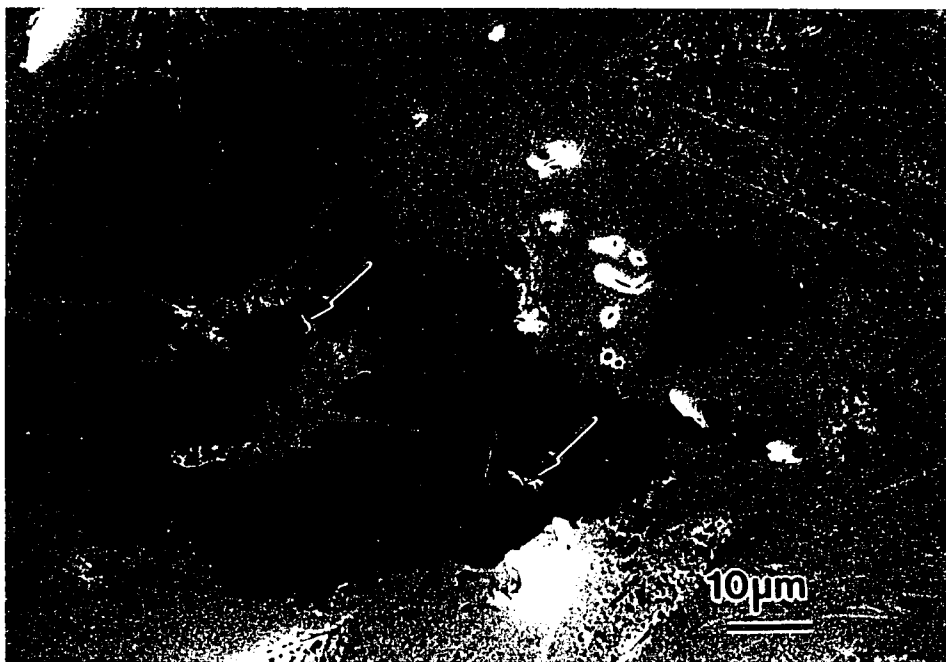


Figure 7.6 Secondary electron micrograph of an alkaline-earth cuprate phase containing embedded CaO particles.

by the divorced eutectic solidification around 750°C of primarily 23x and Cu<sub>2</sub>O with small amounts of 22x and 2201. The tail seen on the first exotherm is consistent with a simple eutectic-type solidification process[78].

The solidification processes become more complex with the addition of oxygen as evidenced by Figures 7.5 and 7.8-7.10. Backscattered electron micrographs of samples cooled from 1000°C at 10°C/min in 1% and 20% O<sub>2</sub> can be found in Figures 7.8 and 7.9. The major phases were identified by EDS analysis in the SEM as 23x, 22x, Cu<sub>2</sub>O/CuO, 2212, 2201, and Sr<sub>1-x</sub>Ca<sub>x</sub>CuO<sub>y</sub> (1:1). CaO is clearly visible in the figures as the large, round, dark particles in the top portions of the samples. The overall microstructure of these samples shows that solidification proceeded from the top surface of the sample down towards

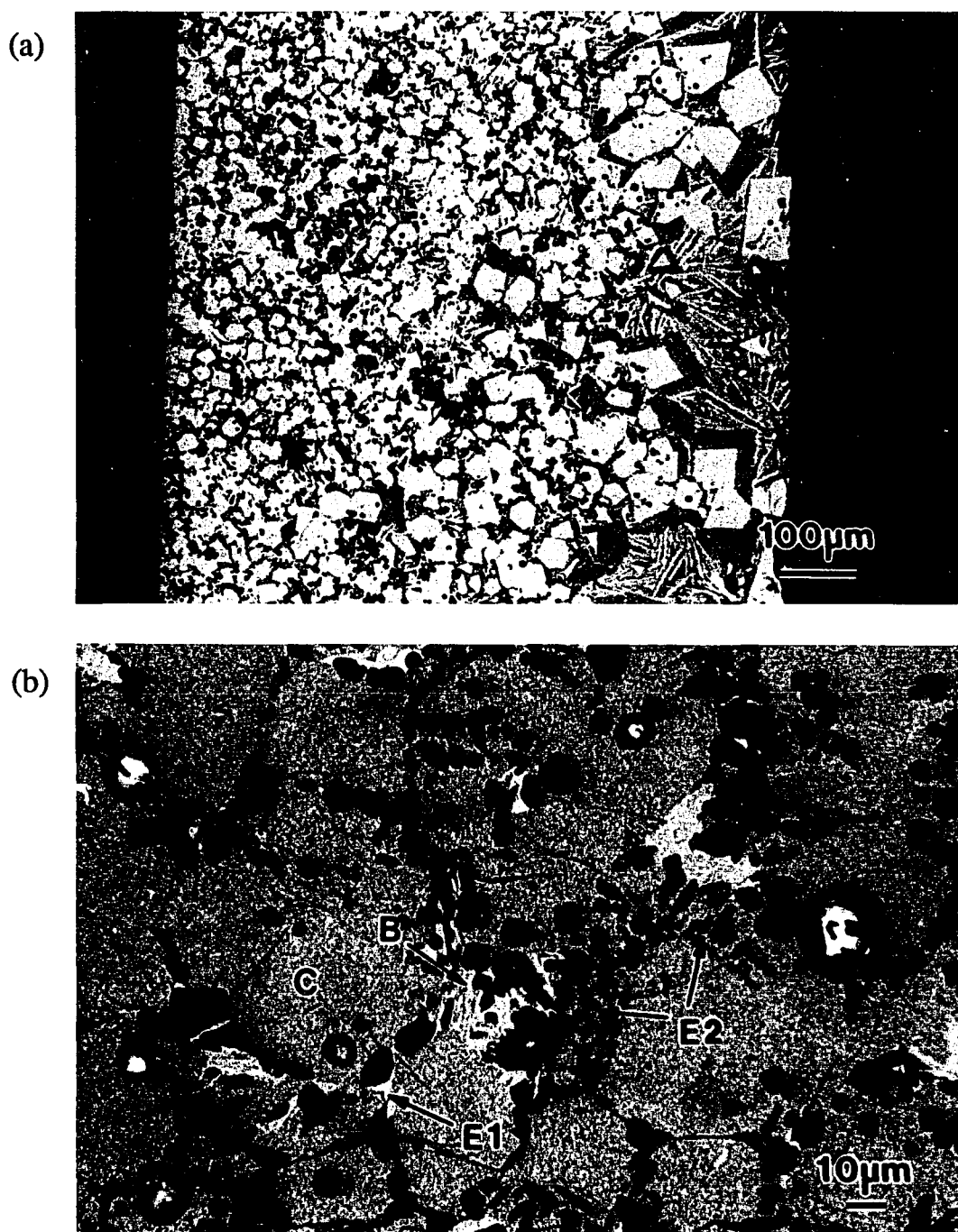


Figure 7.7 Backscattered electron micrographs of a  $\text{Bi}_2\text{Sr}_2\text{CaCu}_2\text{O}_y$  sample solidified in Ar from  $900^\circ\text{C}$  at  $10^\circ\text{C}/\text{min}$ . The phases and structures present were identified as: A - 2212, B - 2201, C - 23x, E1 - divorced eutectic structure of 22x and  $\text{Cu}_2\text{O}/\text{CuO}$ , and E2 - divorced eutectic structure of 23x and  $\text{Cu}_2\text{O}/\text{CuO}$ .

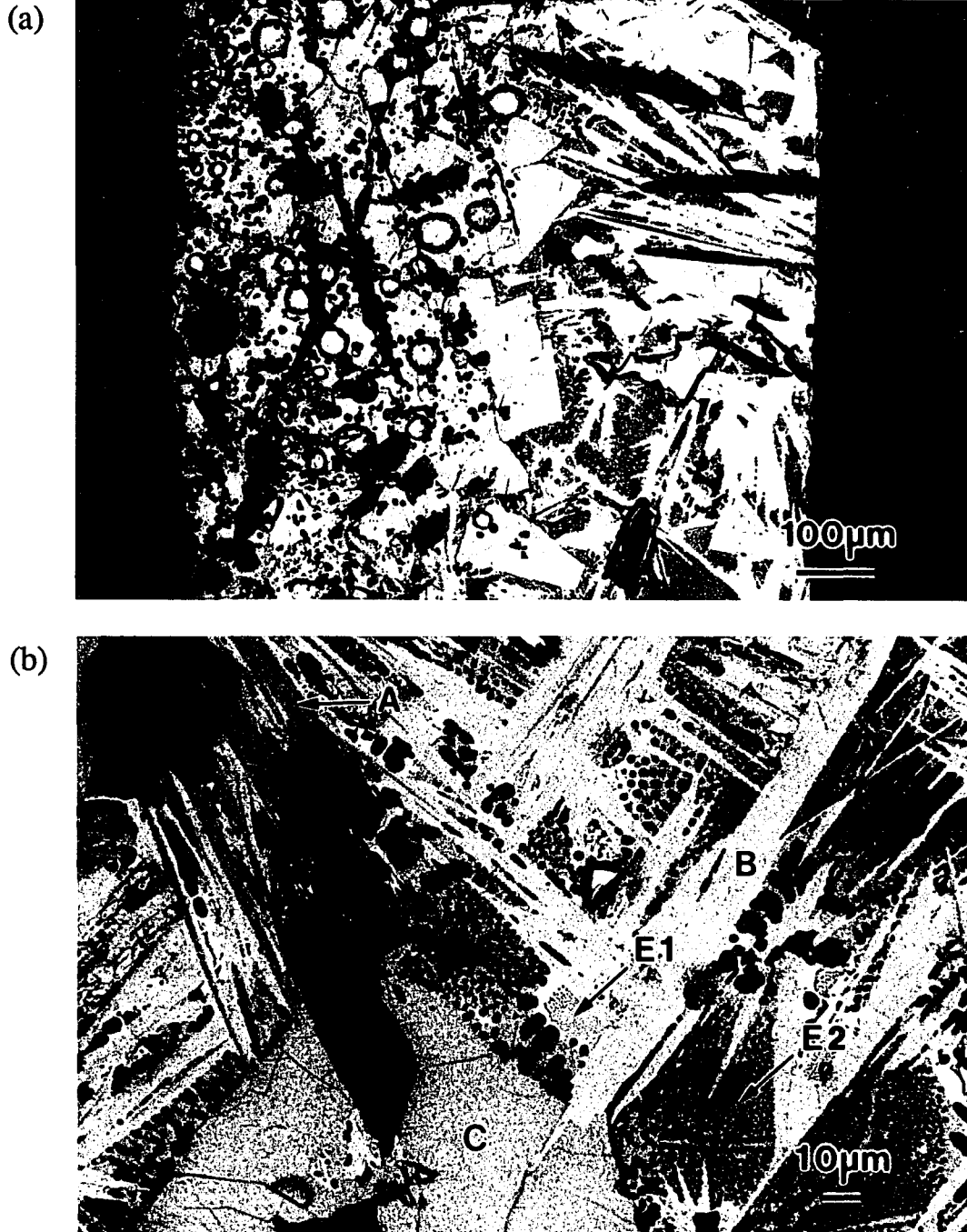


Figure 7.8 Backscattered electron micrographs of a  $\text{Bi}_2\text{Sr}_2\text{CaCu}_2\text{O}_y$  sample solidified in 1%  $\text{O}_2$  (balance Ar) from  $1000^\circ\text{C}$  at  $10^\circ\text{C}/\text{min}$ . The phases and structures present were identified as: A - 2212, B - 2201, C - 23x, E1 - divorced eutectic structure of 22x and  $\text{Cu}_2\text{O}/\text{CuO}$ , and E2 - divorced eutectic structure of 23x and  $\text{Cu}_2\text{O}/\text{CuO}$ .

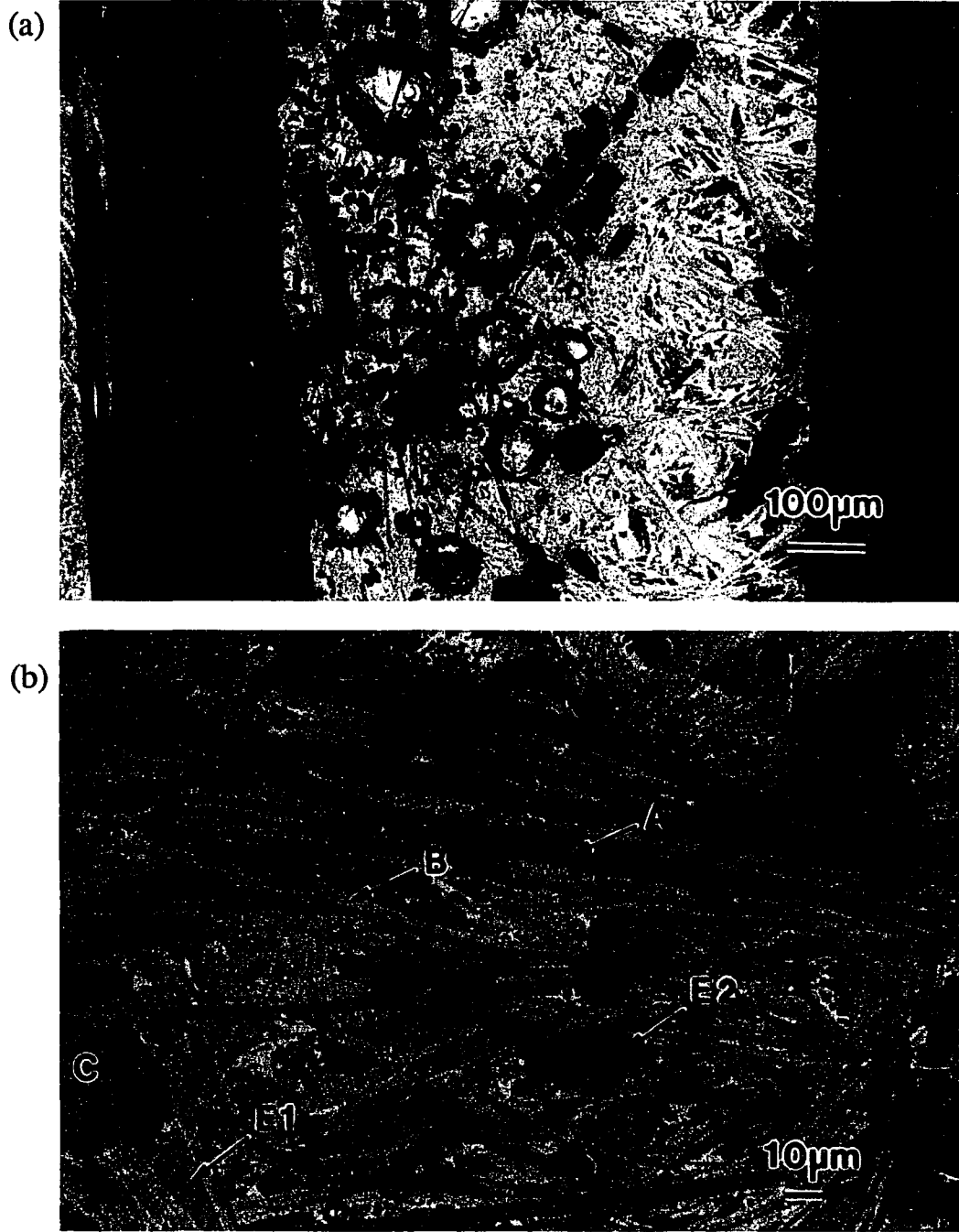


Figure 7.9 Backscattered electron micrographs of a  $\text{Bi}_2\text{Sr}_2\text{CaCu}_2\text{O}_y$  sample solidified in 20%  $\text{O}_2$  (balance Ar) from  $1000^\circ\text{C}$  at  $10^\circ\text{C}/\text{min}$ . The phases and structures present were identified as: A - 2212, B - 2201, C - 23x, E1 - divorced eutectic structure of 22x and  $\text{Cu}_2\text{O}/\text{CuO}$ , and E2 - divorced eutectic structure of 23x and  $\text{Cu}_2\text{O}/\text{CuO}$ .

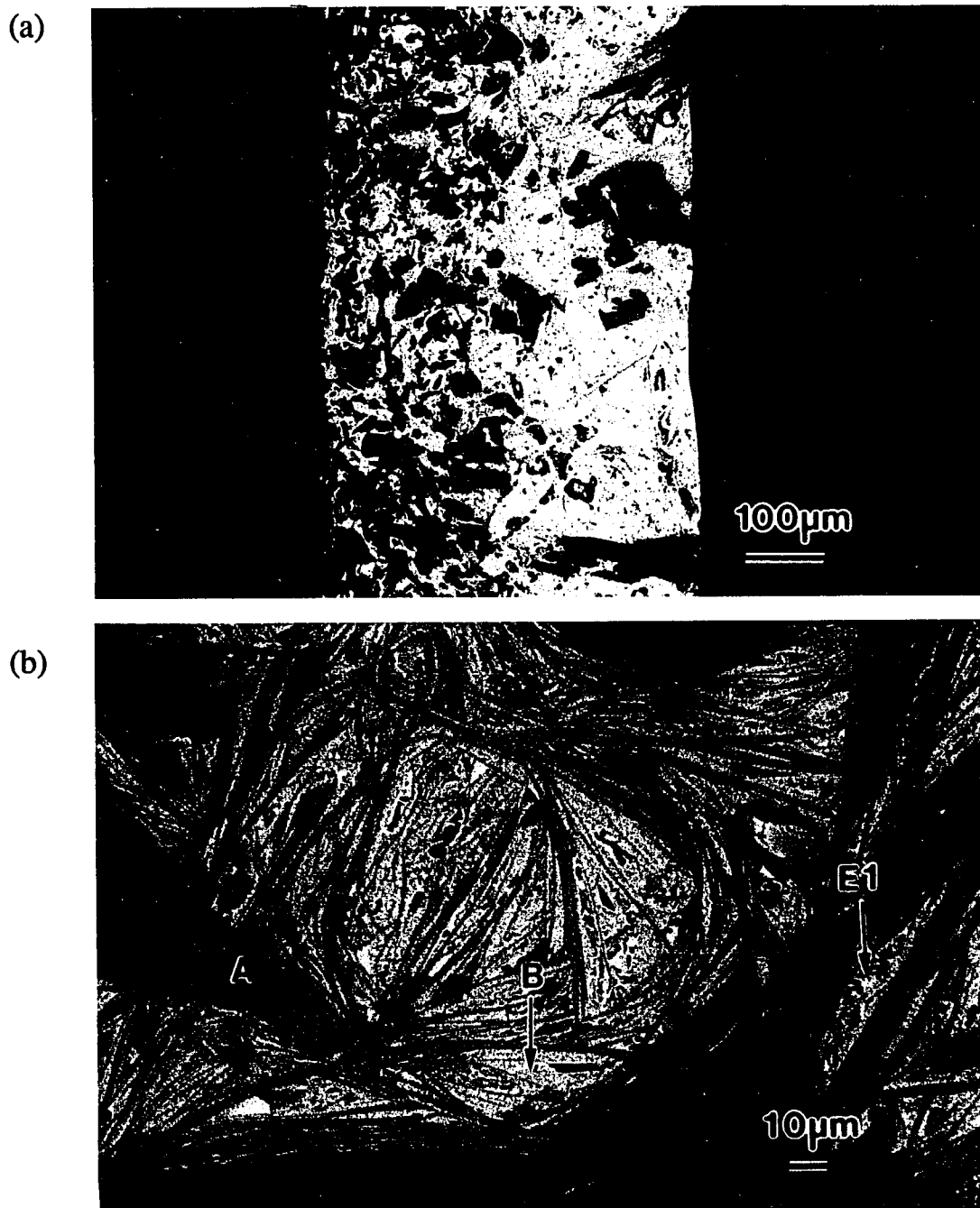


Figure 7.10 Backscattered electron micrographs of a  $\text{Bi}_2\text{Sr}_2\text{CaCu}_2\text{O}_y$  sample solidified in 100%  $\text{O}_2$  from 1000°C at 10°C/min. The phases and structures present were identified as: A - 2212, B - 2201, C - 23x, E1 - divorced eutectic structure of 22x and  $\text{Cu}_2\text{O}/\text{CuO}$ , and E2 - divorced eutectic structure of 23x and  $\text{Cu}_2\text{O}/\text{CuO}$ .



the substrate. Hence, there is very little texturing of the 2212 or 2201 phases parallel to the substrate.

In the samples solidified in 1% and 20% O<sub>2</sub>, the 1:1 phase was found primarily near the surface of the sample indicating that it was one of the first phases to crystallize on cooling. Needles of this phase were found to be rather large and often contained embedded particles of CaO. The separation of CaO in the melt and the crystallization of the 1:1 phase results in a comparatively Bi-rich liquid in the molten state. Hence, several Bi-rich phases can be expected to form during further solidification in addition to 2212 even though the equilibrium phases for this particular composition are 2212 and small amounts of Sr<sub>14-x</sub>Ca<sub>x</sub>Cu<sub>24</sub>O<sub>41</sub>. This indeed seems to be the case as both the 22x and 2201 phases are found in these samples. The 2212 and 2201 phases were generally found together in a layered microstructure. The bottom half of the solidified samples were found to contain, in addition to 2201 and 2212, both primary grains of 23x along with the divorced eutectic microstructure containing 23x, 22x, 2201, and Cu<sub>2</sub>O/CuO. The dark rods of the eutectic structure are Cu<sub>2</sub>O/CuO. At the lower oxygen partial pressures, the solidification rate of 10°C/min did not allow for a complete oxidation of the samples. Hence, oxygen-deficient phases could be found in the interior of the samples near the substrate. As the oxygen partial pressures used during solidification were increased, the amounts of 2201, 2212, and the alkaline-earth cuprates increased at the expense of 23x, 22x, and Cu<sub>2</sub>O/CuO. In addition, proportionately more of the 2212 phase was found compared to the 2201 phase with increased partial pressures of oxygen.

The observed onset temperatures for the first DTA exotherm on cooling were always higher than the melting temperature of the 2212 phase in each of the corresponding heating curves shown Figures 7.4 and 7.5. Since the melting point of 2212 decreases with oxygen partial pressure and the melt is known to be oxygen deficient from the results of Chapter 6, the first exotherm encountered on cooling cannot be associated with the formation of

2201/2212 and is assigned to the crystallization of the 1:1 phase. This is consistent with the observed microstructure showing the 1:1 phase to be primarily near the surface of the sample. This event does not define the liquidus temperature. Well formed particles of CaO can be found in glasses processed in Pt crucibles and quenched from 1075°C suggesting that the primary phase field is CaO plus a liquid. This is consistent with the CaO separation found to occur during melting and solidification in this study. The middle exotherm is assigned to the crystallization of 2201 and/or 2212. Onset temperatures for this exotherm were in all cases lower than the corresponding onsets for the melting events observed during heating. In addition, the tails associated with this latter exotherm suggest that the 2212/2201 phases continue to solidify as the eutectic temperature is approached. The third exotherm corresponds to the eutectic crystallization of 23x, 22x, 2201, and Cu<sub>2</sub>O/CuO. These phases are found primarily in the bottom of the sample and result from an incomplete oxidation of the sample. The onset temperature matches well with the same events seen on cooling in Ar. With decreasing oxygen partial pressures, this peak grows, broadens and finally splits into two exotherms for the samples solidified in Ar.

In 100% oxygen, the first and second exotherms that occur on cooling are much more intense while the third exotherm is, in this case, only a small shift in the baseline. The phases identified by EDS analysis in this sample are 2212, 2201, Sr<sub>1-x</sub>Ca<sub>x</sub>CuO<sub>y</sub> (1:1), Sr<sub>2-x</sub>Ca<sub>x</sub>CuO<sub>y</sub> (2:1), Sr<sub>14-x</sub>Ca<sub>x</sub>Cu<sub>24</sub>O<sub>y</sub> (14:24), Bi<sub>2</sub>Sr<sub>4-x</sub>Ca<sub>x</sub>O<sub>y</sub> (24x), CaO, CuO/Cu<sub>2</sub>O, and 22x. Specific compositions are listed in Table 7.2. Figure 7.10 shows a split microstructure in which 24x and the alkaline-earth cuprates are confined primarily in the top layer of the sample. The 24x phase can be identified in these micrographs by its rather blocky appearance compared with the plate-like morphology of the superconducting phases. The alkaline-earth cuprates and CaO appear as the large dark needles and particles in the backscattered SEM micrographs. The phases present in the bottom half of the sample were primarily 2212 and 2201 with small amounts of a divorced eutectic structure between grains

as shown in Figure 7.10b. This eutectic structure consisted of CuO/Cu<sub>2</sub>O, 2201, and 22x. The presence of this latter structure can be attributed to an incomplete uptake of oxygen during cooling. The amounts of these "oxygen-deficient" phases decreased in all samples as the oxygen partial pressure used during solidification was increased. The solidification of this divorced eutectic structure occurs last and is responsible for the small change in baseline around 750°C in the DTA cooling curve. This assignment is consistent with the previous experiments discussed above. The crystallization of the 1:1 phase and 2212/2201 are again assigned to the first and second exotherms respectively based on both the observed microstructure and the results from previous experiments in 1% and 20% O<sub>2</sub>. The presence of the 24x, 2:1 and 14:24 phases primarily near the top surface of the samples suggests that the crystallization of these phases also occurs with the first exotherm. However, this cannot be completely verified as the second exotherm also contains some structure suggesting an additional crystallization event besides that of the 2212/2201 phases.

### 7.3. Formation Process of 2212

It is difficult to determine whether the 2212 phase solidifies directly from the melt or forms via an intermediate phase. While the techniques used in the study do not allow for a direct observation of its formation, it is believed that the 2212 phase forms via an intermediate 2201 phase based on DTA, microstructural analysis, and the crystallization results of Chapter 6. As shown in Table 7.3, onset temperatures observed during cooling in 100% O<sub>2</sub> for the exotherms associated with the formation of 2201 and/or 2212 were approximately the same in both compositions used in this study. Shown in Figure 7.11 are SEM and TEM micrographs taken from the 2212 sample solidified at 10°C/min in O<sub>2</sub> from 1000°C. The SEM micrograph, Figure 7.11a, shows a layered microstructure of the 2201 and 2212 phases which is typical of nominal 2212 samples solidified under partial pressures of

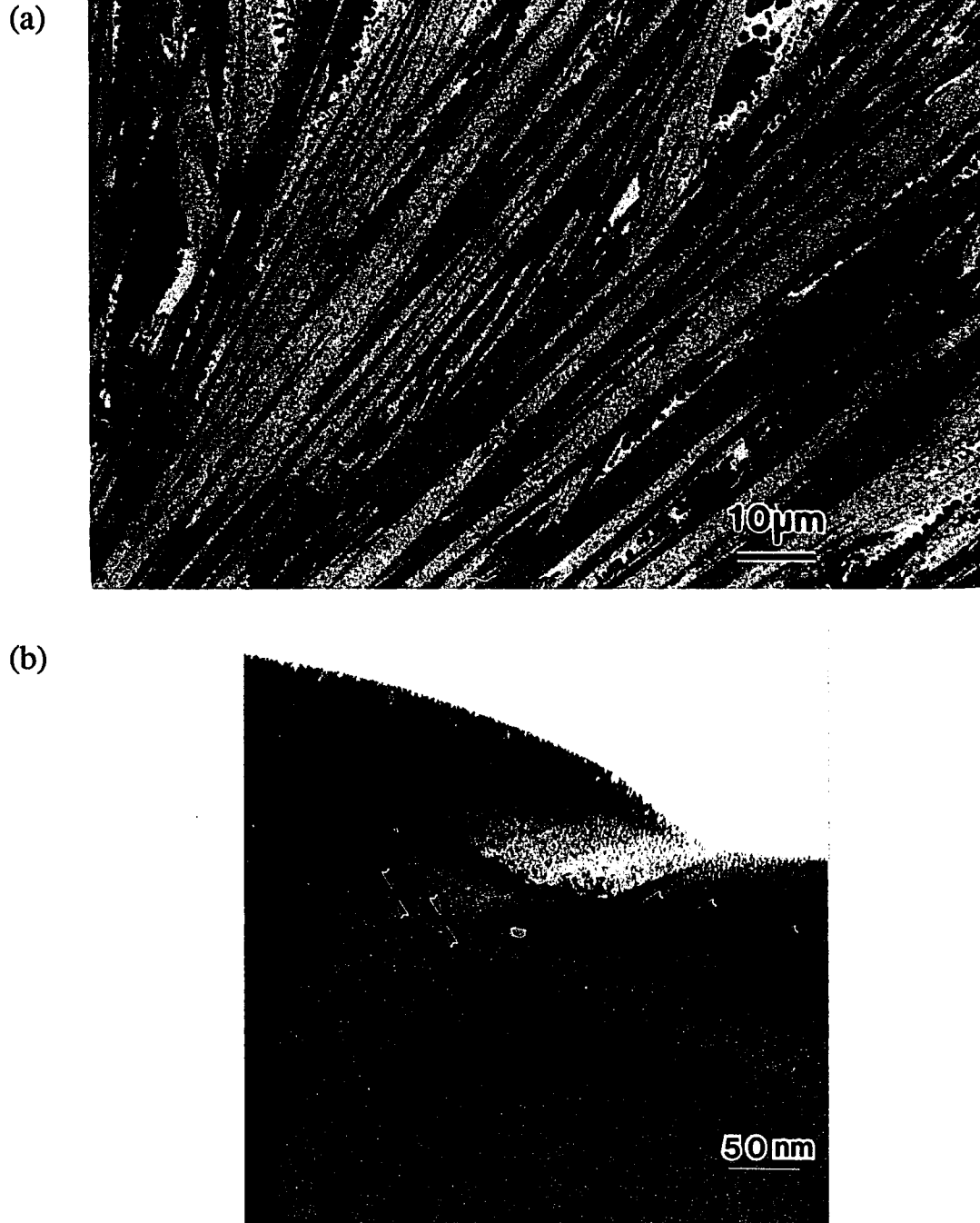


Figure 7.11 Micrographs showing (a) the layered microstructure of 2212 and 2201 in these solidified samples as seen by backscattered electron imaging in the SEM and (b) the individual and multiple intergrowths of the 2201 phase within 2212 grains as observed in the TEM.

oxygen. Furthermore, EDS analysis revealed the 2212 phase to be Bi-rich and Cu-deficient which is an indication of a large number of 2201 intergrowths within the 2212 grains based on the results of Chapter 5. TEM confirmed that the 2212 grains contained single and multiple intergrowths of the 2201 phase as shown in Figure 7.11b. On the other hand, no intergrowths of the 2212 phase were found in grains of 2201. This microstructure suggests that the 2201 phase nucleates first and serves as a template for the growth of the 2212 phase. However, not all of the 2201 can convert into the 2212 phase due to the separation of CaO in the melt and the initial crystallization of the alkaline-earth cuprates. The remaining liquid is Bi-rich from which it is impossible to form only the 2212 phase.

The formation process of the 2212 phase during solidification is in agreement with the results of the crystallization study of Chapter 6. The initial crystallization process was found to be 2201 and  $\text{Cu}_2\text{O}/\text{CuO}$ . The 2201 phase was found to convert into 2212 upon heating above approximately  $600^\circ\text{C}$ . The microstructure of the 2212 phase at this point in the crystallization process, Figure 6.17, is very similar to that shown in Figure 7.11b. Above  $700^\circ\text{C}$ , the rate of conversion of 2212 from 2201 increased significantly due to the presence of a liquid phase resulting from the melting of 23x around  $700^\circ\text{C}$ . During solidification from the molten state, the liquid phase allows for enhanced diffusion of material needed for conversion of 2201 into 2212.

#### 7.4. Reversibility of Phase Formation in Ar and $\text{O}_2$

Since the phases that form during solidification in Ar were also present in samples solidified in 1% and 20%  $\text{O}_2$ , phase formation in  $\text{O}_2$  or Ar should be reversible and the amount and types of each phase that forms should be controllable with a suitable choice of oxygen partial pressure provided elemental losses are minimal. Shown in Figure 7.12 is a set of five sequential DTA scans on an  $\text{O}_2$ -annealed 2212 sample starting in  $\text{O}_2$ , then Ar, and

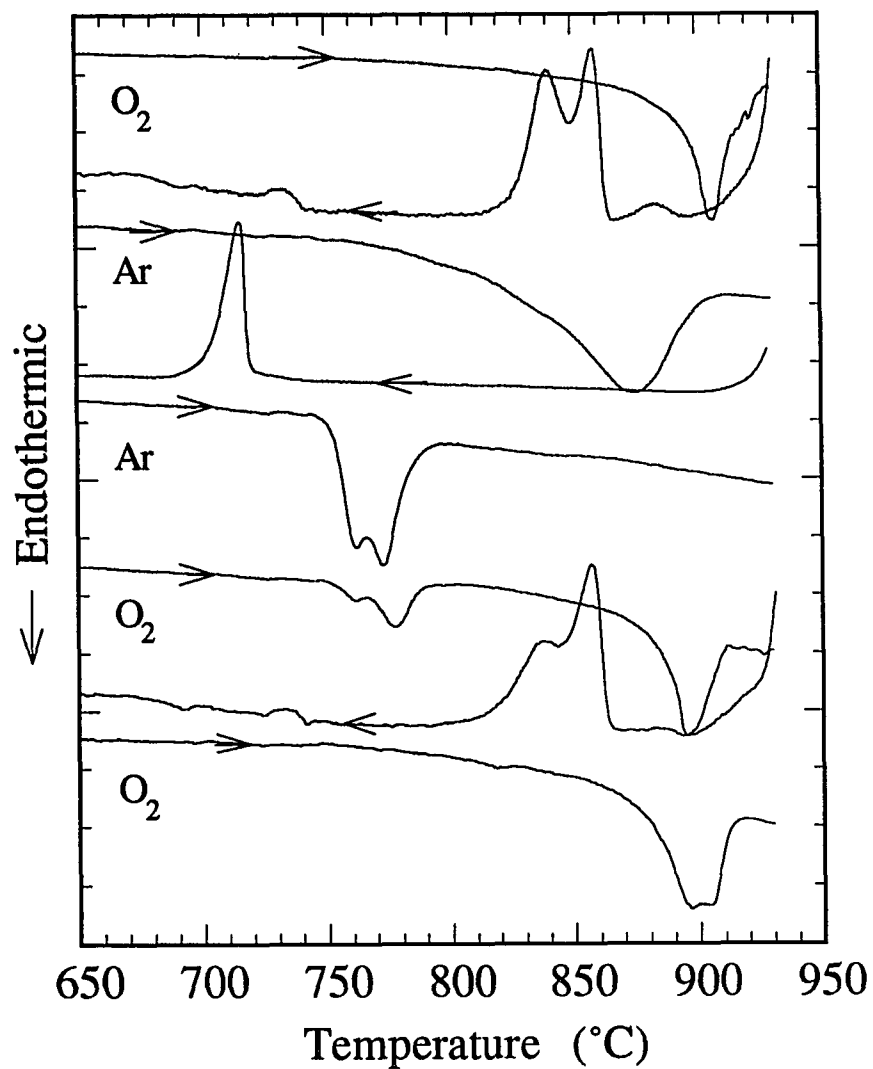


Figure 7.12 Sequential DTA scans of a nominal 2212 sample in oxygen, argon, and finally oxygen showing the reversibility of phase formation in O<sub>2</sub> and Ar. Heating and cooling rates were maintained at 10°C/min.

finally back to O<sub>2</sub>. Heating and cooling rates were held at 10°C/min. The maximum temperature used in this series of scans was 925°C in order to minimize any reactions with the DTA crucible. Some changes are apparent in the shape of the DTA curves compared to Figure 5; however, the same qualitative features are still present. It is clearly seen that the melting point falls from approximately 880°C in O<sub>2</sub> to 750°C in Ar and then rises back to 875°C in O<sub>2</sub>. The final scan in O<sub>2</sub> shows no sign of the phases that melt around 750°C in Ar indicating that the initial phases have been recovered.

### 7.5. Recovery of the Superconducting Properties

All of the samples examined above needed to be annealed after solidification in order to improve the superconducting properties. For example, Figure 7.13 shows magnetization curves for a sample solidified in O<sub>2</sub> and O<sub>2</sub>-annealed samples that were initially solidified in Ar and O<sub>2</sub> respectively. Samples solidified in Ar were not superconducting and were shown by resistivity measurements to be semiconducting. The sample solidified in O<sub>2</sub> had a very broad transition starting at 85K. Both of these solidified samples were then annealed at 850°C in 100% O<sub>2</sub> for 50 hours. After this anneal, the superconducting transitions were found to sharpen considerably. The onset of the diamagnetic signal was 90K in both cases. The difference in signals was due to the amount of material used in the measurements. The phases identified by EDS analysis in the annealed samples are listed in Table 7.2. Fewer phases were found in the samples solidified in Ar and annealed in O<sub>2</sub> although not all of these phases are part of the equilibrium phase assemblage as is clearly seen by comparing with the phases present in the starting material. For the samples solidified in partial pressures of oxygen, the relative size and morphology of Bi<sub>2</sub>Sr<sub>4-x</sub>Ca<sub>x</sub>O<sub>y</sub> and/or the alkaline-earth cuprates were unchanged after the anneal in oxygen indicating that they are relatively stable. On the other hand, none of the phases associated with the divorced eutectic structures were

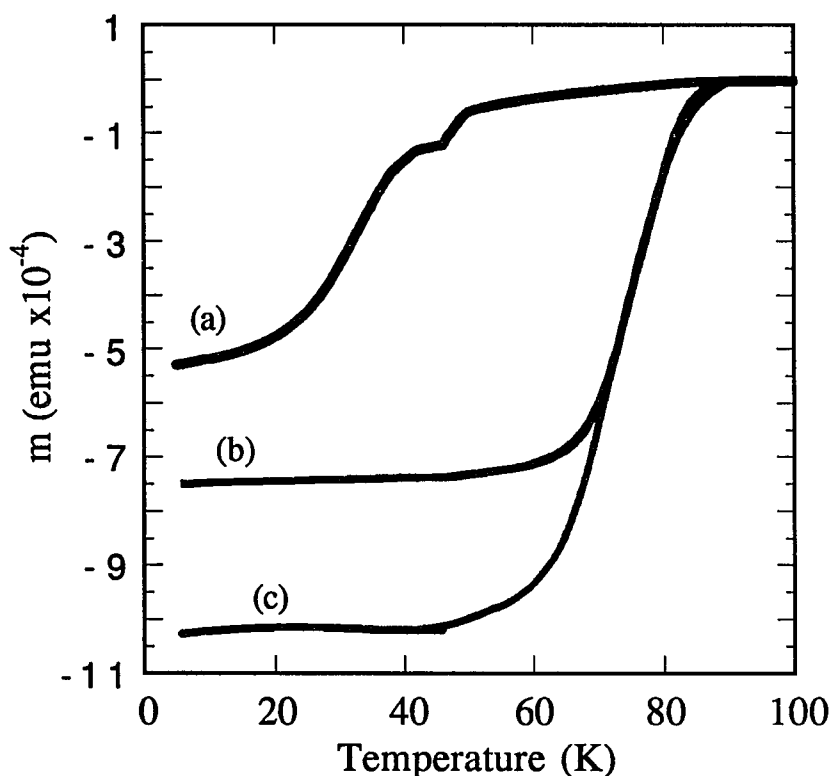


Figure 7.13 Magnetization curves from samples (a) solidified from 1000°C at 10°C/min in O<sub>2</sub> only and samples solidified in (b) Ar from 900°C and (c) O<sub>2</sub> from 1000°C and annealed at 850°C for 50 hours and quenched in air. The sample solidified in Ar from 900°C at 10°C/min only was found to be semiconducting.

present after the anneal in oxygen. The presence of the alkaline-earth cuprates in the sample cooled in Ar could be attributed to the partial melting of the "oxygen-deficient" phases around 750°C on heating in oxygen and the presence of CaO particles which act as nucleation sites for the alkaline-earth cuprates.

## 7.6. Discussion

Understanding the sequence of events and the kinetics of phase formation during solidification from the melt is necessary in order to develop reliable melt-processing techniques for fabrication of these superconductors into practical conductors. The melt-



processing steps used in this study have not been optimized as evidenced by all the secondary phases found in annealed samples that were initially solidified in Ar or O<sub>2</sub>. However, the high melting temperatures used in this study help to exaggerate certain aspects of the solidification process that allow for an easier identification of the crystallization events and examination of problems, such as CaO separation, associated with melt-processing.

In the absence of oxygen, solidification resulted in nearly the same phases as obtained by solid-state annealing of the precursor. The small differences are due to CaO separation in melt. The fact that the phases that solidify in Ar were also found in the samples solidified in various partial pressures of oxygen can be attributed to the oxygen deficiencies that exist in the molten state. This oxygen deficiency lowers the solidus to approximately 750°C. Rapid cooling below this temperature results in the formation of 23x and CuO/Cu<sub>2</sub>O or 2201, depending on the amount of oxygen absorbed during solidification. Since solidification, in general, is a non-equilibrium process, the presence of both CuO and Cu<sub>2</sub>O is possible in these samples. The 23x and 22x phases found in the divorced eutectic structures are not stable when annealed below the melting point of 2212 in a given partial pressure of oxygen, and they subsequently combine with Cu<sub>2</sub>O/CuO to form 2212 and 2201 respectively.

Several interesting aspects of the effects of oxygen on the phase diagram can be found in the DTA results and microstructures of the solidified samples. The presence of only 2201 in the divorced eutectic structures suggests that it is stable to lower oxygen partial pressures than is 2212. Secondly, the presence of 2201 with 22x and 23x in the eutectic structures suggests that at low oxygen partial pressures, eutectic valleys separate the congruently melting 23x and 22x phases from the incongruently melting 2201 and 2212 phases resulting in a depression of the solidus to approximately 750°C. This eutectic reaction is illustrated in Figure 7.14 with a model metal-oxygen binary system in which the congruently melting compound A (23x or 22x) forms a eutectic with the incongruently melting compound A<sub>2</sub>O (2201 or 2212). The oxygen partial pressure at which this eutectic exists in the BSCCO

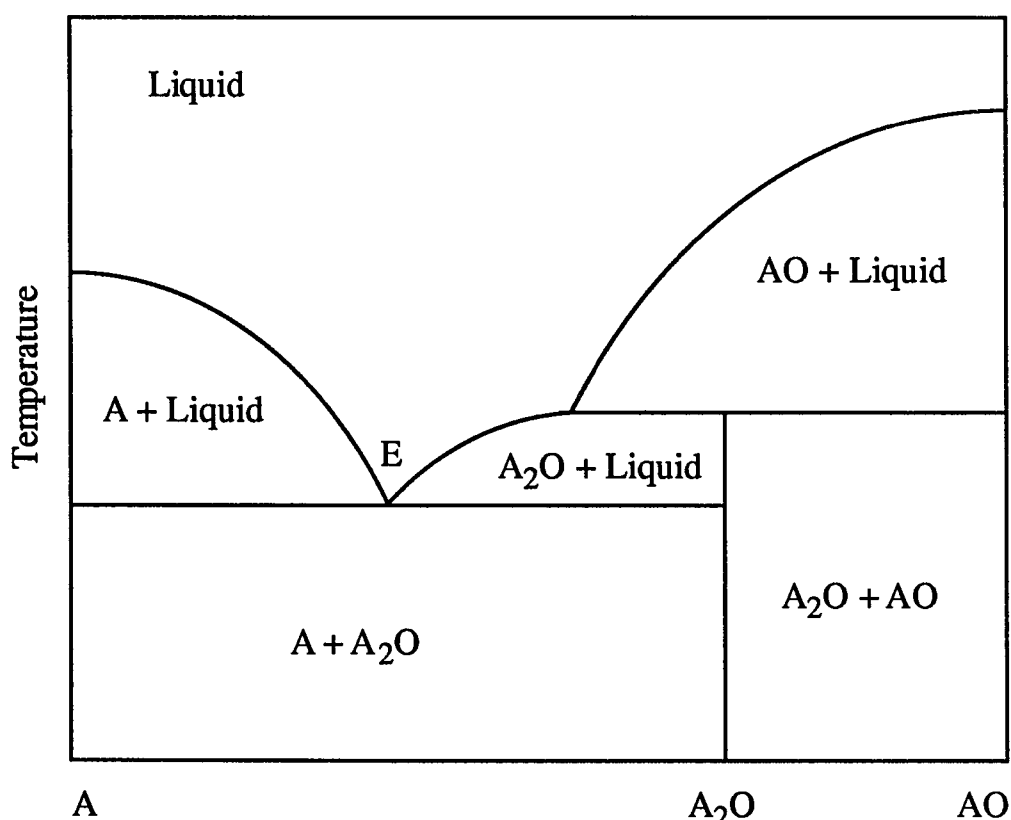


Figure 7.14 Part of a model metal (A) - oxygen (O) binary system used to illustrate the eutectic reaction that results in the combination of 2201 with 22x and 23x in the eutectic microstructures found in the solidified samples.

system is probably below 1%  $O_2$  based on the solidification results. Unfortunately, the exact partial pressure of  $O_2$  at which the eutectic point exists cannot be established from this work due to the non-equilibrium conditions associated with the solidification process and the rather fast cooling rate of  $10^\circ\text{C}/\text{min}$  used in the DTA experiments.

A correct assessment of the eutectic in a BSCCO metal-oxygen phase diagram will require samples that have been carefully equilibrated at various oxygen partial pressures prior to their use in DTA. All of the samples used in the present DTA experiments were equilibrated prior to use in either Ar or  $O_2$ . None the less, the structure of this eutectic can be

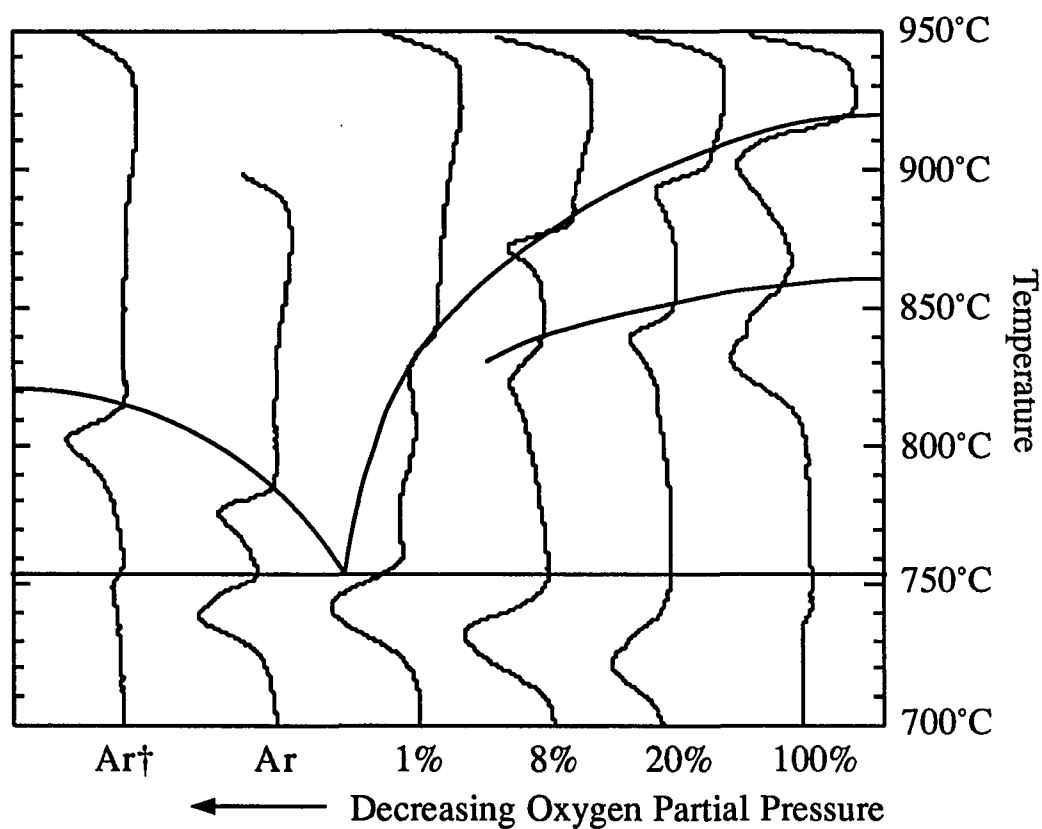


Figure 7.15 DTA data of Figure 7.5 redrawn to show the eutectic valley existing between the congruently melting 23x phase and the incongruently melting 2201/2212 phases. Prior to use in DTA, all samples except (†) were annealed in oxygen. The sample marked (†) was annealed in argon.

seen by reploting the DTA data of Figure 7.5 as shown in Figure 7.15. The third exotherm associated with the formation of the 23x and 22x phases increases in intensity with decreasing oxygen partial pressures and splits into two peaks for the samples cooled in Ar. The lowest exotherm is always located around 750°C. The first phase to solidify in the various oxygen partial pressures was the 1:1 phase whereas the first phase to solidify in Ar was 23x. Lines drawn through the onset of the highest thermal event in each partial pressure of O<sub>2</sub> in Figure 7.15 clearly outline the same type of eutectic structure shown in the ideal metal-oxygen system of Figure 7.14. A similar line of reasoning applied to the DTA data of Figure 7.2 would show a eutectic separating the 22x and 2201 phases. It is interesting to note that splat-quenched glass often show only one melting endotherm in Ar in the DTA. Apparently, the oxygen deficiency that exists in the splat-quenched glasses puts the effective oxygen content of the sample near the eutectic. This would also explain the two-step glass crystallization of 2201 and CuO followed by 23x, SrO, and CaO as described in Chapter 6.

One last point to be drawn from the microstructures of the solidified samples is the presence of a eutectic separating the 22x and 23x phases. The primary crystallization phase of the nominal 2201 sample solidified in Ar was 22x. However, the divorced eutectic structure contained both 22x and small amounts of the 23x phase. Likewise, the primary crystallization phase for the nominal 2212 sample solidified in Ar was 23x, discounting the CaO that separates at higher temperatures in the melt. The eutectic microstructure of this sample contained both the 23x and 22x phases.

There are several factors associated with melt-processing that make it difficult to reach the equilibrium phase assemblage during subsequent anneals below the melting point of 2212. The primary crystallization field for the 2212 composition is CaO plus a liquid phase with the liquidus existing above 1075°C. It was shown in Chapter 6 that glasses processed with Pt crucibles at 1075°C contained large CaO particles. This can be considered the correct phase assemblage at 1075°C since it was shown that very little contamination from the Pt

crucible occurred. CaO tends to float to the top of the melt due to its lower density of 3.25-3.28 g/cm<sup>3</sup>[79]. The density of the liquid is assumed to be close to that of the splat-quenched glasses. The density of a glass with a nominal  $2.15 \text{ Bi} : 0.85 \text{ Ca} : 2 \text{ O}_y$  stoichiometry was calculated to be 5.48 g/cm<sup>3</sup> from measurements of the mass and size of a rectangular piece of glassy material.

The alkaline-earth cuprates and, in the case of pure oxygen,  $\text{Bi}_2\text{Sr}_{4-x}\text{Ca}_x\text{O}_y$ , are the next phases that form on further cooling. All of these phases were found to be relatively stable and do not easily disappear even with extended annealing below the peritectic involving 2212. The amount of the alkaline-earth cuprates may be exaggerated by the presence of CaO. The CaO particles that accumulate near the top of the melt changes the effective local stoichiometry and seem to act as nucleation sites for the alkaline-earth cuprates both on cooling and during subsequent anneals. The separation of CaO certainly poses a problem for melt-processing of wires or large bulk forms. The formation of CaO and the alkaline-earth cuprates during the initial stages of solidification leaves behind a Bi-rich liquid from which it is impossible to form only the 2212 phase. Hence, a large amount of 2201 also forms during cooling. This effect can be clearly illustrated by the model binary phase diagram of Figure 7.16. The peritectic reaction proceeds by the melting of the compound AB (2212) to form phase A (CaO) and a liquid of composition X. If phase A is effectively removed from the system (CaO floating to the top of the melt), the liquid composition X in essence becomes the overall composition of the system. Solidification from this point results in a two phase microstructure, AB (2212) and B (2201).

There are several steps that can be taken to minimize the macroscopic separation of phases that occurs during solidification. The CaO separation problem may be alleviated somewhat with a lower melting temperature than the one used in this study and/or shifting to low-Ca compositions such as  $\text{Bi}_2\text{Sr}_{2.15}\text{Ca}_{0.85}\text{Cu}_2\text{O}_y$  or  $\text{Bi}_{2.15}\text{Sr}_2\text{Ca}_{0.85}\text{Cu}_2\text{O}_y$ . From Table 7.2, it was found that the composition of the 2212 phase in all the samples listed was Bi-rich

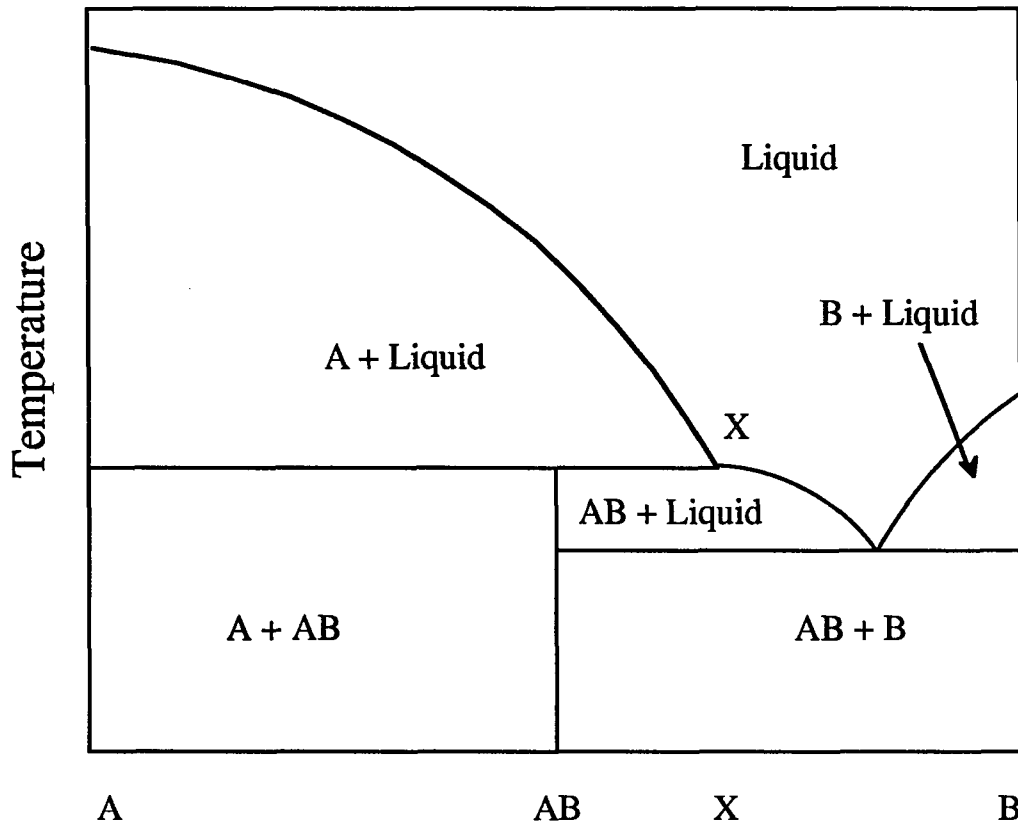


Figure 7.16 Model binary phase diagram used to illustrate the effect of CaO separation in the melt.

and Ca-poor indicating that  $\text{Bi}_{2.15}\text{Sr}_2\text{Ca}_{0.85}\text{Cu}_2\text{O}_y$  may be a good choice for a starting composition for melt-processing. Samples could also be melt processed and cooled in reduced oxygen partial pressures to maximize the amount of the "oxygen-deficient" phases relative to the alkaline-earth cuprates. With careful control on the subsequent anneals, the melting of these "oxygen-deficient" phases around  $750^\circ\text{C}$  should allow for enhanced formation of the 2212 phase while minimizing the formation of the alkaline-earth cuprates. This procedure would be very similar to the melt-casting technique that is reported to result in nearly single-phase 2212 material[80].

There are several groups who argue that 2212 solidifies directly from the melt[44,50,51,52]. Based on the results presented here and in Chapter 6, this does not seem to be the case. Rather, the 2212 phase forms via an intermediate state involving the 2201 phase. From the standpoint of classical nucleation theory, a critical crystal embryo size is required for the spontaneous formation of a crystalline phase from the melt[81]. The clustering of atoms in the melt to form this critically-sized embryo is purely a chance occurrence since the atoms in the melt are constantly in motion. Hence, the simpler the structure of the embryo crystal, the more likely the chance of a successful nucleation event. From this standpoint, the 2201 phase would be easier to nucleate and would serve as an effective catalyst for the growth of the 2212 phase since both phases have very similar lattice parameters in the basal plane. This type of nucleation process is consistent with the observed microstructure of the 2212 and 2201 phases in SEM micrographs and the number of intergrowths of 2201 within the 2212 phase. It is also consistent with the formation of 2212 from the glassy state via an intermediate state involving 2201. The 2212 phase is the stable phase for a nominal 2212 stoichiometry and the formation of 2212 would go to completion if not for the preferential removal of material from the melt resulting from the formation of CaO and the alkaline-earth cuprates. The difficulties associated with determining this process by other methods can be attributed to the presence of liquid phases during solidification which greatly aid in diffusion of the material needed to form 2212 from 2201, and hence, obscure the role of the 2201 phase. This process would be difficult to observe by high-temperature x-ray or neutron diffraction since nucleation and growth proceeds so quickly at these elevated temperatures[44,51,52]. In quenching studies, this conversion process may not be observed since samples are generally equilibrated at specific temperatures before quenching[50].

### 7.7. Summary

A study of the solidification processes for the  $\text{Bi}_2\text{Sr}_2\text{CaCu}_2\text{O}_y$  (2212) and  $\text{Bi}_2\text{Sr}_{1.75}\text{Ca}_{0.25}\text{CuO}_y$  (2201) compositions was undertaken to determine the crystallization processes for each of these compositions as a function of oxygen partial pressure. In either case, the superconducting phases generally were not observed to form during solidification in an inert atmosphere. Solidification in argon resulted in divorced eutectic structures consisting of  $\text{Bi}_2\text{Sr}_{3-x}\text{Ca}_x\text{O}_y$  (23x) and  $\text{CuO/Cu}_2\text{O}$  or  $\text{Bi}_2\text{Sr}_{2-x}\text{Ca}_x\text{O}_y$  (22x) and  $\text{CuO/Cu}_2\text{O}$  for the  $\text{Bi}_2\text{Sr}_2\text{CaCu}_2\text{O}_y$  and  $\text{Bi}_2\text{Sr}_{1.75}\text{Ca}_{0.25}\text{CuO}_y$  compositions respectively. Solidification of the 2212 composition in all partial pressures of oxygen resulted in multiphase samples consisting of 2212, 2201, some alkaline-earth cuprates, and the divorced eutectic structures. The preferential removal of material by the separation of  $\text{CaO}$  and initial crystallization of the alkaline-earth cuprates made it impossible to form a single-phase 2212 material. For both compositions, the solidus is lowered to approximately  $750^\circ\text{C}$  during solidification for all oxygen partial pressures used in this work. The lowering of the solidus and the presence of the divorced eutectic structures can be explained by the oxygen deficiencies present in the melt regardless of the over-pressure of oxygen. It also suggests the presence of an eutectic in a metal-oxygen phase diagram between the congruently melting 23x and 22x phases and the incongruently melting 2201 and 2212 phases. This eutectic structure would explain the two-step crystallization process that occurs for nominal 2212 glasses as discussed in Chapter 6. Finally, the formation process of the 2212 phase during solidification from the melt was determined to proceed from the nucleation of the 2201 phase with subsequent growth of the 2212 phase from these nucleation sites. This formation route is in good agreement with 2212 formation mechanism determined in the crystallization studies of Chapter 6.



## 8. DIRECTIONAL ISOTHERMAL GROWTH

### 8.1. Oxygen Deficient Melt-Processing

The use of high-temperature superconductors for conductor applications will require material with textured microstructures that eliminate or minimize high-angle grain boundaries ("weak-links") which limit intergranular critical current densities[2]. Several approaches have been used for processing and texturing of the  $\text{Bi}_2\text{Sr}_2\text{CaCu}_2\text{O}_y$  superconductor. The coupled use of silver substrates and melt-processing in the partially molten state for the production of highly-textured wires and tapes has been well documented[43,82]. For larger bulk forms, laser heated floating-zone or modified Czochralski techniques have been successfully used to directionally solidify 2212 fibers[83,84]. An important aspect of directional-growth techniques from a pure melt is the use of a temperature gradient between the melt and the solidifying material[85]. These methods work best for congruently melting compounds. However, the 2212 phase melts incongruently as shown in Chapter 7 and, as a result, directional growth processes or melt-processing techniques must maintain slow growth or cooling rates respectively in order for the peritectic phase to be favored during solidification[86]. Hence alternative methods for processing of the 2212 superconductor need to be investigated.

It was clearly shown in Chapter 7 that in the absence of oxygen, the solidus is substantially reduced to approximately  $750^\circ\text{C}$  for compositions around the nominal 2212 stoichiometry. The 2212 phase is not stable in inert atmospheres at high temperatures and decomposes into  $\text{Bi}_2\text{Sr}_{3-x}\text{Ca}_x\text{O}_y$  and  $\text{Cu}_2\text{O}$ . The solidification studies of Chapter 7 showed that the alkaline-earth cuprates that are the products of the peritectic reaction involving 2212 are not present in the absence of oxygen. The resulting microstructure is that of a simple divorced eutectic of  $\text{Bi}_2\text{Sr}_{3-x}\text{Ca}_x\text{O}_y$  and  $\text{Cu}_2\text{O}$ . Discounting the  $\text{CaO}$  that separates in the

melt, the highest temperature at which crystalline phases exist in Ar is approximately 820°C. Hence, it should be possible to solidify an oxygen-deficient melt at a constant temperature by simply switching the oxygen partial pressure. The oxygen gradient that is set up within the sample is analogous to the temperature gradient used during conventional directional solidification processes.

### 8.1.1 The oxygen deficient melt

Compositions used in this study were initially processed by splat-quenching in order to produce a homogeneous starting material that is oxygen deficient[48]. Ground powders of the glassy material were placed in alumina or Ag boats and melted in Ar at 900°C for 6 to 30 minutes. Samples were then cooled in Ar to a temperature between 870°C and 825°C. After the temperature had stabilized, the gas flow in the furnace was switched to oxygen and the samples were held at this temperature for 50 to 100 hours. Gas flows were set to change the equivalent volume of the furnace tube every 0.5 hours. In these initial studies, samples were taken to 900°C to assure a complete melting of the material in Ar although it is clear from the results of Chapter 7 that lower temperatures may be used and should be investigated.

The compositions used in these studies were  $\text{Bi}_2\text{Sr}_2\text{CaCu}_2\text{O}_y$ ,  $\text{Bi}_2\text{Sr}_{1.8}\text{Ca}_{1.2}\text{Cu}_2\text{O}_y$ ,  $\text{Bi}_2\text{Sr}_{2.15}\text{Ca}_{0.85}\text{Cu}_2\text{O}_y$  and  $\text{Bi}_{2.15}\text{Sr}_2\text{Ca}_{0.85}\text{Cu}_2\text{O}_y$ . It was shown in Chapter 7 that CaO separation occurs in all partial pressures of oxygen during melting and solidification. It was found during the course of this study that the CaO separation could be minimized, but not eliminated, by using compositions with less Ca and more Sr or Bi. Glass precursors were used for the directional growth experiments since glass formation of the BSCCO material results in an oxygen deficient material. This helps to lower the amount of oxygen evolved on melting in Ar. In order to determine the approximate composition of the liquid from which grain growth occurs, glassy material with a nominal stoichiometry of 2 2.15 0.85 2 was melted in a small Ag boat in Ar at 900°C for 24 minutes, cooled at 10°C/min in Ar to 850°C,

and then pulled from the furnace and quenched in air on a large metal block. SEM micrographs of the top and bottom layers can be found in Figure 8.1. Most of the air bubbles and CaO particles were found to accumulate towards the top layer of the sample. The exact cause for the air bubbles could not be directly pinpointed from this quench. The porosity may have arisen from additional oxygen evolving from the sample or the trapping of air bubbles within the material when the initial powder melted in Ar. Porosity was a significant problem in most of the samples grown by the directional isothermal growth (DIG) process. Chemical analysis in the SEM of the material below the surface layer of this sample revealed an overall Ca-poor, Cu-rich composition of  $\text{Bi}_{2.09}\text{Sr}_{2.15}\text{Ca}_{0.52}\text{Cu}_{2.24}\text{O}_y$ . Hence, the effective composition from which grain growth occurs lies in a three phase region of 2212, 2201, and CuO as discussed in Chapter 5 and illustrated in Figure 8.2. Similar compositions of the liquid phase can be expected for the other samples used in this study. This can be shown by lines drawn from the CaO corner of Figure 8.2 through each of the compositions used in these experiments.

### 8.1.2 Solidification in an oxygen gradient

Large-grained, textured microstructures were produced with the DIG process as evidenced by the fractured and polished cross sections shown in Figure 8.3a and b. This sample had an overall composition of  $\text{Bi}_{2.15}\text{Sr}_2\text{Ca}_{0.85}\text{Cu}_2\text{O}_y$ . The growth direction of the 2212 and 2201 grains is from the top or surface of the melt to the bottom of the crucible as expected. Although several temperatures were tried, the best results were obtained when the temperature was held at 850°C during directional growth with the oxygen gradient. With the uptake of oxygen, grains of both the 2212 and 2201 phases grew downward from the surface with the orientation of their c-axes (short direction of the grains) approximately perpendicular to the growth direction. The backscattered SEM micrograph of Figure 8.3b shows a colony microstructure for the 2212 and 2201 phases that is not readily apparent in the fractured cross

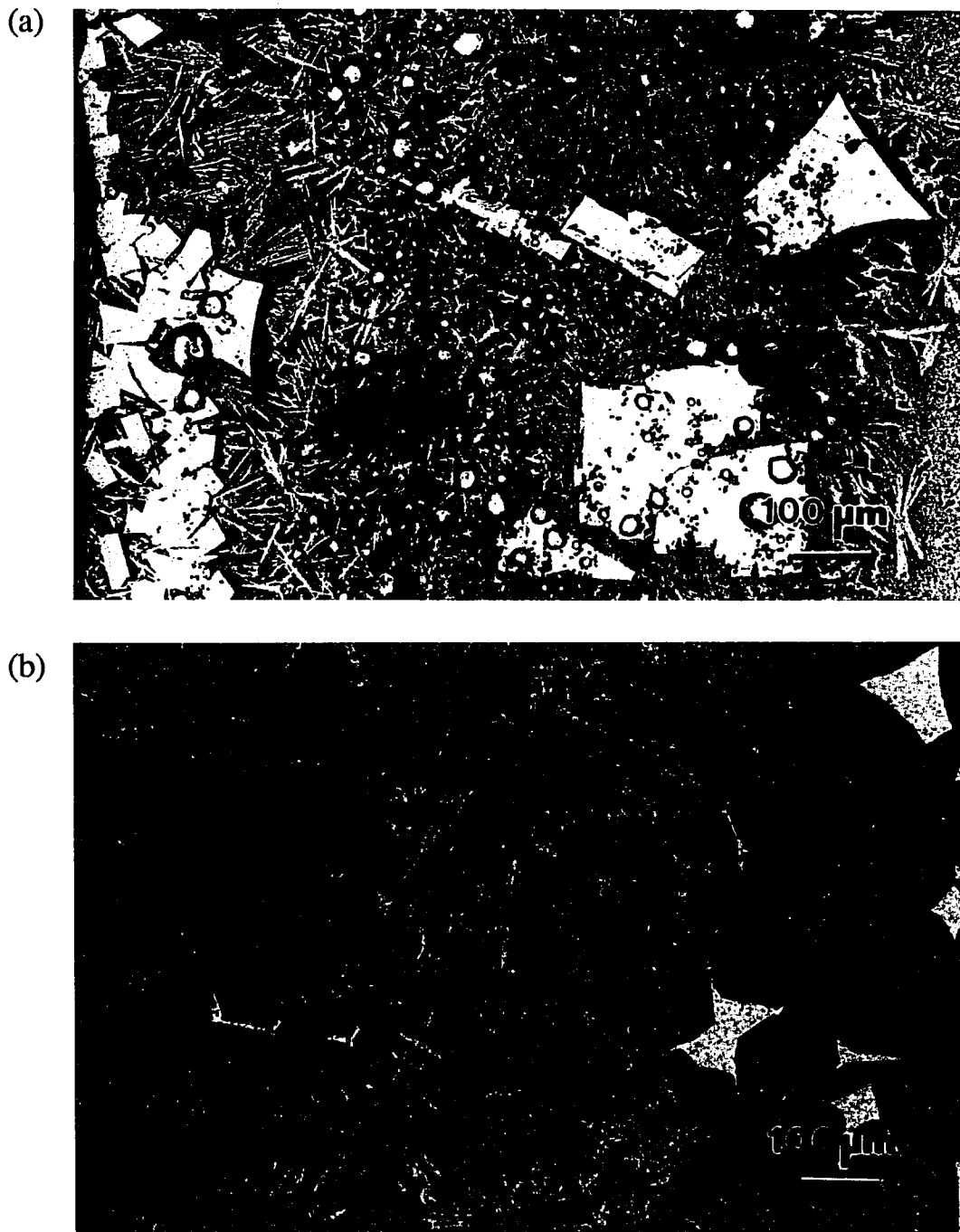


Figure 8.1 Backscattered electron micrographs of the (a) top and (b) bottom regions of a sample with a nominal stoichiometry of  $\text{Bi}_2\text{Sr}_{2.15}\text{Ca}_{0.85}\text{Cu}_2\text{O}_y$ . This sample was melted in Ar at  $900^\circ\text{C}$ , cooled to  $850^\circ\text{C}$ , and then quenched in air on a large metal plate. A surface layer containing a large amount of CaO particles and air bubbles can be seen in (a).

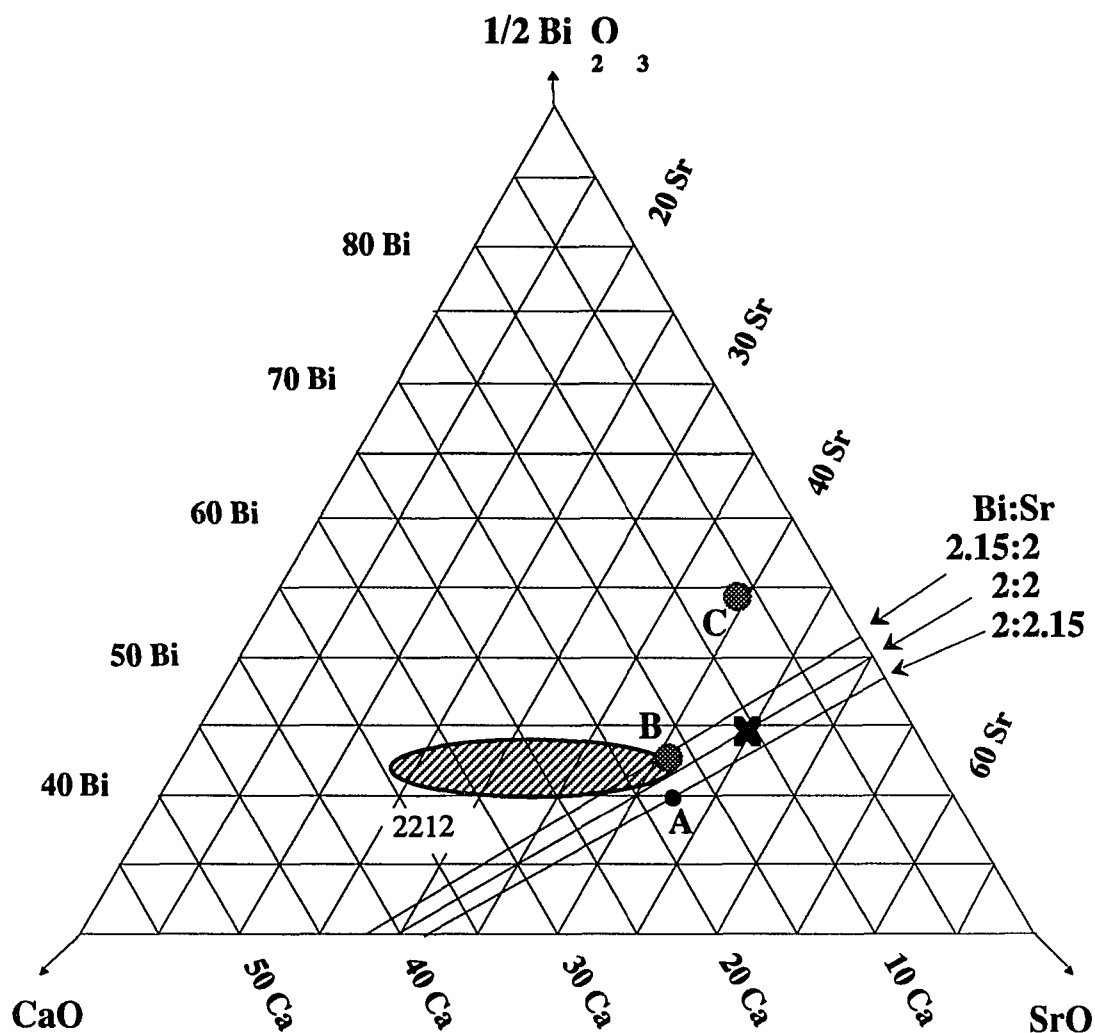


Figure 8.2 Plot of the 2212 solid solution region at 865°C. For the composition (A) -  $\text{Bi}_2\text{Sr}_{2.15}\text{Ca}_{0.85}\text{Cu}_2\text{O}_y$ , the liquid composition from which grain growth occurs is marked by an X. Lines are drawn from the CaO corner to various Bi:Sr ratios. Compositions around the 2212 stoichiometry will have approximately the same liquid composition after CaO separates the samples are melted in Ar. Also plotted are the average compositions of all measurements from all samples of the (B) - 2212 and (C) - 2201 phases.

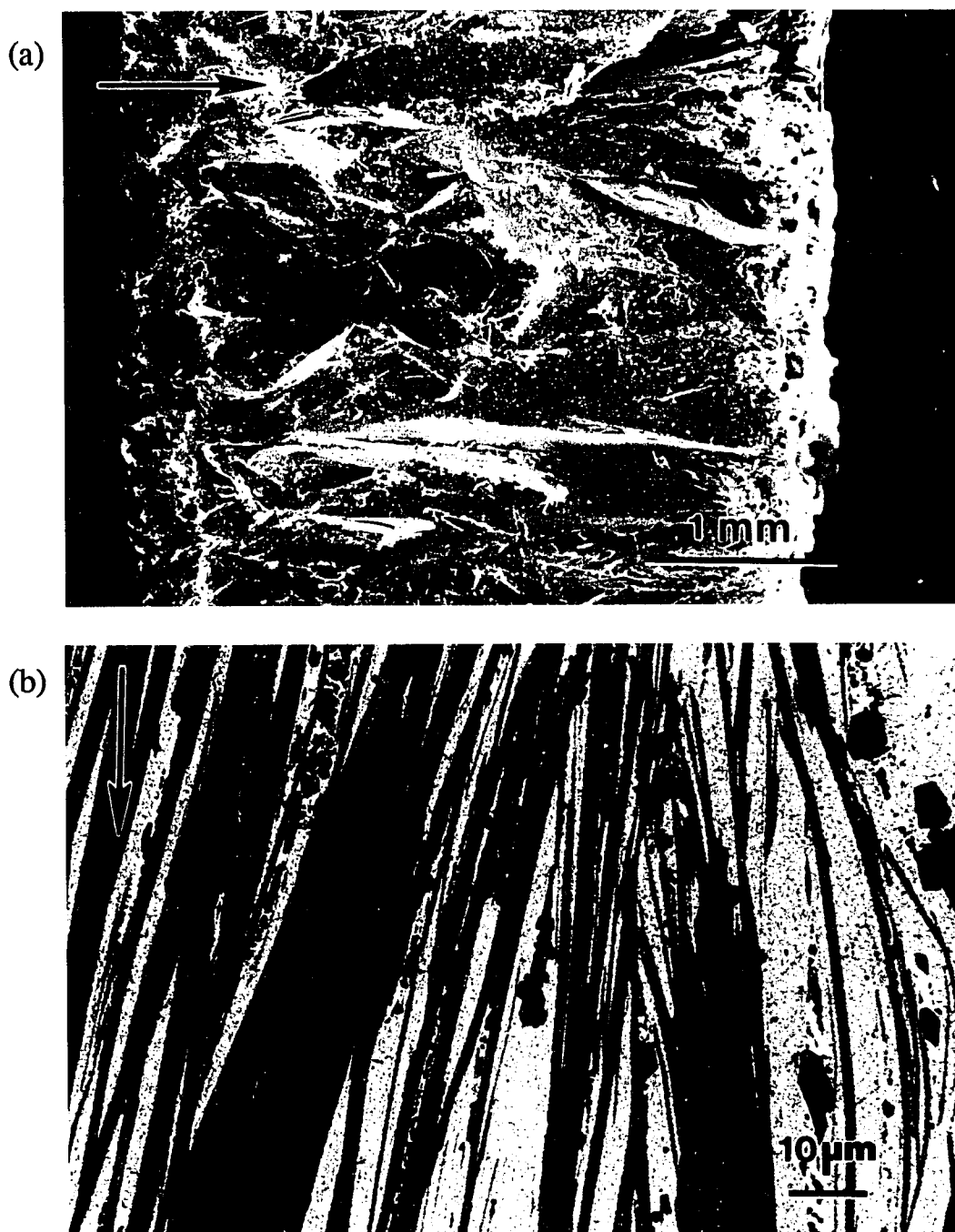


Figure 8.3 Secondary and backscattered electron micrographs of (a) fractured and (b) polished cross sections of a directionally grown sample with a nominal stoichiometry of  $\text{Bi}_{2.15}\text{Sr}_2\text{Ca}_{0.85}\text{Cu}_2\text{O}_y$ . This sample was melted in Ar at  $900^\circ\text{C}$  and directionally grown in  $\text{O}_2$  at  $850^\circ\text{C}$ . The arrows show the direction of growth.

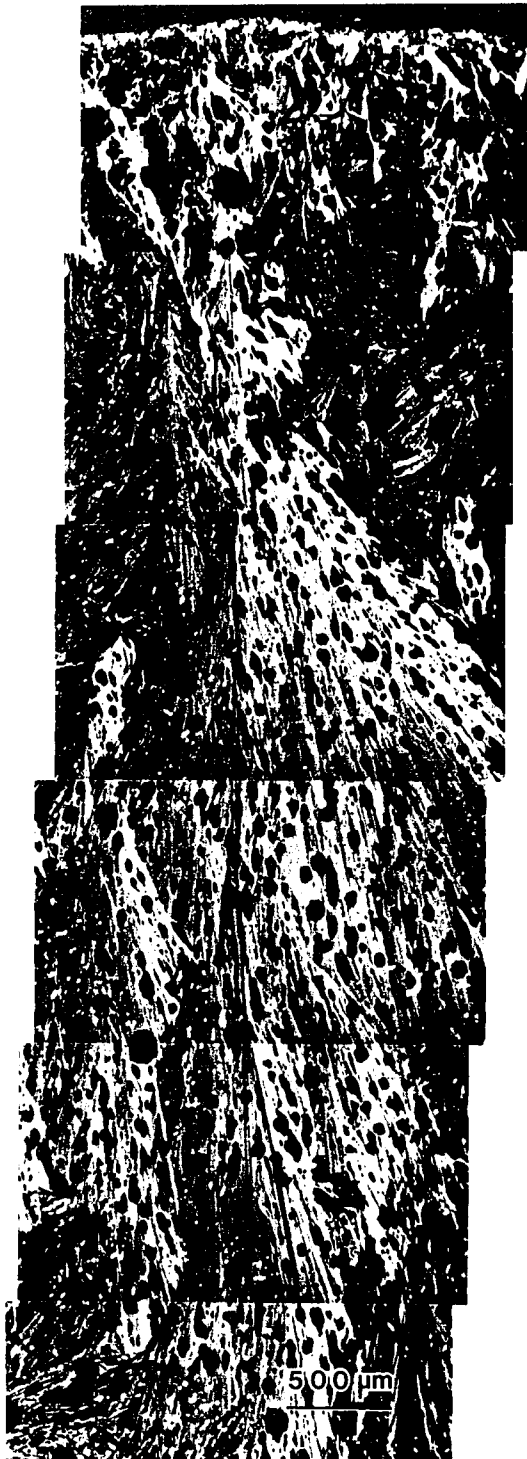


Figure 8.4 Optical micrograph of a DIG sample.

section. It is possible to maintain this type of directional growth for thick samples as shown in composite optical micrograph of Figure 8.4. This sample was approximately 1.5cm thick in the growth direction and had an overall composition of  $\text{Bi}_2\text{Sr}_{2.15}\text{Ca}_{0.85}\text{Cu}_2\text{O}_y$ . It was held at the growth temperature of  $850^\circ\text{C}$  for 50 hours and then allowed to furnace cool. The microstructure of this sample can be thought of as a stack of individual colonies extending from top to bottom that are slightly misoriented by a few degrees from each other. The texturing that results along the growth direction during the DIG process is aided in part from the large anisotropy in the crystallographic growth rates of the 2212 phase. The optical micrograph of Figure 8.5 reveals a random c-axis orientation of the grains within the plane perpendicular to the growth direction.

A surface layer is evident in the micrographs of Figure 8.3a and 8.6 and was found to be a common element of all directionally solidified samples. It was caused by the separation of CaO in the melt

and its accumulation near the surface. Phases identified in this layer by compositional analysis were  $\text{Bi}_2\text{Sr}_{4-x}\text{Ca}_x\text{O}_y$ ,  $\text{Sr}_{1-x}\text{Ca}_x\text{CuO}_y$ ,  $\text{CaO}$ , and 2212. The presence of these phases is consistent with the results of Chapter 5 for the expected phase assemblages of Ca-rich compositions. Figure 8.6 shows that nucleation and growth of the large, oriented grain colonies starts from the bottom of this surface layer.

Various stages of growth from the oxygen-deficient melt are illustrated in Figures 8.7a-d. This sample had an overall composition of  $\text{Bi}_2\text{Sr}_{2.15}\text{Ca}_{0.85}\text{Cu}_2\text{O}_y$  and was held at a growth temperature of  $825^\circ\text{C}$  for 50 hours and then allowed to furnace cool. The overall thickness of the melt was approximately 1.5cm, the same as the sample shown in Figure 8.4. Apparently, the lower temperature resulted in a slower growth rate in which 50 hours was not enough time for the DIG process to go to completion. Figure 8.7a shows an area near the top of the directionally grown sample. In this region, the 2212 phase is well formed. Only small

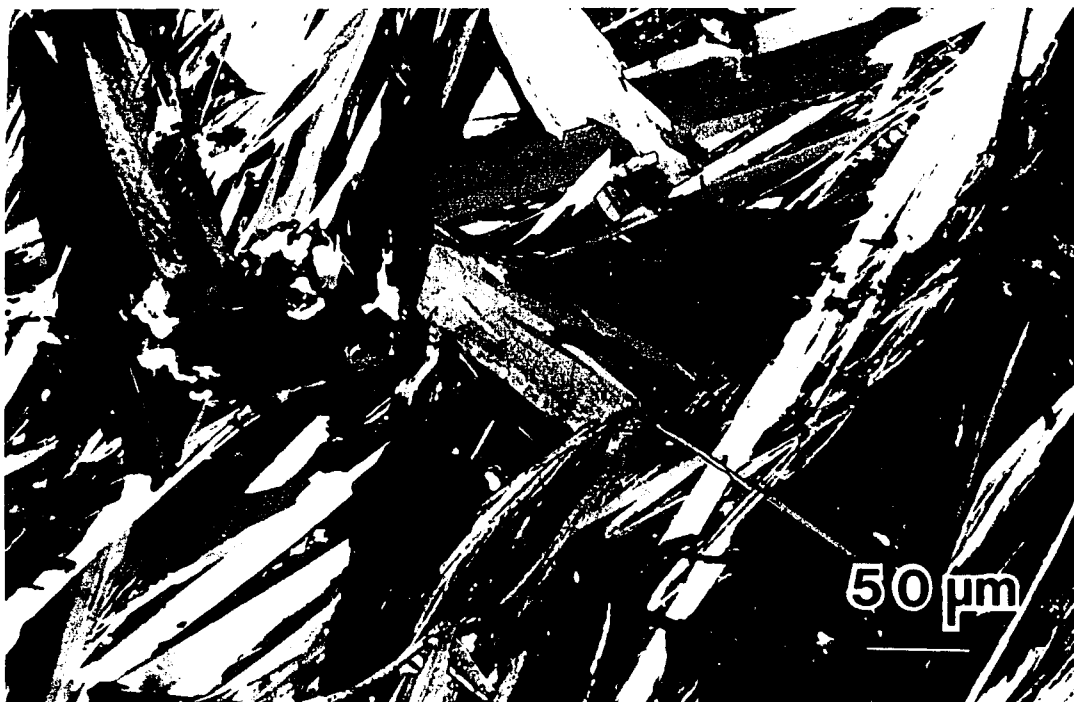


Figure 8.5 Optical micrograph of a directionally grown sample with an overall stoichiometry of  $\text{Bi}_2\text{Sr}_{1.8}\text{Ca}_{1.2}\text{Cu}_2\text{O}_y$ . The growth direction is into the plane of the micrograph.



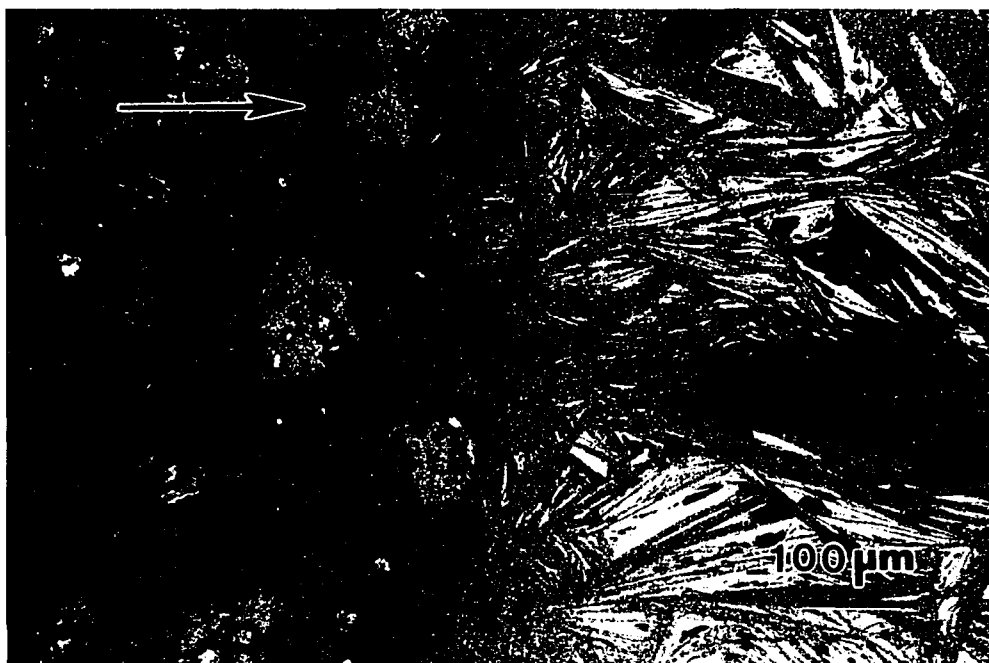
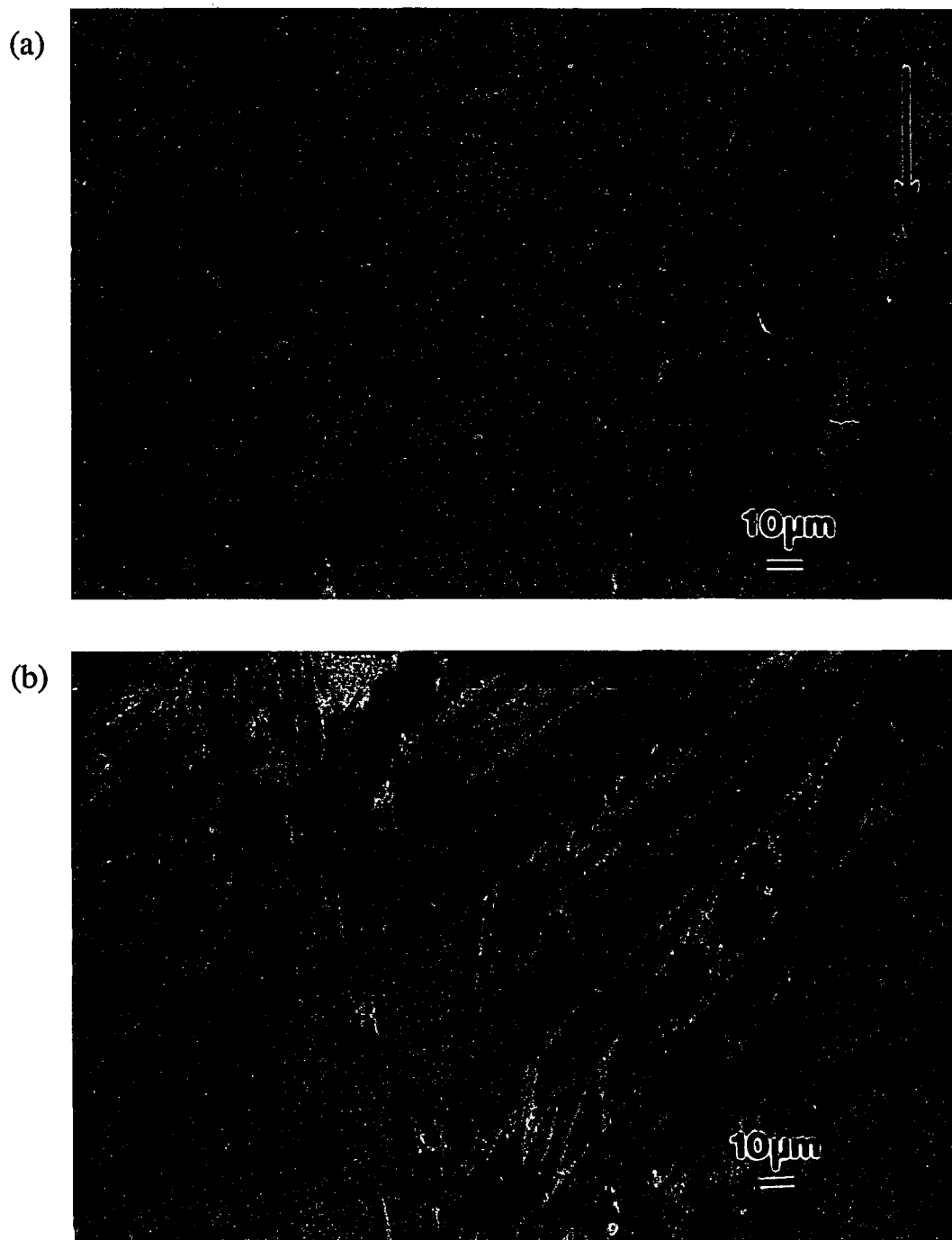


Figure 8.6 Backscattered electron micrograph of the surface layer of a directionally grown sample with a nominal composition of  $\text{Bi}_{2.15}\text{Sr}_2\text{Ca}_{0.85}\text{Cu}_2\text{O}_y$ .

amounts of 2201,  $\text{CuO}$ ,  $\text{SrO}$ , and a divorced eutectic structure consisting of  $\text{Bi}_2\text{Sr}_{2-x}\text{Ca}_x\text{O}_y$  (22x) and  $\text{Cu}_2\text{O}$  are found in and between the 2212 grains. A higher magnification of the microstructure shown in Figure 8.7a can be found in Figure 8.8. The presence of the Bi-rich 22x and 2201 phases indicates that the growing 2212 grains trap small amounts of Bi-rich liquids in between them. This Bi-rich liquid then either forms 2201 or solidifies on cooling as 22x/ $\text{Cu}_2\text{O}$  depending on the amount of oxygen present. The microstructure shown in Figure 8.8 was commonly found in all of the DIG samples; the amounts of the Bi-rich phases was dependent upon the starting composition and the degree of Ca-separation on melting.

Figure 8.7b shows the microstructure approximately two-thirds of the way into the sample. It bears a close resemblance to the microstructures discussed in Chapter 7 of the samples solidified in 1% and 20%  $\text{O}_2$ . The eutectic structures contained both the 22x and



**Figure 8.7** Backscattered electron micrographs showing the various stages of growth from top to bottom (a-d) during directional isothermal growth for a sample in which the process did not go to completion.

(c)



(d)

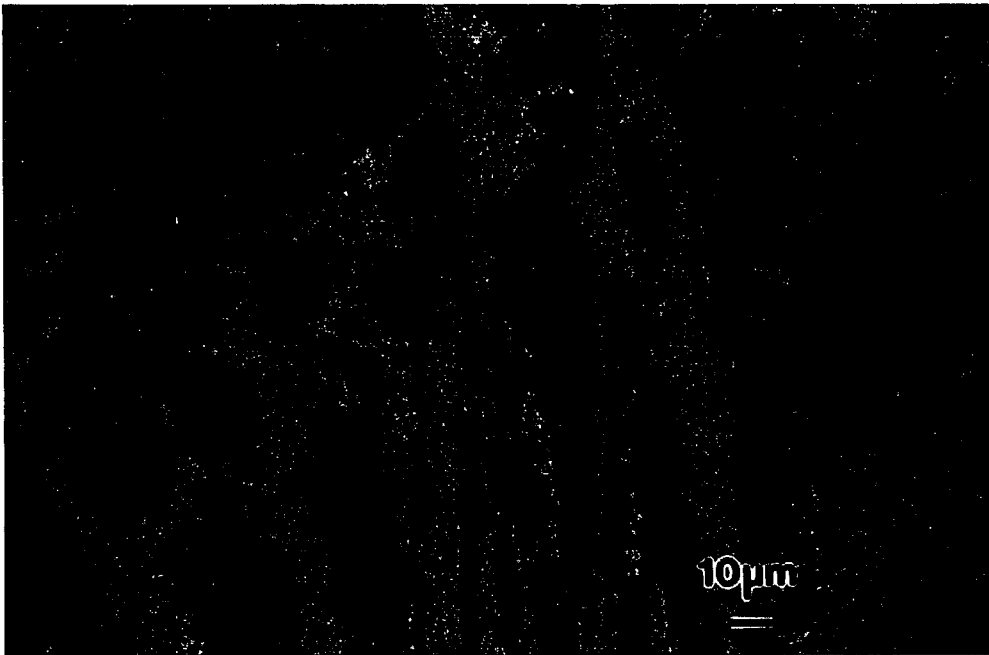


Figure 8.7 (continued)

$\text{Bi}_2\text{Sr}_{3-x}\text{Ca}_x\text{O}_y$  (23x) phases. This area of the sample appears to have been the boundary region between the oxygen-deficient melt and 2212 at the time the sample was cooled. Just below this point, the microstructure changes completely into that of the divorced eutectic structures as shown in Figure 8.7c and d. The majority of the eutectic structures consisted of 23x and  $\text{Cu}_2\text{O}$ . The fine microstructure of 8.7d was found at the very bottom of the crucible and probably results from a slightly faster cooling rate near the crucible walls during the furnace cooling.

### 8.1.3 Composition of the superconducting phase

As shown above, the separation of CaO to the surface region leaves the bulk of the sample comprised of a Cu-rich, Ca-deficient liquid from which it is impossible to grow single-phase 2212 material. Of the compositions used,  $\text{Bi}_2\text{Sr}_{2.15}\text{Ca}_{0.85}\text{Cu}_2\text{O}_y$  yielded

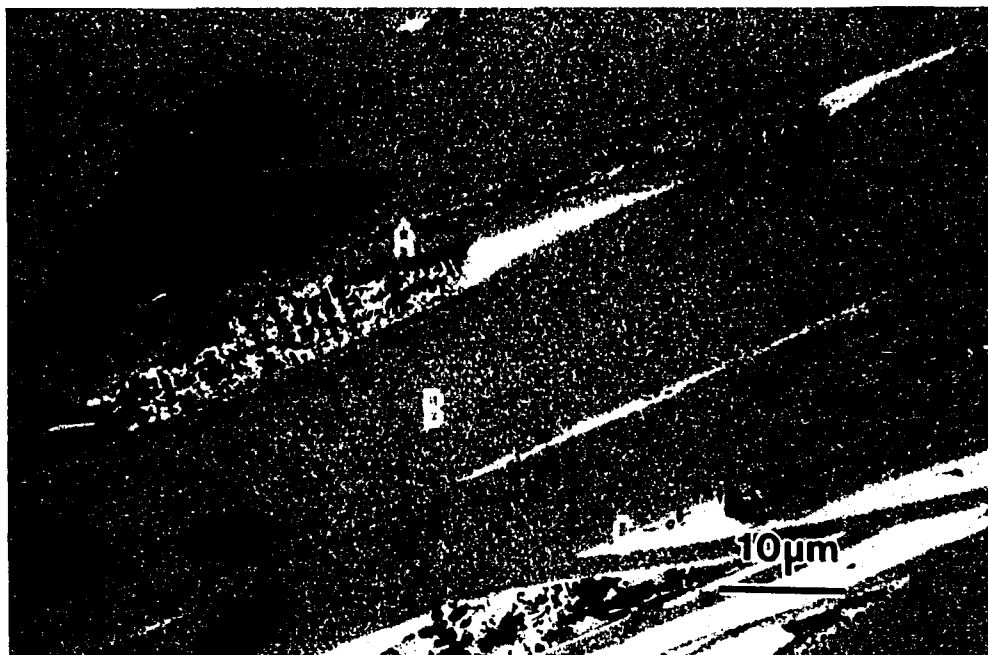


Figure 8.8 Backscattered electron micrograph showing the 2201 and 22x/ $\text{Cu}_2\text{O}$  structures that are often found between the larger grains of the 2212 phase.

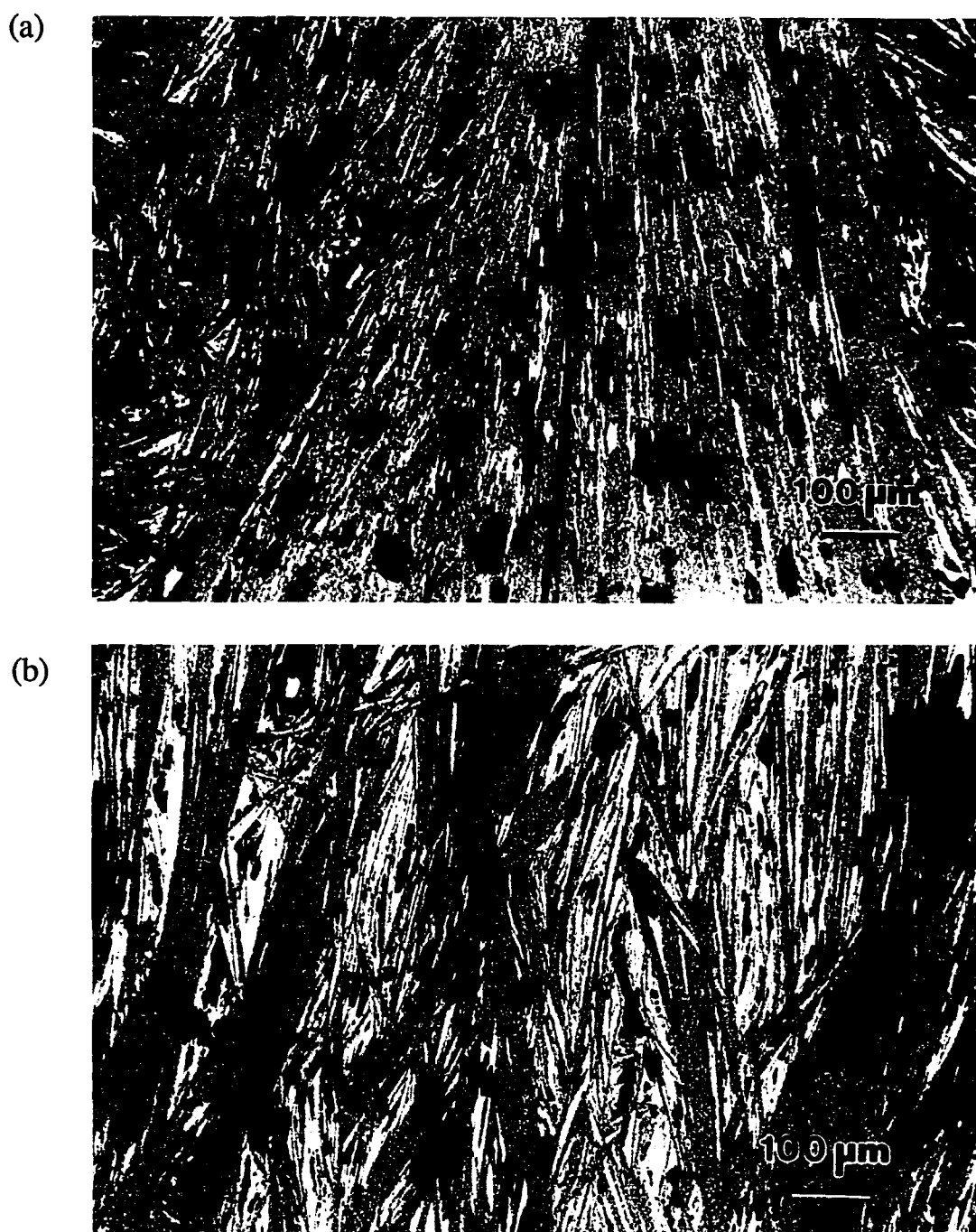


Figure 8.9 Backscattered electron micrographs of polished cross-sections of directionally grown material with nominal compositions of (a)  $\text{Bi}_2\text{Sr}_{2.15}\text{Ca}_{0.85}\text{Cu}_2\text{O}_y$ , (b)  $\text{Bi}_{2.15}\text{Sr}_2\text{Ca}_{0.85}\text{Cu}_2\text{O}_y$ , and (c)  $\text{Bi}_2\text{Sr}_{1.8}\text{Ca}_{1.2}\text{Cu}_2\text{O}_y$ . All samples were grown at  $850^\circ\text{C}$ . The white phase is 2201 or  $22x/\text{Cu}_2\text{O}$ . The growth direction is from top to bottom in each micrograph.

(c)



Figure 8.9 (continued)

samples with the least amount of 2201 as shown in Figure 8.9. It was found that regardless of the starting stoichiometry or growth temperature, the measured compositions of the 2201 and 2212 phases were nearly the same. The average and standard deviation of 105 separate compositional measurements performed in the SEM of the 2212 phase from 14 samples of the various starting compositions around the 2212 stoichiometry was  $\text{Bi}_{2.15 \pm 0.03} \text{Sr}_{2.02 \pm 0.06} \text{Ca}_{0.83 \pm 0.06} \text{Cu}_{2.00 \pm 0.04} \text{O}_y$ . This composition lies on the Sr-rich end of the 2212 solid solution range as illustrated in Figure 8.2. In light of the results of Chapter 5, the measured molar value of 2 for the Cu content and the small standard deviations indicate that the grains are well formed and contain very few intergrowths. The average of 45 separate measurements of the 2201 phase from these samples was  $\text{Bi}_{2.18 \pm 0.04} \text{Sr}_{1.56 \pm 0.06} \text{Ca}_{0.24 \pm 0.05} \text{Cu}_{1.02 \pm 0.03} \text{O}_y$ . For compositions around the 2212 stoichiometry, the separation of CaO during melting in Ar results in a Cu and Sr rich liquid composition lying between the 2212 and 2201 solid solution regions. Hence, contact is always made with the Sr-rich end of the 2212 solid solution region during directional growth.

## 8.2. Superconducting Properties

Transition temperatures of the as-grown material were found to lie between 85K and 90K. The superconducting transition could be raised several degrees and sharpened considerably by a subsequent annealing of the material as shown in Figure 8.10. All anneals were carried out at 850°C for 50 to 100 hours followed by an air quench. The additional annealing step was not observed to change the overall microstructure of the material or the measured composition of the 2212 and 2201 phases even after anneals of 100 hours. Intergranular critical current densities shown in Figure 8.11 were calculated from hysteresis loop measurements at 5K, 10K, and 20K on a 3mm disc (field applied perpendicular to the disc) cut from the same annealed sample shown in Figure 8.10.  $J_c$  values from the as-grown

sample of Figure 8.10 were measured to be approximately half of the annealed sample. The critical currents were assumed to be intergranular and the sample size of 3mm was used as the critical dimension in the calculation of the current densities from equation 3.1. The intergranular nature of the critical currents is supported by the fact that quartering of the discs reduced the M-H loops by a factor of approximately 2. At 20K and higher, the critical current densities were found to drop off quickly with field which is typical of the 2212 phase[87]. The strong field dependence above approximately 20K will limit applications of the 2212 phase to low magnetic fields at liquid nitrogen temperatures unless effective flux-pinning centers can be introduced into the material.

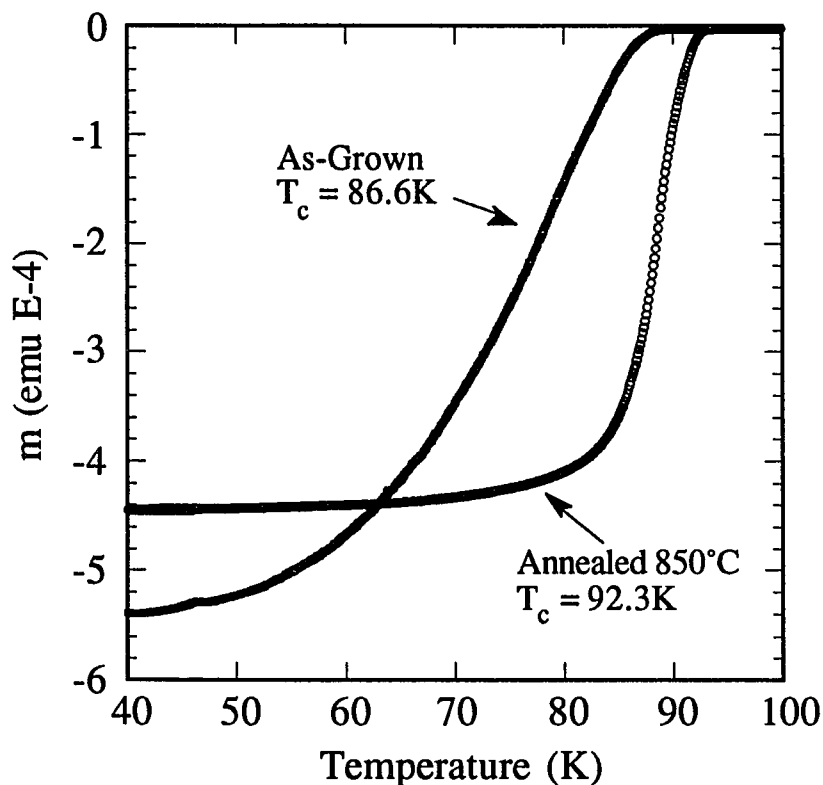


Figure 8.10 Transition temperatures of as-grown and annealed samples of the composition  $\text{Bi}_2\text{Sr}_{2.15}\text{Ca}_{0.85}\text{Cu}_2\text{O}_y$ . Flux exclusion was measured on warming in a 0.5 Oe field.



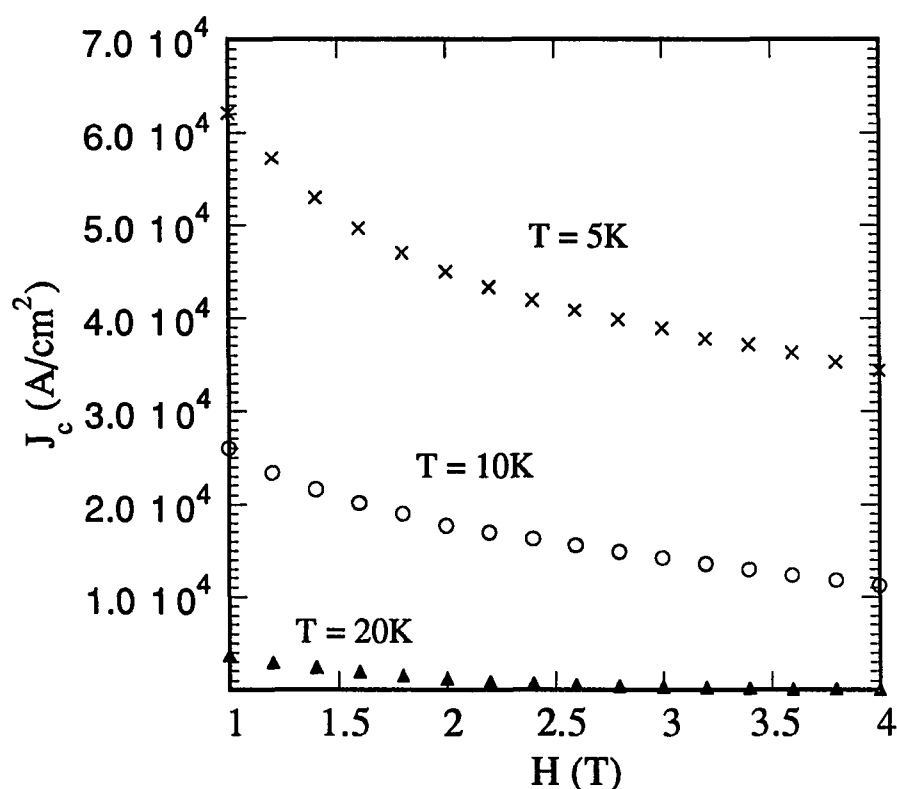


Figure 8.11 Calculated critical current densities from the annealed sample shown in Figure 8.10.

### 8.3. Discussion

The use of an oxygen gradient to directionally solidify an incongruently melting oxide from a pure melt does not appear to have been reported before in the literature. The directional isothermal growth process is clearly an alternative method for melt-processing of bulk 2212 superconductors. This technique has several advantages for melt processing of the 2212 superconductor. The temperatures used during the DIG process are generally lower than those used during conventional solidification processes. It is also much easier to process large samples by the DIG process. The size of the sample is, in principle, limited only by the size of the furnace. Finally, melt processing in reduced oxygen partial pressures may offer more control over the formation of  $\text{Sr}_{1-x}\text{Ca}_x\text{CuO}_2$  and other alkaline-earth cuprates that are

reported to form from the melting of 2212 in air[53]. As shown in Chapter 7, no alkaline-earth cuprates were observed to form during solidification in Ar. The temperature of 850°C is clearly in the stability range of the 2212 phase in oxygen. Hence, there is a stronger driving force to form the 2212 phase as opposed to  $\text{Sr}_{1-x}\text{Ca}_x\text{CuO}_2$  which forms during the incongruent melting of the 2212 phase around 890°C. Examination of the results presented in Chapter 5 shows that  $\text{Sr}_{1-x}\text{Ca}_x\text{CuO}_2$  does not form equilibria with 2212 at 850°C in  $\text{O}_2$  for any composition. With some minor adjustments, this process may be applied to the melt processing of 2212 wires and tapes. This process is probably not suited for the 2223 phase since the CaO separation problem would be even more severe than it is for the 2212 phase. In spite of this problem, a similar approach for melt-processing of the 2223 phase in Ar has been reported[88]. However, the effect of the oxygen gradient on the microstructure and phase assemblages was not investigated.

Although all aspects of the DIG process have not been worked out, the initial results are quite promising as indicated by the high transition temperatures and inter granular nature of the critical currents below 20K in high magnetic fields. One of the next steps to be performed will be to grow bars of 2212 material by the DIG process for the purpose of measuring transport critical currents at 77K. The initial goal is to obtain  $J_c$ 's at 77K in self-field of around 1000 A/cm<sup>2</sup>. These values would be comparable to reported results on bulk 2212 conductors fabricated by the melt-casting technique[89]. Certainly the simplicity of this process lends itself well for producing long lengths of directionally grown material.

The composition that yielded the best results in these initial studies was  $\text{Bi}_2\text{Sr}_{2.15}\text{Ca}_{0.85}\text{Cu}_2\text{O}_y$ . Apparently, this composition is the least affected by the CaO separation. It is hoped that with some minor compositional adjustments and improvements in the melting process, the CaO separation and porosity problems will be minimized or eliminated completely. One possibility for minimizing the CaO separation is to use a lower temperature during melting. In Ar, the highest temperature at which crystalline phases exist,

aside from CaO, is 820°C. Another possibility for controlling the CaO separation is the addition of a small amount of aluminum. As shown in Chapter 6, small amounts ( $\leq 2\text{at.}\%$ ) of Al contamination in the glassy material from the alumina crucibles used during processing resulted in glasses that were free of CaO particles. The same compositions processed in platinum crucibles using the same conditions resulted in glassy material with a significant amount of CaO present. Finally, the porosity problem may be alleviated by performing the initial part of the melting step in a vacuum. Additional studies are planned to try these solutions to the CaO and porosity problems.

#### 8.4. Summary

It is shown that an oxygen gradient can be used to produce large-grained, textured bulk forms of the 2212 superconductor from an oxygen-deficient pure melt held at a constant temperature. The oxygen gradient is analogous to the temperature gradient used in conventional directional growth techniques. Material grown by the directional isothermal growth (DIG) process was found to have high transition temperatures in the range of 85K to 90K and high intergranular critical current densities below 20K. At 20K and above, the measured  $J_c$ 's showed a strong field dependence that is characteristic of the 2212 superconductor. The composition of the 2212 phase was always found to be around  $\text{Bi}_{2.18}\text{Sr}_{1.56}\text{Ca}_{0.24}\text{Cu}_{1.02}\text{O}_y$ . Samples produced in this manner were not single phase due to the CaO separation that occurs on melting. However, improvements in the material and superconducting properties are expected when problems associated with CaO separation and porosity in the melt are minimized or eliminated. The relatively simplistic nature of the DIG process can be easily scaled to produce large rigid conductors suitable for applications such as current leads.

## 9. CONCLUSIONS

Practical and efficient applications of the  $\text{Bi}_2\text{Sr}_2\text{CaCu}_2\text{O}_y$  (2212) superconductor will ultimately need a sufficient amount of information on both the phase equilibria, in particular the solid solution region, and the reaction kinetics associated with the formation of 2212 and other competing phases. Ideally, the goal is to produce single phase material (requiring phase equilibria data) with good superconducting properties (requiring information on the kinetics). In reality, it is often found that improvements in either one of these properties generally occurs at the expense of the other. Hence, compromises have to be made to produce a material suitable for its intended application. The results presented in this thesis represent a balanced approach to addressing each of these areas. While these studies are not comprehensive, they do represent a significant contribution to the scientific community on the materials properties of the 2212 superconductor. Chapter 5 represents the most accurate compositional measurements to date of the 2212 solid solution region. Chapters 6 and 7 provide a good insight into the formation process of the 2212 phase and the effects of oxygen partial pressure on the reaction kinetics. Chapter 8 represents an application of the information gained in these earlier chapters to produce bulk 2212 material that is suitable for high-current, low-field applications at 77K.

The 2212 phase was found to exhibit a wide range of solid solution. However, compositional measurements in the TEM were necessary in order to separate intergrowth and solid solubility effects. Most of the solid solubility exhibited by this phase exists between Sr and Ca. A smaller amount exists between Bi and (Sr+Ca). The solid solution region was found to be quite stable and only shrinks slightly with increasing temperatures in an oxygen environment. It was found that Ca and Bi rich 2212 compositions in the solid solution region had the lowest melting points. At the reduced oxygen partial pressure of 0.1%, a significant

portion of the Ca-rich solid solution region was found to be unstable. This instability appears to be related to the specific reactions by which the 2212 phase decomposes in inert or reducing atmospheres.

By eliminating the effects of intergrowths in the compositional measurements, it was determined that Cu does not significantly contribute to the solid solution nature of the 2212 phase. The measured Cu content of the 2212 phase was always found to be close to the ideal stoichiometric molar ratio of 2. It was also found that the Bi content of the 2212 phase never drops below the stoichiometric molar ratio of 2. Based on these results, two substitution schemes can be evolved. The first is a simple interchange between Sr and Ca. The second is slightly more involved. It appears that Bi can substitute for Sr or Ca. However, it appears to be unfavorable for the reverse substitution to occur. No correlation was found between the length of the c-axis and the transition temperature. Rather,  $T_c$  was found to be proportional to the Sr+Ca content as shown in Table 5.11. It should be noted, however, that considerably more work needs to be done in order to ascertain the exact relationships between cation composition, oxygen partial pressure, and transition temperature.

The 2212 phase was found with a total of 12 separate secondary phases in this work. Compositional measurements of these secondary phases revealed most of these to be solid solutions. Hence, variations in the overall cation stoichiometry and the oxygen partial pressure were accommodated by changes in (1) the amount, types, and composition of any secondary phases which may be present, (2) the number of intergrowths within the 2212 phase (apparent composition), and (3) the solid solution composition of the 2212 phase (actual composition). It appears that the ideal 2212 composition lies on or just outside of the solid solution region which may explain the difficulties in obtaining single phase material starting with this composition. The small solubility limit of Cu in the 2212 phase makes local fluctuations in stoichiometry on a microscopic scale more likely to lead to the formation of secondary phases for overall compositions on the boundary of the solid solution region as

opposed to compositions within the solid solution region. Hence, compromises may have to be made on the choice of an overall composition to use in order to prepare single-phase material with the highest possible  $T_c$ .

The study of the crystallization process found the oxygen deficiency in the splat-quenched glasses to play a major role in determining phase formation from the glassy state. The crystallization of 2212 glass occurs in two steps. The first crystallization event results in the formation of 2201 and  $\text{Cu}_2\text{O}$ . The second crystallization event converts the remaining glassy material into  $\text{Bi}_2\text{Sr}_{3-x}\text{Ca}_x\text{O}_y$  (23x),  $\text{SrO}$ , and  $\text{CaO}$ . The 23x phase is unstable in oxygen for compositions around the 2212 stoichiometry and converts to other phases upon annealing below  $700^\circ\text{C}$ . Rapid heating of the glass above  $700^\circ\text{C}$  results in the melting of the 23x phase. The 2212 phase was found to evolve from the 2201 nuclei that formed during the initial crystallization event. The formation of 2212 below  $800^\circ\text{C}$  was found to be kinetically limited by diffusion. In contrast, most of the glassy material could be converted to the 2212 phase after only one minute of annealing at  $800^\circ\text{C}$  or above. Extended anneals at these higher temperatures were needed, however, in order for the system to reach its equilibrium state as shown by compositional measurements on individual grains and changes in the secondary phases present.

The solidification processes for the  $\text{Bi}_2\text{Sr}_2\text{CaCu}_2\text{O}_y$  (2212) and  $\text{Bi}_2\text{Sr}_{1.75}\text{Ca}_{0.25}\text{CuO}_y$  (2201) compositions were determined as a function of oxygen partial pressure. In either case, the superconducting phases were not observed to form during solidification in an inert atmosphere. Solidification in argon resulted in divorced eutectic structures (oxygen-deficient phases) consisting of  $\text{Bi}_2\text{Sr}_{3-x}\text{Ca}_x\text{O}_y$  (23x) and  $\text{CuO}/\text{Cu}_2\text{O}$  or  $\text{Bi}_2\text{Sr}_{2-x}\text{Ca}_x\text{O}_y$  (22x) and  $\text{CuO}/\text{Cu}_2\text{O}$  for the  $\text{Bi}_2\text{Sr}_2\text{CaCu}_2\text{O}_y$  and  $\text{Bi}_2\text{Sr}_{1.75}\text{Ca}_{0.25}\text{CuO}_y$  compositions respectively. Solidification of the 2212 composition in all partial pressures of oxygen resulted in multiphase samples consisting of 2212, 2201, some alkaline-earth cuprates, and the divorced eutectic structures. The rather rapid solidification rate of  $10^\circ\text{C}/\text{min}$  and the preferential

removal of material by the separation of CaO and initial crystallization of the alkaline-earth cuprates made it impossible to form a single-phase 2212 material. The rapid solidification rate of 10°C/min also did not allow the samples to equilibrate with the over pressure of oxygen resulting in the presence of oxygen deficient phases for all oxygen partial pressures used in this work. However, it was found that increasing the oxygen partial pressure during solidification resulted in the formation of more 2212/2212 at the expense of the oxygen deficient phases.

The lowering of the solidus and the presence of the divorced eutectic structures can be explained by the oxygen deficiencies present in the melt regardless of the over-pressure of oxygen. It also suggests the presence of an eutectic in a metal-oxygen phase diagram between the congruently melting 23x and 22x phases and the incongruently melting 2201 and 2212 phases. The presence of the eutectic would explain the two-step crystallization process that occurs for nominal 2212 glasses as discussed in Chapter 6. Apparently, the oxygen deficiency of the splat-quenched glasses puts the overall composition near this eutectic resulting in the presence of both 23x and 2201 in the initial crystallization products. Finally, the formation process of the 2212 phase during solidification from the melt appears to proceed from the nucleation of the 2201 phase with subsequent growth of the 2212 phase from these nucleation sites. This formation route is in good agreement with 2212 formation mechanism determined in the crystallization studies of Chapter 6.

Chapter 8 is one application of the basic information gained in the studies of Chapters 5-7. Using information on the effects of low oxygen partial pressures, it was shown that an oxygen gradient can be used to produce large-grained, textured bulk forms of the 2212 superconductor from an oxygen-deficient, pure melt held at a constant temperature. The oxygen gradient is analogous to the temperature gradient used in conventional directional growth techniques. Material grown by the directional isothermal growth (DIG) process was found to have high transition temperatures in the range of 85K to 90K and high intergranular

critical current densities below 20K. At 20K and above, the measured  $J_c$ 's showed a strong field dependence that is characteristic of the 2212 superconductor. The composition of the 2212 phase was always found to be around  $\text{Bi}_{2.18}\text{Sr}_{1.56}\text{Ca}_{0.24}\text{Cu}_{1.02}\text{O}_y$ . Samples produced in this manner were not single phase due to the CaO separation that occurs on melting. However, improvements in the material and superconducting properties are expected when problems associated with CaO separation and porosity in the melt are minimized or eliminated. The relatively simplistic nature of the DIG process can be easily scaled up to produce large rigid conductors suitable for low-field applications at 77K such as current leads.



## REFERENCES

1. J.G. Bednorz and K.A. Muller, *Z. Phys. B* **64**, 189-193 (1986).
2. J.W. Ekin, A.I. Braginski, A.J. Panson, M.A. Janocko, D.W. Capone II, N.J. Zaluzec, B. Flandermeyer, O.F. de Lima, M. Hong, J. Kwo, and S.H. Liou, *J. Appl. Phys.* **62**, 4821-4828 (1987).
3. D. Dimos, P. Chaudhari, J. Mannhart, and F.K. LeGoues, *Phys. Rev. Lett.* **61**, 219-222 (1988).
4. M. Kawasaki, E. Sarnelli, P. Chaudhari, A. Gupta, A. Kussmaul, J. Lacey, and W. Lee, *Appl. Phys. Lett.* **62**, 417-419 (1993).
5. S. Jin, T.H. Tiefel, R.C. Sherwood, R.B. van Dover, M.E. Davis, G.W. Kammlott, and R.A. Fastnacht, *Phys. Rev. B* **37**, 7850-7853 (1988).
6. K. Salama, V. Selvamanickam, L. Gao, and K. Sun, *Appl. Phys. Lett.* **54**, 2352-2354 (1989).
7. P. McGinn, W. Chen, N. Zhu, M. Lanagan, and U. Balachandran, *Appl. Phys. Lett.* **57**, 1455-1457 (1990).
8. K. Heine, J. Tenbrink, and M. Thoner, *Appl. Phys. Lett.* **55**, 2441-2443 (1989).
9. J. Kase, N. Irisawa, T. Morimoto, K. Togano, H. Kumakura, D.R. Dietderich, and H. Maeda, *Appl. Phys. Lett.* **56**, 970-972 (1990).
10. C. Michel, M. Hervieu, M.M. Borel, A. Grandin, F. Deslandes, J. Provost, and B. Raveau, *Z. Phys. B* **68**, 421-423 (1987).
11. H. Maeda, Y. Tanaka, M. Fukutomi, and T. Asano, *Jpn. J. Appl. Phys.* **27**, L209-L211 (1988).
12. O. Eibl, *Physica C* **168**, 249-256 (1990).
13. D.P. Matheis and R.L. Synder, *Powder Diffraction* **5**, 8-25 (1990).
14. S.N. Ruddlesden and P. Popper, *Acta. Cryst.* **10**, 538-545 (1957).
15. J.H. Sharp, *Br. Ceram. Trans. J.* **89**, 1-7 (1990).
16. F.S. Galasso, Structure, Properties, and Preparation of Perovskite-Type Compounds (Pergamon Press, New York, 1969), pp 1-25.

17. S.A. Sunshine, T. Siegrist, L.F. Schneemeyer, D.W. Murphy, R.J. Cava, B. Batlogg, R.B. van Dover, R.M. Fleming, S.H. Glarum, S. Nakahara, R. Farrow, J.J. Krajewski, S.M. Zahurak, J.V. Waszczak, J.H. Marshall, P. Marsh, L.W. Rupp, Jr., and W.F. Peck, *Phys. Rev. B* **38**, 893-896 (1988).
18. C.C. Torardi, M.A. Subramanian, J.C. Calabrese, J. Gopalakrishnan, E.M. McCarron, K.J. Morrissey, T.R. Askew, R.B. Flippen, U. Chowdhry, and A.W. Sleight, *Phys. Rev. B* **38**, 225-231 (1988).
19. R.M. Hazen, C.T. Prewitt, R.J. Angel, N.L. Ross, L.W. Finger, C.G. Hadidiacos, D.R. Veblen, P.J. Heaney, P.H. Hor, R.L. Meng, Y.Y. Sun, Y.Q. Wang, Y.Y. Xue, Z.J. Huang, L. Gao, J. Bechtold, and C.W. Chu, *Phys. Rev. Lett.* **60**, 1174 (1998).
20. D.R.F. West, Ternary Equilibrium Diagrams, 2nd ed. (Chapman and Hall, New York, 1982), pp. 1-15.
21. Y.K. Rao, in Phase Diagrams: Materials Science and Technology, edited by Allen M. Alper (Academic Press, New York, 1970), Vol. 1, Chap. 1, pp. 1-29.
22. R.S. Roth, C.J. Rawn, B.P. Burton, and F. Beech, *J. Res. Natl. Inst. Stand. Technol.* **95**, 291 (1990).
23. R.S. Roth, C.J. Rawn, J.J. Ritter, and B.P. Burton, *J. Am. Ceram. Soc.* **72**, 1545 (1989).
24. R.S. Roth, B.P. Burton, and C.J. Rawn, Paper presented at the Anaheim meeting of the American Ceramic Society, Nov. 1, 1989.
25. B.Hettich, B. Freilinger, P. Majewski, T. Popp, and K. Schulze, Paper presented at DGM Meeting: High Temperature Superconductors Materials Aspects, Garmisch-Partenkirchen, FRG, 9-11 May 1990.
26. Phase Diagrams for High T<sub>c</sub> Superconductors, edited by J.D. Whitler and R.S. Roth (The American Ceramic Society, Westerville, OH, 1991), pp. 120-163.
27. R. Muller, Th. Schweizer, P. Bohac, R.O. Suzuki, and L.J. Gauckler, *Physica C* **203**, 299-314 (1992).
28. C.L. Lee, J.J. Chen, T.P. Perng, J.M. Wu, T.S. Chin, R.S. Liu, and P.T. Wu, *J. Mater. Res.* **5**, 1403 (1990).
29. B. Hong, J. Hahn, and T.O. Mason, *J. Am. Ceram. Soc.* **73**, 1965 (1990).
30. U. Endo, S. Koyama, and T. Kawai, *Jpn. J. Appl. Phys.* **27**, L1476-L1479 (1988).
31. P. Strobel, W. Korczak, J.L. Hodeau, and J.L. Tholence, *Physica C* **161**, 155 (1989).

32. P. Majewski, B. Freilinger, B. Hettich, T. Popp, and K. Schulze, Paper presented at DGM Meeting High Temperature Superconductors Materials Aspects, Garmishch-Partenkirchen, FRG, 9-11 May 1990.
33. B. Hong and T.O. Mason, *J. Am. Ceram. Soc.* **74**, 1045 (1991).
34. R.S. Roth, C.J. Rawn, and L.A. Bendersky, *J. Mater. Res.* **5**, 46 (1990).
35. G.S. Grader, E.M. Gyorgy, P.K. Gallagher, H.M. O'Bryan, D.W. Johnson, Jr., S. Sunshine, S.M. Zahurak, S. Jin, and R.C. Sherwood, *Phys. Rev. B* **38**, 757-760 (1988).
36. T.G. Holesinger, D.J. Miller, L.S. Chumbley, M.J. Kramer, and K.W. Dennis, *Physica C* **202**, 109-120 (1992).
37. P. Majewski, H.L. Su, and B. Hettich, *Adv. Mater.* **4**, 508-511 (1992).
38. S.J. Golden, T.E. Bloomer, F.F. Lange, A.M. Segadaes, K.J. Vaidya, and A.K. Cheetham, *J. Am. Ceram. Soc.* **74**, 123-129 (1991).
39. D.R. Dietderich, B. Ullmann, H.C. Freyhardt, J. Kase, H. Kumakura, K. Togano, and H. Maeda, *Jpn. J. Appl. Phys.* **29**, L1100-L1103 (1990).
40. J. Kase, K. Togano, H. Kumakura, D.R. Dietderich, N. Irisawa, T. Morimoto, and H. Maeda, *Jpn. J. Appl. Phys.* **29**, L1096 (1990).
41. J. Tenbrink, K. Heine, and H. Krauth, *Cryogenics* **30**, 422 (1990).
42. K. Sato, T. Hikata, H. Mukai, M. Ueyama, N. Shibuta, T. Kato, T. Masuda, M. Nagata, K. Iwata, and T. Mitsui, *IEEE Trans. Mag.* **27**, 1231 (1991).
43. J. Kase, N. Irisawa, T. Morimoto, K. Togano, H. Kumakura, D.R. Dietdreich, and H. Maeda, *Appl. Phys. Lett.* **56**, 970 (1990).
44. M.F. Garbauskas, R.H. Arendt, J.D. Jorgensen, and R.L. Hitterman, *Appl. Phys. Lett.* **58**, 2987 (1991).
45. B. Heeb, S. Oesch, P. Bohac, and L.J. Gaukler, Accepted *J. Mater. Res.* June 1992.
46. R. D. Ray II, and E.E. Hellstrom, *Physica C* **172**, 435 (1991).
47. J. Bock, and E. Preisler, *Solid State Comm.* **72**, 453 (1989).
48. T.G. Holesinger, D.J. Miller, and L.S. Chumbley, *J. Mater. Res.* **7**, 1658 (1992).
49. J. Bock and E. Preisler, paper presented at the ICMC '90 Topical Conference on Materials Aspects of High Temperature Superconductors, Garmisch-Partenkirchen, May 9-11, 1990.

50. R.D. Ray II and E.E. Hellstrom, *Physica C* **175**, 255 (1991).
51. Y. Oka, N. Yamamoto, H. Kitaguchi, K. Oda, and J. Takada, *Jpn. J. Appl. Phys.* **28**, L213 (1989).
52. T. Hasegawa, T. Kitamura, H. Kobayashi, H. Kumakura, H. Kitaguchi, and K. Togano, *Appl. Phys. Lett.* **60**, 2692 (1992).
53. J. Polonka, M. Xu, Q. Li, A.I. Goldman, and D.K. Finnemore, *Appl. Phys. Lett.* **59**, 3640 (1991).
54. D.G. Hinks, L. Soderholm, D.W. Capone, II, B. Dabrowski, A.W. Mitchell, and D. Shi, *Appl. Phys. Lett.* **53**, 423-425 (1988).
55. K. Nassau, A.E. Miller, E.M. Gyorgy, and T. Siegrist, *J. Mater. Res.* **4**, 1330-1338 (1989).
56. T. Komatsu, R. Sato, C. Hirose, K. Matusita, and T. Yamashita, *Jpn. J. Appl. Phys.* **27**, L2293-L2295 (1988).
57. M.R. DeGuire, N.P. Bansal, and C.J. Kim, *J. Am. Ceram. Soc.* **73**, 1165-71 (1990).
58. T. Komatsu, R. Sato, K. Imai, K. Matusita, and T. Yamashita, *Jpn. J. Appl. Phys.* **27**, L550-L552 (1988).
59. M. Yoshimura, T.H. Sung, Z. Nakagawa, and T. Nakamura, *Jpn. J. Appl. Phys.* **27**, L1877-L1879 (1988).
60. H. Takei, M. Koike, H. Takeya, K. Suzuki, and M. Ichihara, *Jpn. J. Appl. Phys.* **28**, L1193-L1196 (1989).
61. Y. Ibara, H. Nasu, T. Imura, and Y. Osaka, *Jpn. J. Appl. Phys.* **28**, L37-L40 (1989).
62. B. D. Cullity, Elements of X-ray Diffraction, 2nd ed. (Addison-Wesley, Reading, MA, 1978), pp. 460-462.
63. D.J. Miller and T.G. Holesinger, *Applied Superconductivity* **1**, 121-129 (1993).
64. J.I. Goldstein, D.E. Newbury, P. Echlin, D.C. Joy, C. Fiori, and E. Lifshin, Scanning Electron Microscopy and X-ray Microanalysis (Plenum Press, New York, 1981), p. 306.
65. G. Cliff, and G.W. Lorimer *J. Microsc.* **103**, 203.(1975).
66. K.G. Vandervoort, G. Griffith, H. Claus, and G.W. Crabtree, *Rev. Sci. Instrum.* **62**, 2271-2275 (1991).
67. C.P. Bean, *Phys. Rev. Lett.* **8**, 250 (1962).

68. Handbook of Chemistry and Physics, 63rd ed., edited by R.C. Weast (CRC Press, Inc., Boca Raton, 1983), pp. B73-B165.
69. T. Siegrist, L.F. Schneemeyer, S.A. Sunshine, J.V. Waszczak, and R.S. Roth, *Mat. Res. Bull.*, **23**, 1429-1438 (1988).
70. A. Fuertes, C. Miravittles, J. Gonzalez-Calbet, M. Vallet-Regi, X. Obradors, and J. Rodriguez-Carvajal, *Physica C* **157**, 525-530 (1989).
71. T. Satoh, T. Yoshitake, Y. Kubo, and H. Igarashi, *Appl. Phys. Lett.* **53**, 1213-1215 (1988).
72. R.G. Buckley, J.L. Tallon, I.W.M. Brown, M.R. Presland, N.E. Flower, P.W. Gilberd, M. Bowden, and N.B. Milestone, *Physica C* **156**, 629-634 (1988).
73. D.E. Morris, C.T. Hultgren, A.M. Markelz, J.Y.T. Wei, N.G. Asmar, and J.H. Nickel, *Phys. Rev. B.* **39**, 6612-6614 (1989).
74. D.C. Sinclair, J.T.S. Irvine, and A.R. West, *J. Mater. Chem.* **2**, 579-580 (1992).
75. H. Rawson, Inorganic Glass-Forming Systems (Academic Press, New York, 1967), p. 9.
76. R. Bormann, and J. Nolting, *Physica C* **162-164**, 81-83 (1989).
77. M.J. Kramer, Iowa State University, Ames (private communication).
78. M.I. Pope and M.D. Judd, Differential Thermal Analysis (Heyden, London, 1977), p. 53.
79. Handbook of Chemistry and Physics, 63rd ed., edited by R.C. Weast (CRC Press, Inc., Boca Raton, 1983), p. B-88.
80. J. Bock, S. Elschner, and E. Preisler, Advances in Superconductivity III: Proceedings of the 3rd International Symposium on Superconductivity (ISS '90), November 6-9, 1990, Sendai, edited by K. Kajimura and H. Hatakawa (Springer-Verlag, Tokyo, 1991), pp. 797-800.
81. M.F. Berard and D.R. Wilder, Fundamentals of Phase Equilibria in Ceramic Systems, (R.A.N. Publishers, Marietta, OH, 1990), pp. 12-15.
82. K. Heine, J. Tenbrink, and M. Thoner, *Appl. Phys. Lett.* **55**, 2441-2443 (1989).
83. D. Gazit and R.S. Fiegelson, *J. Crystal Growth* **91**, 318 (1988).
84. A. Kurosaka, M. Aoyagi, H. Tominaga, O. Fukuda, and H. Osanai, *Appl. Phys. Lett.* **55**, 390 (1989).

85. B.N. Roy, Crystal Growth From Melts (John Wiley and Sons, New York, 1992), pp. 1-59.
86. M.J. Cima, X.P. Jiang, H.M. Chow, J.S. Haggerty, M.C. Flemings, H.D. Brody, R.A. Laudise, and D.W. Johnson, *J. Mat. Res.* **5**, 1834 (1990).
87. D.H. Kim, K.E. Gray, R.T. Kampwirth, J.C. Smith, D.S. Richeson, T.J. Marks, J.H. Kang, J. Talvacchio, and M. Eddy, *Physica C* **177**, 431 (1991).
88. T. Kanai, T. Kamo, S.P. Matsuda, and R. Shiobara, *Supercond. Sci. Techno.* **4**, 153 (1991).
89. P.F. Herrmann, C. Albrecht, J. Bock, C. Cottevielle, S. Elschner, W. Herkert, M-O. Lafon, H. Lauvray, A. Leriche, W. Nick, E. Preisler, H. Salzburger, J-M. Tourre, and T. Verhaege, submitted to proceedings of ASC '92, Chicago, USA August 23-28, 1992.